Investigating Cathode Catalyst Layer Degradation in Polymer Electrolyte Fuel Cells by Lab-based X-ray Computed Tomography

by

Robin Thomas White

M.A.Sc. (Material Science and Engineering), University of Toronto, 2014

B.Sc.H. (Nanoscience), University of Guelph, 2012

Thesis Submitted in Partial Fulfillment of the
Requirements for the Degree of
Doctor of Philosophy

in the
School of Mechatronic Systems Engineering
Faculty of Applied Sciences

SIMON FRASER UNIVERSITY

Fall 2019

Approval

Name:	**Robin T. White**
Degree:	**Doctor of Philosophy**
Title:	**Investigating Cathode Catalyst Layer Degradation in Polymer Electrolyte Fuel Cells by Lab-based X-ray Computed Tomography**

Examining Committee: **Chair:** Helen Bailey
Lecturer

Erik Kjeang
Senior Supervisor
Associate Professor _____

Gary Wang
Supervisor
Professor _____

Francesco P. Orfino
Supervisor
Research Associate _____

Mirza Faisal Beg
Internal Examiner
Professor
Engineering Science _____

Xianguo Li
External Examiner
Professor
Mechanical and Mechatronics Engineering
University of Waterloo _____

Date Defended/Approved: September 20, 2019 _____

Abstract

The commercial viability of polymer electrolyte fuel cells (PEFCs) has increased rapidly over recent years with applications in public and commercial transportation, back-up power, and un-manned autonomous systems. This has come as a direct result toward increasing evidence and severity of climate change due to greenhouse gas emissions; pushing the need for government regulations to introduce stricter limits on fossil fuel combustion in new passenger cars, as well as in other light-to heavy-duty vehicles. Further cost and durability improvements in PEFCs present significant opportunities as the technology continues to be refined. PEFCs are assembled as a series of layers, each having specific functionalities to optimize the cell performance during electrochemical conversion of chemical potential energy, in the way of hydrogen and oxygen, into useable electrical power, heat, and water. These PEFC materials can undergo considerable changes during operation, and lifetime testing through critical degradation processes, which can be uniquely captured using X-ray Computed Tomography (XCT) in this complex multi-layered system. XCT provides a unique ability to delve into the innermost structures through non-destructive imaging in diverse and extensive application areas. In this thesis, a novel small-scale fuel cell fixture that mimics the performance and degradation features of a full-scale PEFC assembly is presented. By combining the 3-dimensional visualization through repeated identical location tomography using XCT scans at various temporal stages of this small-scale fixture, powerful *in-situ* and *operando* investigations of dynamic material properties are obtained. This methodology is termed as 4D CT. By means of applying accelerated stress tests focused on cathode catalyst layer degradation, unique insight into the lifetime, dynamics and interactions between the catalyst layer and surrounding components was uniquely obtained using custom developed tools and analysis methods. These new methods allow for new investigations into the temporal changes of water saturation and cathode catalyst layer morphology. It has been found that during ageing, the morphological interaction between different layers can have a considerable impact on degradation mechanisms such as crack propagation. These results uncover unique evidence around the strongly interactive nature of material degradation within a fuel cell that has previously been unobserved.

Keywords: X-ray Computed Tomography, Fuel Cell, Durability, Catalyst Layer, Image Processing, Morphology

To my loving wife

Acknowledgements

First and foremost, I would like to express my most sincere gratitude toward my senior supervisor, Prof. Erik Kjeang and all the members of the SFU Fuel Cell Research Laboratory for their support, motivation, and enthusiasm through countless discussions and meetings. I would not have had the opportunity to learn so much without you all. I would like to take the opportunity to express my gratitude toward a few individuals who had to cope with my antics on a (far too) regular basis: Yadvinder Singh for his immense knowledge, eloquent scientific investigations and terrific taste in Indian cuisine; Dilip Ramani for his patience, support and unwavering ability to stay on pace during presentations; Frank Orfino for his technical knowledge, joyful nature and ability to extend short discussions into long (and loud) conversations. I would also like to thank Dr. Sebastian Eberhardt for his incredible depth of knowledge and saint-like patience. Many of the most important breakthroughs through the later course of my work resulted from your mentorship and I am incredibly grateful for your friendship. I would also like to thank Alan Young, Lida Ghassemzadeh, Warren Williams, Shanna Knights and the many extremely knowledgeable people at Ballard Power Systems for their support and meaningful discussion, and direction. I would also like to express my gratitude toward Ron Mott for his time and effort in assisting the many requests for hardware support. I would like to take this opportunity to express my sincere gratitude toward Monica Dutta who was not only patient and considerate toward a bunch of PhD students creating havoc, but also put in significant time and effort into supporting the research efforts of the project. The success of the research collaboration is directly related to your efforts, and I know we are all grateful.

I would like to take the opportunity to thank Maggie and Tony Luong; your love and friendship brought laughter, distraction, and motivation through this long and, at times, tiring adventure in a new city. As well, I would like to acknowledge my friends and teammates Ara Cho, Scott Dixon, Sun Jiang, Abe Robiso, Ben Cooper and all members of Caledonia Weightlifting/Crossfit Burnaby, without whom I would certainly have enjoyed my time far less.

Finally, I would like to acknowledge my wife, Hilary. Your unwavering love and support allowed me to pursue my passion to my greatest ability and I will forever be grateful.

Table of Contents

List of Tables

List of Figures

List of Acronyms

AST	Accelerated Stress Test
BOL	Beginning of Life
CAD	Computer Aided Design
CCL	Cathode Catalyst Layer
CNC	Computer Numerical Control
ECSA	Electrochemically Active Surface Area
EDS	Energy Dispersive Spectroscopy
EIS	Electrochemical Impedance Spectroscopy
EOL	End of Life
GSV	Greyscale Value
GUI	Graphical User Interface
keV	Kilo Electron Volt
MEA	Membrane Electrode Assembly
PEFC	Polymer Electrolyte Fuel Cell
SEM	Scanning Electron Microscopy
UTS	Ultimate Tensile Strength
XCT	X-ray Computed Tomography
XRM	X-ray Microscopy

Glossary

Capped	Refers to the incorrect scaling such that the expansion of greyscale values to their correct value are limited due to the restriction of maximum values for a datatype, e.g. 65535 for 16-bit.
Eccentricity	A measure of how much a conic section deviates from being circular. The eccentricity of a circle is 0. Related to the inverse of aspect ratio.
Ex-situ	Performing imaging when the sample is removed from its operational hardware and often manipulated but either cutting, polishing or embedding.
Greyscale	A numerical integer range of values that correspond to the scalar, one-dimensional value of a pixel in an image. This value range is dependent on the byte-scaling of the image i.e. 0 to 255 for 8-bit, 0 to 65535 for 16-bit.
In-situ	Performing imaging when the sample is still within its operational hardware such that the environment is maintained.
Membrane Electrode Assembly	Components that make up a polymer electrolyte fuel cell. It is comprised of the anode and cathode catalyst layers as well as the perflourosulfonic acid membrane.
Operando	Performing imaging when the sample is still within its operational hardware and operated to draw current in the case of a fuel cell.
Segmentation	Partitioning components of a digital image into labelled regions with the goal of simplifying the image to allow for further analysis.

Preface

The following thesis focuses on the methodology and tools developed for the investigation of degradation mechanisms in polymer electrolyte fuel cells utilizing X-ray computed tomography. It is compiled from a combination of peer reviewed publications, as well as unpublished reports and procedures. Where a formatted manuscript is used, a summary paragraph is provided along with any other relevant information. The following contributions are included in this dissertation:

Chapter 3

Contains excerpts from:

R. T. White, F. P. Orfino, M.E. Hannach, O. Luo, M. Dutta, A. Young and E. Kjeang, **3D Printed Flow Field and Fixture for Visualization of Water Distribution in Fuel Cells by X-ray Computed Tomography**, *J. Electrochem. Soc.*, 163 (2016) F1337-F1343. This is an open access article distributed under the terms of the Creative Commons Attribution 4.0 License (CC-BY-NC-ND, http://creativecommons.org/licenses/by/4.0/), which permits unrestricted reuse of the work in any medium, provided the original work is properly cited.

R. T. White, M. Najm, M. Dutta, F. P. Orfino, and E. Kjeang, **Communication—Effect of Micro-XCT X-ray Exposure on the Performance of Polymer Electrolyte Fuel Cells**, *J. Electrochem. Soc.*, 163 (2016) F1206 - F1208. Reproduced with permission from *J. Electrochem. Soc.*

Y. Singh, *R. T. White*, M. Najm, T. Haddow, V. Pan, F. P. Orfino, M. Dutta, and E. Kjeang, **Tracking the evolution of mechanical degradation in fuel cell membranes using 4D in situ visualization**, *J. Power Sources*, 412 (2019) 224-237. All co-authors agreed to publish the relevant section of this manuscript in this thesis. Reproduced with permission from *J. Power Sources.*

Chapter 5

Contains excerpts from *R. T. White*, A. Wu, M. Najm, F. P. Orfino, M. Dutta, and E. Kjeang, **4D in situ visualization of electrode morphology changes during**

accelerated degradation in fuel cells by X-ray computed tomography, *J. Power Sources*, 350 (2017) 94-102. Reproduced with permission from *J. Power Sources.*

Chapter 6

Contains excerpts from *R. T. White*, S.H. Eberhardt, Y. Singh, T. Haddow, M. Dutta, F. P. Orfino and E. Kjeang, **Four-dimensional joint visualization of electrode degradation and liquid water distribution inside operating polymer electrolyte fuel cells**, *Sci. Rep.*, 350 (2019) 94-102. This is an open access article distributed under the terms of the Creative Commons Attribution 4.0 License (CC BY, http://creativecommons.org/licenses/by/4.0/), which permits unrestricted reuse of the work in any medium, provided the original work is properly cited.

Chapter 7

Contains excerpts from *R. T. White*, D. Ramani, S.H. Eberhardt, M. Najm, F. P. Orfino, M. Dutta, and E. Kjeang, **Correlative X-ray tomographic imaging of catalyst layer degradation in fuel cells**, *J. Electrochem. Soc.*, 166 (2019) F914-F925. This is an open access article distributed under the terms of the Creative Commons Attribution 4.0 License (CC BY, http://creativecommons.org/licenses/by/4.0/), which permits unrestricted reuse of the work in any medium, provided the original work is properly cited.

Chapter 1.

Introduction

1.1. Motivation

We have entered a new era for alternative energy sources. Government regulations and proposals by various countries to ban the sale of internal combustion engine vehicles in the next 20-30 years aim to significantly reduce greenhouse gas emissions over the next half century [1], [2]. Clean energy technologies have thus been accelerated into the fore-front of today's scientific and engineering endeavors. Fuel cells promise to provide an alternative energy option to various diesel driven and other fossil fuel combustion technologies; from trains, unmanned aerial vehicles, automobiles (both commercial and consumer) as well as marine vehicles. In recent years, commercialization of these technologies are the result of significant investment by numerous transportation powerhouses, with almost all major automotive companies selling, or planning to sell, alternative energy vehicles, as well as government agencies looking to reduce emissions from public transportation services [3]–[6].

There is a wide range of fuel cell technologies, each with their own pros and cons. The most commonly used is polymer electrolyte fuel cells (PEFCs), which convert oxygen to water, electrochemically, through the oxidation of a fuel, providing a source of electrons to perform work through a circuit. This is common among all fuel cell types, however for PEFCs utilizing hydrogen gas as the fuel, separating the two platinum rich electrodes is a perfluorosulfonic acid polymer membrane. Other fuel cell types utilize a different fuel such as methanol in direct methanol fuel cells (DMFC), or even different electrodes and electrolyte such as solid oxide fuel cells (SOFC) using ceramics. Fuel cells can even use biological materials in the case of microbial fuel cells which use electroactive bacteria to degrade organic compounds to produce the hydrogen ions and electrons necessary to complete the reaction [7]. To continue to improve fuel cells and bring them to the level of commercialization required to significantly reduce our dependence on fossil fuels and non-renewables, there is a need to increase performance and improve lifetime, which in turn will reduce cost, the main barrier for most developing technologies. For fuel cells this means understanding complex interactions of transport phenomena and degradation

mechanisms over a wide range of materials. PEFCs, being the most promising candidate for transportation applications (as well as others), have low operating temperature, high power density, and easy scale-up, however, in general are affected by various degradation mechanisms. The membrane can suffer from pinhole formation and thinning, following chemical attack by radicals and mechanical stress. The catalyst and catalyst layer support can be prone to various degradation mechanisms, specifically carbon corrosion causing cracking and thinning as well as catalyst dissolution, migration, and agglomeration. Hydrophobicity of the gas diffusion layer can also decrease over operation time, which decreases its water transport ability, possibly causing flooding and reducing performance. Water management is crucial to maintain performance within a PEFC. Accumulation within the membrane and catalyst layer ionomer is beneficial and necessary for conductivity, however flooding of macro pores in the catalyst layer limits diffusion of reactant gases and reduces the active area available for the electrochemical reaction to take place. SOFCs on the other hand, do not suffer from this complexity; their simple construction and high temperature of operation allows for natural gas reformation and fast electrocatalysis using nonprecious metals as catalysts, in addition to the added benefit of high-quality heat by-product allowing for cogeneration boosting the efficiency to well above 70%, makes SOFCs ideal for stationary power applications [8]. However, power efficiency losses can result from changing composition and microstructure of cell components during operation [9].

Various analytical methods are thus used to study fuel cells, given their wide range of material properties. Common techniques are polarization curves to study performance losses over the operational range, cyclic voltammetry is used to obtain electrochemically active surface area, and electrochemical impedance spectroscopy is used to study reaction kinetics and monitor the change in the electrical properties of materials. Various imaging methods have also been used to provide unique insight into morphological structure, degradation mechanisms, and water management. Scanning electron microscopy (SEM) and transmission electron microscopy (TEM) can provide high resolution images on morphological changes to catalyst layers and membrane to study degradation mechanisms of PEFCs and even environmental SEM (ESEM) can be used for visualization of condensation on a surface [10]–[12]. However, these methodologies of imaging require significant sample preparation and are destructive in the sense that samples need to be cut and mounted and are limited exclusively to *ex-situ* type imaging.

Magnetic resonance imaging as well as neutron imaging have been used to better understand fuel cell systems by *in-situ* imaging, however limitations to availability as well as spatial and temporal resolution reduces the range of visualization applications [10]. X-ray computed tomography is a non-destructive imaging technique that is widely used in numerous scientific fields, primarily for its unique ability to probe inside complex structures and obtain 3-dimensional visualization with high spatial resolution with good temporal resolution. A novel and prevalent application of this technique is to acquire a set of tomographies at different experimental stages to assess any dynamic changes and obtain 4-dimensional imaging of a system under study. This methodology is well suited for the study of fuel cell systems and has been employed by various groups to study various fuel cell systems. The advantage of 3D imaging also includes expanding the scope of failure analysis compared to existing techniques (e.g. FIB SEM) greatly facilitating the study of interaction effects between various components during failure as well as dynamics of the materials during operation providing insights that have never before been observed. A summary of recent publication data is shown in Figure 1.1, highlighting publications focused on using X-ray computed tomography to study fuel cells (of various types). The number of publications has grown steadily since 2006 from researchers around the world. A large focus for previous research has been on understanding water distribution within the gas diffusion layer, as well as general structure of components with combined catalyst layer and gas diffusion layer accounting for 36%. These two cumulate to more than 50% of all publications. It should be noted that the figure below includes publications related to this thesis work, initiated in 2014. [9], [13]–[104].

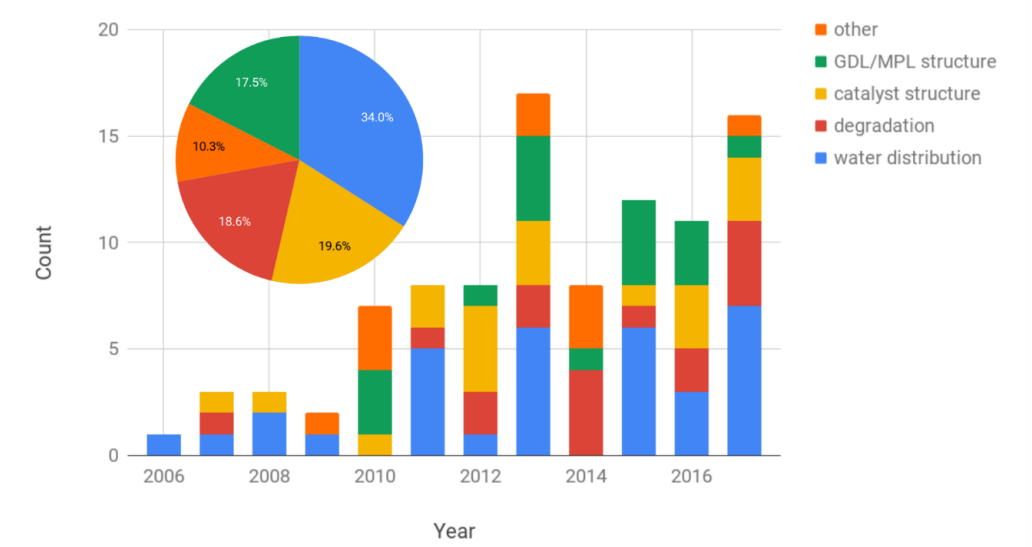

Figure 1.1: Summary of publications utilizing X-ray computed tomography to study fuel cells of various types. Water distribution can be any component although dominated by gas diffusion layer analysis, degradation can be any component, structure analysis is strictly beginning of life or material properties, other is anything which does not directly fit into these categories. Pie chart corresponds to total cumulative percentage.

1.2. Objectives

As identified above in Figure 1.1, there is a considerable volume of research focussed around the visualization and understanding of water within a fuel cell. This is indeed important information which is otherwise impossible to obtain without imaging methods such as Neutron tomography or X-ray tomography, however it is only part of the story. There has been a separation between the investigation of water distribution within an operating fuel cell, and the characterization of fuel cell material behaviour *in-situ*. Previously, synchrotron X-ray tomography has been used to visualize the fast, dynamic behaviour of water through the GDL, and separately, lab-based X-ray tomography has been used typically in visualization of individual components such as the GDL porosity, or cathode catalyst layer morphology (using nano-XCT). This has primarily been for 2 reasons: 1) Beam-time at a synchrotron facility is extremely competitive and widely unavailable limiting research to a small community who's research focus is on fluid mechanics within fuel cells as these facilities are essential in visualizing these types of dynamic systems at short time-scales; 2) Lab-based XCT technology has been applied only to characterization, either due to research group interest, or available technology. Through a combined approach to study both morphological changes as well as water

distribution, a greater understanding on the interconnectivity of components and their relation to lifetime and performance can be gained.

The aim of this thesis is to utilize X-ray computed tomography to study degradation mechanisms in PEFCs, primarily with a focus on cathode catalyst layer degradation. This presents the first combined effort to characterize morphological changes during fuel cell operation, as well as visualize water distribution, and the impact that both material morphological changes, and water distribution play with each other. The proposed research can be separated into the following major activities: design and development of a small-scale fuel cell fixture with validation of adopted operation protocols; integration of this fixture into a 4-dimensional visualization workflow to assess degradation features within the cathode catalyst layer during carbon corrosion; integration of this workflow to incorporate visualization during operation to image and quantify the liquid water distribution; combined correlative imaging of the cathode catalyst layer porosity through nano-scale XCT imaging at various corrosion stages with 4-dimensional visualization of cathode catalyst layer morphological changes and water distribution changes.

Through the development of hardware to enable *in-situ/operando* 4-dimensional imaging, cathode catalyst layer degradation as well as alternative degradation mechanisms in relation to membrane mechanical fatigue, and the role of interaction of components, such as gas diffusion layer morphology on catalyst coated membrane behaviour, were investigated in this work. Hardware alone would not fully support quantitative analysis and thus additional image processing workflows and tools were also developed. These tools were created specifically for fuel cell component analysis as well as investigation of liquid water by-product from the electrochemical reaction during operation. Using these tools, new insights into local degradation features were observed and quantified for the first time. Catalyst layer crack formation, propagation and interaction were investigated utilizing an accelerated stress test (AST) to target carbon corrosion specifically. Combined analysis of catalyst layer degradation and liquid water accumulation during operation were performed for the first time with new insights into the dynamic behaviour of fuel cell components. Nano-scale analysis on morphology changes and relation to fuel cell performance were also investigated through a correlative workflow that was developed and applied for the first time in PEFCs. Using this method, exact location analysis can be achieved to understand local effects on degradation mechanisms and the resulting impact on nanoscale structure.

1.3. PEFC Fundamentals

1.3.1. Working Principle and Component Materials

Fuel cells in general are electrochemical devices which convert chemical energy into electrical energy and heat to form a power source. Specifically, in polymer electrolyte fuel cells (PEFCs), the fuel used is hydrogen which undergoes oxidation at the anode to form protons and free electrons. These protons migrate through an electrically insulating, but ion conducting polymer electrolyte membrane, typically made from Nafion®; a sulfonated tetrafluoroethylene-based fluoropolymer. Meanwhile, the electrons are transferred via an external electrical circuit to be used to perform work. On the other side of the membrane is the cathode, which reduces oxygen that combines with the migrated protons and electrons to form water. Written out, the chemical reactions are as follows:

Anode: $\mathbf{H_2 \rightarrow 2H^+ + 2e^-}$

Cathode: $\mathbf{\frac{1}{2}O_2 + 2H^+ + 2e^- \rightarrow H_2O}$

Total: $\mathbf{H_2 + \frac{1}{2}O_2 \rightarrow H_2O}$ **(1.1)**

Depicted in Figure 1.2 are the various components each with a specified functionality to optimize performance and efficiency. Housed around the Membrane Electrode Assembly (MEA) are the flow field plates which act to distribute the gases inside the fuel cell. Additionally, they also act to connect the external electrical circuit to the MEA and act as a thermal conductor. Typically, these plates are fabricated from compressed carbon/graphite with cured resin to allow for sufficient electrical and thermal conduction as well as be non-porous to prevent gas leaks.

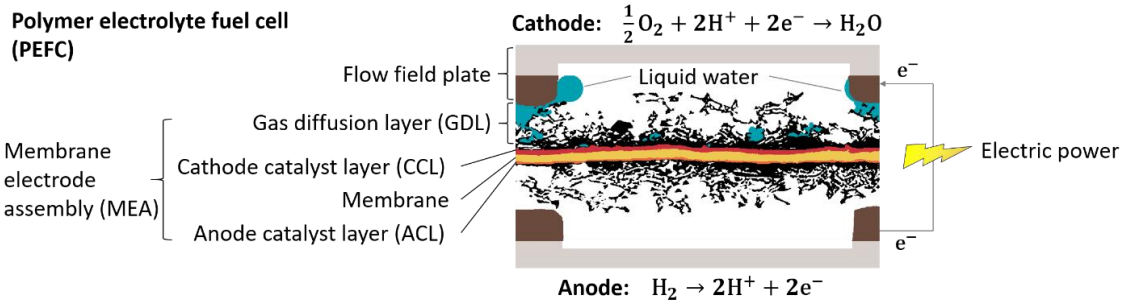

Figure 1.2: Schematic of polymer electrolyte fuel cell (PEFC) components obtained from XCT visualization of an operating fuel cell, outlining the electrochemical reactions, electronic transport and liquid water generation. The inset highlights a simplified illustration of the cathode catalyst layer composition and structure. Modified from White et al. Sci. Rep., 350 (2019) 94-102

The gas diffusion layer's main purpose is to allow for distribution of gas evenly over the whole area of the MEA. In addition, it also employs a high electrical conductivity to allow for efficient flow of electrons from the anode to the cathode catalyst layer from connection with the flow field plates. Usually, it consists of carbon fibers arranged into a cloth or paper, which can be held together by a teflonated binder to improve water removal. Porosities of GDLs are typically quite high when uncompressed, with ranges from 70-90 % and pore diameters between 10 and 80 µm and have a thickness between 200 and 400 µm [105]–[107]. Compression of the GDLs has a direct impact on the permeability and transport properties as well as the electrical connection between the flow field plates, and as such is an important parameter. Typically compression of about 25% thickness is employed, however based on specific architecture this number can vary [106]. Often, at the interface between the catalyst layer (anode or cathode) a microporous layer (MPL) is added onto the GDL which is composed of carbon black powder mixed with polytetrafluoroethylene (PTFE) with pore sizes typically between 100 and 500 nm. The main function is to enhance performance by improved water management and mitigate cathode catalyst layer flooding at high current density operation [30].

Anode and cathode catalyst layers of PEFCs are typically composed of similar materials unlike many other electrochemical devices. The main function of the anode catalyst layer is to lower the activation energy of the hydrogen oxidation reaction, while the cathode catalyst layer lowers the same for the oxygen reduction reaction. For this purpose, platinum (Pt) and platinum-based alloy nanoparticles is the most effective material, however due to its relatively high cost [108], a significant amount of research is being conducted into lower Pt loadings as well as non-platinum group metal catalysts

which can significantly reduce the cost of fuel cells [109]. The catalyst nanoparticles are typically on the order of 5 nm in diameter and are supported on larger carbon nanoparticles to allow for high Pt dispersion and high electrical conductivity [110]. In addition, high porosity is important to allow for efficient gas flow. The pore structure is formed by carbon black particles forming agglomerates in the range of 20 – 100 nm, with porosity between the primary particles and between the agglomerates. Typically, the anode catalyst layer has a much lower Pt loading compared to the cathode without suffering kinetic losses due to the much faster hydrogen oxidation reaction.

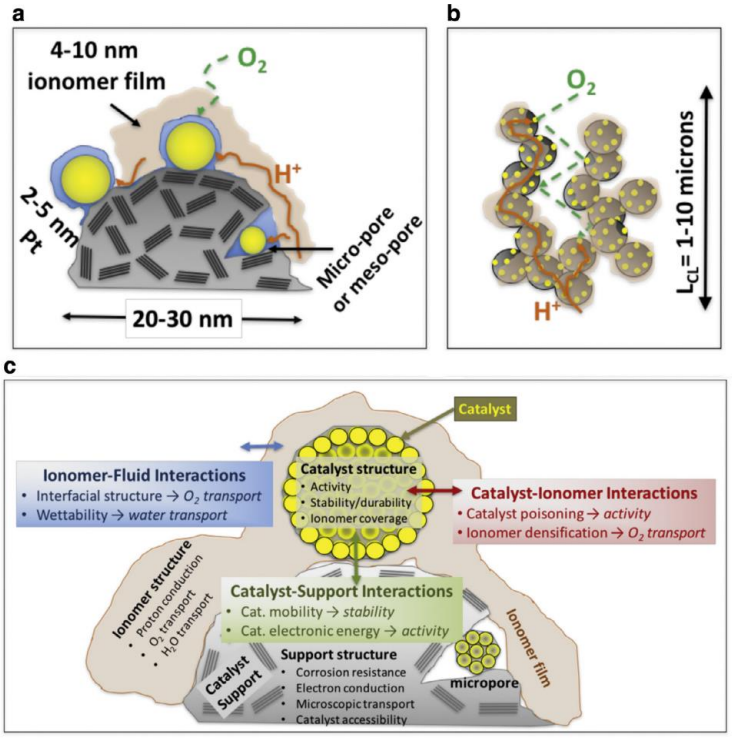

Figure 1.3:a) Schematic of a cathode catalyst particle with carbon support, Pt nanoparticles (yellow) and ionomer film demonstrating the flow of H^+ ions and oxygen reactant gas. (b) Agglomerate of catalyst particles demonstrating the approximate diffusion length required for reactants. (c) Summary of overall interaction between ionomer, Pt catalyst particle and catalyst carbon support. Reprinted with permission from Elsevier. Copyright 2018 Current Opinion in Electrochemistry. [109]

Surrounding the catalyst particle in a thin 4-10 nm shell, as depicted in Figure 1.3a, is the perfluorosulfonated ionomer. [109] This material's main function is to allow for the conduction of protons and create a triple point where gas, electron and proton conducting phases meet for the completion of the electrochemical reaction. Additionally, it acts to

facilitate water transport as well as a binder for the catalyst particles. The catalyst structure is possibly the most complex within a PEFC and the overall CL structure arises from agglomeration of the basic 100 – 130 nm aggregated Pt/C-ionomer structures [109]. A summary is shown in Figure 1.4 of the underlying interactions and approximate structure. The ionomer weight percent can play a significant role on structure and performance by balancing between coverage and transport, as well as blockage; too low a value and activation sites that form a triple point are minimal, too high a value and potential activation sites can become blocked by insufficient O_2 pathways, as demonstrated in Figure 1.4 for two common catalyst layer support structures Ketjen black and Vulcan XC-72 [110].

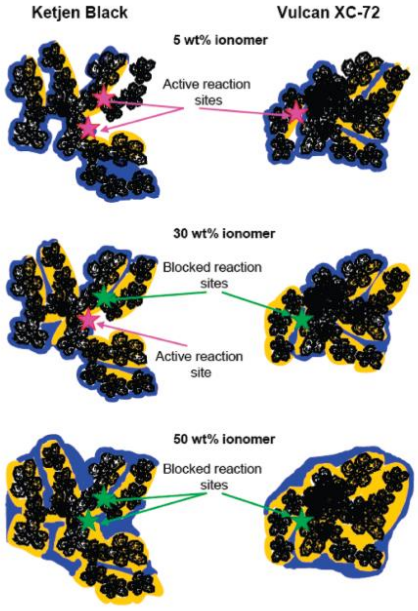

Figure 1.4: Schematic demonstrating the active site location where gas, electron and proton conducting phases meet and the impact of ionomer weight percent as well as excess water on blocking these sites. Reprinted with permission from [110]. Copyright 2018 American Chemical Society.

1.3.2. Efficiency and Voltage Losses

The behaviour of a fuel cell under operation is typically measured using a polarization curve. This measurement characterizes the change in voltage as a current density is drawn from the fuel cell, which from the electrical power equation, describes the

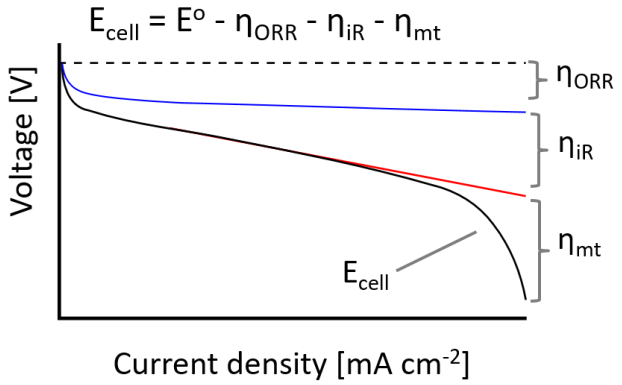

Figure 1.5: Representation of polarization curve with dashed line indicating the equilibrium potential and associated overpotential losses resulting in the final cell potential indicated by the solid black line.

over-all ability to create useable power. The conversion of fuel to work by conventional methods such as through thermo-mechanical engines are described by the Carnot cycle. Their efficiency is limited by the difference between source and sink temperatures and typically have a value of 20% efficiency [111]. The operating efficiency of a fuel cell is compared to the equilibrium potential E^o as predicted by the Nernst equation:

$$\mathbf{E^o = E^{oo} - \frac{RT}{nF} \ln\left(\frac{\prod a_{products}^{v_{products}}}{\prod a_{educts}^{v_{educts}}}\right)} \qquad \mathbf{(1.2)}$$

where E^{oo} is the standard potential, R is the ideal gas constant, T is the cell temperature, F is Faraday's constant, n is the number of electrons transferred and $a_{products/educts}^{v_{products/educts}}$ is the activity and stoichiometric factors for products and educts, respectively. For the overall reaction in a PEFC from Eq 1.1, assuming product water to be in liquid phase (a_{H2O} = 1), this can be simplified to:

$$\mathbf{E^o = E^{oo} - \frac{RT}{nF} \ln\left(\frac{1}{p_{H_2} p_{O_2}^{\frac{1}{2}}}\right)} \qquad \mathbf{(1.3)}$$

For simplicity, considering room-temperature operation at $\boldsymbol{p_{H_2}}$=$\boldsymbol{p_{O_2}}$ = **1 atm** this yields an equilibrium potential of 1.23 V. This is shown in Figure 1.5 as the dashed line. In

reality, the starting open circuit voltage (OCV) for a fuel cell is still below this potential even before a current has been applied. This is often referred to as the mixed potential. This is typically due to losses associated with electrical shorts, impurities and gas crossover. When a current is drawn from the cell, the system is no longer in equilibrium and an overpotential associated with the reaction kinetics is created. This is described by the Butler-Volmer equation for net oxidation and reduction reactions:

$$j = j_0 \cdot \left[\exp\left(\frac{a_a F}{RT}\eta_{act}\right) - \exp\left(\frac{-a_c F}{RT}\eta_{act}\right)\right] \quad \textbf{(1.4)}$$

where j is the current density, j_0 is the exchange current density, a_c and a_a are the cathode and anode transfer coefficient, respectively, F is the Faraday constant, and η_{act} is the activation overpotential. In a PEFC the exchange current density is approximately six orders of magnitude smaller for the oxygen reduction reaction (ORR) than for the hydrogen oxidation reaction [112]. For this reason, cathode activation overpotentials are considered to dominate and therefore η_{act} is often written as η_{ORR} as in Figure 1.5.

Ohmic resistance losses occur linearly according to Ohm's Law, with the dominant loss occurring from ionic resistance of the membrane. Additional resistance losses are associated with the catalyst layers, gas diffusion layers, bipolar plates and contact resistances at interfaces between materials, as well as resistance of the electrical connections. These losses become more dominant at moderate to high current densities.

At high current densities, mass transport losses become the dominant factor for performance loss. As the name suggests, this overpotential is caused mainly due to the limited diffusive transport of reactants from the gas channels to the triple point reaction sites in the catalyst layer. It is especially apparent for diluted reactants such as oxygen in air. In addition, the high volume of water being produced can limit the flow of reactant gases and is often referred to as flooding – where liquid water can clog pathways for diffusion of reactant gases, in particular of oxygen in the cathode catalyst layer.

Considering all these factors, typical fuel cell efficiency is lowered to 40 – 60% depending on operating conditions and architecture. Added heat recovery and utilization can boost the overall efficiency to as high as 80% [111].

1.4. Cathode Catalyst Layer Degradation

The performance lifecycle of fuel cells can be affected by degradation of the membrane electrode assembly (MEA) due to a number of chemical and mechanical stresses associated with operational cycles. Conditions such as cell environment, temperature, pressure, current, voltage, fuel or oxidant stream impurities, as well as transient and continuous operation, represent some of the factors that can impact the life of PEFCs [113]–[115]. The cathode catalyst layer (CCL) is particularly susceptible to degradation as it is exposed to oxidizing conditions. One of the major degradation mechanisms faced is the corrosion of the carbon support generated by high potential fluctuations. Additionally, the agglomeration and dissolution of platinum nanoparticles can significantly reduce the number of active sites, negatively impacting performance. In order to meet and exceed the durability required for fuel cell technology, understanding of these degradation mechanisms are crucial.

1.4.1. Carbon Corrosion

While the kinetics of carbon corrosion under typical PEFC operating conditions are usually slow, local fuel starvation and cell reversals may result in significant performance losses due to an accelerated loss of active surface area and alteration of pore morphology over time [116], [117]. These adverse conditions can arise from a number of operating situations such as transient power demands and localized water blockage causing regional fuel starvation [118].

At potentials greater than 0.2 V_{RHE} the carbon support is thermodynamically unstable (1.5-1.7), although even in the presence of platinum, the kinetics of carbon oxidation are relatively slow. However, prolonged periods of high potential such as during low electric power demand can still cause adverse degradation effects. In reality, potentials greater than 1.2 V_{RHE} are required to oxidize carbon at reaction rates high enough to cause sudden adverse structural damage [119].

$$\mathbf{C_{(s)} + 2H_2O \rightarrow CO_{2(g)} + 4H^+ + 4e^-} \quad \mathbf{E^0 = 0.207 V_{RHE}} \qquad \textbf{(1.5)}$$

$$\mathbf{C_{(s)} + H_2O \rightarrow CO_{(g)} + 2H^+ + 2e^-} \quad \mathbf{E^0 = 0.518 V_{RHE}} \qquad \textbf{(1.6)}$$

$$\mathbf{CO_{(g)} + H_2O \rightarrow CO_{2(g)} + 2H^+ + 2e^-} \quad \mathbf{E^0 = -0.103 V_{RHE}} \qquad \textbf{(1.7)}$$

During the lifetime of an automotive fuel cell stack, a multitude of start-up/shutdown (SU/SD) cycles occur. During these cycles, complete or even partial fuel starvation from a progressing hydrogen/air front can happen without appropriate operating strategies. This state requires that water electrolysis and carbon oxidation occur on the fuel cell anode in order to provide the necessary protons and electrons for the reduction of oxygen on the cathode. Local fuel (hydrogen) starvation from non-uniform distribution of fuel to the anode (see Figure 1.6) and the crossover of oxygen through the membrane causes potential shifts which can cause the cathode half-cell potential to reach $1.5V_{RHE}$, leading to significant carbon corrosion through oxidation of the carbon support resulting in unsupported an inactive platinum [12], [120]. A schematic is shown in Figure 1.6 demonstrating a local fuel starvation event creating an air/fuel boundary (region B) causing carbon corrosion on the cathode [121].

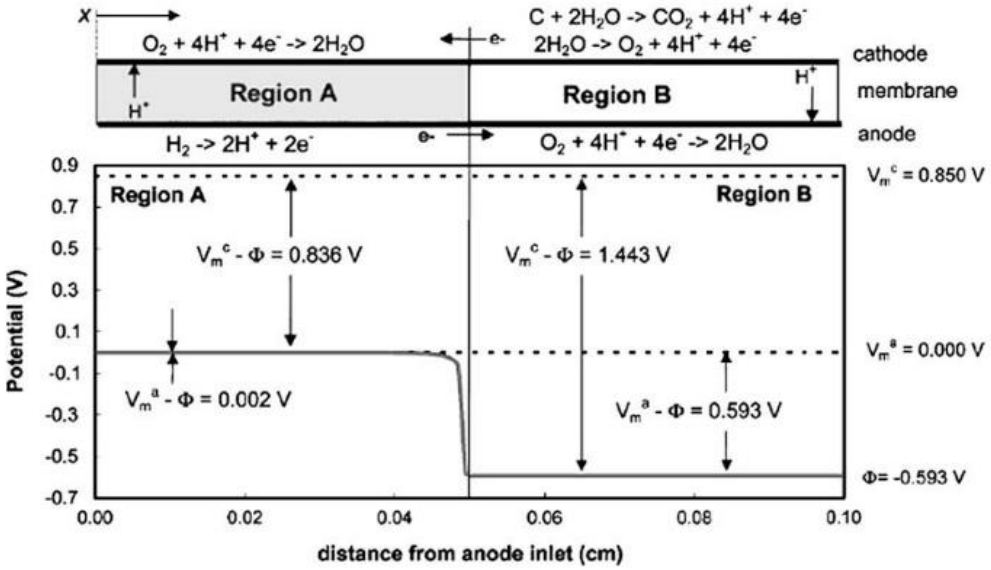

Figure 1.6: Schematic illustration of the potential distribution along the anode flow path under reverse-current conditions; region A denotes the section of the cell where hydrogen is available; region B denotes the section exposed to oxygen from crossover and fuel starvation. Reproduced with permission from Electrochemical and Solid-State Letters, 8, A273-A276 (2005). Copyright 2005, The Electrochemical Society [121]

Although there is adequate electrochemical understanding of the corrosion of carbon support, the morphological impact that causes performance losses is still a topic of current research. Thickness reduction and cracking have been observed using *ex-situ* SEM imaging, see Figure 1.7 [103], [122]–[125], however due to the nature of sample preparation, quantification of the direct impact of carbon corrosion is limited. The advanced understanding to overall interfacial effects, such as between the membrane and catalyst layer under operation conditions, or GDL and catalyst layer following stages of corrosion cannot be observed from limited two-dimensional views. In addition, the distribution of water plays a significant role on further degradation by flooding and gas blockage, as well as it is directly involved with the corrosion reaction. As such, observing degradation in relation to water distribution is of vital importance to improve understanding. Furthermore, knowing changes in catalyst layer porous nanostructure requires three-dimensional visualization. In order to develop improved mitigation techniques as well as new materials for enhanced lifetime a more thorough understanding of the adverse effects of carbon corrosion is needed which can only be obtained by direct visualization. In particular to local morphological features, which act as nucleation sites for significant degradation mechanisms upon corrosion and fatigue that can lead to complete failure of the fuel cell.

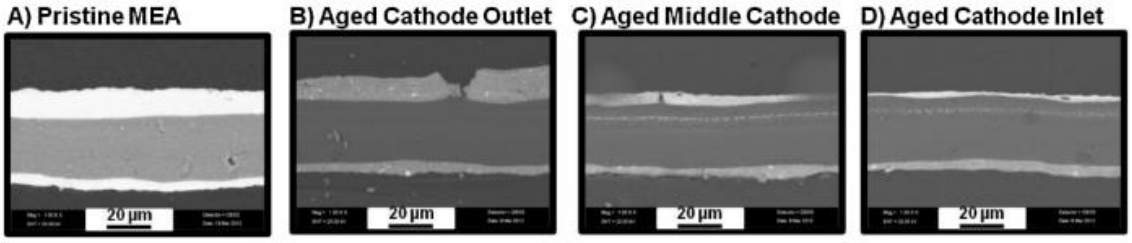

Figure 1.7:SEM images of (A) a pristine MEA and of (B–D) the MEA, aged under SU/SD cycles, taken at different locations. Thickness decrease of the cathode catalyst layer as well as platinum in the membrane band is observable. Reproduced with permission from Elsevier. Copyright 2013 Applied Catalysis B: Environmental [122]

1.4.2. Platinum Dissolution

In order to improve performance and reduce cost of a PEFC, nanometer sized particles of platinum are supported on high surface area carbon support. This increases the electrochemically active surface area (ECSA) and allows for lower platinum loading, typically $O(10^{-1})mg/cm^2$, however this also leads to a more unstable platinum, with the

equilibrium potential for dissolution decreasing with particle size [126]. The Pt particles have been shown to dissolve according to the following mechanism [118], [127]–[129]:

$$\mathbf{Pt} + \mathbf{H_2O} \rightarrow \mathbf{PtO} + \mathbf{2H^+} + \mathbf{2e^-} \quad \textbf{(1.8)}$$

$$\mathbf{PtO} + \mathbf{2H^+} + \mathbf{2e^-} \leftrightarrow \mathbf{Pt^{2+}} + \mathbf{H_2O} \quad \textbf{(1.9)}$$

Platinum dissolution is a transient process occurring significantly during potential change from formation and reduction of Pt-oxides, as described above, and has been observed at potentials around +0.6–0.7 V vs. RHE. Once dissolved, Pt ion migration toward the anode side of the membrane occurs as a result of diffusion and electric field, resulting in a band of platinum observable in the membrane. The distance of band formation is dependant on the partial pressure of crossover H_2, as H_2 will reduce Pt ions to form metallic platinum in the membrane [130]. In other cases, platinum ions will dissolve in ionomer, migrate toward neighbouring particles and agglomerate, leading to an increase in average particle size [131], [132]. This mechanism of dissolution and redeposition is an example of Ostwald ripening, where surface energy minimization is the driving force for agglomeration [133]. Nevertheless, the resulting impact of either form of migration of platinum is a decrease in ECSA and thus a decrease in lifetime performance. A schematic of these processes is shown in Figure 1.8. [132]

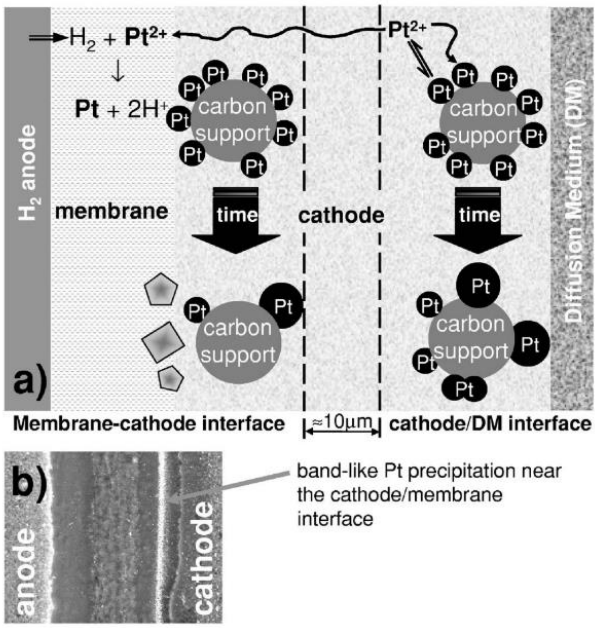

Figure 1.8: (a) Schematic representing platinum surface area loss through dissolution and precipitation, and Ostwald ripening; (b) SEM cross-section showing platinum band in the membrane. Reproduced with permission from J. Electrochem. Soc., 152, A2256 (2005). Copyright 2005, The Electrochemical Society.[132]

A summary of the overall mechanisms leading to performance loss and the measurable characteristics is shown in Figure 1.9, which has been adapted from [128] to show imaging characterization. Overall there are many mechanisms to electrode degradation however the ability to observe these processes can lead to a greater understanding and improved fuel cell design.

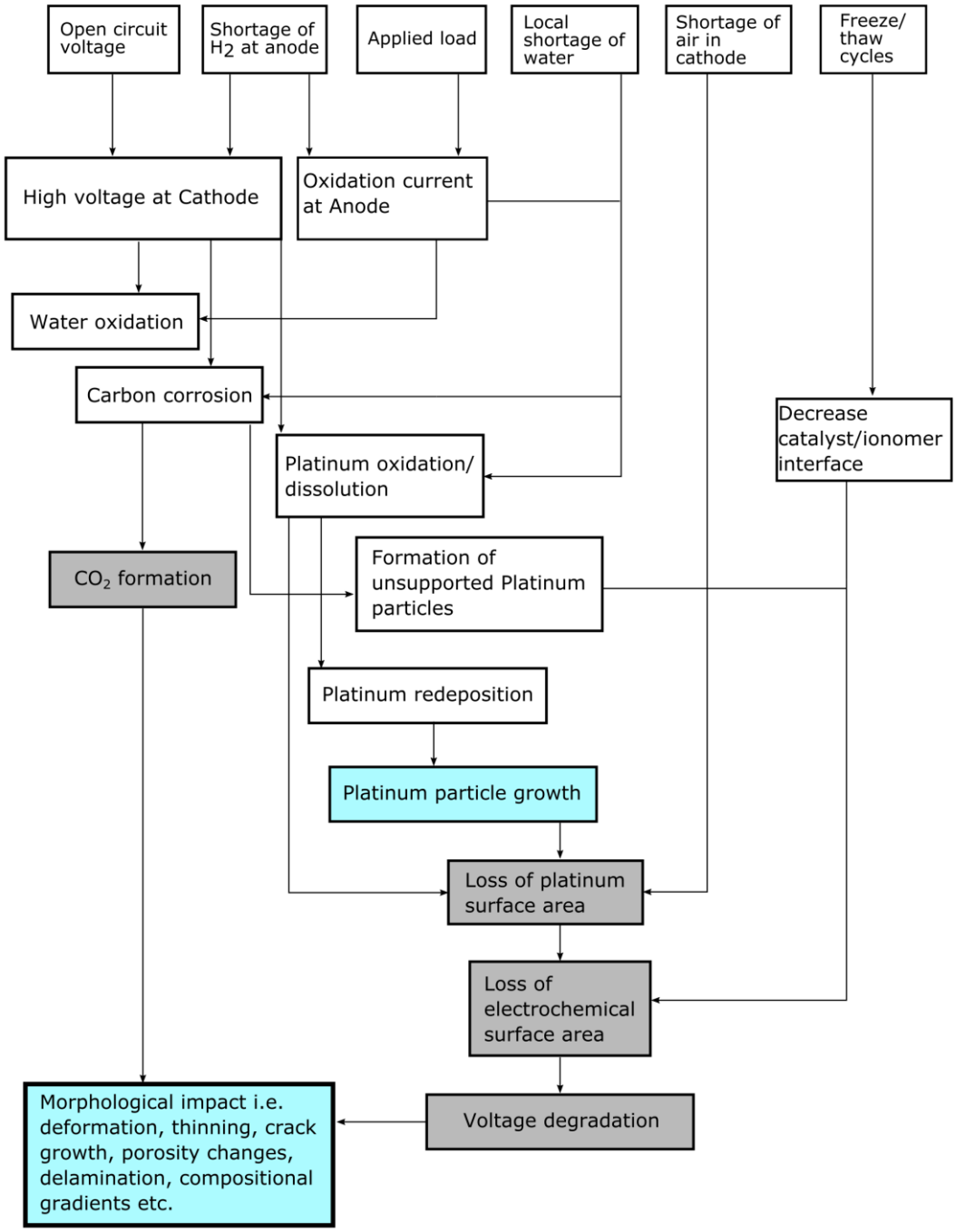

Figure 1.9: Summary of mechanisms known to cause performance losses resulting from cathode catalyst layer degradation. Measurable impact is shown in shaded boxes with observable effects via imaging shown in light blue boxes. Adapted from [128]

Chapter 2. X-ray Computed Tomography

Commercial laboratory-based X-ray Microscopes (XRM) were used to perform X-ray Computed Tomography (XCT) of all visualizations through the course of this work. The two systems are the Zeiss Xradia Versa 520, providing resolution on the macro-scale, as well as the Zeiss Xradia Ultra 810 which provides nano-scale resolution imaging. The term XRM is to be used in differentiation from micro-XCT systems which imply that geometrical magnification is used. In XRM, optical lenses are used to provide additional magnification without the need to go to extraordinary distances, since with geometrical magnification the resolution scales with the distance separating the divergent X-ray source and detector. The following chapter provides a brief overview of the working principles of XCT imaging, differences between synchrotron and laboratory systems as well as differences between the systems themselves.

2.1. Synchrotron vs. Laboratory Systems

X-ray Computed Tomography is an imaging method which allows for a full three-dimensional representation of an irradiated object to be calculated. The three-dimensional visualization is a virtual reconstruction of the object, as it is not directly observed but reproduced using a principle proved by Bohemian mathematician Johan Radon. He showed that the distribution of material in an object can be calculated if the integral values along any number of lines passing through the same layer are known, where this integral is known as the Radon transform [134]. Later the Nobel prize in Medicine was awarded to engineer Godfrey Hounsfield who is credited with the invention of the first CT scanner in 1972 [135] and physicist Allan Cormack [136] who developed a method for calculating absorption distributions based on transmission measurements [137]. Simply, XCT works through a process where a collection of multiple X-ray radiographs, which are single images where each pixel represents the relative attenuation through the irradiated object, are collected at various angles allowing for the collection of a sinogram. Much like a Fourier transform, a sinogram is the Radon transform representation of the object which contains the necessary data to reconstruct the original object. The reconstruction is then performed by back projecting each projection and then summing all backprojections to generate an image slice. This is then repeated through the full volume of the object. In addition, filters are applied to reduce blurring as presented by Shepp and Logan [138]. By

using a higher number of projections, a more accurate representation of the original object can be formed, as shown in Figure 2.1.

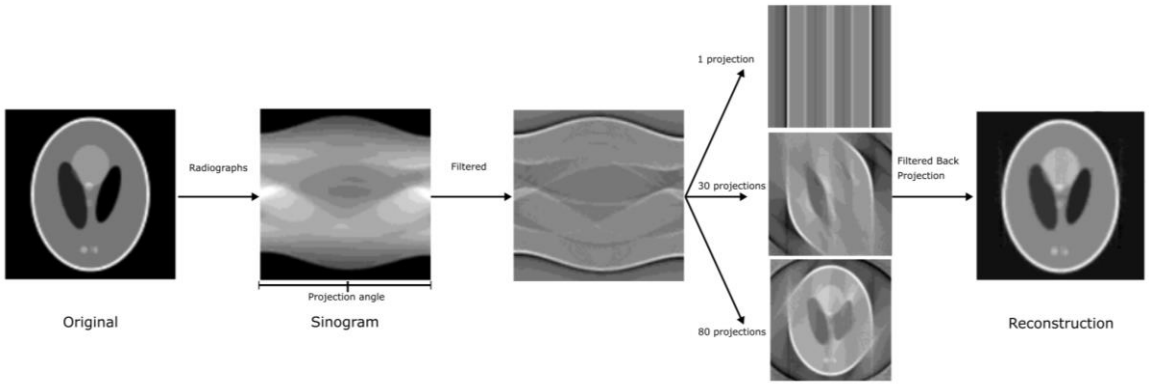

Figure 2.1: The principle of X-ray Computed Tomography reconstruction after obtaining a Sinogram and the effect of the number of projections on the quality of the reconstructed visualization [134].

The principle of computed tomography as described above is the same regardless of the imaging source, it is even used in other imaging methods such as positron emission tomography (PET) and ultrasound tomography [139]. The difference between laboratory and synchrotron systems is primarily the source. Laboratory systems, such as those used in the present work, rely on accelerated electrons striking a metal target to produce X-rays, such as Tungsten used in the Versa system and Chromium used in the Ultra system. These incident electrons excite atoms in the target material which release energy in the form of photons in the X-ray spectrum [140]. Different characteristic emission lines are produced corresponding to specific electron orbital energy as well as broad-band emission spectra up to the maximum energy of the accelerating voltage. This creates a polychromatic X-ray source [141]. Synchrotron X-ray sources are produced from electrons travelling around a large track (~170m) known as a storage ring near the speed of light, these electrons are then diverted into auxiliary compartments which create strong magnetic fields perpendicular to the beam which are used to create high energy photons [142]. Following this, the photons then pass through a monochromator as well as various X-ray optics to be used at the end station. This is the main difference between the two systems. Synchrotron sources have the luxury of monochromatic photons, as well as high flux, whereas laboratory systems are limited by much lower flux and usually polychromatic

spectra; a further comparison is discussed in section 3.3. This lower flux typically means that imaging times are much longer in laboratory systems, however access to synchrotron stations is extremely limited. A synchrotron end station can cost tens of millions of dollars and time availability is very limited, requiring proposal submission and selection through a lengthy process. Laboratory systems cost approximately $1/10^{th}$ of synchrotron end stations and can be much more readily available [143]. For slower temporal effects such as those of degradation mechanisms in PEFCs this makes laboratory systems perfect for 4-dimensional in-situ imaging experiments.

2.2. Interaction of X-rays with Matter

X-ray imaging is typically performed in the range of $O(10^{1\text{-}2})$ keV. This is because of the attenuation of the X-ray beam which occurs from the interaction with the object material constituents. A high attenuation difference can mean high contrast sensitivity, and low energy X-rays typically have high attenuation. The attenuation of X-rays in this imaging energy range is a result from a combination of scattering events as well as photoelectric absorption, an example of this is shown for carbon in Figure 2.2 [144], [145].

The photoelectric effect is described by the absorption of an incident photon by a core electron. This electron is consequently emitted from the atom, which results in a hole which is subsequently filled by an electron in an outer orbital following emission of a photon. X-rays have similar energy to the binding energy of core shell electrons and so this form of interaction is dominant [146]. Scattering events occur when a photon is scattered and changes direction without losing energy (elastic or coherent) or when some amount of energy is transferred to a bound electron (inelastic or incoherent).

The relative amount of attenuation is usually described as either mass attenuation with units cm^2/g or linear attenuation which considers the density of the material and has units of cm^{-1}. The decrease in incident X-ray intensity is described by Beer-Lambert's law:

$$\boldsymbol{I(x,E) = I_o e^{-\int \mu(E) dx}} \qquad \textbf{(2.1)}$$

where μ is the attenuation coefficient of the material with thickness *x* and at energy *E*. In addition to X-ray attenuation, a phase change upon interaction with material also occurs. This phase shift can be used to improve contrast when attenuation difference is small

between different materials of similar density and/or similar atomic number. This is discussed further in section 2.3.3.

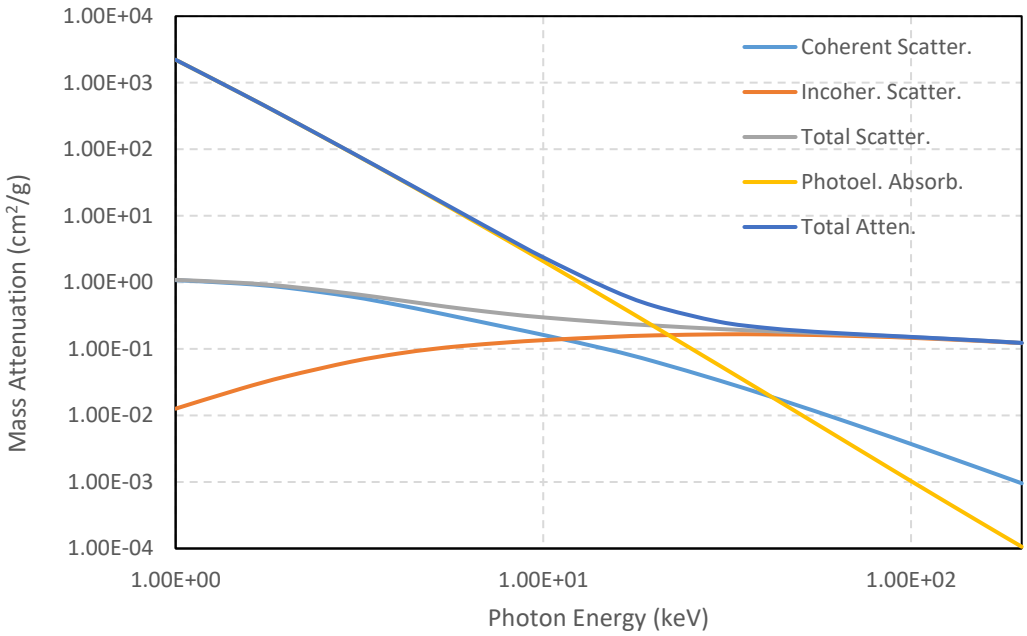

Figure 2.2: Plot of the interactions of X-rays with matter which cumulate to form the attenuation coefficient as a function of X-ray incident energy [144], [145].

2.3. Computed Tomography Systems and Imaging Modes

2.3.1. Micro-scale Imaging

As previously mentioned, the system used for micro-scale resolution imaging is the Zeiss Xradia Versa 520 XRM. A schematic of the system layout and optics is shown in Figure 2.3. This system employs a transmission X-ray source with Tungsten anode and accelerating voltage range of 30 – 160 kV. It also houses an automated filter wheel which can be used to tune the X-ray spectrum and improve imaging; the filter materials are proprietary, however they perform low energy filtering. In addition, four optical magnification lenses are used which are 0.4x, 4x, 20x and 40x. These are placed after the scintillator and allow for magnification without limiting the source and detector distances when using geometrical magnification alone, see Figure 2.3b. With geometrical magnification alone the system resolution is described by the following [143]:

$$r_s = S\left(\frac{b}{a}\right) \quad \textbf{(2.2)}$$

$$M = \frac{a+b}{a} \quad \textbf{(2.3)}$$

$$r_{total} = \sqrt{\frac{r_D{}^2 + r_s{}^2}{M}} \quad \textbf{(2.4)}$$

where *S* is the source spot size, *a* is the source to object distance, *b* is the object to detector distance, r_D is the detector pixel size, and M is the geometrical magnification. As can be inferred from the above (2.2 – 2.4), resolution without optical lenses requires the source to be extremely close to the sample, limiting sample size, and the detector to be far away, meaning longer scan times from decrease in X-ray flux. By employing the use of optical lenses the magnification is enhanced allowing for high resolution with larger source and detector spacing. This exact feature is necessary to obtain *in-situ* and *operando* visualization of PEFCs as hardware and sample size would otherwise limit the achievable resolution.

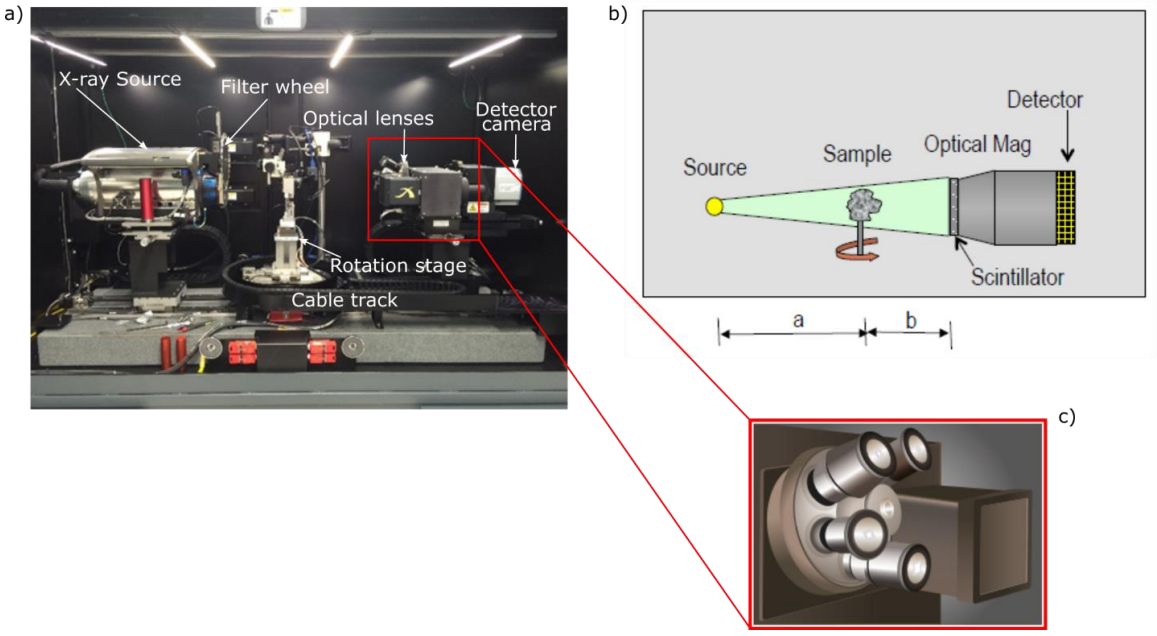

Figure 2.3: a) Labelled photograph of the Zeiss Xradia Versa 520 system. b) Schematic of the distances used in geometrical magnification as well as the principle of additional optical magnification using visual light lenses placed after the scintillator. c) Schematic view of the optical lens carousal used for automated changing of lenses.

2.3.2. Nano-scale Imaging

Nano-scale imaging was performed using the Zeiss Xradia Ultra 810. Unlike the Versa system, this system uses X-ray lenses to perform magnification. X-rays cannot be focused by using refractive or magnetic lenses like light microscopes or electron microscopes, instead a combination of diffraction and reflection is employed. Following emission using a chromium anode, X-rays are focused to an Annulus using an elliptical capillary condenser which employs total internal reflection, see Figure 2.4. [147] The beam is then further cleaned and collimated using a pin-hole aperture. After transmission and diffraction from interacting with the sample material, X-rays are focused again using a Fresnel Zone plate which employs diffraction through a circular grating. [148] These X-ray optics are energy-selective creating a monochromatic beam with the Ultra 810 system optimized for 5.4 keV X-rays. [149] The specificity of these X-ray lenses are designed for high-resolution imaging in two-modes: a 64 µm field-of-view with 150 nm resolution and a 16 µm field-of-view mode with 50 nm resolution. In addition, phase contrast mode is also employed using a specific design utilizing an annular phase ring, also known as Zernike phase contrast, which is discussed in the following section 2.3.3. The majority of the flight path of the X-rays is also filled with Helium gas to reduce attenuation of the low energy X-rays employed in this system enabling high contrast.

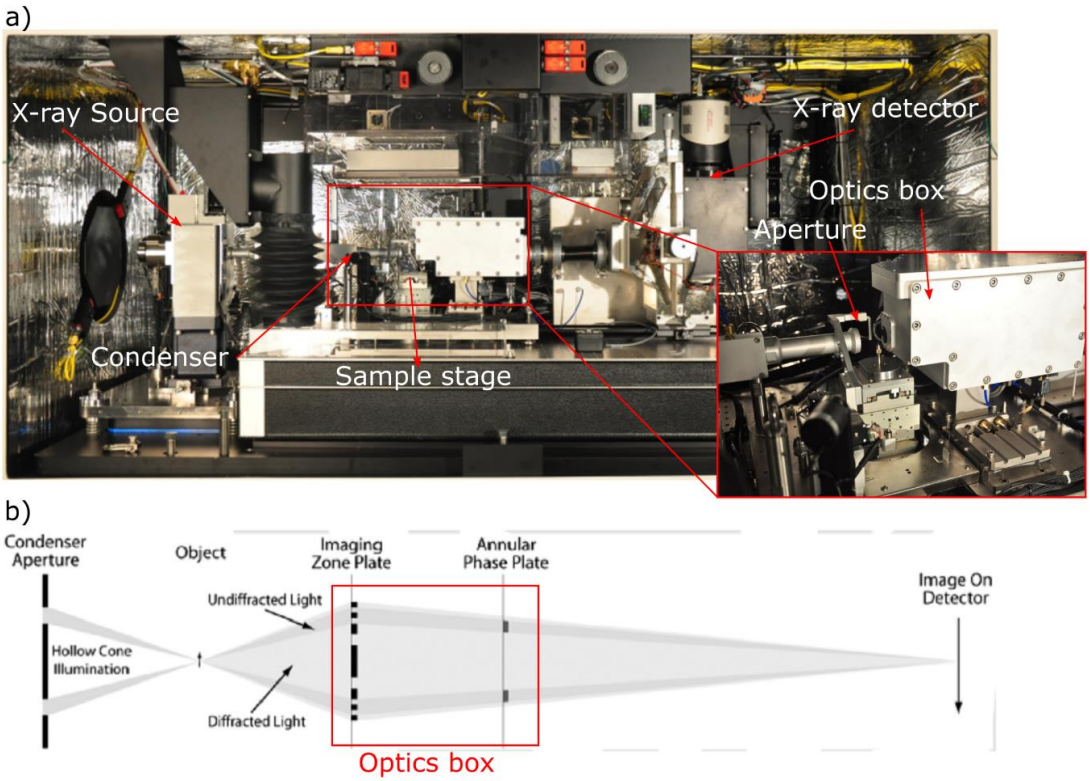

Figure 2.4: a) Labelled photograph of the Zeiss Xradia Ultra 810 system. b) Schematic representation of components as well as the X-ray path with diffracted and undiffracted light used in phase mode imaging.

2.3.3. Absorption Contrast vs. Phase Contrast

The relative greyscale value that is produced in a reconstructed image of an irradiated sample following tomography is based on the relative attenuation of the sample material. As described in equation 2.1 above, the attenuation is dependent on the density and effective atomic number through the linear attenuation coefficient of the irradiated material, as well as the incident X-ray energy. A scaling is used in the final step which assigns the pixel greyscale value such that the lowest attenuating pixel is given a value of 0 and the highest attenuating pixel is given a value of 65535. In this way a material that is higher in density will appear brighter, with a higher greyscale value. This method works well for materials where contrast between the different compositional components is produced from a sufficient difference in relative attenuation. For materials with relatively similar attenuation, this does not provide sufficient contrast in the final image to clearly resolve features of interest, such as in the case of low attenuating specimens. Fortunately, an alternative imaging mode can be employed which takes advantage of the shift in phase

of the incident X-rays after interaction with matter, in particular at the edges between air and another material. This gives rise to small changes in propagation direction of adjacent parts of the wavefront leading to interference fringes, shown in Figure 2.5a which enhances edges through constructive and destructive interference [150], [151]. This is also known as propagation phase contrast and allows for clear definition of edges seen in Figure 2.5b.

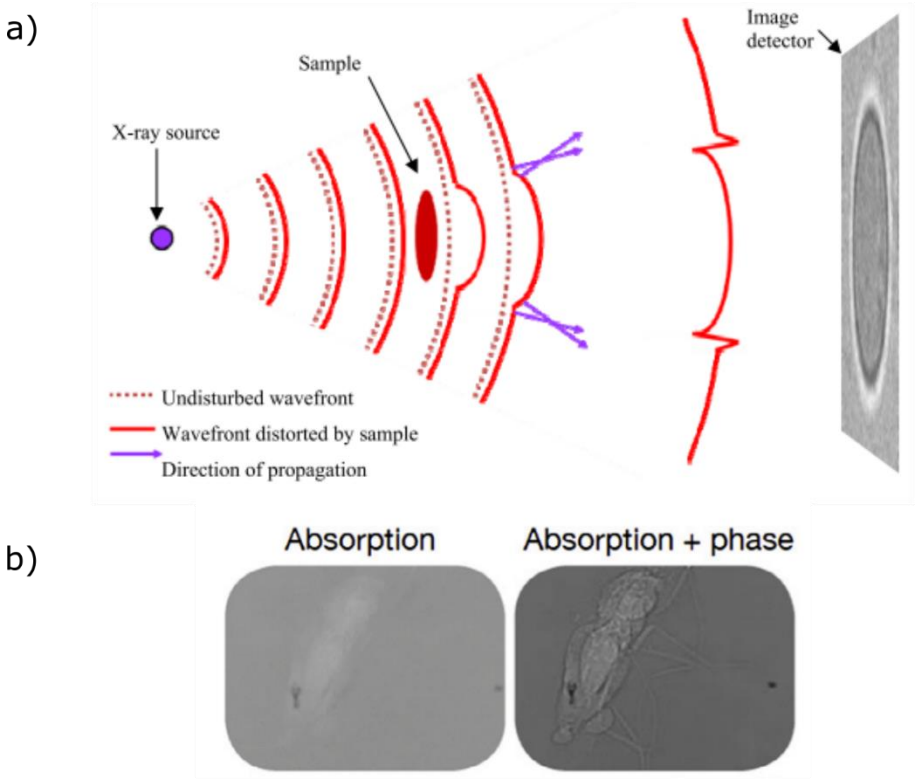

Figure 2.5: a) Schematic of the X-ray wavefront as it propagates and is phase-shifted by the sample resulting in bright and dark edges seen on the detector [150]. b) Example application where a low attenuating sample cannot be clearly visualized in absorption mode from surrounding medium but has enhanced edges when employing phase contrast imaging. Reproduced with permission from Elsevier, copyright 2014 Nucl. Instruments Methods Phys. Res. Sect. B Beam Interact. with Mater. Atoms, vol. 324, pp. 118–123 [151]

Alternatively, an active method of enhancing the phase interference is achieved using an annular Zernike Phase ring, as shown in section 2.3.2 Figure 2.4. This additional lens shifts the phase of undiffracted X-rays by 3π/2 allowing for constructive and destructive interference to occur at the scintillator, yielding pronounced edge contrast. [147] Further application of this method in nanoscale imaging is discussed in Chapter 7.

Chapter 3. Experimental Development

One of the primary objectives of this thesis was to develop methodology and tools to be used in the study of degradation mechanisms in PEFCs utilizing XCT. This work combined the specialized development of hardware, software and workflows, such as: custom fuel cell device and holder to allow for *in-situ/operando* imaging, test station and cable management for operation inside and outside the XCT system enclosure, fabrication and assembly methods, testing methods, safety procedures, XCT system parameters and image processing analysis, to name a few. To achieve this, various methods and equipment was utilized, such as: 3D printing, CNC machining, CAD software, potentiostat and impedence spectrometers, XCT systems, python/MATLAB/ImageJ programming, fuel cell test stations, various temperature, pressure and flow regulators as well as specialized materials and equipment for fuel cell material assembly and fabrication. In the following chapter, an overview of the primary methods and initial development is discussed however more exhaustive workflows and safety procedures have been released as internal documents or are combined in subsequent chapters in Experimental sections.

3.1. Small-scale Fuel Cell Fixture

3.1.1. 3D Printed Fixture

Initial prototyping of the small-scale fuel cell fixture involved 3D printing for rapid prototype development. Several designs with variation in channel number and spacing, to compression method, size, and shape were investigated as shown below in figure 3.1.

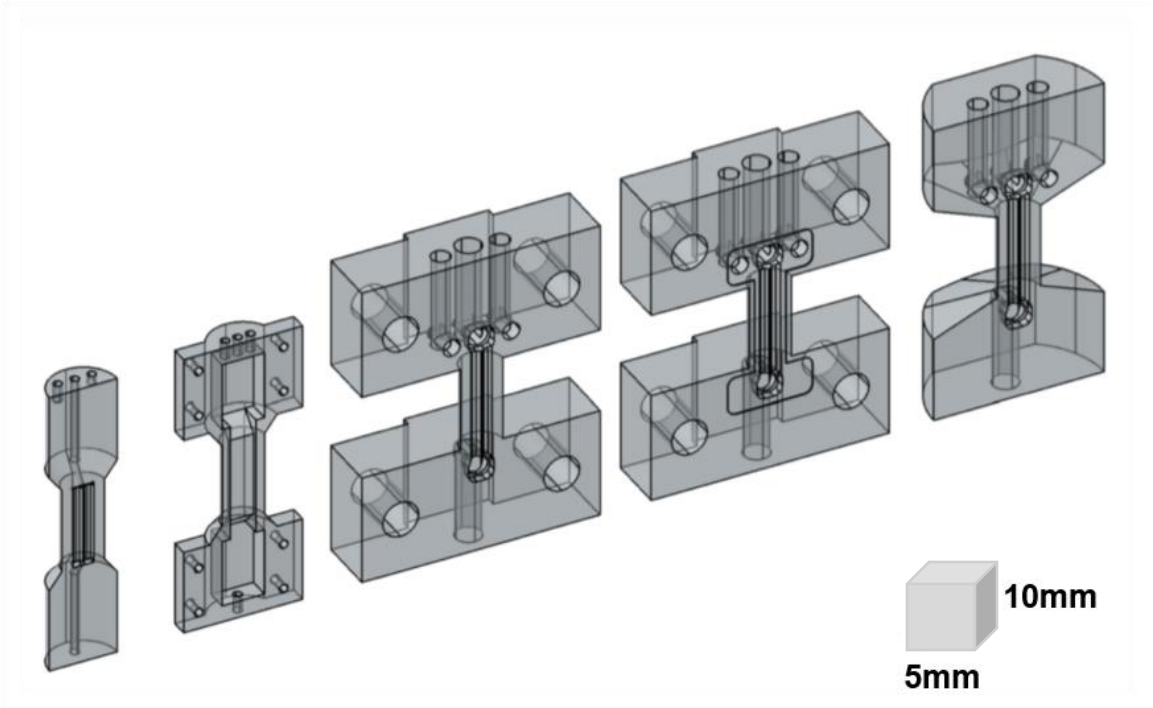

Figure 3.1: Various prototype designs for small-scale fixture development.

Following results obtained from prototyping, an operational small-scale fixture made from 3D printed flow channels was developed to investigate initial imaging parameters, segmentation procedures and visualization capabilities during operation. These initial results are included below in a formatted version of R. T. White, F. P. Orfino, M. El Hannach, O. Luo, M. Dutta, A.P Young and E. Kjeang, **3D Printed Flow Field and Fixture for Visualization of Water Distribution in Fuel Cells by X-ray Computed Tomography**, *J. Electrochem. Soc.*, 163 (2016) F1337 - F1343.

In this work, we present a novel approach to image PEFCs using rapid prototyping of 3D printed materials, demonstrated by the visualization of individual MEA components as well as water distribution in the GDL, all within a commercial micro-XCT system. These low X-ray absorber materials allow full 3D imaging to take place with the MEA *in situ* at various stages of operation. Additionally, the use of rapid prototyping materials allows for any variation of flow field or cell design to be constructed and tested quickly, which can

aid with new flow field designs to improve water management and increase cost efficiency. Unlike previous research, water condensation, formation and transport within a fuel cell can be observed by drawing current from the MEA to allow for operation before imaging at an equilibrium state using a commercial XCT system. This is the first known 3D printed flow field fixture with full operational capability used for imaging of fuel cells in an XCT scanner. We outline below the initial testing procedures and design as well as image processing techniques to extract water saturation profiles and porosity, followed by a comprehensive suite of results and analysis.

Experimental

Materials

All fuel cell materials used in this study consisted of catalyst-coated membranes (CCMs) and gas diffusion layers (GDLs). The CCM was composed of a Dupont Nafion® NR211 membrane core with cathode and anode catalyst layers each with a 50:50 Pt/C ratio at 0.4/0.1 mg cm^{-2} loadings, respectively. Separate anode and cathode GDL materials were used, each consisting of teflonated Avcarb® non-woven carbon paper coated with micro-porous layer (MPL).

X-ray Imaging

For *in situ* imaging, a commercial micro-XCT was employed (ZEISS Xradia 520 Versa, Carl Zeiss X-ray Microscopy, Pleasanton, CA). This instrument uses a tungsten target to generate X-rays with characteristic energies of 59.3 keV ($K_{\alpha 1}$-line) and 8.40 keV ($L_{\alpha 1}$-line). The anode voltage used to generate the X-ray beam ranges from 50 kV (4 W) to a maximum of 160 kV at a maximum power of 10 W; thus, at most anode voltages, the emitted X-ray beam is not monochromatic. In the present work, all images and tomographic data sets were acquired at an accelerating voltage of 80 kV and 7 W, which corresponds to an emitted X-ray spectrum with a mean energy of ~25 keV, determined through simulation. [152] (This value was refined further using experiment – see Chapter 4 and 5). These system settings provided the most appropriate energy spectrum to enhance the contrast between the various fuel cell components and liquid water. The contrast in XCT is provided by the mass attenuation coefficient of each material that

depends on the component constituents and density as well as the thickness. This is summarized by the Beer-Lambert Law, which can more generally be written as:

$$\boldsymbol{I(E) = \int I_o(E) e^{-\sum(\mu)_i(E)\cdot x_i} dE} \qquad \textbf{(3.1)}$$

where E is the energy of the non-monochromated X-ray source and $(\mu/\rho)_i(E)$ is the linear attenuation coefficient for each material, which is a function of the energy of the X-ray and x_i is the thickness. Other imaging parameters such as source and detector locations were tuned for the present experiment following standard operating procedures provided by the instrument manufacturer. The resultant pixel resolution was 1.8 µm in a 3.0 x 3.0 mm field of view.

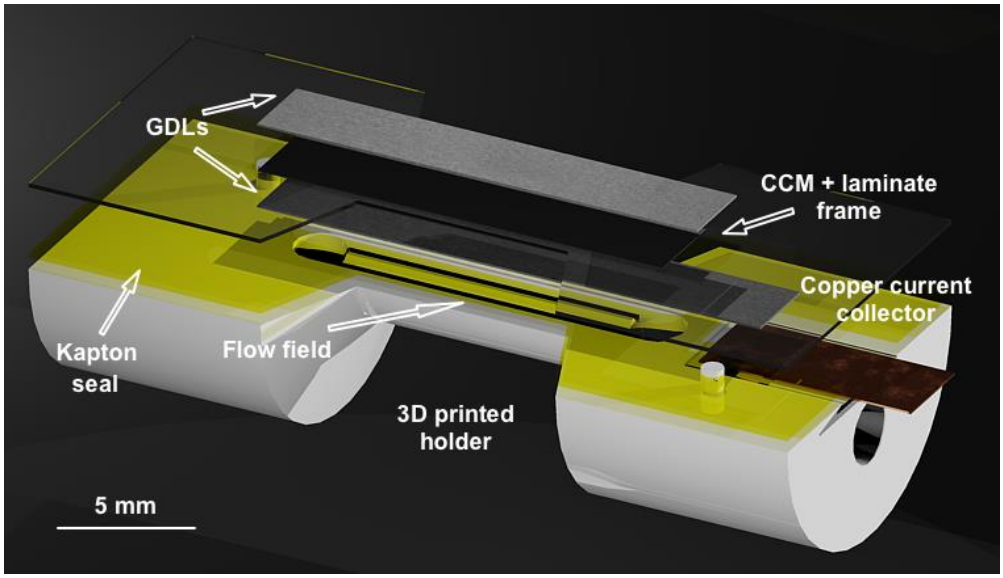

Figure 3.2: Computer aided design of MEA and 3D printed flow field fixture, showing from top to bottom: GDL, CCM with laminate frame, GDL, adhesive Kapton seal and 3D printed holder with two-channel flow field. An identical 3D printed holder was used in the top part of the assembly (not shown here). Copper current collectors were used to provide electrical contact with the GDLs.

Fixture Design and Fabrication

The MEA was situated between two Kapton adhesive sheets to provide a seal and had an active area of 0.24 cm^2. Internally, the CCM was also framed with a laminate frame to aid the isolation of gases and provide electrical insulation, as illustrated in Figure 3.2. The compression plates surrounding the MEA and providing gas flow channels were

printed using an Objet30 Desktop 3D printer and Stratasys Objet RGD525 high temperature material. The material was chosen because of its low X-ray absorbance compared to conventional fuel cell materials such as graphite or any metal casings and current collectors. Table 3.1 shows the mass attenuation value determined through experimentation for various materials tested.

Table 3.1: Attenuation loss at non-monochromated 80 kV acceleration voltage for various machinable materials compared to 3D print material.

Material	$\mu \pm 0.1$ (cm^{-1})
Objet 3D print RGD525	0.35
Acrylic (Polymethyl methacrylate)	0.45
PEEK (Polyether ether ketone)	0.82
PAI (Polyamide – imide)	0.86
PTFE (Polytetrafluoroethylene)	1.42
Graphite with cured resin	1.76

The 3D printing technique also provided a rapid and cost effective way to design a fixture small enough to achieve good signal-to-noise ratio when using low intensity X-rays provided by commercial XCT scanners that would otherwise be difficult (or impossible) to manufacture through conventional machining. The cell was designed to have a two-channel flow field, each with 0.5 mm radius. The length of the flow field was 10 mm and the total length of the cell was 30 mm. As shown in Figure 3.2, the fixture was comprised of two sections: a larger radius (manifold) section and a smaller radius (viewing) section. The larger radius section had a radius of 7.5 mm and allowed connection of the inlet and outlet gas lines as well as current collection and thermocouple placement for temperature monitoring. The viewing section had a radius of only 3 mm to minimize the signal loss from attenuation and provide an active area that fits into the field of view. A cylindrical design was used to provide a constant background signal from attenuation of the surrounding material while undergoing rotation during imaging in XCT. The combination of a viewing section and active area that fits into the field of view provided suitable contrast to MEA materials and good signal to noise ratio. The 3D print material used in this work showed no significant signs of gas permeation through the material, under the operating and flow conditions applied.

Fuel Cell Operation

Operation of the fuel cell was performed on a Scribner 850C Fuel Cell Test System with capabilities of 1.0/2.0 slpm maximum flow, 50 V, 20 A and 50 W maximum operating conditions. The assembled fuel cell was conditioned with 100% RH H_2 and air with 0.2/0.3 slpm flows at 25^{o}C for the anode and cathode, respectively, for 8 hours at 0.1 A cm^{-2}. Current collection from the fuel cell was performed through a copper strip that was connected to the GDLs outside the imaging field of view to avoid interference from the metal strips with the X-ray signal. After conditioning, a polarization curve for the cell was acquired at 25^{o}C, with results shown in Figure 3.3(a). Relatively low fuel cell performance is observed as a result of the low operating temperature and the high resistive losses of the current collection method. Other 3D printing techniques such as selective laser sintering or metallic deposition [153], [154] could be used to create a conductive 3D printed flow field; however, this would result in substantial loss in visualization capabilities using XCT. Subsequently following diagnostic measurement, the cell was equilibrated for 2 hrs at 0.1 A cm^{-2}, followed by disconnection of load, closure of all inlet and outlet ports and installation of the cell assembly in the XCT system for imaging. The experimental set-up in the XCT system is shown in Figure 3.3(b) where the fuel cell fixture is centrally located on the rotating stage with the X-ray source and detector on the left and right, respectively.

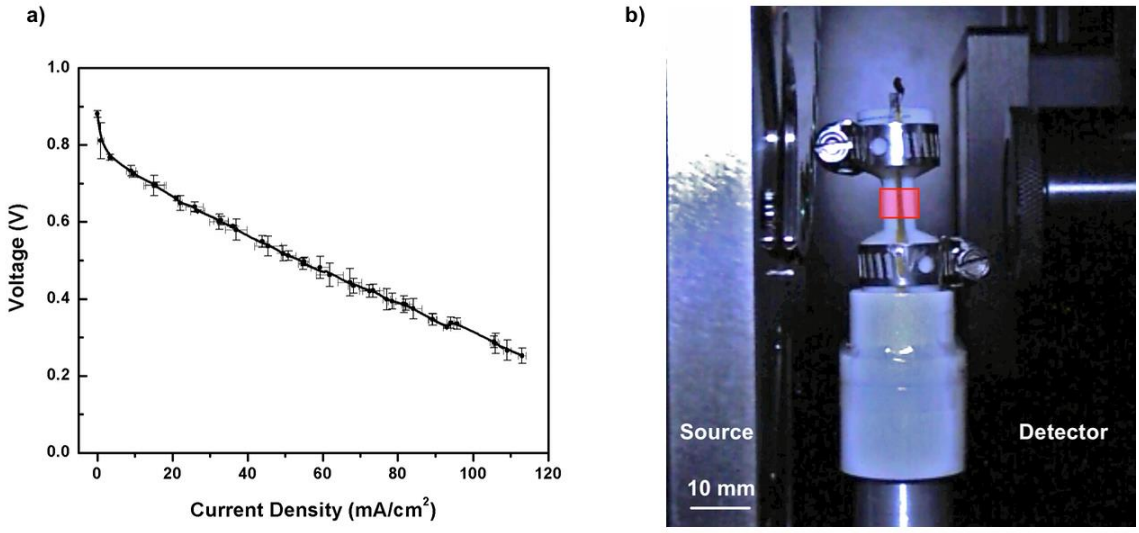

Figure 3.3: a) Polarization curve of the fuel cell operating inside the 3D printed fixture at 25^{o}C with H_2/air. A large resistive loss occurs due to the current collection set-up. b) Visualization set-up inside the XCT system with X-ray source and detector positioned as close as possible without collision, approximately 25 mm from the center of the fixture installed on the rotating stage. The imaging field of view is highlighted in red.

Liquid Water Identification

Both cathode and anode GDLs used in fuel cells are specifically designed to allow for gas flow of reactants and removal of product water, while providing an electrical pathway for current collection from (or to) the catalyst layers. Gas phase transport can only proceed through the pores in the GDL structure, which can become blocked if liquid water removal is not managed sufficiently. For these reasons porosity and saturation of the GDL provides important information about the ability of the fuel cell to operate at high current density conditions. When imaging materials with X-rays, suitable contrast between material phases is obtained by differences in mass attenuation coefficients and densities of the constituent elements. Imaging fuel cell components thus poses a challenge since the majority of the constituents have very similar mass attenuation values at typical X-ray energy ranges. Imaging liquid water is an additional challenge since the corresponding differences in grey scale values between carbon, water and air through XCT are small at best. Other noise contributions such as variations in X-ray energy, phase interface effects and sample movement all add up to make it more difficult to separate constituent components within an operational MEA. The specific grey scale values for the three main phases present in the GDL (solid, gas and liquid water) are shown in Figure 3.4. Although there is a grey scale range distinction between the solid and gas phases, the water phase overlaps with the solid phase due to the similar mass attenuation coefficients. Image processing operations can be used to overcome the challenges of limited contrast, improve thresholding and yield quantitative results from segmentation such as porosity and saturation of the GDLs.

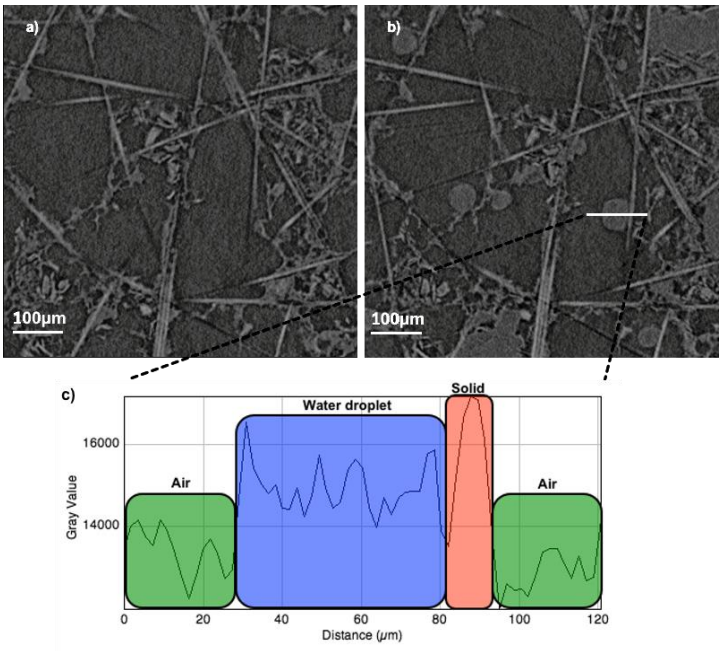

Figure 3.4: Identical location images of the cathode GDL in the a) unconditioned and b) conditioned state showing that conditioning has no effect on the GDL. The images represent an in-plane section of the GDL substrate extracted virtually from the full tomographic data sets obtained by XCT of a full MEA inside the 3D printed fuel cell fixture. c) Grey scale values along the measurement line applied across the water droplet indicated in b).

First, the MEA was imaged in a pre-conditioned dry state before operation on the test station using carefully controlled imaging settings to be used again for identical location imaging after operation. This provided a reference to be used to enhance water contrast in the wet MEA (operated as stated above) by subtracting the dry image set from the wet image set [77]. By using image subtraction this removes most of the solid phase, improving segmentation of water droplets. Any deviations in location or imaging conditions will result in an imperfect subtraction as well as potential noise that is not subtracted out. Image processing operations can then be applied to remove the noise and allow for a more accurate representation of the water content to be calculated. The dry MEA was also used to calculate the porosity of the GDL; a parameter used in the saturation calculations.

Segmentation of phases was performed using the multi-thresholding function in MATLAB, which utilizes the Otsu method of thresholding. Alignment of wet and dry images for the cathode and anode GDLs in each of the two image sets was done separately using ImageJ. Separate alignment of the anode and cathode GDLs was performed to correct for

the possibility of non-symmetric changes in the CCM due to the swelling of the membrane after humidification or movement in the sample. As a result of these changes, complete alignment of the wet and dry image sets in the CCM region was not possible; thus, segmentation and water content was only calculated in the GDL region where good alignment between wet and dry image sets could be applied. The alignment transformation was determined by the overlay of reference images from the dry and wet image sets (See Chapter 4 and Appendix A for further details). Using the affine transformation matrix, the transformation was applied to the whole image set. Various locations were used through the length of the GDL to confirm consistent alignment after the transformation was applied. Further image processing to reduce noise and improve contrast was also performed through MATLAB. After subtraction and thresholding, a Gaussian filter with radius of two pixels was used to reduce the noise, yielding smoother segmentation from thresholding. Next, a fill holes morphological function was applied as well as statistical removal of noise by removing objects with an area below 9 pixels^2 which reduced the amount of false solid or liquid segmented pixels that could not be identified as such. Since liquid water accumulates in pores and as droplets, objects that still resembled GDL fibers were also removed given their unique long, cylindrical shape. These steps allowed for consistent segmentation from solid with an accuracy of objects greater than 3 µm in radius. Representative images of the cathode GDL after each key stage of the image processing method are shown in Figure 3.5.

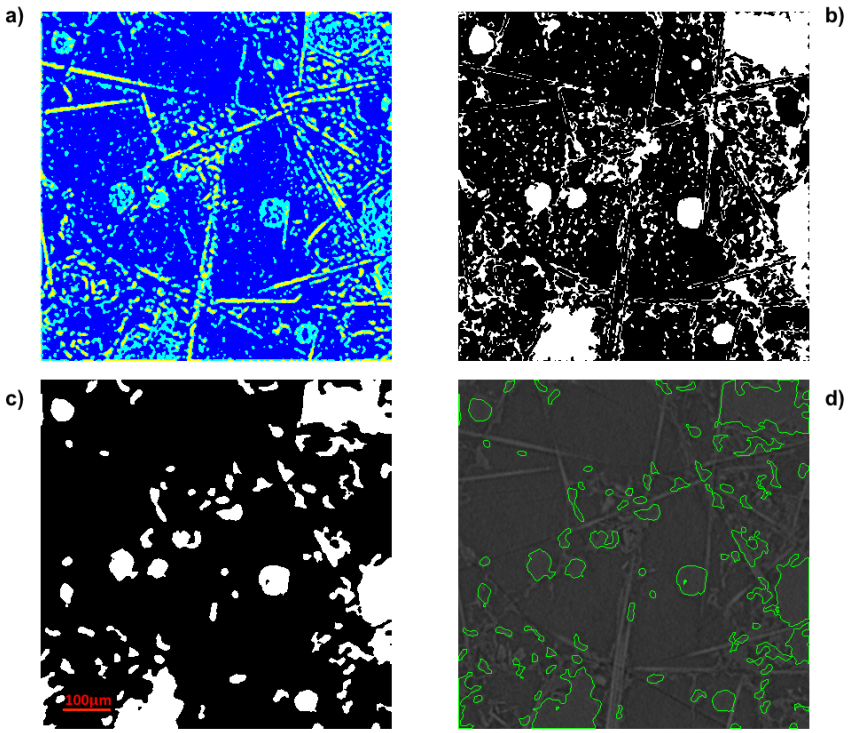

Figure 3.5: XCT image processing stages shown for the cathode GDL in the hydrated state: a) initial multi-thresholding after performing wet-dry subtraction, where the colours represent segmented labels with dark blue as air, yellow as solid, and light blue as water, including noise; b) binarization using a joint threshold range for remaining solid and water; c) noise removal and filling of holes; and d) final binary image overlaid on original image segment to verify the obtained water selection (marked in green outline).

Results and Discussion

Complete tomographic image sets of the MEA inside the 3D printed flow field fixture were captured in the original dry state and in the wet state after fuel cell operation. A representative cross-sectional view of the fuel cell extracted from the dry and wet tomography datasets is provided in Figure 3.6, where the individual MEA components and flow channels in the fixture can readily be observed. Upon operation, the membrane was observed to swell and form undulations in the MEA, indicating a substantial increase in water uptake from hydrated gases and formation of water from the cathode reaction. The outline of the catalyst layers in orange has been included to better highlight changes seen in the membrane after swelling due to hydration. The thickness of each MEA component was quantified from the XCT data using cross-sections such as those shown in Figure 3.6. While there was no statistically significant change in the catalyst layer thicknesses, the membrane thickness was observed to expand by 25% on average, from 20 to 25 µm, due

to ionomer hydration during fuel cell operation. This level of through-plane expansion is generally expected from the relatively high water uptake of Nafion ionomer, albeit in situ measurements are generally absent in previous literature. For comparison, the through-plane thickness of a PFSA ionomer membrane assembled in an MEA was measured ex situ to expand by ~4 µm during a relative humidity ramp from 50% to 90% [155], in reasonable agreement with the present results. The oscillations seen in the CCM structure were most likely formed due to stresses caused by the expansion of the membrane from its increased water uptake [155], [156], in combination with the CCM confinement within adjacent GDLs, flow field plates and seals. Both findings in terms of *in situ* membrane expansion and CCM undulation during fuel cell operation are significant and uniquely enabled by the present XCT technique and cannot be readily detected through other means.

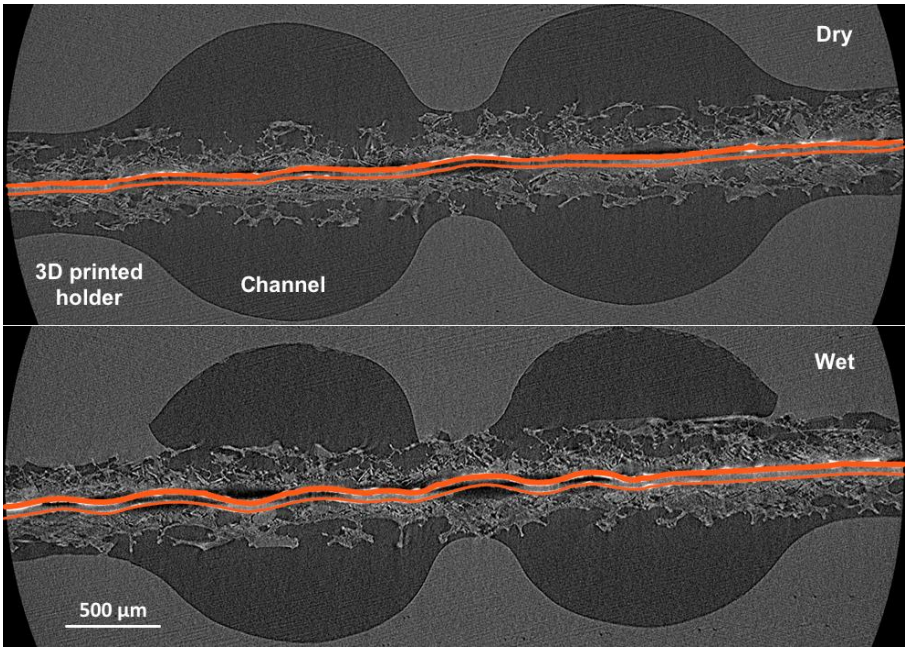

Figure 3.6: Representative cross-sectional XCT images of the MEA situated inside the 3D printed flow field fixture at dry and wet conditions. During fuel cell operation in the wet state, the increased hydration of the membrane caused an increase in the membrane thickness and significant undulations of the CCM. The outline of the catalyst layers in orange has been included to better highlight changes seen in the membrane after swelling due to hydration.

In addition to the water absorbed in the membrane, a considerable amount of liquid water was also detected in the channels and GDLs, while the resolution of the presently used instrument was insufficient for water detection in the catalyst layers and MPLs. Significant water pooling was observed at the edges of the channels adjacent to the cathode GDL-land interface, suggesting liquid water condensation at the surface of the lands and accumulation in the channel parts with low local flow velocity. This effect is likely supported by the more hydrophilic character of the fixture material compared to the teflonated GDLs. A similar effect is also expected for typical fuel cell plate materials, such as compressed graphite, having similar surface properties. Under the present operating conditions (100% RH, 25^{o}C), evaporation of this liquid water into the channel flow is unlikely, and any water removal from this region would likely have two-phase slug flow characteristics. Hence, liquid water accumulation in these spaces can be expected during fully humidified conditions. The present results also demonstrate the usefulness of XCT visualization of 3D printed fixtures for comprehensive studies of liquid water accumulation effects, which could be carried out with rapid turnaround for various flow field designs, compression levels and operating conditions.

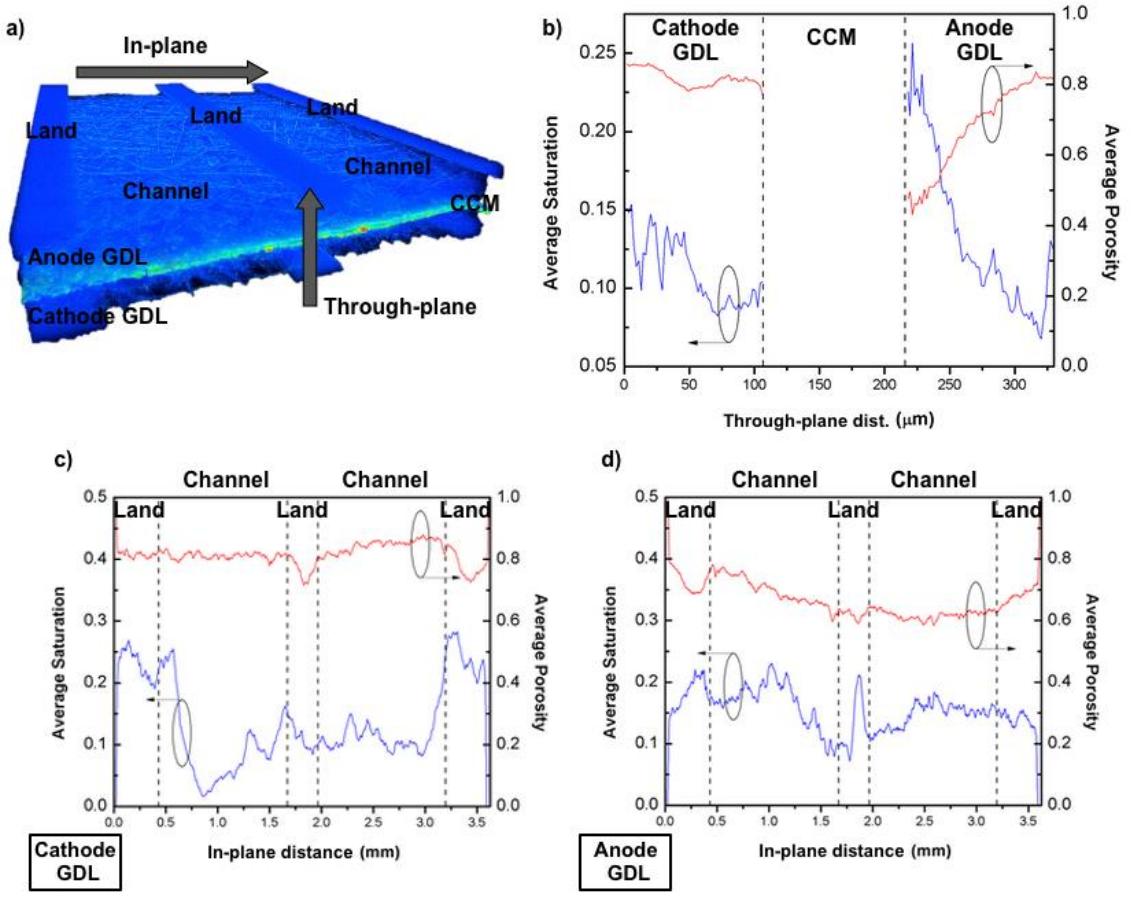

Figure 3.7: a) 3D reconstruction of GDLs and full MEA indicating the direction of summation for average GDL saturation and porosity plots shown in the through-plane direction (b) and the in-plane direction for the cathode (c) and anode (d). Dotted lines indicate the location on the MEA.

The porosity and liquid water saturation of the two GDL substrates (anode and cathode) were calculated from the phase segmented XCT data obtained upon water and solid segmentation, with results shown in Figure 3.7. The anode and cathode GDL regions used for the calculations were selected to not include any catalyst layer parts, which may undergo undulations during membrane hydration. Similarly, GDL regions immediately adjacent to the land and channel interfaces were also excluded in order to avoid interferences from compression changes during operation. Porosity was calculated using the dry image set where the pore space was divided by the total space (pore and solid). This was averaged through the in-plane or through-plane direction, as shown in Figure 3.7. Saturation was calculated as the liquid space divided by the pore space, with the pore space obtained using the dry image set used in the porosity calculation. An average dry

porosity of approximately 80% and 70% was obtained for the cathode and anode GDLs, respectively, which agrees well with expected results of typical non-woven GDL substrates. The anode GDL appears to have a gradient in porosity toward the anode catalyst layer side, presumably due to MPL overlap, thus suggesting that the thresholding is accurate [84], [157], [158]. Upon measurement of the GDL thickness in specific regions located under the channels and lands, a compression of approximately 15% was calculated in the land regions, which is reasonable for fuel cell GDLs [159]. The cathode GDL is shown to have a higher porosity than the anode side, thus allowing for water transport pathways while retaining good oxygen diffusion into the cathode catalyst layer.

The saturation plots in Figure 3.7 show a significant amount of liquid water through the depth of the GDLs. The liquid water present inside the MEA may have originated either from equilibration with the fully humidified gas conditions in the channels or from the water production on the cathode which supports water transport into the cathode GDL as well as back diffusion of water through the membrane across to the anode side. The average liquid water saturation in the cathode GDL was found to be significantly higher under the lands (~25%) than under the channels (~10%). Interestingly, however, the saturation in the anode GDL was approximately uniform in the in-plane direction and did not increase under the lands. The through-plane saturation distribution in the cathode GDL (from the CCM side to the channel side) was relatively constant at ~10-15% with a marginal increase toward the channel side. In contrast, the anode GDL saturation was observed to rise considerably from the channel side to the CCM interface, where 25% saturation was reached. The steady increase in saturation was however accompanied by a reduction in porosity near the anode catalyst layer, and the amount of liquid water was therefore relatively constant across the anode GDL. Nevertheless, the combination of low porosity and high saturation at the MPL side can introduce significant gas phase transport resistance. Small droplets of water were visible at the CCM/GDL interfaces on both anode and cathode sides, as shown in Figure 3.8; again, indicating condensation at the catalyst layer or MPL surfaces which may be exacerbated in the presence of voids or delamination at the interface. The typical droplets seen at the catalyst layer interface were approximately 20 µm in diameter, which corresponds to a spherical volume of ~4 pl. The droplets were preferentially found at the catalyst layer surface and had a variation in size of about 5 µm with an asymmetric distribution toward the smaller size droplets. This may indicate a limiting size before agglomeration and removal from the surface resulting from

larger mass to surface adhesion ratio. The approximate coverage was calculated to be 17 ± 6% based on area of droplets to area of catalyst interface. The droplets were likely formed from product water generated by the oxygen reduction reaction on the cathode, even at relatively low current densities, and thus demonstrate the capability of the 3D printed fixture for unique in situ observation of water formation at the catalyst layer and GDL interface. Operation with dry gas in future runs may yield more accurate investigation of water production *in situ*, provided that the cell can be properly humidified to achieve standard performance of the membrane.

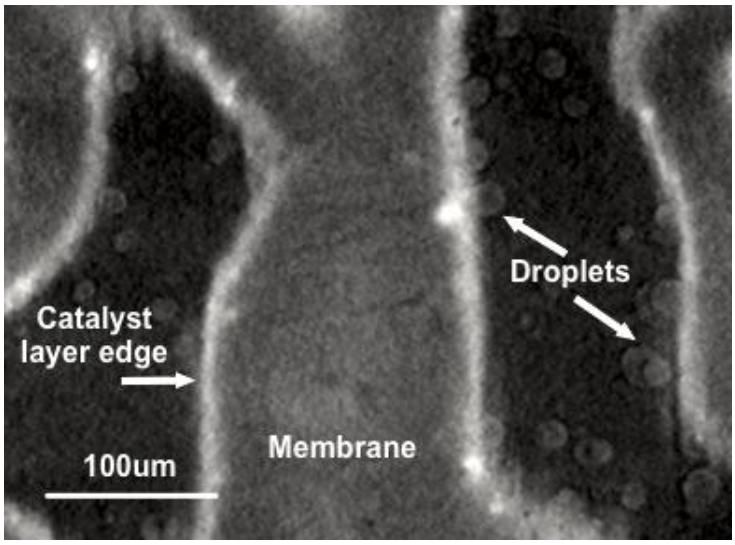

Figure 3.8: Water droplets seen at the cathode catalyst layer surface by 2D in-plane slice. Brighter areas are catalyst layer and larger grey areas are membrane. Water droplets seen in dark areas before catalyst appears indicate droplets on the surface in areas not contacted by the MPL/GDL.

Summary

Commercial XCT scanners have previously been limited in non-invasive imaging of fuel cells due to low X-ray intensity compared to synchrotron sources. In the present work, this gap was bridged using a custom developed 3D printed flow field fixture for high resolution in situ XCT visualization. We have shown that using a novel material selection and design along with simple image processing techniques, high resolution XCT of a full MEA including water segmentation can be obtained using commercial laboratory scanners. The obtained reconstructed, segmented 3D images were utilized to calculate the porosity and liquid water saturation distributions throughout the anode and cathode

GDLs after fuel cell operation at 100% RH and room temperature. Average porosity and saturation values on the order of 80% and 20% respectively were obtained. Liquid water droplets were also observed on the catalyst layer surface with an approximate diameter of 20 µm and area coverage of 17%. The high resolution of the XCT scan also allowed for the determination of through-plane membrane swelling by 25% under humidification, by measuring the thickness change after operation. This level of membrane swelling was further shown to cause CCM undulations due to confinement inside the fuel cell. Both findings in terms of in situ membrane expansion and CCM undulation during fuel cell operation are significant and uniquely enabled by the present XCT technique and cannot be readily detected through other means. Overall, the present results demonstrate the ability of commercial XCT scanners to provide useful *in situ* information about various phenomena that occur during fuel cell operation and the novel use of 3D printed materials to fabricate housing fixtures, with any number of intricate designs, which can be used in a wide range of future experiments at low cost.

3.1.2. Small Scale Fixture for Degradation Study

Slight refinement of the design used for the 3D printing prototype was achieved to aid in the fabrication of the final small-scale fixture to be used in future testing, as well as allow for adequate operation performance and diagnostic testing following the application of AST cycles, such as in the application discussed in Chapter 5. The final design used standard compressed graphite plates with resin, which have a much higher level of X-ray attenuation as shown above in Table 3.1, but are still suitable for sufficient signal to noise ratio projections and material contrast for high resolution XCT images. This material also provides excellent electrical and thermal conduction and is robust to voltage and temperature conditions, which are required for degradation testing and typical fuel cell performance diagnostics. A schematic of the design is shown in Figure 3.9 which was created using Solidworks CAD software, where an accurate design could be developed and fabricated. The final design housed a fuel cell composed of a CCM and GDL with active area of 0.24 cm^2. This ensured the majority of the active area was within the field of view of the X-ray imaging. Additional cell compression plates and housing were fabricated using fusion deposition modeling (FDM) 3D printed plastic or high-temperature UV cured resin, which have high enough heat tolerance to support the heated small-scale fixture at operational temperatures of 70-80^oC.

The small-scale fixture was designed with X-ray imaging in mind. For optimal results while imaging, the size of the sample being viewed should lie within the field of view of the X-ray scan. For a magnification resulting in 1.5-1.8 μm resolution, a sample size of 3-5 mm is required. The MEA active area is thus ~3x8 mm. With this, having the X-ray source and detector as close to the sample as possible will yield optimal signal/noise ratio and shortened operation time. The material selection was made to match technical cells, where possible, while still being sufficiently transparent to X-rays to allow for non-invasive imaging. No metal can thus be placed in the field of view area. The cell design has a tapered section at the imaging area and active area of the MEA to minimize unwanted X-ray absorption. Top and bottom portions allow for heating, gas line inlet/outlet, temperature monitoring as well as current collection to be connected to the Scribner 850C test station for full operation. Current collectors were securely attached using regular solder which has extremely low resistance. Compression of the GDL was controlled by a polyimide shim of 50-80 μm thickness adjacent to the framed CCM. This provides a stopping point for the compression of the GDL to 25-30%. Some variation in GDL and CCM thickness from manufacturing variation was observed, giving the compression percentage some deviation since it employed a hard-stop configuration as opposed to a pressure feedback or bladder. The shim also acts as a seal and insulation to mitigate shorting between electrodes and collector plates. Currently, compression pressure is implemented using cylindrical pipe clamps. 3D printed compression plates are used to protect the collector plates and transfer compression pressure from the cylindrical clamps to the square design of the collector plates. For additional information on the fixture design components refer to Section 5.

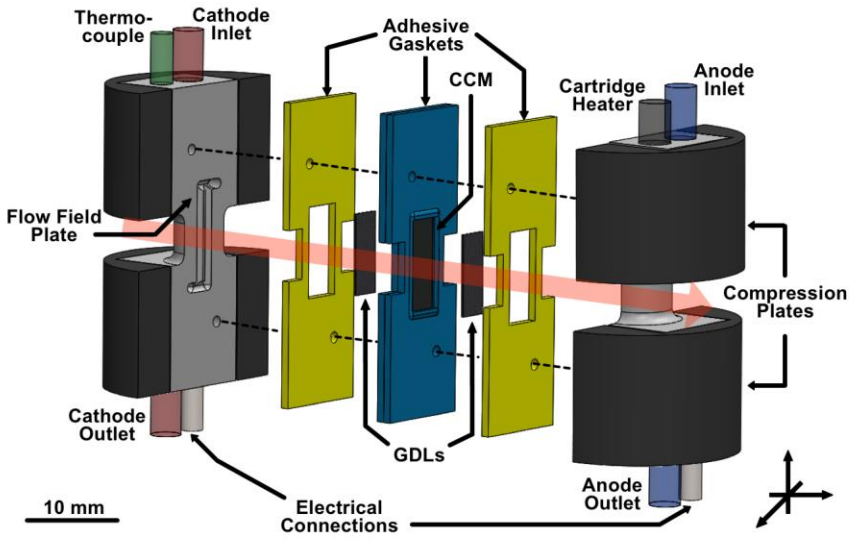

Figure 3.9: Schematic of the small-scale fuel cell fixture showing MEA components, flow field plates, compression plates, gaskets, inlet/outlet gas ports, temperature sensor, heater, and electrical leads. The X-ray beam path is described by the red arrow. The rotation axis is vertical.

Assembly of the small-scale fixture and miniature MEA requires precision due to the small dimensional tolerances and possible impact on fuel cell performance characteristics. As such, laser cutting and assembly using design masks were employed. Following hot-pressing of standard CCM (see Section 3.1.1), these were then cut and sealed using Kapton adhesive sheets. Using an alignment mask and vacuum table ensured a good seal and accurate alignment as shown in Figure 3.10a. Alignment pins were included in the fabrication of the small-scale fixture to assist with assembly, with sealing layers of Teflon and Kapton having guide holes designed to align and secure, shown in Figure 3.10b. The final assembly is housed in a custom designed holder, shown in Figure 3.10c to allow for integration with the XCT sample stage holder and wiring track.

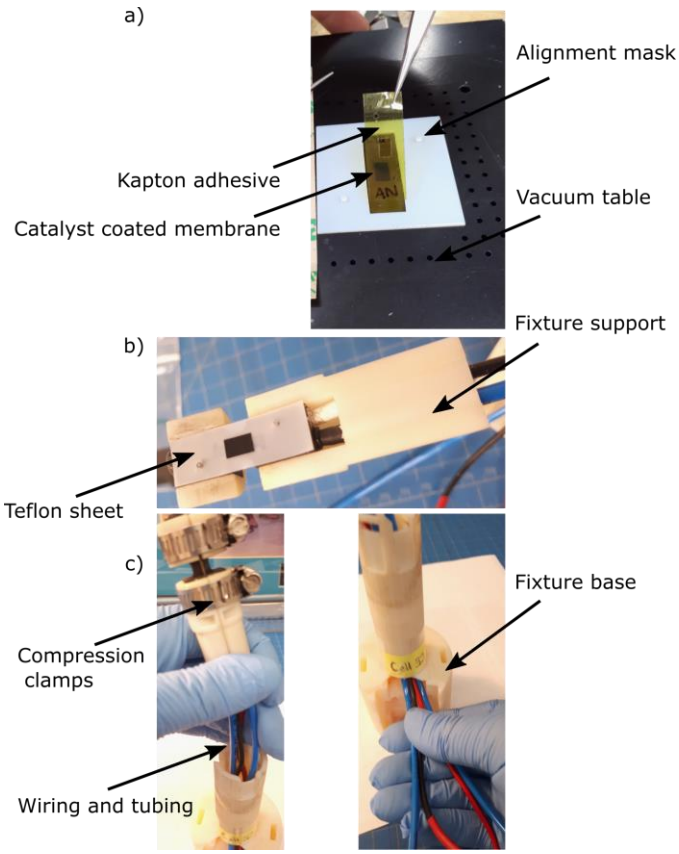

Figure 3.10: a) Assembly of laser cut CCM with Kapton adhesive sheets using vacuum table and mask. b) Addition of compression plates with extended base for fixture support and Teflon sheet shim. c) Integration of assembled small scale fixture with fixture base, wiring and tubing.

Operation of the small-scale fixture was enabled by the use of Scribner 850c test station (see Section 3.1.1). This was housed on a custom-built cart which was situated directly outside the XCT enclosure. Operation of the small-scale fixture could be performed in either *ex-situ* or *in-situ/operando* mode by simply rearranging and connecting tubing and electrical connections from the test station. Insulated and heated tubing was used for both configurations and a cable management track was employed to allow for rotation without sample movement during imaging. An overview of the set-up in the two modes is shown in Figure 3.11. Further details on operational set-up and conditions are given in Chapters 5 and 6. To enable *ex-situ* or *in-situ/operando* mode with the addition of temporal changes resulting from application of AST cycling such as voltage cycling to target cathode catalyst layer degradation or wet/dry cycling to target membrane mechanical fatigue, the workflow presented in Figure 3.12 was employed.

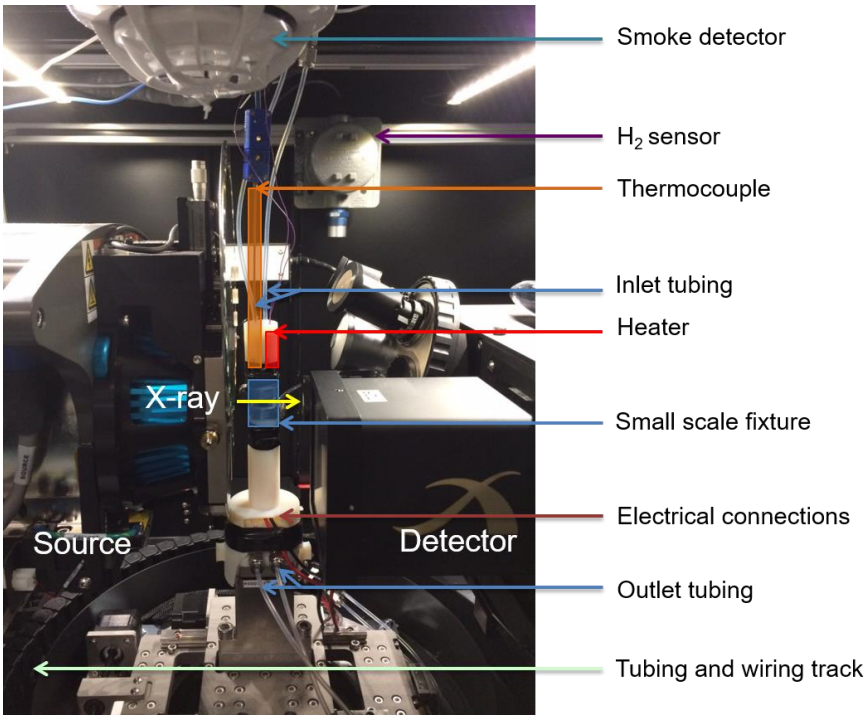

Figure 3.11: a) In-situ configuration with small-scale fixture secured on the sample stage with connections to the test station housed outside the enclosure. Additional safety systems such as smoke detector and H_2 sensor are also shown.

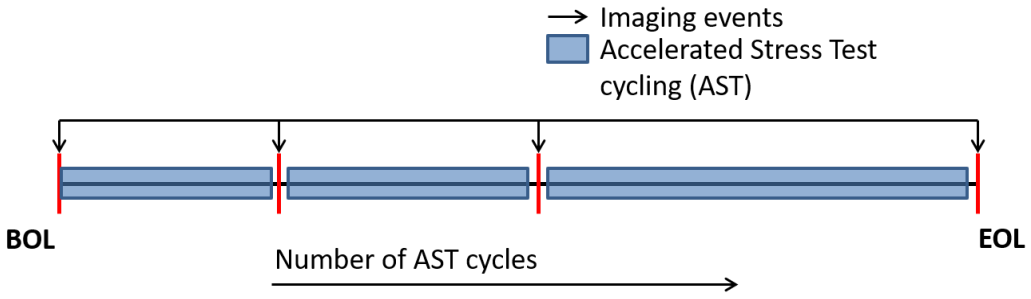

Figure 3.12: In-situ/operando workflow enabling the investigation of same location tracking with temporal changes resulting from the degradation mechanism targeted by the applied accelerated stress test.

3.2. Effect of X-ray Exposure on PEFC Materials

3.2.1. Impact on Cathode Catalyst Layer

The following is a formatted version of R. T. White, M. Najm, M. Dutta, F. P. Orfino, and E. Kjeang**, Communication—Effect of Micro-XCT X-ray Exposure on the Performance of Polymer Electrolyte Fuel Cells**, *J. Electrochem. Soc.,* 163 (2016) F1206 - F1208.

Recently, it has been shown that the use of synchrotron radiation (SR) as an X-ray source causes severe degradation to component materials, leading to immediate performance loss as well as affecting typical operational attributes such as water distribution [77], [152]–[155]

An in-depth study by Roth et al. [155] showed that X-rays primarily impacted the PTFE, membrane and ionomer constituents as well as removal of catalyst by disintegration of supporting substrates. Even more surprising is that when using SR, a decrease in performance of >200 mV occurs after just 200 s of exposure at 13.5 keV [155]. The usefulness of SR is its high signal to noise ratio from high radiation flux; however, this is also expected to be the primary cause for the observed degradation, which may invalidate the technique for long and repetitive scans and constrain its prospective use for in situ studies. In contrast, commercial micro-XCT (μ-XCT) scanners use accelerating electrons and target anode to provide the source of X-rays, with intensity considerably lower than that of SR [156]. This requires that μ-XCT scans take approximately 10-100 times longer than those of SR for a similar field of view (FOV) and pixel size to obtain good signal to noise ratio [77]. This longer collection time could be expected to cause similar degradation with μ-XCT as was observed with SR. The objective of the present work is therefore to elucidate the difference between SR and μ-XCT by investigating performance and diagnostic data of fuel cells at varying levels of X-ray exposure from a μ-XCT scanner.

Experimental

The fuel cell was assembled and operated in a cylindrical custom designed holder of low atomic weight material to meet the requirements of imaging within a μ-XCT [157]. Thus, the custom designed holder consisted of carbon/graphite with cured resin flow field plates whose X-ray transmission allowed for visualization of the MEA. The active area of

the MEA was 8 x 3 mm^2. A Scribner 850C Fuel Cell Test System was used to control gas flows and application of load as well as monitoring temperatures and humidity. Each fuel cell was initially conditioned at constant current, 750 ± 10 mA cm^{-2}, for 10 hours in H_2/air at 75°C and 100% RH. Subsequently, the fuel cell was installed perpendicular to the X-ray beam axis and equilibrated for 2 hours *in situ* in the μ-XCT analysis enclosure under H_2/air at 60°C, 100% RH, and at constant current of 750 ± 10 mA cm^{-2}. Then, diagnostic polarization curves were collected followed by five cyclic voltammetry (CV) scans from 0.05 to 0.8 V at 20 mV s^{-1} under H_2/N_2. Three polarization curves were measured at each time interval and averaged with standard deviation indicated by error bars. The electrochemical active surface area (ECSA) was calculated by integrating the area under the hydrogen adsorption peak during the reverse scan of a CV [158].

Exposure was affected with a commercial μ-XCT (ZEISS Xradia 520 Versa, Carl Zeiss X-ray Microscopy, Pleasanton, CA), see section 2.3.1 for further details. Here, 50 kV and 4 W was used. The beam produced is non-monochromatic energy, spanning 50 keV, and is composed of the wide Brehmsstrahlung background radiation and the tungsten characteristic line at 8.40 keV ($L_{\alpha 1}$-line). This accelerating voltage was chosen to produce an average energy similar to that used in other studies involving SR with monochromatic energy of 13.5 keV [77], [152], [153]. The divergence of the beam from the X-ray source is 35° vertically and 60° horizontally. The fuel cell sample holder was perpendicularly situated 27 mm along the beam axis from the X-ray source allowing for the active area to be fully exposed to the X-ray beam. Under these conditions, the photon intensity at the sample is of the order of 10^9-10^{10} photons s^{-1} cm^{-2} [155].

Results and Discussion

The performance of an operating polymer electrolyte fuel cell was monitored prior to and during X-ray exposure. Figure 3.12 shows the cell voltage at 750 mA cm^{-2} measured during a 2 hour period before X-ray exposure; also plotted is the voltage collected during X-ray exposure from the μ-XCT source for the same time period. A constant voltage for the duration of 120 minutes was observed in both cases within the ~5 mV variability of the measurement. If any degradation occurred as a result of X-ray exposure, a decrease in voltage during the course of the 2 hours would be expected. The time period of 2 hours is a typical time required to measure a full 3-D tomography scan in this experimental set-up with FOV and resolution similar to those used in previous reports [77].

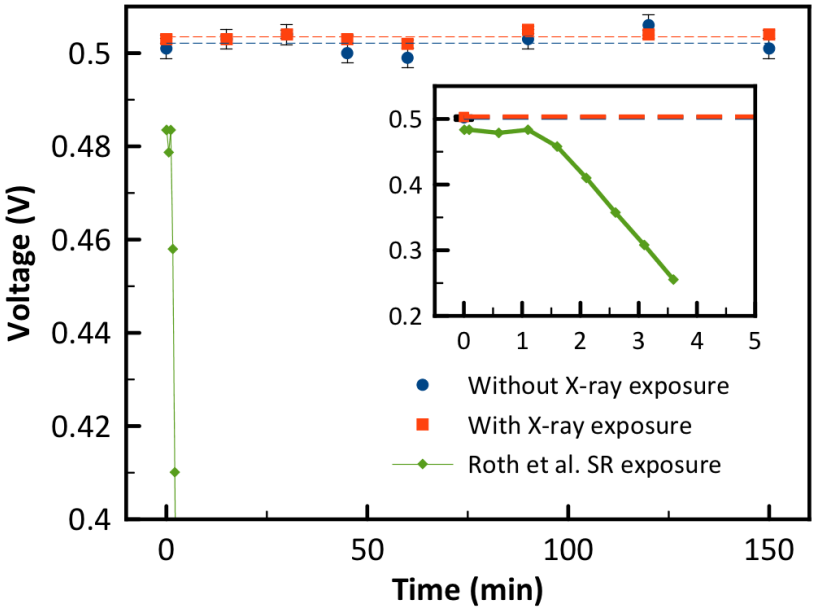

Figure 3.13: Fuel cell voltage measured under constant current of 750 ± 10 mA cm-2 prior to and during X-ray exposure using a micro-XCT X-ray source operated at 50 kV accelerating voltage and 4 W power.

To determine the extent of damage during the time interval for several full XCT scans, diagnostic data was collected after 10 hours of X-ray exposure. Exposure was done on the small-scale fixture with the fuel cell in its native environment with operating gases and humidity during this work. As can be seen from the ECSA data in Table 3.2 and the polarization curves in Figure 3.15(MEA #1), no change beyond the inherent variability of the measurement was observed over this time span.

Table 3.2: Electrochemical active surface area (ECSA) values obtained from CV at different exposure times. CVs were collected at 60oC and 100% RH H2/air conditions.

	Average before X-ray exposure	After 2 hours X-ray exposure	After 10 hours X-ray exposure	After 20 hours X-ray exposure
Cathode ECSA (m^2/gPt)	40 ± 3	38 ± 2	39 ± 2	39 ± 3

It was suggested that the decrease in performance seen in previous SR studies by Roth et al. was due to the decrease in ECSA; in the present case, however, the ECSA had no statistically significant change due to exposure. The inset shown in Figure 3.14 also indicates that no significant change occurred in the activation loss region of the polarization curve, further confirming that no loss in ECSA is expected. In the case of high resolution XCT scans, longer exposure times are sometimes required which may be up to 8 hours or more. In an effort to investigate whether these types of scans would have an

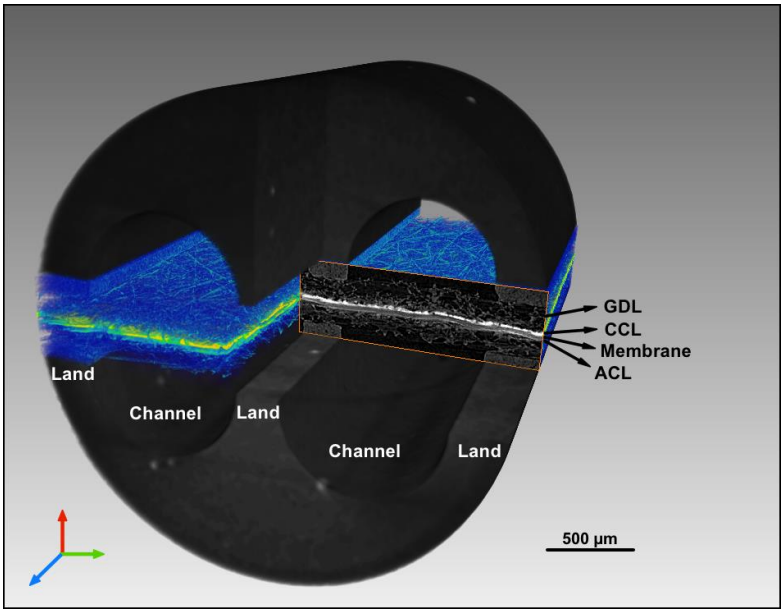

Figure 3.14: Reconstructed tomography of the fuel cell assembly. The two flow field plates are shown in black with the fuel cell MEA highlighted in pseudo-colour. A sample 2D slice is shown in the digitally removed section of the reconstruction. The reconstruction was obtained by collecting 1601 projections with an exposure time of 4 seconds. The field of view shown is 3x3 mm2 with a pixel size of 3.09 µm.

effect, exposure for over 20 hours was performed. As can be seen in Figure 3.14 (MEA #2) and Table 3.2, no effective change in the fuel cell was observed between a fresh MEA and an MEA exposed to 20 hours of irradiation. This exposure time of 20 hours is approximately 500 times longer than that used in the previous studies by SR where significant degradation was observed. Since in this study, similar or greater photon energy was used, a possible explanation for the observed results can be found by examining the difference in intensity, or photon flux Φ. It has been reported that SR Φ used in other fuel cell research experiments is on the order of 10^{13}-10^{14} photons s^{-1} cm^{-2} [58], [77], [155]. This value is approximately four orders of magnitude higher than the expected photon intensity from the XCT X-ray source used in this study and would suggest that similar degradation effects could only be expected to be observed in the time period of >100 hours using this energy range.

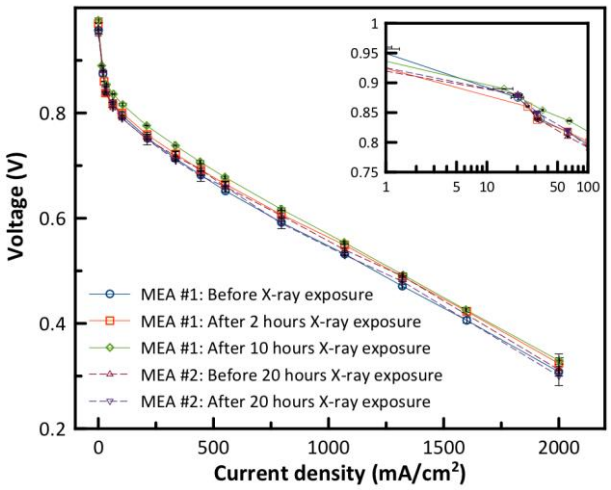

Figure 3.15: Fuel cell polarization curves measured before X-ray exposure and at varying times of exposure using a micro-XCT X-ray source.

Summary

The degradation effects of low-intensity X-ray exposure of fuel cells were investigated by collecting performance and diagnostic data before, during, and after exposure to X-rays. For up to 20 hours of continuous exposure, no measurable change was seen in the fuel cell performance as evaluated from polarization curves and ECSA data, indicating no observable loss in ECSA from disintegration of support material or damage to PTFE or ionomer. The difference can be attributed to the orders of magnitude lower photon flux from μ-XCT X-ray sources compared to SR. Thus, exposure of fuel cells over nominal experimental times does not lead to measurable damage, in contrast to previous reports with SR scans for similar FOV and resolution. It is expected that significant degradation effects will not be observed for exposures less than approximately 100 hours.

3.2.2. Impact on Membrane

The sensitivity of the impact of ionizing radiation, such as X-rays, on material properties is highly dependant on the composition. This is primarily due to the mass attenuation coefficient which relates to the atomic composition of the material, as well as the impact that radicals formed by ionization can result in chemical changes. In order to accurately investigate membrane degradation by *in-situ* visualization using the small-scale

fixture and XCT, correlation between the impact of X-ray exposure and any possible material property changes needs to first be established. Following this, ASTs performed on the membrane and features observed such as cracking or delamination can be conclusively attributed to expected membrane behaviour during typical PEFC lifetime, and not as a result of X-ray exposure. The following study was used to validate results obtained by Y. Singh during experiments on membrane degradation using the small-scale fixture and any future investigations of this kind.

The following is an excerpt of Y. Singh, R. T. White, M. Najm, T. Haddow, V. Pan, F. P. Orfino, M. Dutta, and E. Kjeang**, Tracking the evolution of mechanical degradation in fuel cell membranes using 4D in situ visualization**, *J. Power Sources,* 412 (2019) 224-237.

Ex situ tensile testing was performed on X-ray irradiated CCM samples (made with Nafion NR211 membranes) to evaluate the effect of X-ray exposure on their mechanical properties during 4D in situ visualization experiments. X-ray irradiation of 25 mm x 3 mm rectangular CCM samples was carried out by enclosing the samples within a representative small-scale fuel cell fixture comprising of GDLs, gaskets, flow-field plates, etc., and subjecting them to multiple tomography scans lasting approximately 25 and 50 hours using the same imaging parameters and conditions as those used during the 4D in situ visualization experiment, see [159] and Chapter 5 for specific details. The tensile testing was conducted on a dynamic mechanical analyzer (TA Instruments Q800 DMA) using a 10 mm sample gauge length at 23°C, 50% RH, and 0.01 min^{-1} strain rate [160]. For benchmarking, an additional test was conducted on a sample set not exposed to any X-ray irradiation.

Stress-strain curves obtained from the tensile testing and associated mechanical properties, viz. elastic modulus, yield strength, fracture strain, and ultimate tensile strength (UTS), as a function of X-ray exposure duration are shown in Figure 3.16. The qualitative nature of the membrane's constitutive response is found to be unaltered even after 50 hours of X-ray exposure, and it continues to retain typical characteristics of initial linear (Hookean) elasticity, followed by gradual rollover yielding and post-yield strain hardening [161]–[163]. A minor quantitative variation, on the order of 10% decay or less, is observed in the examined mechanical properties, which is significantly lower than the fluctuations experienced by these properties during typical fuel cell hygrothermal variations [162].

Moreover, the fracture point shifts marginally from ~160% strain in the unexposed case to ~150% strain after 50 hours exposure, suggesting negligible material embrittlement. In contrast, severe material embrittlement has been observed during ASTs involving individual and/or combined chemical and mechanical membrane degradation [130], [160], [164]. The decay in both fracture strain and UTS, which characterize a material's fracture resistance/toughness, after 50 hours exposure is still milder than the decay at 20% lifetime of these ASTs. Given the retention of the membrane material's fundamental constitutive character and lack of embrittlement, AST-induced failure modes and degradation mechanisms are not expected to be significantly altered during micro-XCT based 4D in situ visualization experiments involving up to 50 hours of X-ray exposure. Albeit the slight decays in elastic modulus and yield strength may marginally affect the rate of degradation, the key aspects of 4D in situ degradation analysis, such as root cause of failure(s), interaction between components, spatial distribution and evolution of damage features, etc., are unlikely to be significantly altered.

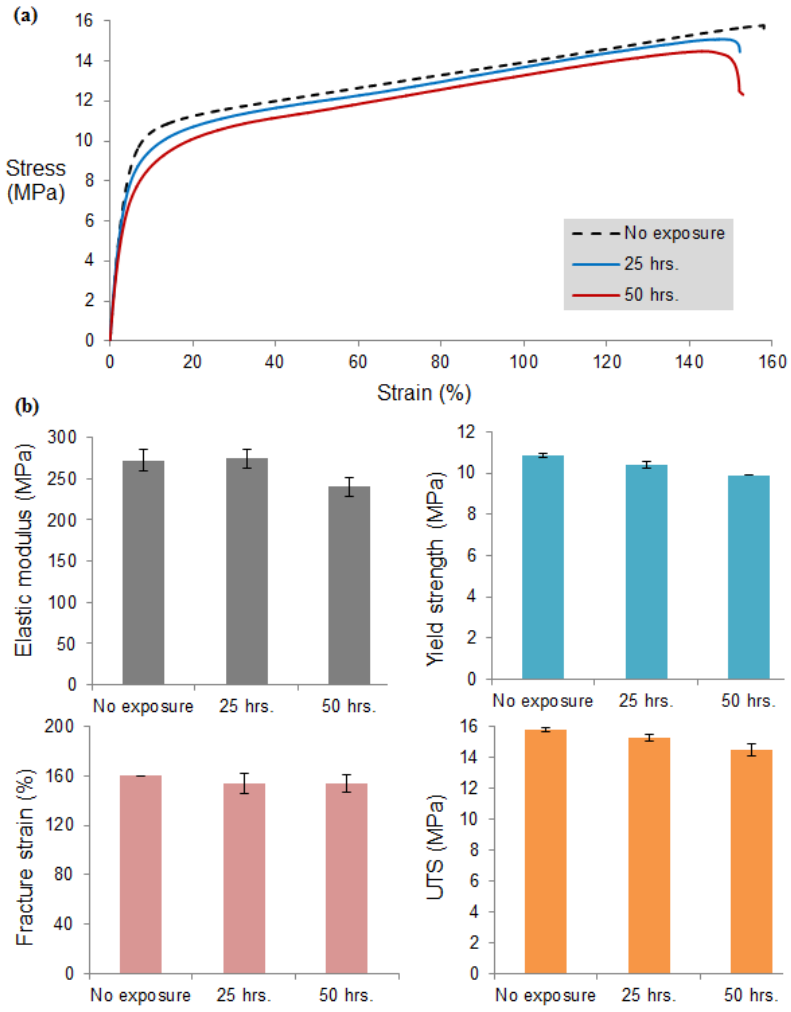

Figure 3.16: (a) Tensile stress-strain data obtained at 23°C, 50% RH, and 0.01 min^{-1} strain rate for CCM samples before and after exposure to 25 and 50 hours of X-ray irradiation on a ZEISS Xradia 520 Versa® micro-XCT system. (b) Mechanical properties, viz. elastic modulus, yield strength, fracture strain, and UTS, extracted from the stress-strain curves. The elastic modulus is obtained from the initial slope up to 5% strain, while the yield strength is obtained from the intersection of this initial linear region with the post-yield linear region from 40 to 100% strain. The data represents average results from two experiments at each condition with error bars indicating one standard deviation. [159]

Chapter 4. Image Processing

To obtain quantitative information from images, segmentation of components is required to then be further analyzed. Segmentation is the method of labelling objects within an image such that identification is simplified. Consider, for example, the computed tomography image shown below in Figure 4.1a. [165]. Using our eyes we identify 3 groups of pixels by their relative greyscale: dark, medium, and bright. The dark pixels (or low value greyscale) correspond to air or voids due to the relatively low attenuation of the X-rays, whereas the brightest (highest greyscale value) correspond to bone due to the relatively high attenuation of X-rays. The medium value is thus the soft tissue of this animal. Consider that one wanted to know the relative proportion of soft tissue to bone. In order to perform this calculation, we would need to know the relative volumes of each. To do this in an efficient manner, an algorithm that allows the computer to count the number of pixels for soft tissue and bone could be used to perform this analysis. The first step is to thus tell the computer which pixels should be labelled as soft tissue, and which should be labelled as bone. The most accurate method would be to have a human user manually label each pixel, since not only can we consider pixel value information, but also the whole view and knowledge of what we are identifying. This may be possible for a single image and is often performed in medical imaging, however consider now doing this for thousands of images to create the 3-dimensional volume. This could take hundreds of hours and is completely impractical. Instead, more automated methods are used, at a cost of accuracy at times. The simplest method is where the objects are identified by their pixel value alone, this is known as histogram segmentation, or thresholding. A range in the histogram of pixel values is assigned to one object and repeated for as many objects as needed, shown in Figure 4.1b, with result shown in Figure 4.1c. This way, every image in the stack of images is automatically segmented to create a 3-dimensional volume, shown in Figure 4.1d. Due to noise and sometimes similarities in greyscale value however, there is error in this method, and is not suitable for segmentation of PEFC components. The section below will describe the algorithms and routines developed to perform segmentation of all PEFC components necessary in this thesis.

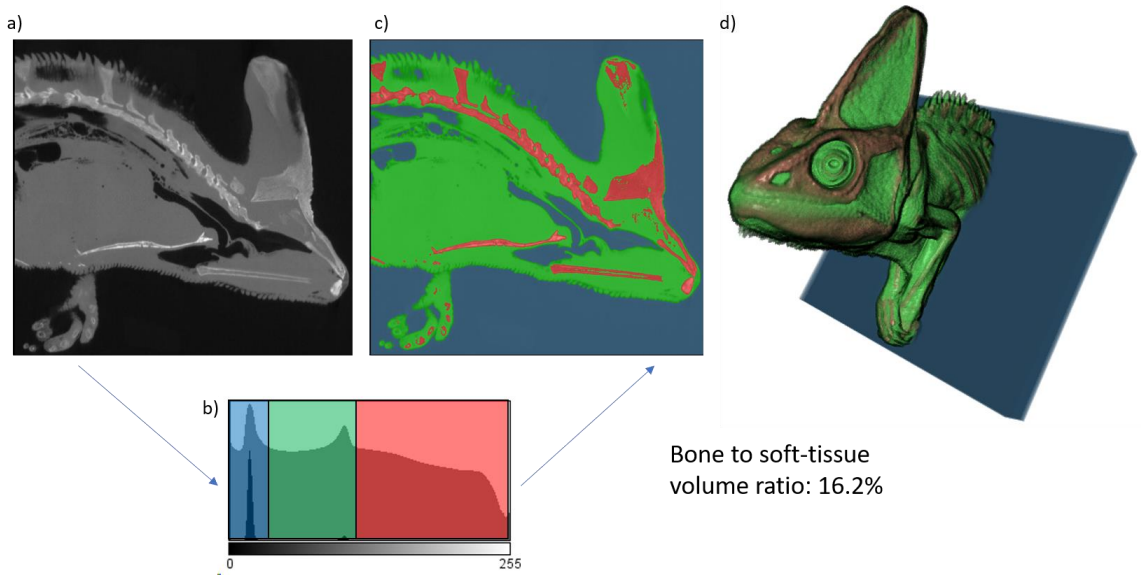

Figure 4.1: Schematic, demonstrating segmentation to perform quantitative analysis. a) Single grayscale image from computed tomography stack. (b) Grayscale histogram with segmentation range overlay. (c) Result of segmentation with greyscale image simplified to regions of three labels, blue is air, green is soft-tissue, red is bone. (d) Resulting volume illustrated and quantified by performing this segmentation automatically over the full stack of images.

4.1. Segmentation of PEFC Components

Within this thesis work, the development of necessary post processing tools was required to allow for quantitative analysis of fuel cell component properties that have not been quantified in such a way before. Extraction of quantitative information regarding material/geometrical properties, such as thickness, porosity, saturation, and local composition, as well as variation in these properties and material morphology during any degradation process, is vastly facilitated by advanced image processing and visualization methods. In this work, custom tools and analysis methods are developed and allow for new insights into the temporal changes of water saturation, cathode catalyst layer morphology, and membrane crack propagation. Various analysis algorithms used for crack width, average island size, porosity, saturation, tortuosity, chord length, dynamic movement and diffusion analysis are discussed with reference in Chapters 5, 6 and 7 where the results obtained are presented and discussed. Prior to using these algorithms however, accurate segmentation of the necessary components was required. The following section discusses the developed workflows and tools, with additional information presented in the Appendix. An overview of the results achieved is presented in Figure 4.2

as a summary showing each component (anode side not shown for simplicity) segmented, to be available for quantification.

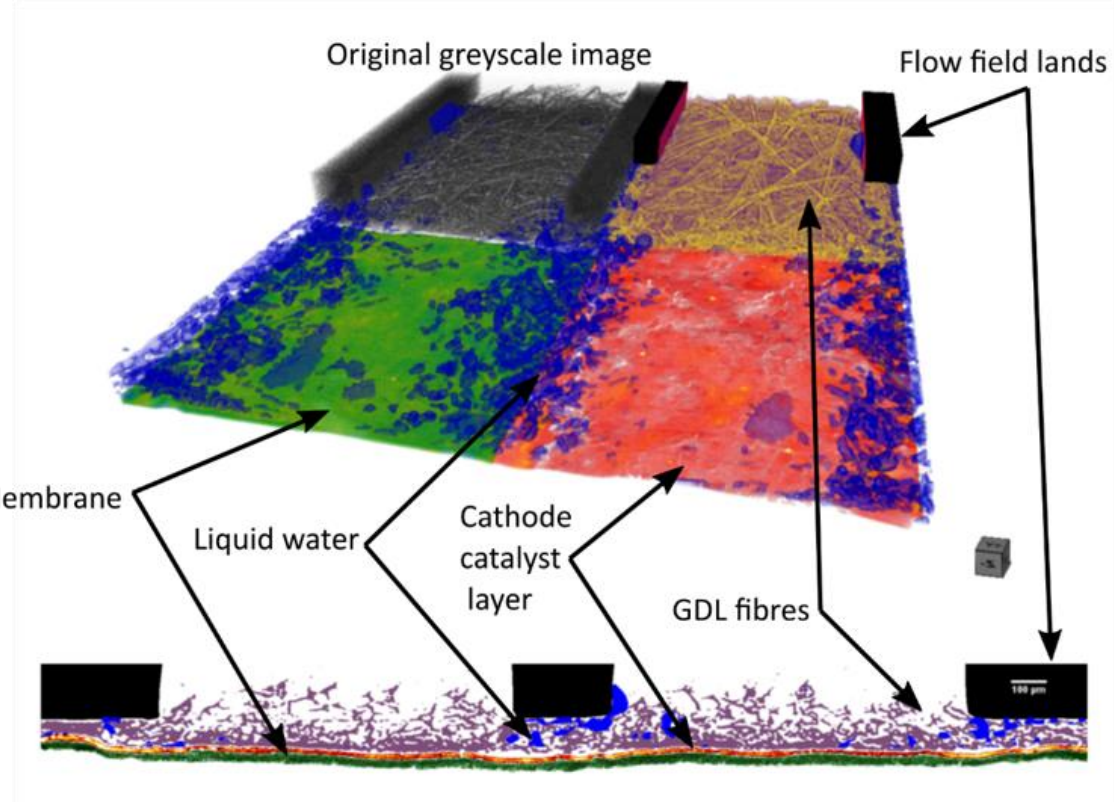

Figure 4.2: Full segmentation and visualization of all PEFC component layers and liquid water by advanced processing methods (anode side not shown).

4.1.1. Gas Diffusion Layer and Liquid Water

Segmentation of the GDL is typically straightforward in that contrast between fibers and air is sufficient to apply simple greyscale thresholding. A median filter can be applied to reduce noise as a pre-processing step depending on the quality of the tomography. For the typical imaging parameters used for 4D *in-situ/operando* imaging, some error in the region of the MPL due to resolution limits is unavoidable and typically the data is cropped to not include this region in calculations as the porosity is unresolvable. Other errors associated with resolution limits are typically small when calculating only bulk porosity of the GDL. For improved accuracy, a higher resolution scan with limited field-of-view can be collected and extrapolated to these areas combining datasets [71]. Shown in Figure 4.3 is the segmentation by simple thresholding of the GDL fibers to calculate bulk porosity. Even

from this zoomed in scale, few errors can be observed. The region shown is about 4% of the total area of the actual dataset.

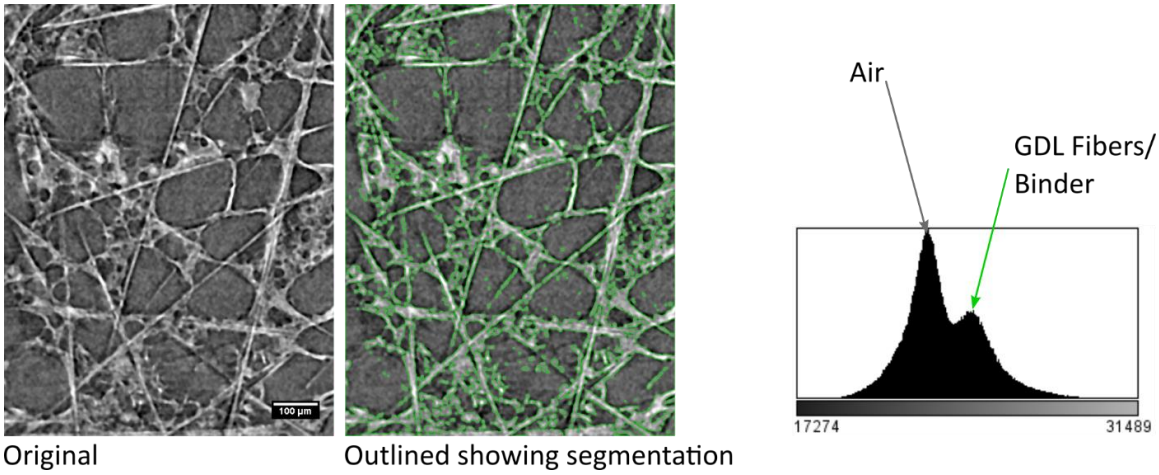

Figure 4.3: Sample segmentation of GDL fibers using simple thresholding from original 3mm x 3mm view after applying a median filter to reduce noise in the original tomography.

In order to accurately segment liquid water within the GDL, a ‘dry’ reference must first be subtracted from the ‘wet’ dataset. This is necessary to improve the contrast sufficiently to automatically determine water volume within a GDL and surrounding air. In this context, the ‘dry’ scan is a reconstructed 3D tomography dataset in which the MEA is imaged in a dry state by flowing dry nitrogen to remove all liquid water, and the ‘wet’ scan is the state in which the exact same MEA has liquid water present in the GDL following equilibration while drawing current under operating conditions. Before this subtraction can be applied however, an alignment step is required, and the reconstructed datasets must have the same greyscale byte scaling. These two steps are crucial not only for segmentation of liquid water, but all analysis in which a temporal change is being imaged utilizing the 4D imaging methodology to properly compare across multiple datasets. A more detailed outline of the algorithm steps and example application is described in Appendix A specific to the small-scale fixture and XCT system that utilizes custom macros written for ImageJ/Fiji. A general overview is provided in this section, summarized in Figure 4.4.

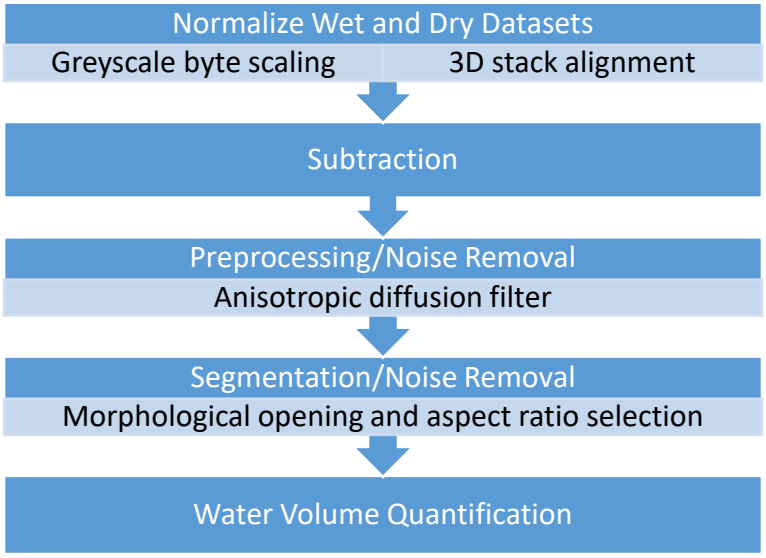

Figure 4.4: Summary of steps used to perform segmentation of liquid water within the GDL.

In the preprocessing and noise removal step of Figure 4.4, a median filter of size 3x3 pixels is applied followed by an anisotropic diffusion filter. This filter aims to improve segmentation accuracy by reducing greyscale variation from within a single phase. The algorithm used is an implementation in python of the original application by Perona and Malik [166]. It aims to smooth regions of the same phase and preserve edges by treating them as a boundary, prohibiting energy transfer. It requires a user input for the number of iterations which will impact the level of smoothing, as well as a constant which is chosen based on the standard deviation of greyscale values within a single phase [167]. Segmentation is then performed using simple greyscale thresholding. An additional noise removal step is also applied to remove any fibers which were not fully subtracted. This step is performed using morphological opening followed by removal of objects with eccentricity above 0.98. The stepwise result of this procedure is shown in Figure 4.5 for a portion of a GDL under ‘dry’ (no current) and ‘wet’ (with current) conditions.

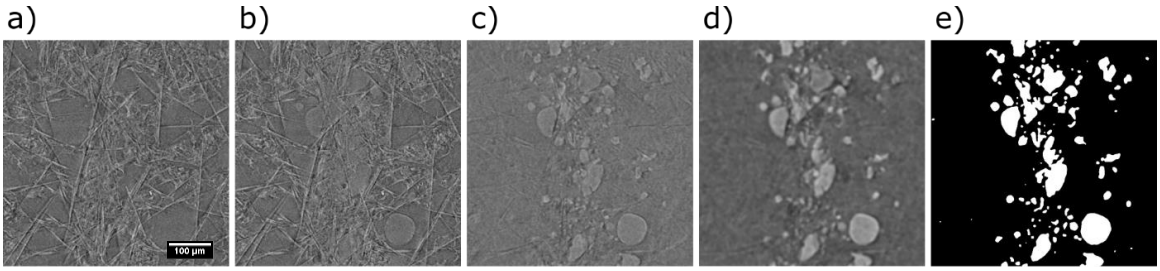

Figure 4.5: Sample images from original 3mm x 3mm dataset. a) Dry GDL, b) wet GDL after operation at 250mA/cm^2, c) after subtraction step d) after anisotropic diffusion processing, e) final segmentation.

4.1.2. Cathode Catalyst Layer

The need to segment the cathode catalyst layer (or anode, which can be done with the same following steps but different parameters) is important in failure analysis of polymer electrolyte fuel cells, whether it be from images collected by SEM or XCT. Measurements such as catalyst layer thickness loss can be used to describe the level of carbon corrosion, for instance. Crack formation or delamination also show potential future damage feature initiation sites, such as pin-holes and membrane cracks. To quantify the changes following degradation and corrosion, accurate segmentation is first required. Using global thresholding is inaccurate since the anode will also be included and needs to be differentiated, in addition GDL fibers also have similar greyscale to many parts of the catalyst layer. An algorithm developed in this thesis is describe in the following to allow for accurate segmentation of the catalyst layers. The algorithm is compiled in an ImageJ macro titled 'Cathode Separator'. A detailed overview of the steps is described in Appendix B. First, coarse segmentation is required to define the catalyst layers, additional GDL noise and separation of anode from cathode are implemented in subsequent steps (for anode isolation, the cathode is masked, see membrane segmentation in section 4.3). Following greyscale thresholding by the user a large 2-dimensional Gaussian blur is used to connect the isolated islands created from catalyst layer cracks. Following this, an automated selection based on overall volume differentiates the cathode from anode catalyst layer. These steps are shown in Figure 4.6 below. In some MEA configurations the anode and cathode can have similar volume, in which case if the anode is incorrectly selected, it can be masked out; with the algorithm repeated to correctly select the cathode layer only.

Figure 4.6: a) Initial segmentation following crop and thresholding from in-situ XCT image. b) 2-dimensional Gaussian blur applied and thresholded to connect cathode as single object. c) Using binary logic to select only the cathode catalyst layer from volume selection of b).

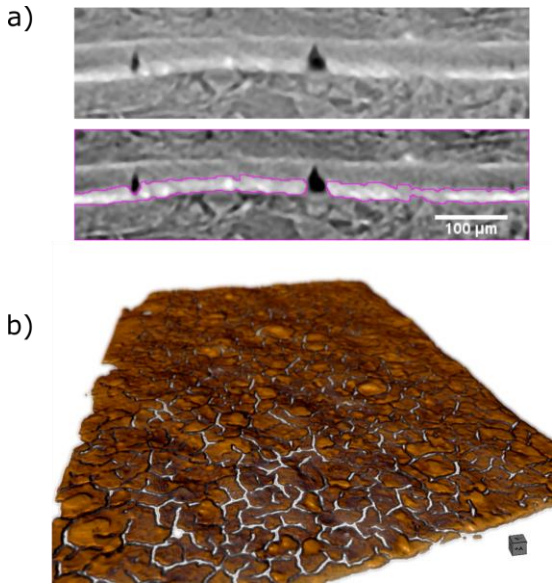

Figure 4.7: Sample in-situ XCT images of degraded cathode catalyst layer with cathode layer segmented and outlined in a), with full 3D rendering of cathode catalyst layer in b).

An example output of running the following algorithm is shown above in Figure 4.7 with images collected using the Zeiss Versa 520 XCT. This is performed in 3-dimensions over a full stack of images. This is the necessity of this algorithm, as there are approximately 2000 images for each dataset creating the 3-dimensional volume, rendering this impossible for manual segmentation.

The thickness value is calculated by summing the number of vertical pixels at that location within the segmented catalyst layer structure. This is simpler than considering the possible angle with which to draw a perpendicular line to measure the

cathode thickness, which can be non-trivial when the angle is different between top and bottom interface, see Figure 4.8. The error of using vertical summation is within the standard deviation error of the measurement when the angle is less than about 40 degrees for average thickness of 12 µm. This is shown in Figure 4.8a below, as well as empirical measurements of angles for the catalyst layer which all fall well below this angular value. For these measured angles the error is approximately 1 µm, which is less than the pixel value and therefore a negligible impact on the accuracy of the measurement. It can be also seen how different top and bottom angles are present and even manually deciding how to draw a line measurement for thickness is not clear. Using the above method also improves consistency in this way, where different users may otherwise obtain different thickness values at the same location.

A thickness map can subsequently be output in which each pixel corresponds to the thickness of the cathode catalyst layer at that location, providing a detailed map of the variation in thickness over a large area which has not been visualized previously. An example of this is shown in Figure 4.9 below.

Accuracy of the algorithm was correlated to high resolution images as well as established SEM analysis already in use, with average values shown below in Table 4.1.

Measurement images	**Average thickness calculated (µm)**
XCT 1.5 µm pixel size (9mm^2 area)	11.6 ± 3.8
XCT 0.68 µm pixel size (0.42mm^2 area)	11.04 ± 3.6
SEM	11.8 ± 3.3

Table 4.1: Quantification of thickness values using automated catalyst layer segmentation compared with SEM manual measurement.

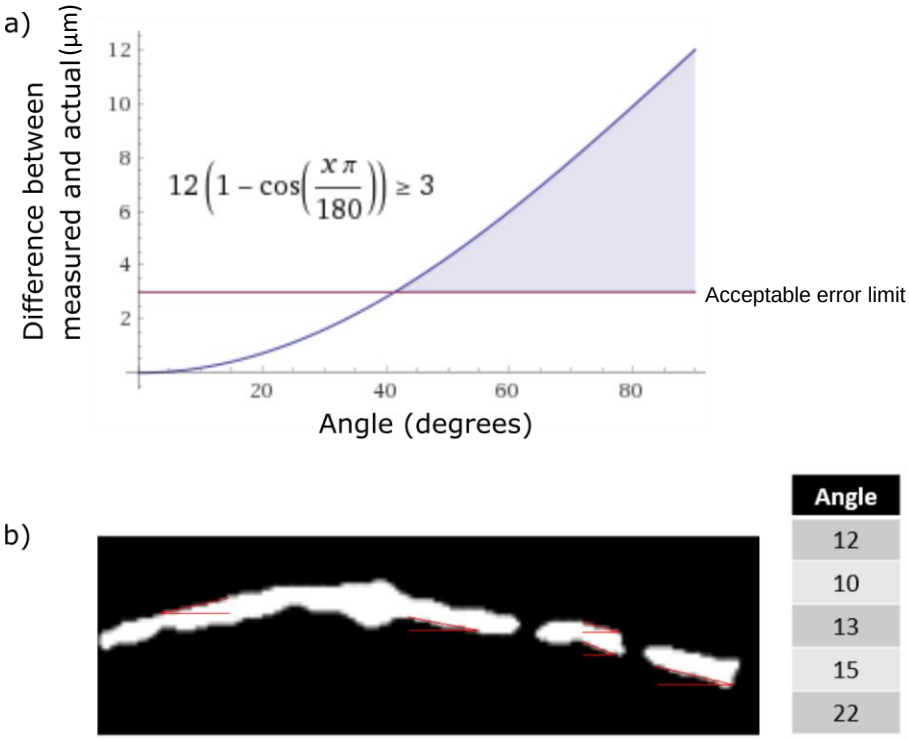

Figure 4.8: a) Plot for the effect of catalyst layer undulation angle on average value of catalyst layer thickness and approximate acceptable error; b) Measurements of catalyst layer angles for a highly undulated region, with measured angles shown.

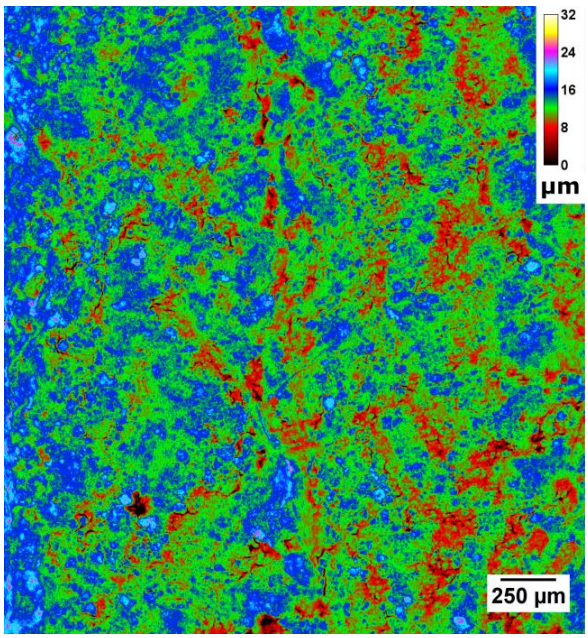

Figure 4.9: Thickness map of operando cathode catalyst layer.

4.1.3. Membrane

The segmentation of the membrane is of particular interest as it relates to degradation analysis. Similar to the catalyst layer, crack formation and thinning are dominant features relating to the level of degradation and of significant scientific interest [18], [159], [168], [169]. However, analysis doesn't come without its difficulties. The membrane has low attenuation and is similar in grayscale value to air and surrounding low attenuating carbon in the GDL, see Figure 4.10a. The addition of cracks in the catalyst layer as well as thin membrane regions increases difficulty of accurate segmentation. Finally, the addition of noise and artifacts from the adjacent catalyst layer make the greyscale value of the membrane non-uniform and unable to segment using algorithms used previously under more idyllic imaging conditions [13]. The solution to these considerations is incorporated in a custom application titled 'MemSeg', which instead uses the catalyst layers as boundaries and allows for the accurate and rapid segmentation of the membrane with very minimal user knowledge of post-processing methods, such as machine learning. In addition, it also provides a useful analysis tool titled 'dynamic slicing' which aids in the visualization of internal degradation features. An overview of the algorithm steps and discussion is provided below.

The membrane segmentation starts with the segmentation of the cathode and anode catalyst layers, shown in Figure 4.10b. This uses the algorithms discussed in 4.1.2. The segmentation of these layers is used to create a region which bounds the membrane and which it must fall between. Catalyst layer cracks and degradation features can cause errors in boundary selection for the membrane; as well as, the anode catalyst layer can be particularly difficult to segment. The anode may have a thickness of 5 µm or less which comes close to resolution limits of the in-situ/operando set-up. However, even with partial segmentation, this is sufficient, as joining of the boundary pixels is performed using linear interpolation with an applied median filter providing a moving average smoothing which best follows the natural undulation of the membrane. The result of creating these two boundaries is shown in Figure 4.10d This method is better than others tested such as nearest neighbor or polynomial methods, which can have significant errors when large gaps are present or if cropping forces a boundary to be on an edge of the image.

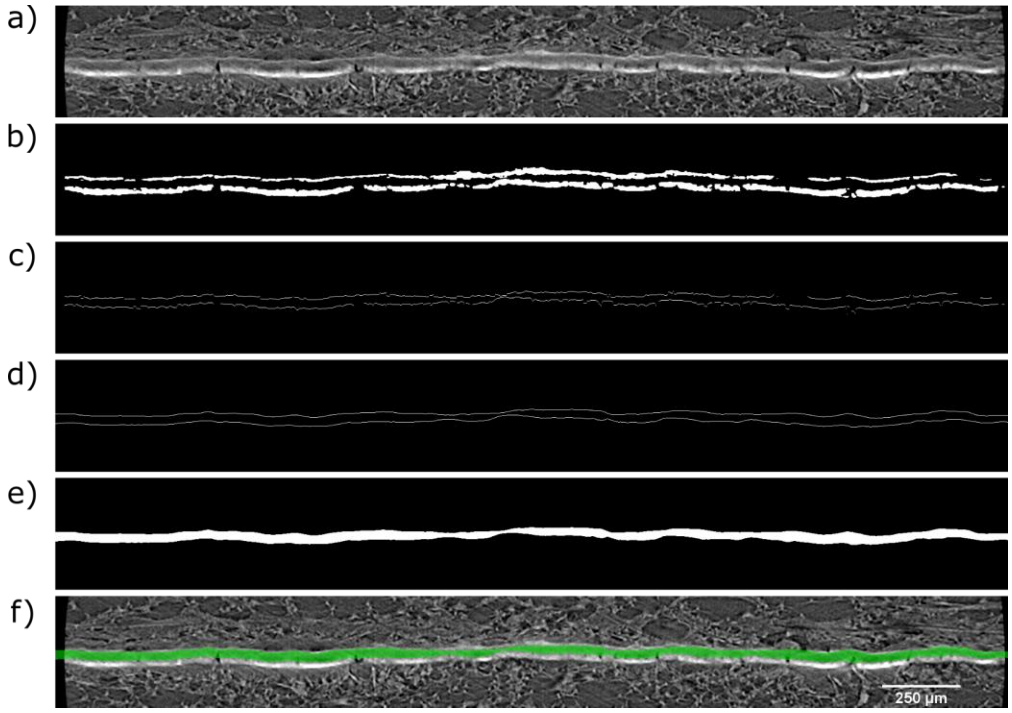

Figure 4.10: Membrane segmentation. a) Single slice from original 3D dataset of full MEA. b) Following segmentation of catalyst layers (see section 4.1.2). c) Interface boundary between catalyst layers and membrane. d) Applied interpolation and smoothing to fill regions between catalyst layer cracks. e) Segmentation of membrane using interpolated boundary. f) Overlay of segmented membrane region on original greyscale image.

Dynamic slicing algorithm is a newly designed tool which allows for the user to step through the 3D dataset in such a way that each image step follows the undulation of the membrane, see Figure 4.11a. It also allows the user to specify locations relating to the relative distance from the catalyst layers, which proves to be especially useful when identifying how cracks are initiated in the membrane [159]. This also allows for the identification of cracks which are fully through the membrane (through-thickness cracks) or not, which can be used to discriminate cracks that contribute to gas-crossover and performance loss [19], [170]. The result of this is the ability of the user to analyze the membrane alone and understand 3D spatial correlation with all other MEA components.

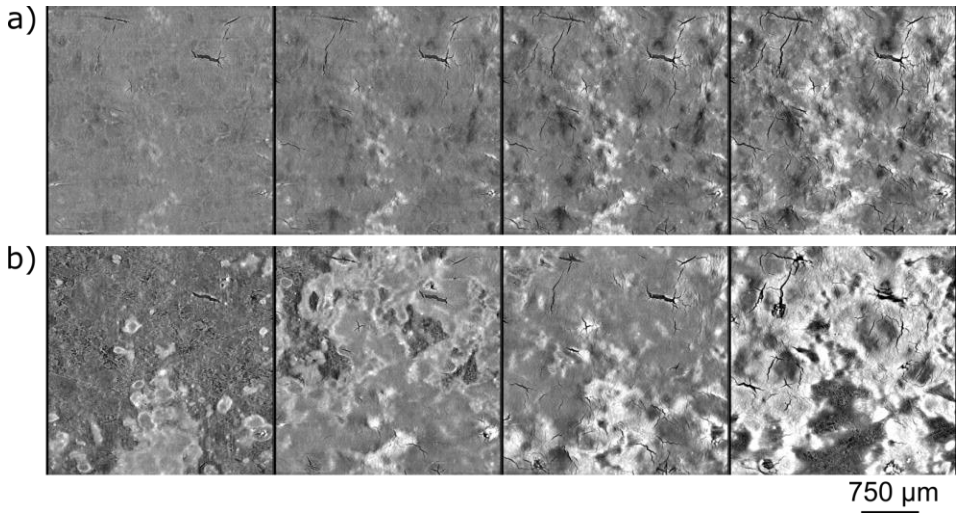

Figure 4.11: a) Dynamic slicing at various locations through membrane. b) Typical (static) slicing where portions of other components such as GDL and catalyst layer convolute the visualization of the membrane.

The difference in time between manual segmentation and MemSeg is roughly 33-66% per slice. Using MemSeg will save hours of time over the course of a single image stack; with stacks usually 1000+ slices, MemSeg can save thousands of hours in processing data over the course of an experiment. When comparing how close the thickness is based off manual segmentation as the base line, the CCL 3.5% difference, ACL 18% difference, and membrane 22% difference. Measurements were done using a macro to compute the average thickness on the single slice then compare the two values from each method. The 22% difference translates into a 3 pixel thickness difference or 4.77 um (1.59um/pixel). Discrepancies can come from the MemSeg outputs having interpreted results in the boundaries and membrane masking. Other errors can come from not the entire layers being segmented, particularly the ACL which can often have areas not segmented requiring more interpolation. Also, these results are comparing a single slice of the image stack so using more than one slice may improve the differences by statistical averaging. Overall there is a tradeoff of accuracy for time saved when using the MemSeg however, the errors are consistent and can be used well when comparing changes.

4.2. Compositional Analysis

As discussed in section 2.2, the greyscale pixel values produced from XCT imaging are in direct relationship with the material properties such as density and composition. For a simple example, bone will have a higher greyscale value than air because it is denser and contains highly attenuating calcium atoms, compared with low density air, and low attenuating oxygen and nitrogen components. The property that describes the amount of X-ray interaction is the mass attenuation coefficient; it is a complex combination of properties associated with the interaction of atoms with X-rays and is a function of the incident X-ray energy. Tabulated values from institutes such as National Institute of Standards and Technology (NIST) are available for each element and compound [144], [171]. The linear attenuation coefficient describes the additional impact of the density of the material:

$$\boldsymbol{\mu_{\mathrm{Lin}}(E) = \rho \cdot \mu_{\mathrm{Mass}}(E)} \qquad \textbf{(4.1)}$$

where $\boldsymbol{\rho}$ is the density of the material. As such, provided that the composition of the material is known as well as the density, a relationship between the greyscale value and the linear attenuation coefficient can be empirically determined as relative scaling is used when creating the reconstruction images. Therefore, by using materials of known values, a linear relationship between greyscale value and linear attenuation coefficient can be determined for a set of images, which can subsequently be used to determine the attenuation coefficient of an unknown material [172], see Figure 4.12.

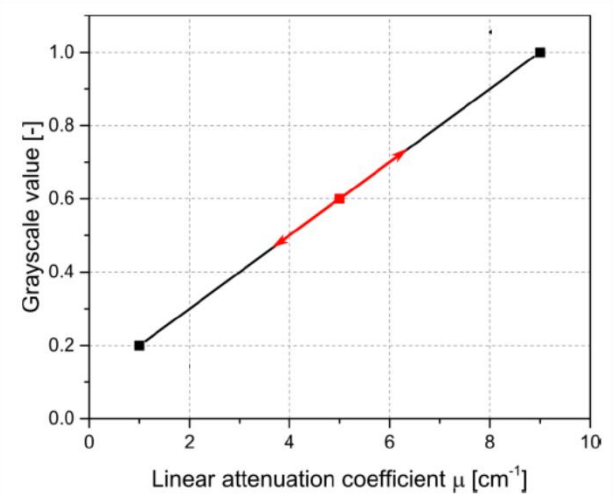

Figure 4.12: Principle of quantitative absorption contrast tomography to determine a material composition. Considering a material with a minimum and maximum density shown, it is possible to calculate the unknown composition by correlating the minimum and maximum grayscale value to a linear attenuation coefficient.

The cathode catalyst layer of a PEFC is a porous composite material comprised of carbon, platinum as well as ionomer, which is typically a perflourosulfonic acid based polymer. Due to the fabrication process, the distribution of these components is not purely uniform but can have some variation. This variation is presented in differences of local thickness as well as greyscale pixel values (relating to density and composition variances). Using this information, it is the goal of this section to back calculate the approximate local cathode catalyst layer composition and provide insight into possible causes relating to degradation vulnerability. In addition, by following this calculation through different stages of degradation, the local compositional change of the catalyst layer can be tracked; see section 5 and 6 for the application study.

The above linear scale shown in Figure 4.12 is assumed for a monochromatic X-ray source. The XCT system employed in this work is lab based, with a non-monochromatic X-ray source. However, filters are provided which can be used to tune the X-ray spectra and the effective X-ray energy can be calculated empirically. In addition, a comparison to a monochromatic light source using a synchrotron system (Canadian Light Source) was employed for validation. This is shown in Figure 4.13 below where clear higher attenuating local regions of the cathode catalyst layer are seen in both images and line profiles without any additional artifacts when comparing lab-based XCT system to

synchrotron XCT system. Additionally, a calibration curve to determine the conversion of linear attenuation to greyscale value was obtained by imaging known materials and fitting to a linear curve where the energy used allows a straight line to join all points within experimental uncertainty. Shown below in Figure 4.14 is the calibration curve for four known materials (shown in blue) and nominal cathode catalyst layer value (shown in orange) using an effective X-ray energy of 32.5 keV. The calibration curve obtained follows an expected linear trend, indicating that a single energy assumption is valid in this case. This is the mean energy after applying filters to the X-ray beam to remove the low energy contributions. The known materials were imaged using a custom designed calibration puck which was composed of the same material as the small-scale fixture as well as the same dimensions and imaging parameters to ensure any additional filtering was as consistent as possible. The materials used were air, flow field graphite plate, sulfuric acid and titanium foil. These materials gave a good distribution of values to properly determine an accurate calibration curve. With these experimental considerations, a model can be implemented. The calculation required is as follows:

$$\boldsymbol{GSV = m_{\text{cal}} \cdot \mu_{C_xH_xF_xO_xS_xPt_x} + b_{\text{cal}}} \qquad \textbf{(4.2)}$$

Where m_{cal} and b_{cal} are slope and intercept from the calibration curve, respectively, and $\mu_{C_xH_xF_xO_xS_xPt_x}$ is the linear attenuation coefficient from the constituents of the catalyst layer. Variation in the cathode catalyst layer greyscale value can then be converted to linear attenuation (μ), and with known thickness from segmentation, density and composition can then be inferred.

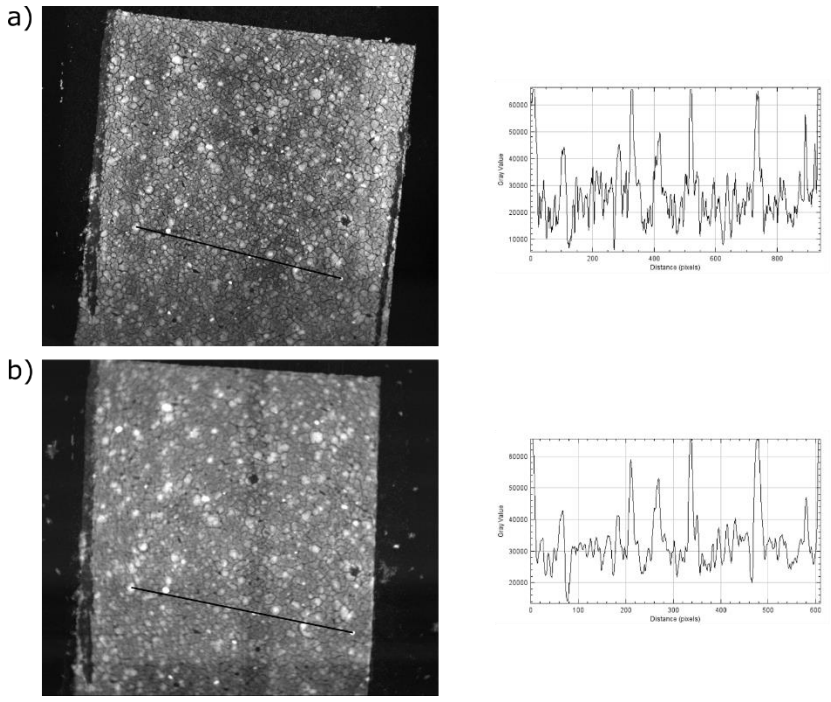

Figure 4.13: a) Average projection from 3D reconstruction of cathode catalyst layer by lab-based XCT used in this thesis with line profile shown. b) The exact same cathode catalyst layer and average projection from reconstruction collected by monochromatic synchrotron X-ray source. Note the profile for same location identifies the same peaks in greyscale as a result of composition variation. The pixel size of b) was greater than that of a) due to limitations in detector, as such the noise is lower resulting in slightly smoother profile.

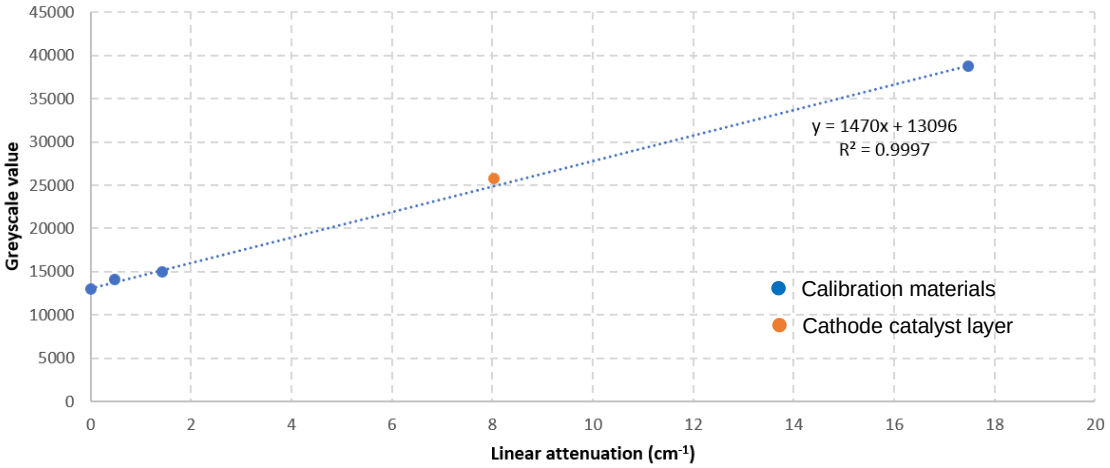

Figure 4.14: Calibration curve for greyscale value and linear attenuation of materials to be used as conversion in the model calculation. The known materials used in the calibration are air, flow field graphite plate, sulfuric acid and titanium foil (blue, lowest to highest attenuation values). The cathode catalyst layer with nominal composition and thickness is shown in orange.

To calculate the mass attenuation of a composition of the cathode catalyst layer, values obtained from NIST (https://physics.nist.gov/PhysRefData/FFast/html/form.html) were fitted to a model using Support Vector Machine (SVM) regression with radial basis function in order to efficiently calculate the unknown composition of the catalyst layer's attenuation coefficients. The obtained values from NIST are shown in Figure 4.15a as data points with the implicit model shown as the color area fit. The fitted model has an accuracy of 0.15 $cm^2\ g^{-1}$ which is less than 1.5% error for nominal cathode catalyst layer composition values. From the experimentally obtained greyscale values by XCT imaging, linear attenuation can be determined from the above calibration curve. To obtain linear attenuation values, the mass attenuation determined from the implicit model was multiplied by the density, which was calculated using the local thickness determined after segmentation of the CCL. Using this model, a constrained optimization routine was then implemented to minimize the difference between the experimental greyscale pixel value and the calculated value by varying the catalyst layer composition. The optimization routine uses constrained optimization by linear approximation (COBYLA) from scipy python library. The constraint function is the porosity calculation limited between 0 and 1:

$$\boldsymbol{\phi = 1 - \frac{\rho_{bulk}}{\rho_{particle}}} \qquad \textbf{(4.3)}$$

where void space is assumed to be filled with air; ρ_{bulk} is the calculated density from composition obtained from the optimization routine and local thickness; and $\rho_{particle}$ is calculated based on the known densities for carbon (graphite), platinum and ionomer, as listed in Table 4.2.

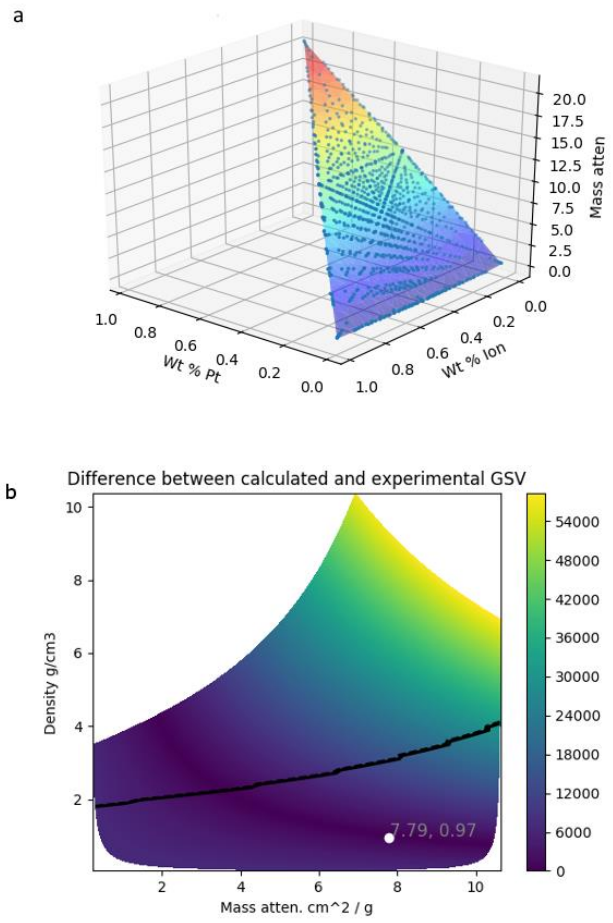

Figure 4.15: a) Implicit model and obtained mass attenuation values from NIST for variation in Pt, carbon (not shown) and ionomer composition to be used in greyscale model calculation. b) Plot of the optimization search space with the constraint function shown in black. Values below this line are possible composition values, with the found optimization point indicated by the white dot which falls close to initial nominal values.

Greyscale model input parameter	Value
X-ray energy	32.5 keV
ρ_C	2.3 g cm^{-3}
ρ_{Pt}	21.5 g cm^{-3}
$\rho_{Ionomer}$ [173]	2.0 g cm^{-3}
$Nominal_{Pt}$	0.4 mg cm^{-2}
$Nominal_C$	50 wt %
$Nominal_{Ionomer}$	23 wt %

Table 4.2: Greyscale analysis input parameters and nominal values for initial condition for optimization search.

This is shown in Figure 4.15 with the constraint boundary in black and the obtained optimization point shown at a mass attenuation value of 7.79 cm^2 g^{-1} and density of 0.97 g cm^{-3}, which falls close to the initial guess (nominal) values for beginning-of-life (BOL) composition. An overview of the model workflow is shown in Figure 4.16. A limitation with the calculation model presented is that the solution is not unique. A high density of low effective atomic number materials will produce the same greyscale since the effective attenuation is a multiplication of both properties. This means that a region with high ionomer content will increase the density by filling pores, and even though the mass attenuation will decrease with higher ionomer content the resulting composition will yield the same greyscale. Typically, rich ionomer regions have been observed to be very thick from dense agglomerates forming and have been used as a que for possible ionomer regions during the calculation where the bias toward higher ionomer content is dependent on the thickness. A comparison with energy dispersive spectroscopy (EDS) has been used for validation, see Figure 4.17 where a region outside the nominal composition is selected with higher than normal ionomer content and is identified in both EDS map and XCT composition analysis. The model cannot be used for an unknown material; however, as shown in section 6 of this thesis, it can be used to determine variation around initial composition and changes resulting from degradation.

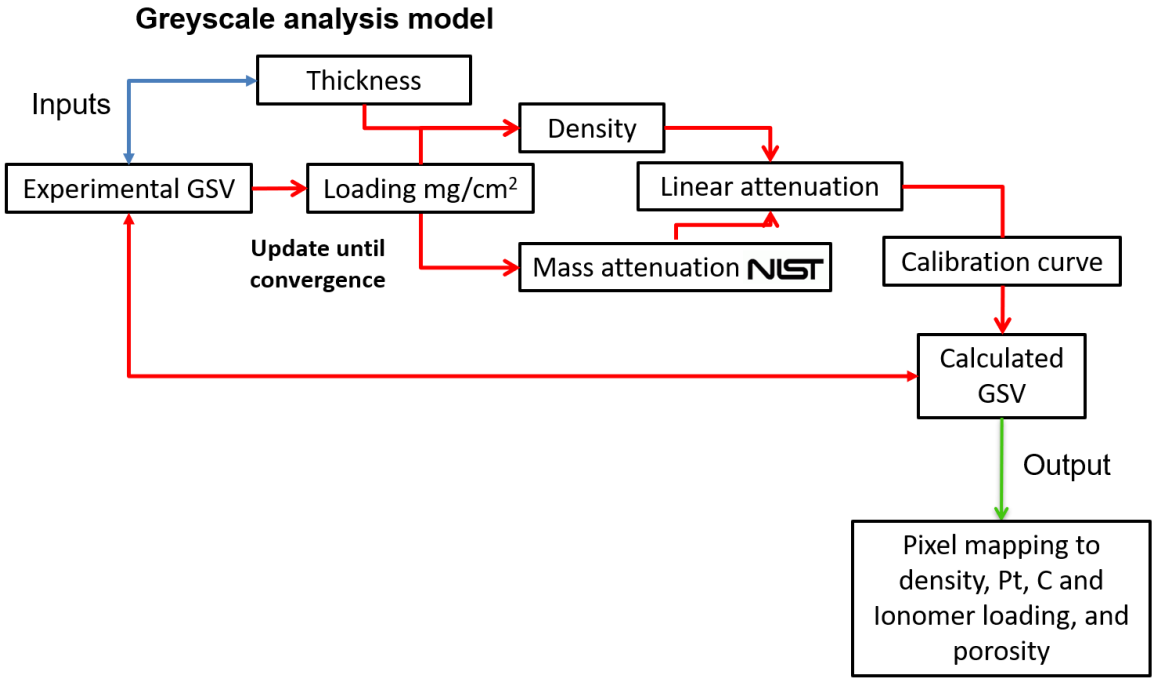

Figure 4.16: Algorithm workflow for compositional analysis from XCT data for cathode catalyst layer.

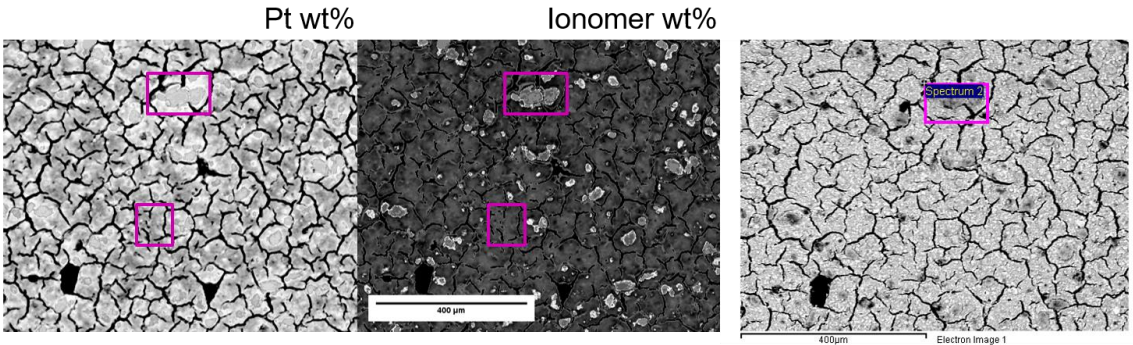

Figure 4.17: Comparison of calculated values using proposed method above and EDS. The values shown correspond to the same location on the same sample catalyst layer. Visual correspondence can also be seen in the Ionomer wt% image compared to different greyscale in backscatter SEM image which appears darker thus indicating lower effective atomic number.

Using the above described model sample outputs such as the Pt content distribution can be visualized as shown in Figure 4.18. The greyscale images used in this model are 2-dimensional averages of the catalyst layer through the thickness. The ionomer is more uniformly distributed with some regions of high content, similar to those seen in Figure 4.17. The Pt distribution is less uniform with regions of high and low content. When averaging over the full area however, the result is the expected nominal value at BOL.

To determine changes in composition over time as shown in Section 5 and 6 for a cathode catalyst layer undergoing degradation, the experimental greyscale values were obtained from the zero-current density ('dry') image set and projecting the average through-plane greyscale values to a single 2D image after segmentation of the CCL. For BOL, nominal values of the CCL composition were given as initial guess for the optimization routine. To limit possible solutions, an assumption that the ratio between platinum and carbon remained constant was employed for the BOL state, since these are derived from Pt/C powders before mixing with ionomer solution where variation is more likely. The ionomer content was subsequently assumed to not change following the voltage cycling AST procedure (see Section 5 and 6) and was not altered during the subsequent optimization routine from BOL, while carbon and platinum were free to change due to degradation. Initial values were taken from the previous stage (e.g. BOL composition was given as initial starting values for 250 AST cycles, 250 AST cycles composition output were given as initial values for 450 AST cycles etc.). That is, the model was applied to the BOL catalyst layer to determine local variation in ionomer, C and Pt content, while calculations following AST cycles used these local values as inputs and adjusted the C and Pt content to match the greyscale values obtained from the experiment. Further validation and comparison to carbon dioxide measurement is discussed in Section 6.

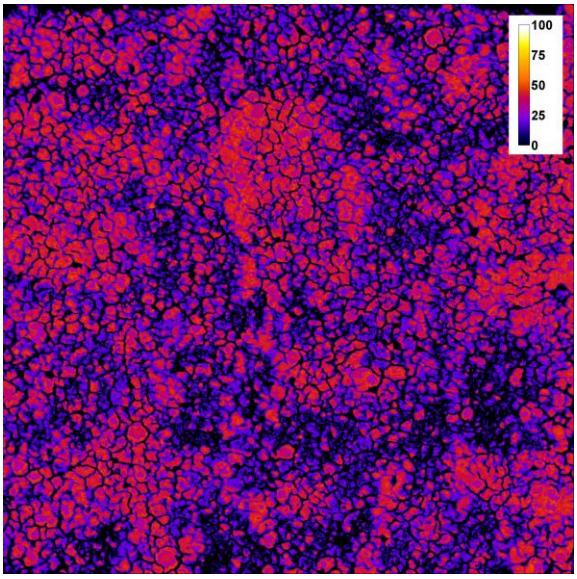

Figure 4.18: Platinum content distribution in a cathode catalyst layer presented as weight percent at BOL obtained by using the compositional model.

Chapter 5. 4D In-Situ Visualization of Cathode Catalyst Layer Morphological Degradation

The ability to non-invasively visualize the complex nature of fuel cells during their lifetime is the primary objective of development in this thesis. This methodology has far reaching applications not only in the focus of cathode catalyst layer degradation, but in membrane degradation, MPL interfacial effects, GDL morphology, water distribution changes, compression effects and MEA dynamics; among other investigations. These investigations in turn yield great understanding to the nature of fuel cells that have never been observed before, as well as validate models proposed through other methods of analysis.

The aim of the presented work is to introduce the application of the developed small-scale fixture with lab-based X-ray computed tomography; providing an overview of the design as well as validation to the proposed workflow using cyclic voltage accelerated stress test (AST) to perform accelerated cathode catalyst layer degradation focussing on carbon corrosion. Novel insight into the local degradation behaviour of the cathode catalyst layer is presented with same location tracking of catalyst layer crack growth. In addition, proposed compositional changes relating to density are discussed, by observations of greyscale value changes; a first complete and accurate visualization of this result.

The following section is a formatted version of R. T. White, A. Wu, M. Najm, F. P. Orfino, M. Dutta and E. Kjeang**, 4D in situ visualization of electrode morphology changes during accelerated degradation in fuel cells by X-ray computed tomography**, *J. Power Sources.,* 350 (2017) 94-102.

R.T.W., and E.K. conceived the project; R.T.W. designed the small-scale fixture; A.W., M.N. and R.T.W. performed fabrication, and operated and collected diagnostic measurements of the small-scale PEFC; R.T.W. collected and analysed XCT data; R.T.W. drafted the manuscript.

A four-dimensional visualization approach, featuring three dimensions in space and one dimension in time, is proposed to study local electrode degradation effects during voltage cycling in fuel cells. Non-invasive *in situ* micro X-ray computed tomography (XCT) with a custom fuel cell fixture is utilized to track the same cathode catalyst layer domain throughout various degradation times from beginning-of-life (BOL) to end-of-life (EOL). With this unique approach, new information regarding damage features and trends are revealed, including crack propagation and catalyst layer thinning being quantified by means of image processing and analysis methods. Degradation heterogeneities as a result of local environmental variations under land and channel are also explored, with a higher structural degradation rate under channels being observed. Density and compositional changes resulting from carbon corrosion and catalyst layer collapse and thinning are observed by changes in relative X-ray attenuation from BOL to EOL, which also indicate possible vulnerable regions where crack initiation and propagation may occur. Electrochemical diagnostics and morphological features observed by XCT are correlated by additionally collecting effective catalyst surface area, double layer capacitance, and polarization curves prior to imaging at various stages of degradation.

Introduction

Increasing evidence and severity of climate change due to greenhouse gas emissions has pushed the need for government regulations to introduce stricter limits on fossil fuel combustion in new passenger cars, as well as in other light- to heavy-duty vehicles [174]. The need to produce electrical power from renewable energy sources and utilize zero-emission engines has now become the forefront of today's technological evolution, in which electrochemical energy conversion has a central role. Polymer electrolyte fuel cells (PEFCs) are beginning to demonstrate their ability to produce reliable zero-emission power in a variety of commercial applications including automotive and stationary power systems. Further cost and performance degradation improvements present significant opportunities as the technology continues to be refined [108], [175].

The lifecycle performance of automotive fuel cells can be affected by degradation of the membrane electrode assembly (MEA) due to a number of chemical and mechanical

stresses associated with operational cycles in automotive systems. This performance degradation is a result of various processes which may occur to varying extents, such as corrosion of the catalyst support, membrane thinning, catalyst particle agglomeration and oxidation, loss of hydrophobicity, as well as interfacial effects such as delamination [11], [19], [176], [177]. The detailed understanding of these degradation mechanisms is imperative to mitigating their effects and has motivated the need for new methods of investigation to study the state of components at various stages of their lifetime.

Currently, a wide variety of visualization techniques are being used to study PEFC degradation. These include: electron microscopy, neutron imaging, magnetic resonance imaging, X-ray imaging, optical visualization, and thermal mapping [11], [47], [178], [179]. Among these, only X-ray computed tomography (XCT) has shown to have the ability to obtain sufficient resolution to observe electrode related degradation effects while being non- invasive [18], [30], [47], [82], [180]. Typically, research regarding XCT has been performed through the use of synchrotron beamlines, which are very costly and of limited availability. It has also been shown that great care must be taken when exposing fuel cell components to the high intensity incident X-ray beam which can compromise fuel cell components, with significant radiation damage occurring after merely 200 seconds of exposure [155]. This makes repeated scans of the same fuel cell impractical. The use of a laboratory scale micro-XCT, with incident beam intensity orders of magnitude lower than the synchrotron beam, has recently been shown to overcome such radiation damage effects during the exposure time of multiple imaging events while still yielding adequate and relevant radiograms and tomography data sets [181].

Micro-XCT investigations related to fuel cell degradation have so far been primarily limited to *ex situ* studies where the sample has been removed from the fuel cell hardware and cut to size for optimal imaging [82], [182], [183]. This methodology poses a number of unforeseen problems that may affect the interpretation of the images acquired, including: compression changes, additional mechanical stresses from handling, and changes in relative humidity (RH). Also, previously there have been no visualizations of progressive morphological changes, primarily due to the limitations of the experimental procedure. In order to overcome these effects and limitations, the fuel cell can be visualized *in situ*, where the cell is situated in X-ray transmissive test hardware that also provides necessary operating conditions such as temperature, supply of reactant gases, and monitoring of the cell voltage and current. A unique hardware design would need to

be employed which embodies all these elements. Consideration that the X-ray beam attenuates with material thickness, density, and atomic number would imply that no metal components or other non-essential materials should be within the field of view of the imaging area [77], [81], [180].

In this work, we propose the use of four-dimensional *in situ* visualization of electrode degradation processes in fuel cells. This unique approach is facilitated by a custom-designed, X-ray transparent small-scale fuel cell fixture integrated with a commercial, micro-XCT scanner for non-invasive, repetitive viewing of the same fuel cell domain at various points in time. This effectively provides 4D data across space and time. The proposed approach is demonstrated in this work by visualization of morphological changes in the cathode catalyst layer during various stages of degradation due to voltage cycling.

Experimental

Materials

All fuel cell materials used in this study consisted of catalyst-coated membranes (CCMs) and gas diffusion layers (GDLs). The CCM was composed of a Dupont Nafion® NR211 membrane core with anode and cathode catalyst layers each with a 50:50 Pt/C ratio at 0.1/0.4 mg cm^{-2} Pt loadings, respectively. The anode and cathode GDLs consisted of teflonated Avcarb® non-woven carbon paper coated with an MPL. Due to the interest in cathode catalyst layer corrosion in this study, a high crack density CCM was employed. The MEA forged from these parts was framed by Kapton® adhesive sheets with a thickness of 80 μm. Kapton® adhesive sheets were also used as gaskets to aid sealing and limit the compression of the GDLs to 20 ± 5%.

Fixture Design and Fabrication

The design of the small-scale fuel cell fixture used in this work has been developed to allow for full operation, at temperature, while applying voltage cycling during accelerated stress testing as well as for *in situ* imaging using a lab-based, commercial XCT system. The fixture design, shown in Figure 3.9, was fabricated from compressed carbon/graphite with cured resin (SGL Group), which allows for sufficient transmission of the incident X-ray beam, good electrical and heat transport, and sealing of hydrogen and air gases under pressure. The design was machined by Computer Numeric Control (CNC) to precisely cut

the graphite plates into an hourglass shape. As discussed previously, the design is limited in size due to the conditions required for obtaining high signal-to-noise ratio projections to be used in reconstruction of the 3D volume of the sample area [77], [180]. The active area was thus limited to 8 x 3 mm^2, predominantly situated in the central, thin section of the fixture design, as shown in Figure 3.9, which was placed in the field of view during imaging. The flow-field was cut to meet similar design requirements of a technical cell consisting of parallel channels [119], [125]. Other components necessary for full functionality were positioned in the wide section of the fixture (Figure 3.9), including current collectors and voltage measurement leads connected by conductive silver epoxy (8330S, M.G. Chemicals Ltd.), inlet and outlet ports for reactant gases, thermocouple, and miniature cartridge heater (Omega Engineering Inc.). The thermocouple and cartridge heater extended down to approximately 1 mm away from the thin viewing section of the fixture, thereby minimizing temperature gradients within the active area. Housing and compression plate parts were printed from high temperature 3D print material (Object RGD525, Objet Ltd.) which was subjected to a thermal treatment process to increase its heat deflection temperature beyond the PEFC operating temperature.

Fuel Cell Operation and Diagnostics

Operational control of the small-scale fuel cell fixture was affected from a Scribner 850C Fuel Cell Test System (Scribner Associates Inc.). The assembled fuel cell was conditioned by first performing cyclic voltammetry (CV) scans from 0.1 to 1 V to clean and reconstruct the platinum surface. This was followed by operation at 75°C and 100%RH with H_2 and air at 0.2/0.5 slpm for the anode and cathode, respectively, for 15 hours at 750±10 mA cm^{-2}. High stoichiometric flow rates and small-scale fixture design reduced the temperature, pressure, and concentration gradients along the length of the cell. After conditioning, BOL diagnostics were performed by initially collecting five CV scans from 0.05 to 0.8 V at 20 mV s^{-1} with flows of H_2/N_2 at the anode and cathode, respectively with same temperature and RH as initial conditioning. The electrochemical active surface area (ECSA) was calculated by integrating the area under the hydrogen adsorption peak during the reverse scan of a CV. Next, electrochemical impedance spectroscopy (EIS) was performed by taking the average of three scans from 75 kHz to 0.05 Hz at 0.45 V bias under H_2/N_2 and 120% RH. Details of these measurements as well as the extraction of properties such as double layer capacitance and cell resistance are reported elsewhere [119], [125]. Additionally, three fuel cell polarization curves were measured and averaged

with standard deviation indicated by error bars. Following diagnostic testing, the fuel cell fixture was allowed to cool while purging with humidified N_2 gas for approximately 15 minutes in preparation for mounting in the XCT scanner and visualization at ambient temperature. Inlet and outlet gas access ports were covered to retain moisture during imaging. The *in-situ* imaging conducted here is thus different to that of *in operando* imaging where the fuel cell is operated during imaging. Here, fuel cell operation is not necessary for accurate imaging, provided that a suitable equilibrium condition of the cathode catalyst layer can be achieved by imaging the MEA in its natural state, similar to an OCV condition, inside the hardware.

Accelerated Stress Testing

The accelerated stress test (AST) conditions used in this work were adopted from [119], [125], with some operational changes to facilitate the small-scale fixture. In brief, the cell voltage was cycled in H_2/air from a lower potential of 0.6 V for 30 seconds, to an upper potential of 1.4 V for 60 seconds in a square wave pattern. The high upper potential was held for 60 seconds in order to accelerate degradation; in an operating system the PEFC would generally only experience high potentials for much shorter durations during start-up/shutdown events. The cyclic voltage AST protocol applied here is intended to induce cathode degradation similar to that observed for typical start-up and shutdown operation, but over a much shorter time period [119], [179]. An end-of-life (EOL) condition was established when the cell voltage at 500 mA cm^{-2} was less than half of that at BOL. Subsequent results were based on an average of three repeated AST experiments with two cells reaching 450 cycles for EOL and one cell reaching 550 cycles for EOL.

X-Ray Imaging

In situ X-ray imaging was accomplished with a state-of-the-art commercial micro-XCT system (ZEISS Xradia 520 Versa, Carl Zeiss X-ray Microscopy). Details of this instrument and imaging settings are described elsewhere [180], [181]. The electron accelerating voltage and power used to produce the X-ray beam were 80 kV and 7 W, used in conjunction with a high-pass filter, which provided the most appropriate energy spectrum to enhance the contrast between the various fuel cell components, including the cathode catalyst layer. Imaging parameters such as source and detector locations were tuned for the present experiment and the resultant pixel resolution was 1.55 µm in a 3.3 x 3.3 mm^2 field of view. The source and detector distances were set to 25 and 30 mm,

respectively, each measured from the fixture location. Each tomography scan required approximately 2.5 hours of exposure time for 1,601 projections with 5 seconds per projection. High aspect ratio tomography (HART) was also employed to increase the density of projections in the MEA region to improve imaging quality, using a fan angle of 12° from the center and 4x scaling, meaning that each angular step was refined four times in this fan region. Four sets of tomography scans were taken during the lifetime of a PEFC undergoing the voltage cycling AST. This puts the total exposure time well under the time before possible unintentional radiation damage effects may occur from X-ray exposure [181].

Image Processing

Following the completion of each XCT scan, the tomography sets were reconstructed using ZEISS 3D reconstruction software. This software allows corrections for center shift as well as beam hardening prior to the rendering of the full 3D reconstruction. To account for any variation in greyscale values, which were seen to vary between each tomography set due to the automatic scaling in the reconstruction software, manual CT scaling was performed which aided in post-processing. Each scan was scaled based on the greyscale values of air and graphite in the flow field plate which allowed for comparing relative X-ray attenuation changes in the cathode catalyst layer. Quantitative information regarding the changes in the catalyst layer morphology from voltage cycling required the cathode catalyst layer to be segmented before being processed in MATLAB (MathWorks®). To do this, a threshold value was calculated using a variation of the Mixed Gaussian Threshold model [184], which uses Gaussian distributions to model the histogram of the tomography. Gaussian curves were fitted to the resolvable materials using MagicPlot software (MagicPlot systems, LLC). Histograms and fits of the different material compositions are shown in Appendix C, with a representative full MEA histogram shown in Figure 5.2. Higher and lower attenuation carbon Gaussian curves agrees with the variation between polytetrafluoroethylene (PTFE) dominated regions and carbon fibers [51], while higher and lower attenuating cathode catalyst areas correspond to dense, Pt and ionomer rich regions and more homogenously distributed regions, respectively. The threshold value obtained from the intercept of overlapping Gaussian curves corresponding to catalyst layer was then applied to the dataset. A 3 x 3 x 3 voxel despeckle function was also applied to reduce noise. The binarized sub-domain was then exported as 2D tiff image slices for calculations in MATLAB, such as thickness and area fraction

measurement. To determine a confidence level the threshold value was varied by ±1.5% with subsequent calculations with variation included in the error bars. The resultant 2D segmented view of the cathode catalyst layer is shown in Figure 5.2. The figure also illustrates the overall image processing steps taken to reach this result. The threshold value obtained by the Mixed Gaussian model is compared to the Otsu method, which is a common segmentation algorithm, which does not segment the region adequately as does most two-level threshold algorithms. The area fraction calculation required a 2D top-down view, which was achieved by applying a projection in the Z-direction producing a representation of the cathode catalyst layer in 2D.

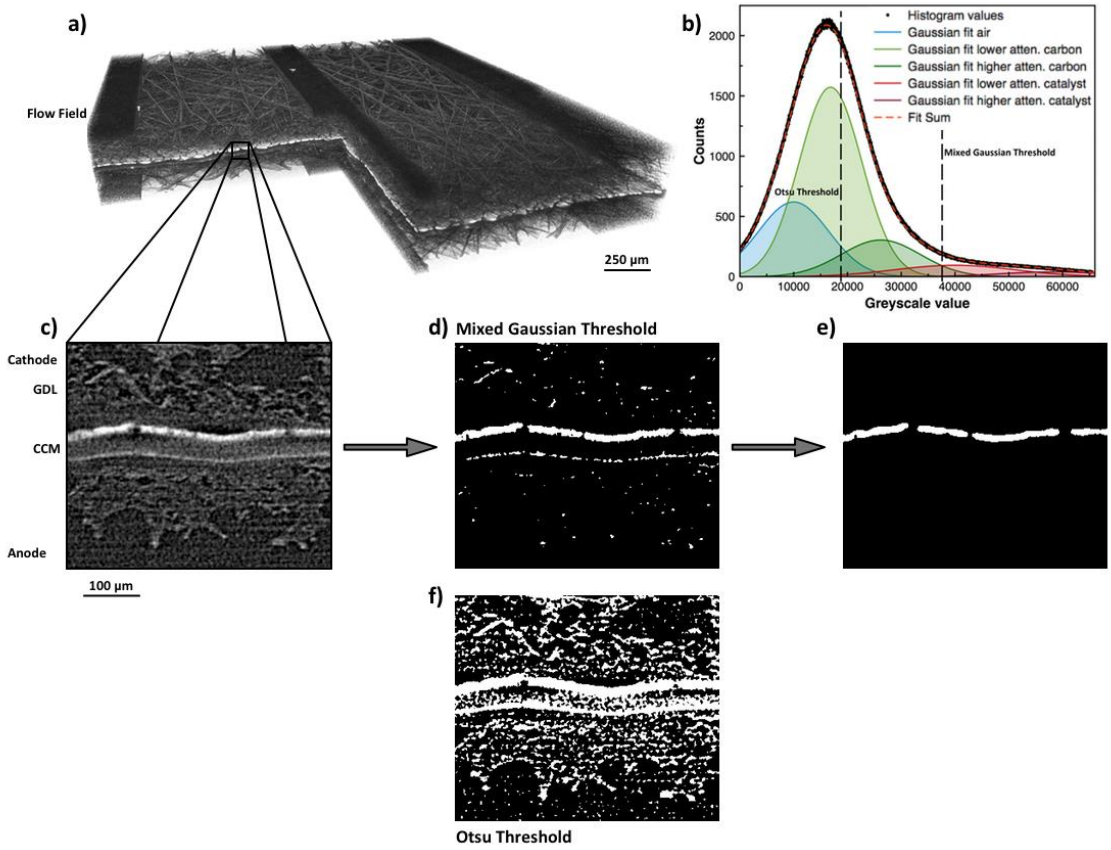

Figure 5.1: Step-wise image processing scheme from full MEA 3D reconstruction to segmented cathode catalyst layer structure: a) 3D view with cut-out; b) histogram with fitted Gaussian curves for separate identifiable regions; c) 2D raw greyscale image after reconstruction; d) region after applying threshold value from mixed Gaussian model; e) noise removal isolating the cathode catalyst layer; f) comparison of thresholding using the Otsu algorithm.

Results and Discussion

Electrochemical diagnostics

Polarization curves summarizing the change in fuel cell performance from the applied cyclic voltage AST are shown in Figure 5.3a. As can be seen, performance loss is evident after only 150 cycles and becomes more severe after approximately 200 cycles where substantial increases in ohmic and mass transport losses occur, eventually reaching EOL by low performance after 450 cycles. The performance loss was initiated in the kinetic region, as can be observed in the inset in Figure 5.3a as well as from the ECSA measurements reported in Figure 5.3b. Carbon loss at the cathode catalyst layer (CCL) from carbon oxidation and corrosion resulting from the high upper potential is known to cause reduction in the ECSA by leaving unsupported platinum and ionomer [12], [119], [125], [179], [185]. Platinum dissolution from the formation of oxides during the upper potential hold and reduction on the downward potential swing is also expected to cause reduction in ECSA and performance loss [108], [119], [125]. The EIS curves shown in Figure 5.3c highlight the changes in combined cell resistance at the high frequency real-axis intercept, as well as the changes in pore size and shape, which have been shown to affect the impedance curve shape by changing the ratio between double layer capacitance and catalyst layer protonic resistance [122], [125], [186]. These results agree well with expected trends following carbon corrosion where the cell resistance, quantified in Table 1, increases due to loss of carbon and its associated electronic connectivity. Additionally, decrease in ionic connectivity between catalyst particles and membrane, as well as possible increase in interfacial resistance due to delamination or layer separation, also contribute to the trends seen in ionic resistance increase and cell resistance increase [125]. Due to degradation, reduced current density will also reduce the production of water and therefore reduce the moisture content, increasing CL ionomer resistance. The marginal initial reduction in both cell resistance and CCL ionomer resistance in the first 150 cycles is likely due to additional cell conditioning, though the majority of this change is within the uncertainty of the measurement. The double layer capacitance (C_{dl}) extracted from the EIS measurements is also plotted in Figure 5.3b. Initial increase in the C_{dl} is hypothesized to be a result from carbon surface oxidation, and the value is then seen to decrease due to the loss of surface area by corrosion of the carbon – oxygen surface groups [119]. This trend is only seen to occur when UPL > 1.2 V Here, carbon corrosion coincides with the increased cell and ionomer resistance in the late stages of degradation

after the midpoint of the AST. Overall, the electrochemical diagnostic measurements for the small-scale fixture agree well with previous measurements using a larger technical cell [119], [125], [179], and thereby validate the intended use of the small-scale fixture for cyclic voltage AST operations.

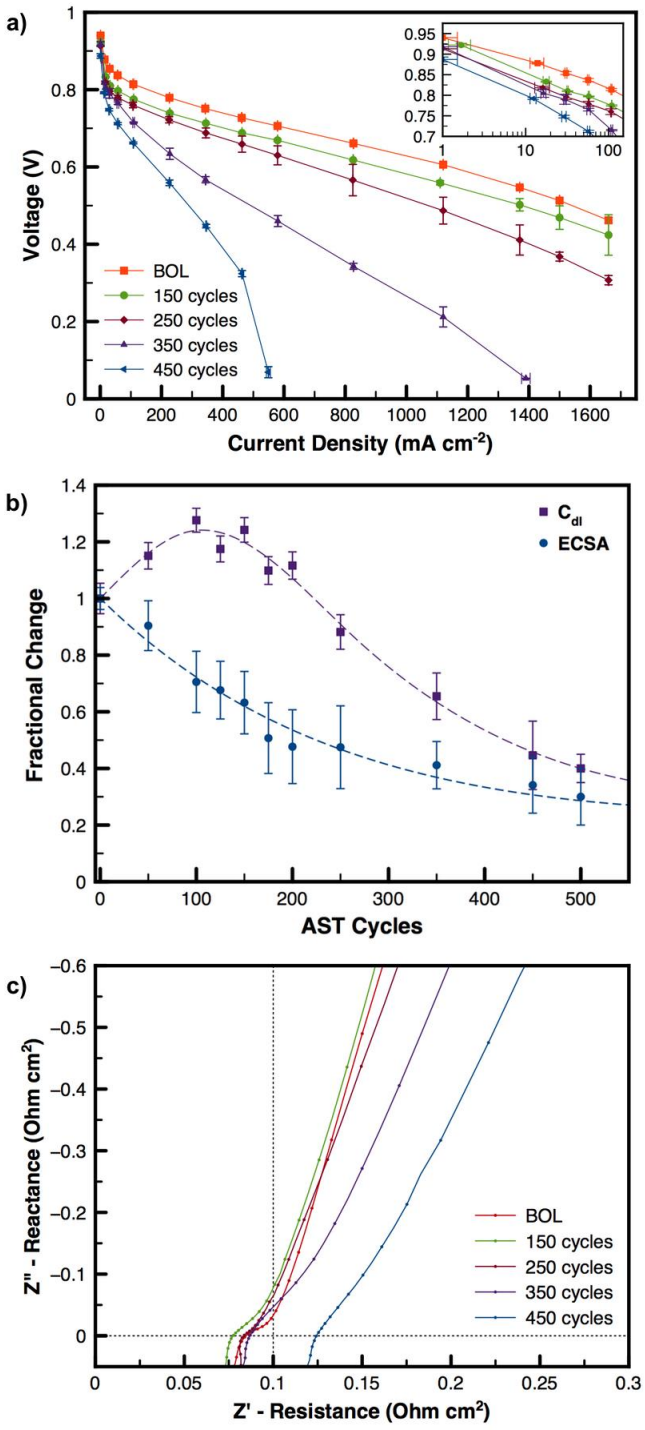

Figure 5.2: Electrochemical diagnostics of the MEA inside the small-scale fuel cell fixture: (a) polarization curves, (b) double layer capacitance from EIS and ECSA from CV, and (c) high frequency impedance curves recorded at various stages of degradation by cyclic voltage AST.

	BOL	150 cycles	250 cycles	350 cycles	450 cycles
HF cell resistance (Ω cm^2)	0.085	0.078	0.084	0.087	0.124
CCL ionomer resistance (Ω cm^2)	0.103	0.097	0.096	0.126	0.170

Table 5.1: High frequency (HF) cell resistance and cathode catalyst layer (CCL) ionomer resistance extracted from the EIS curves following cyclic voltage AST from BOL to EOL (450 cycles).

Thickness measurements

The collapse of the carbon support from carbon corrosion has been shown to cause a decrease in the thickness of the CCL [117], [187]. Typically, thickness measurements are performed ex situ by cross-sectional scanning electron microscopy [117], [119], [187], which involves destructive cutting, handling, and preparation of the sample as well as viewing under vacuum conditions. Here, the small-scale fuel cell fixture viewed as-is by XCT provides a full 3D visualization of the MEA in a completely non-destructive manner. The reconstructed data set provides hundreds of 2D slices with sufficient resolution to obtain accurate cross-sectional thickness measurements; a process which can be repeated several times for the same MEA due to its non-destructive nature. Figure 5.4 shows measurements obtained from such cross-sectional views using ImageJ local thickness measurement at different stages of degradation [188]. The standard deviation (shown by the error bars) includes the inherent variation in the thickness of the membrane, cathode, and anode catalyst layers as well as the confidence interval resulting from ±1.5% variation in the threshold value. The thickness measurement by using non-overlapping circles accounts for undulations in the planar view since the orientation is irrelevant, as opposed to measuring vertically. Significant contrast of the catalyst layer and surrounding areas allowed for accurate measurement of the thickness by clear segmentation. Considerable decrease in the CCL thickness by approximately 40% resulting from collapse of the carbon support can be seen, whereas membrane and anode thicknesses remain constant, within statistical variation.

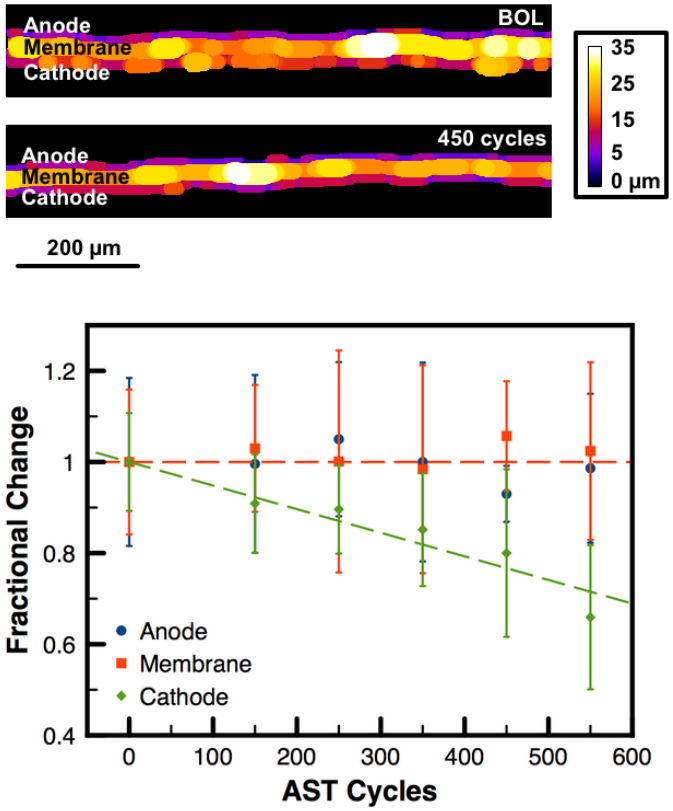

Figure 5.3: XCT based local thickness measurement of MEA components and progressive decrease in cathode catalyst layer thickness by corrosion during the cyclic voltage AST.

Cathode catalyst layer structure

As a result of the degradation pathways brought on by the cyclic voltage AST, the solid phase regions of the cathode catalyst layer (CCL) structure were reduced in size as seen by thinning, while the void regions dominated by catalyst layer cracks expanded and propagated, as shown in Figure 5.5a. To better understand the morphological changes resulting from voltage cycling, the results were quantified in terms of solid area fraction and average crack width parameters calculated from the segmented CCL by circle packing in MATLAB for each degradation state. The obtained solid area fraction data shown in Figure 5.5b, supplemented by specific values for the cross-sections shown in Figure 5.5a, demonstrate a significant reduction in solid phase area over time during the present degradation process, up to approximately 25% at the EOL state. The change was marginal during the first 150 cycles, after which a more substantial, gradual decay was observed. The crack width data in Table 2 show consistent trends, i.e., the crack width was found to

increase at a rate that is similar to the gradual reduction in solid area. The considerable change in CCL structure observed after approximately 200 cycles and onwards to EOL can also be correlated to losses in fuel cell performance. This was confirmed through the polarization curves in Figure 5.3a, where significant performance losses primarily in the form of ohmic and mass transport losses were found to coincide with the morphological changes observed here. The decay in double layer capacitance (Fig. 3b) is also in good agreement with the current trend, indicating a loss in active surface area of the carbon. This is likely a result of severe carbon corrosion and collapse of the catalyst support during the later stages of the degradation process, which may also be influenced by erosion from water flooding [47], [117], [119].

Additionally, Figure 5.5a shows a comparison of specific CCL regions located under the channels and middle land, which was consistent with results in comparison with the two edge lands (Fig. 5d). Initial observations suggested possible degradation heterogeneities under channel and land, and separate calculations for these areas were hence performed. As can be seen in Figure 5.5b, there is a considerable difference between the solid area fraction values, indicating a different level of corrosion of the CCL in regions under the channel compared to that under the land. Although both areas showed a significant decrease in area fraction from corrosion, the change under the channel took place at a higher rate. This was confirmed and averaged from three different MEAs undergoing the same procedure. This result, however, is contrary to the work of Durst et al. [122] who showed a more significant thinning under the land compared to under the channel in a technical cell subjected to start-up/shutdown cycling. It is proposed that the difference in findings is a result of the stress test procedure and the effect of GDL compression. In start-up/shutdown procedures, degradation occurs as a result of fuel starvation or gas switching conditions, which allows for the infiltration of oxygen into the normally hydrogen filled anode flow field, causing a localized voltage increase on the cathode side. Portions of the cathode facing an anode land region will suffer longer fuel starvation than those facing an anode channel region, thereby increasing the local corrosion rate [122]. Thinning in this region may also be elevated by local compression under the lands acting on a weakened CCL structure. In the cyclic voltage AST, the voltage is applied along the full MEA, without gas switching, creating a more uniform degradation environment. However, similar to the start-up/shutdown procedure, gas diffusion under the land region will be slower than under the channel region as a result of reduced porosity

from compression [179], [189]–[191]. Through-plane bulk porosity was therefore calculated by segmentation of the cathode GDL, indicating a substantially lower porosity under the land, to a certain depth, as shown in Figure 5.5c. This could result in reduced oxygenation, and water formation by decreased current density at the catalyst layer under the land [43], [189]–[191], thus also reducing the rate of degradation in this region. It is also postulated that higher liquid water production and higher local temperature under the channels, may lead to increased degradation in this region [43], [179], [192], [193]. It should be noted that due to inherent variation, it was not possible to resolve differences in CCL thickness under the land and channel with statistical significance. Since the thickness was seen to decrease uniformly under land and channel, the increased structural degradation under the land may indeed point to erosion under these conditions.

	BOL	150 cycles	250 cycles	450 cycles
Average crack width (µm)	9.1 ± 4.3	9.2 ± 4.1	10.8 ± 5.1	11.6 ± 4.3

Table 5.2: Average width of cathode catalyst layer cracks.

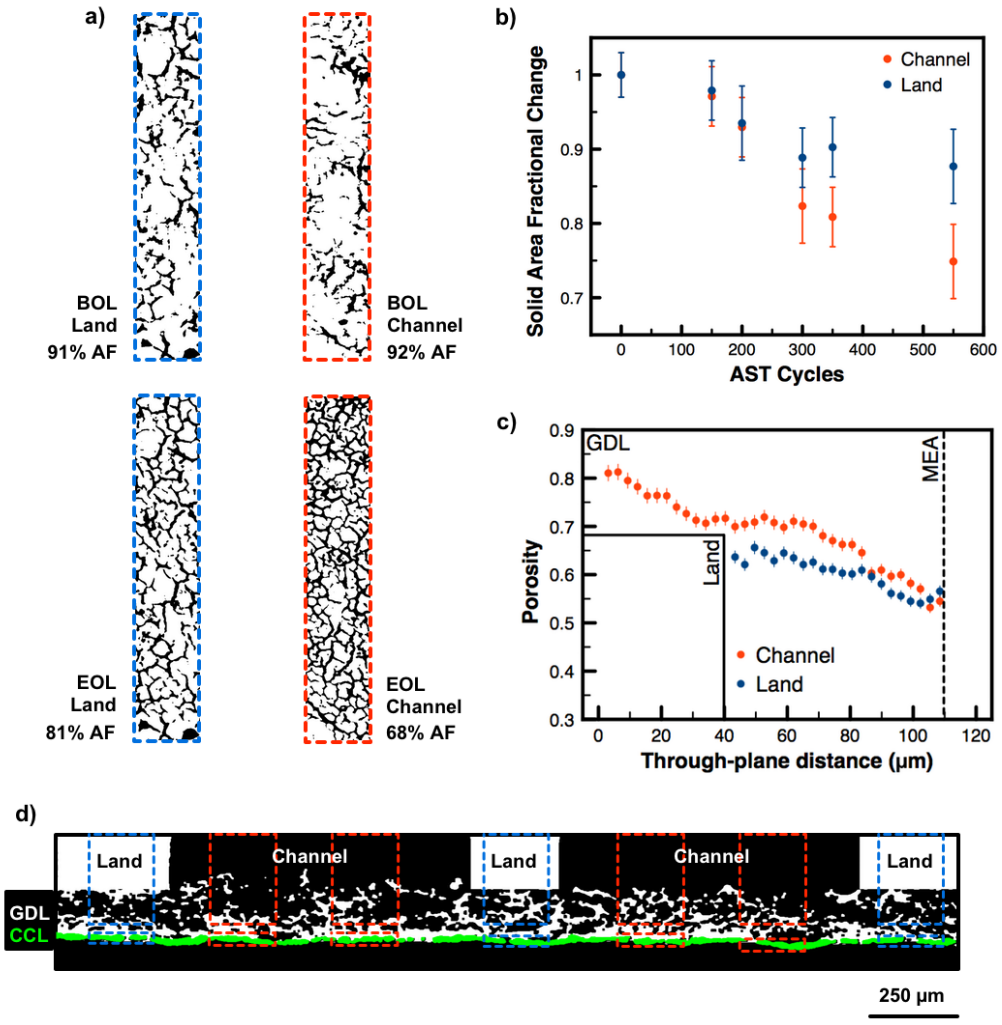

Figure 5.4: MEA structural analysis under land and channel: a) segmented and flattened view of the cathode catalyst layer at BOL and EOL with solid area fraction values; b) progression in cathode catalyst layer solid area fraction during cyclic voltage AST; c) bulk porosity of the segmented cathode GDL; and d) segmented cross-sectional view of the MEA showing the regions used for the land and channel analysis.

Crack propagation

A MEA with pre-existing cathode catalyst layer (CCL) cracks formed during fabrication was utilized in this work in order to explore the role of cracks in the cathode degradation process. A MEA with regular presence of CCL cracks allowed for a rich set of results in terms of the structural evolution of the electrode. Both pre-existing cracks from manufacturing and cracks generated during *in situ* degradation are relevant for real-world fuel cell operation, both of which are investigated here. Possible heterogeneities in the

composition at the crack edges could cause them to be vulnerable to higher amounts of carbon corrosion and erosion, propagating the cracks and increasing their size during periods of potential cycling such as those during cyclic voltage AST or start-up/shutdown. Here, CCL crack formation and propagation is uniquely monitored for the first time using the proposed 4D *in situ* visualization approach. Specific regions-of-interest (ROIs) located under the channels and lands were selected and tracked during the degradation process by periodic XCT scans. Figure 5.6a shows a planar view of a CCL ROI located under the channel and how it evolved from BOL to EOL (550 AST cycles), with histograms to highlight X-ray attenuation variation which are a result of changes in density and composition (Pt/C/ionomer volume %), as described by the Beer-Lambert equation [180] with a clear shift in histogram peaks to higher greyscale value. As can be seen, propagation of cracks along the length is first observed followed by an increase in crack width. Lower attenuating regions are seen to be more vulnerable for new crack formation as well as for propagation of existing cracks. This may suggest that slight variations in composition, such as local ionomer content, could have a strong impact on CCL degradation. Figure 5.6c and 6d show cross-sectional views of the same ROI. As can be seen, initial crack formation is observed in the lower attenuating regions of the CCL, this time shown in raw greyscale. Decrease in thickness during degradation is also observed as well as increase in attenuation, both resulting from a loss of carbon support and collapse. The increased attenuation is likely due to severe carbon corrosion leading to collapse of the catalyst layer structure, which dramatically reduces the thickness and porosity of the remaining material [124], [185]. Reduced porosity will play a significant role in mass transport losses as observed in the polarization curve by reducing oxygen diffusivity [185].

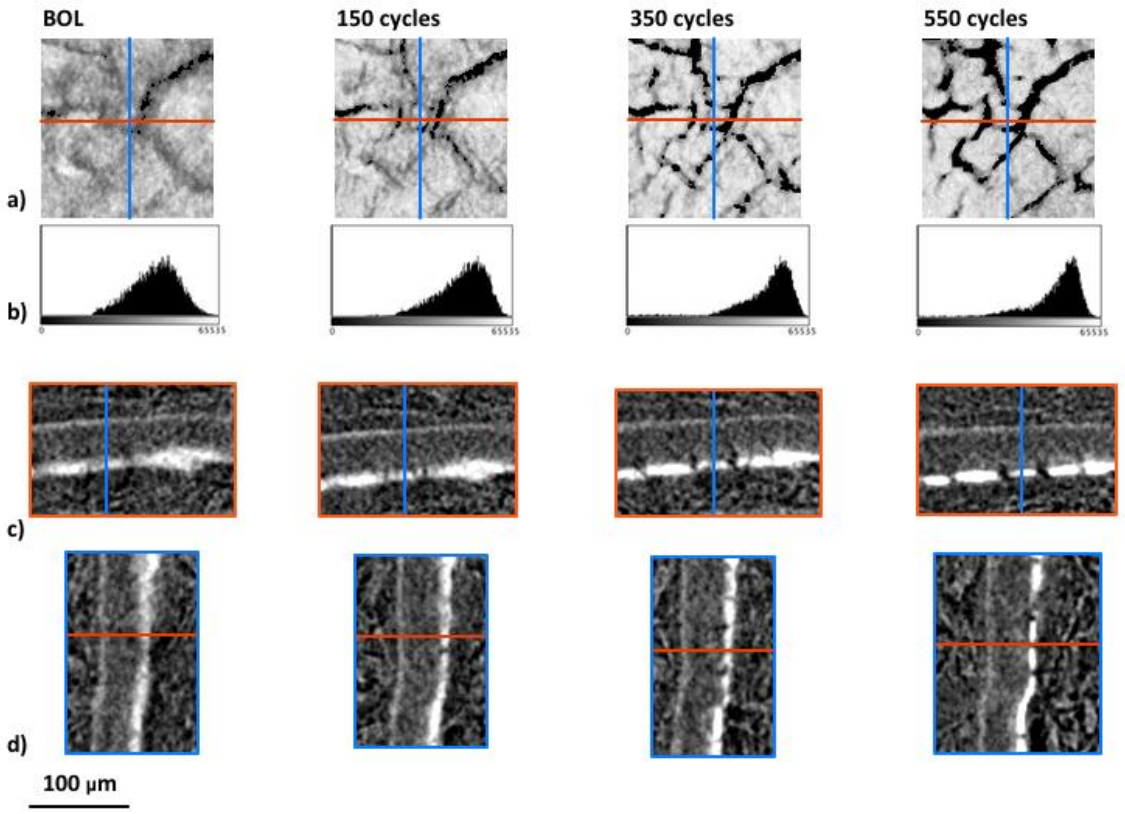

Figure 5.5: Cathode catalyst layer crack propagation captured by identical-location tracking in 4D: a) planar view of the segmented cathode catalyst layer; b) histogram of greyscale values to show changes in X-ray attenuation from changes in material density and composition, c,d) cross-sectional views as seen through the blue and red vertical lines in the planar view in a).

Summary

Four-dimensional *in situ* visualization of cathode catalyst layer degradation was achieved by the use of a custom small-scale fuel cell fixture compatible with accelerated stress testing and non-destructive micro-XCT characterization at different points in time. Upon cyclic voltage AST, a gradual progression in cathode catalyst layer thinning up to 40% was measured by quantitative XCT analysis. The thinning was correlated to a gradual increase in density by collapse of the carbon support structure as observed by changes in cathode catalyst layer relative attenuation of incident X-ray spectra from beginning-of-life to end-of-life. The solid area fraction of the cathode catalyst layer was calculated after the application of a segmentation method using mixed Gaussian histogram fitting. Analysis

comparing specific regions under land and channel showed a higher rate of degradation under the channel. This difference was attributed to the higher local reactions rates and higher rates of water production and erosion under the channels. Finally, identical-location tracking of individual cathode catalyst layer cracks was demonstrated for the first time. Both formation of new cracks and propagation/growth of existing cracks were observed. Local variation in the relative attenuation of the X-ray beam suggests regions with high vulnerability to corrosion as shown by crack initiation and propagation. New insight into the crack formation and correlation with electrochemical measurements such as double layer capacitance and resistance is allowed by 4D *in situ* measurements. Most notably, the increasing morphological changes observed during the later stages of the cathode catalyst layer degradation process were in good agreement with the gradually increasing losses in fuel cell performance as well as the distinct decay trend in electrochemical double layer capacitance. This demonstrates a clear correlation between conventional *in situ* diagnostics and the new XCT results: severe carbon corrosion, responsible for losses in electrode capacitance and mass transport performance, manifests itself in the form of catalyst layer thinning, crack growth and overall compaction of the remaining porous solid phase, and triggers eventual electrode failure. Future work to investigate alternate degradation protocols such as start-up/shutdown cycling and voltage cycling with different upper potential limits is recommended to provide additional information about specific degradation processes that occur during fuel cell operation in the field.

Chapter 6. Impact of Cathode Catalyst Layer Degradation on Liquid Water Distribution and Dynamic Cell Behaviour

Prior research investigating the visualization of cathode catalyst layer degradation has been exclusively through an *ex-situ* approach. This greatly limits our understanding of the complex interaction between all PEFC components. As a result of the development of the small-scale fuel cell fixture to enable *in-situ* visualization of cathode catalyst layer degradation, a more thorough understanding of the impact of degradation can be investigated.

In the present work the *in-situ* workflow was extended to allow for *operando* visualization, whereby the fuel cell is operated during XCT imaging, liquid water distribution is also visualized as well as dynamic changes between zero current (dry) conditions and various current densities at each stage of degradation. The obtained results have never been visualized before and surprising behaviour was observed which extended the impact of cathode catalyst layer degradation to membrane behaviour and possible fatigue related damage. As well, behaviour relating to further current density loss by local delamination of GDL and catalyst layer, increasing contact resistance and possibly locations for flooding and decreased reactant transport was visualized. In addition, a quantitative analysis routine on the greyscale value changes observed and discussed in Chapter 5 relating to compositional changes was developed. This also marks the first application of lab-based XCT for *operando* visualization of PEFCs.

The following section is a formatted version of R. T. White, S.H. Eberhardt, Y. Singh, T. Haddow, M. Dutta, F. P. Orfino and E. Kjeang, **Four-dimensional joint visualization of electrode degradation and liquid water distribution inside operating polymer electrolyte fuel cells**, *Sci. Rep.*, 350 (2019) 94-102.

R.T.W., S.H.E. and E.K. conceived the project; R.T.W. designed the small-scale fixture; T.H. and R.T.W. performed fabrication and operated and collected diagnostic measurements of the small-scale PEFC; R.T.W. and S.H.E. operated the small-scale PEFC during *operando* imaging; R.T.W. and S.H.E. collected XCT data; R.T.W. wrote python code and ImageJ macros used for segmentation and morphological quantification of catalyst layer and membrane; S.H.E. wrote ImageJ macros for alignment of image

stacks; R.T.W. and T.H. analyzed all results; Y.S. analyzed membrane changes; R.T.W. drafted the manuscript with revision from all other authors.

Understanding of degradation mechanisms present in polymer electrolyte fuel cells (PEFCs) is important to continue the integration of this clean energy technology into everyday life. Further comprehension of the interaction between various components during fuel cell operation is also critical in this context. In this work, a four-dimensional *operando* X-ray computed tomography method is developed for combined visualization of all PEFC components as well as transient water distribution residing in the cell, which results as a by-product of the electrochemical reaction. *Operando* identical-location visualization through degradation stages, is uniquely enabled by the non-invasive and non-destructive qualities of this method. By applying an accelerated stress test that targets cathode catalyst layer (CCL) corrosion, novel observations resulting from morphological changes of the CCL such as reduction in the water volume in the adjacent gas diffusion layer, CCL crack formation and propagation, membrane swelling, as well as quantification of local carbon loss is achieved. Additionally, insight into features that contribute to reduced fuel cell performance is enabled by the use of this specialized imaging technique, such as increased membrane undulation causing delamination and separation of the CCL from the microporous layer, which greatly affects liquid water pathways and overall device performance.

Introduction

In recent years there has been considerable increase in the commercial adoption of polymer electrolyte fuel cells for power generation from hydrogen. This is owing to the high efficiency and low environmental impact of their operation; making them attractive as alternative power sources for automotive applications, material handling, stationary combined heat and power (CHP) applications, unmanned aviation vehicles and wherever high energy demands exist and short recharge intervals are desirable [3], [6], [194]–[197].

Polymer electrolyte fuel cells (PEFCs) are designed as a series of layers as shown in Figure 6.1; beginning with a proton conductive and electron insulative polymeric electrolyte membrane at the center, which separates the anode and cathode electrodes that are coated on its opposite sides in the form of a nano-porous catalyst layer (CL)

composed of platinum nanoparticles on carbon support intermixed with ionomer. The complete membrane electrode assembly (MEA) further comprises of two macro-porous gas diffusion layers (GDLs), each coated with a micro-porous layer (MPL) on the surface adjacent to the CL interface. Water is formed in the CCL as a by-product of the electrochemical cell reaction involving hydrogen oxidation at the anode and oxygen reduction at the cathode. While adequate hydration of the ionomeric membrane and CLs is desirable for maintaining high proton conductivity and low ohmic losses, excessive hydration also causes liquid water accumulation (or flooding) in the porous structures and limits the diffusion of reactants to the active sites in the CCL. Accordingly, effective water management across the multi-scale porous structures of the GDLs, MPLs and CLs, is vital for high fuel cell performance and durability [115], [116].

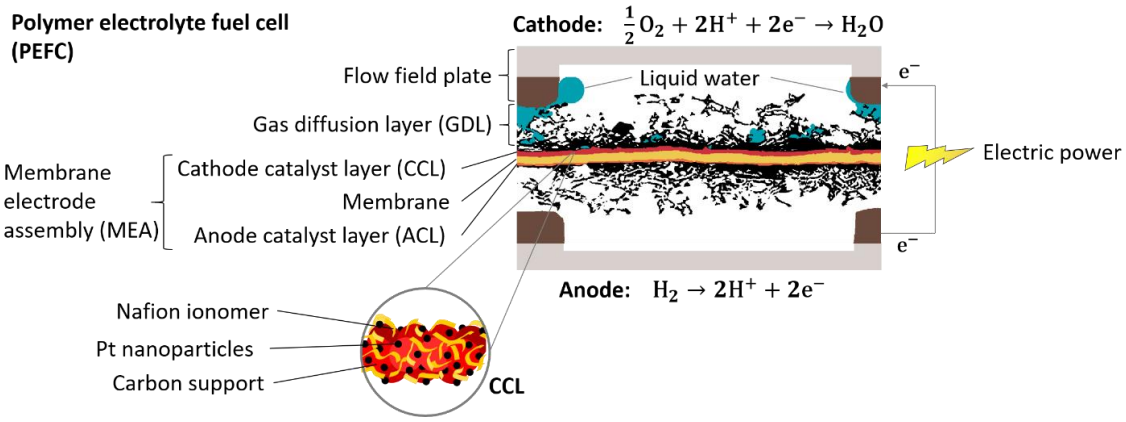

Figure 6.1: Schematic of polymer electrolyte fuel cell (PEFC) components obtained from XCT visualization of an operating fuel cell, outlining the electrochemical reactions, electronic transport and liquid water generation. The inset highlights a simplified illustration of the cathode catalyst layer composition and structure.

While considerable research efforts have been made to understand the liquid water distribution in the GDL in order to improve fuel cell performance [16], [58], [68], [77], [198], [199], investigations that encompass CCL degradation and its consequential changes to the GDL water distribution within an operating fuel cell are largely absent. During operation, the CCL can often undergo substantial structural, mechanical and chemical degradation associated with high cathode potentials and concomitant corrosion of all carbonaceous components, most importantly the catalyst support material [108], [119], [200], [201]. Damage features as a result of this degradation are: crack formation,

thickness loss, decrease in electrochemically active platinum surface area (EPSA) and changes in diffusive and electric pathways due to partial collapse of the porous carbon structure leading to increase in transport losses and decreased performance [24], [185], [202], [203]. Additionally, generation of hydrophilic oxygenated carbon surface groups can cause increased flooding at the surface of the CL leading to further mass transport losses [119]. Accurate characterization of these damage features is important in order to relate any changes in liquid water distribution to electrode degradation, as well as properly understand the performance losses observed. Previously, Fairweather et al. [179] used neutron imaging to investigate the impact of CL degradation on the water distribution inside an operating PEFC. Limitations associated with neutron imaging such as low resolution (13 μm spatial) and low material contrast, however, restricts the ability to clearly visualize and thus accurately correlate the structural changes within the CCL that may have impacted the water distribution and performance.

Lab-based X-ray computed tomography (XCT) has been shown to allow for high resolution (< 3 μm) three-dimensional (3D) imaging of fuel cells [13], [19], [21], [26], [169], [204], while periodically performing same location tracking across degradation stages during a typical accelerated stress test (AST), thus adding a fourth imaging dimension (i.e., degradation time) [24]. This enables the quantification of various temporal changes in the electrode morphology during its degradation. Previously, only synchrotron based X-ray tomography has been used to investigate 3D liquid water distribution in the GDL of operating PEFCs, owing to the short scan time and high signal-to-noise ratio requirements [40], [58], [63], [77], [81], [205]. Degradation of a fuel cell cathode is a slow process, even when using AST cycles with high (>1.2 V) upper potential limits, thus making the use of a synchrotron impractical with much of the allotted beam time devoted to running degradation protocols rather than image acquisition. However, the convenience of lab-based XCT allows for repeated image acquisition and visualization at studying steady state conditions, such as steady state water distribution at constant current density. The attenuation of X-rays is dependent on the mass attenuation coefficient (μ) and density (ρ) of the material [180], [206]. In a material comprising of several phases, such as the CCL, this dual dependence of X-ray attenuation results in variation of greyscale values of pixels after reconstruction. Additionally, any relative changes in material composition or density can theoretically be observed in a degrading CCL by comparing greyscale changes, thus allowing for an opportunity to infer its material property changes. This dependence of X-

rays on material composition has been suitably leveraged in scanning transmission X-ray microscopy (STXM) to obtain spatial distributions of carbon and ionomer within the catalyst layers [207], [208]. However, SXTM suffers from specific limitations in terms of sample size requirements and housing, thus not allowing for operando imaging wherein the imaging is performed in a current-producing operating fuel cell.

Given their sufficient spatial resolution for characterizing CCL morphology, ability to periodically image under steady state fuel cell conditions, and accommodation of housing accessories needed for a fully operational fuel cell, lab-based XCT systems are presently the most suited instruments for simultaneously investigating CCL degradation and liquid water distribution along with their interaction. A small-scale fuel cell fixture, which allows for imaging the active area within a small field of view without strongly attenuating the X-ray beam in a lab-based XCT system, was designed and presented previously [24]. This experimental fixture is leveraged in the present work to perform four-dimensional operando visualization of fuel cell cathode degradation, see Figure 6.2. To the best of the authors' knowledge, the combined visualization of water distribution and cathode morphology is first published here. Additionally, post processing analysis to obtain compositional information on CCL changes following degradation is also presented here. Using these novel analysis methods, we present results of water distribution changes following CCL degradation, as well as compositional and morphological changes within the CCL itself. These results are further compared to fuel cell performance losses and supplementary diagnostic data that uncovers key pieces of information that may aid in the development of next generation fuel cell electrodes.

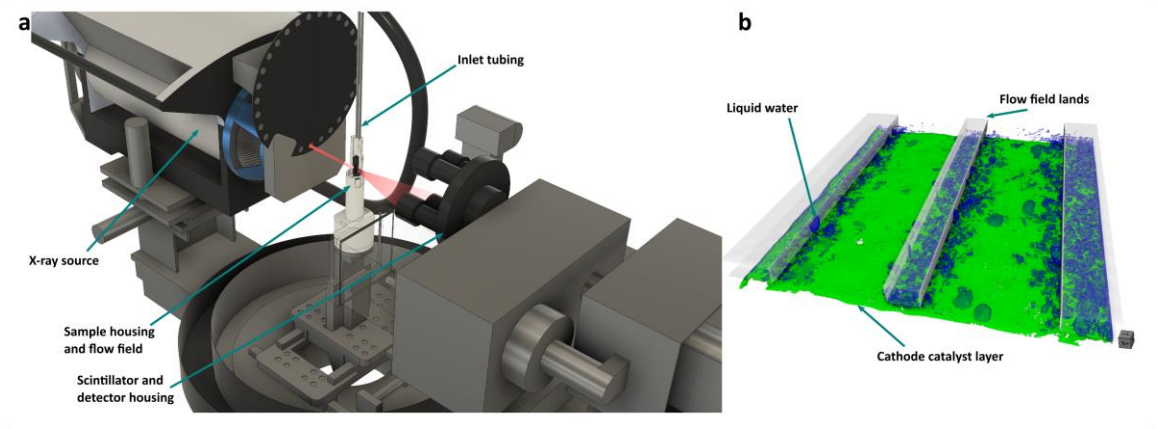

Figure 6.2: (a) Schematic of Zeiss Xradia Versa XCT system showing the customized small-scale fuel cell fixture and sample housing developed for operando imaging. (b) 3D segmented views highlighting the liquid water visualization and cathode catalyst segmentation.

Methods

Operando imaging and accelerated stress testing

The design of the small-scale fuel cell hardware used in this study has been previously presented, with details found in White *et al.* [24]. To allow for *operando* imaging, a support base was designed and printed by fusion deposition modelling using a Stratasys uPrint SE with ABSPlus material. This support base allowed for secure attachment of the small-scale fixture to the sample stage within a Zeiss Xradia Versa 520 XCT system, as well as provide necessary compression for proper fuel cell operation. The support base also allowed for electrical connections and exhaust gas line management from the fixture. To stop impingement of exhaust gas tubing and electrical connections during rotation of the sample base while imaging, a cable management system was used which was installed in the XCT enclosure by Zeiss. Inlet gas lines, which can be seen in Figure 6.2, were supported from the ceiling of the XCT enclosure so as not to interrupt the X-ray beam path during imaging. Because of this, the tubing needed to be flexible and long enough to allow for smooth rotation; for this, high-temperature soft Viton fluoroelastomer was used. Insulated and temperature-controlled gas lines were used to connect the fixture inside the XCT system to the fuel cell test station which was situated externally to the XCT system. The heated gas lines were managed using a custom aluminum framing designed to avoid intervention of XCT system function. Additionally, a hydrogen sensor and a smoke

detector were installed on this framing to allow for safe operation and shutdown in the event of a significant leak or ignition event during *operando* imaging. Inlet/outlet gas lines and electrical connections were fed outside the XCT enclosure through a specially designed side baffle with two orthogonal turns in order to prevent stray X-ray radiation by eliminating a direct line-of-sight exit to the lab environment. This opening and the additional attached safety cover on the Versa 520 system was supplied by Zeiss.

The control of the fuel cell operation, gas humidity and electrical measurement was affected by a Scribner 850C Fuel Cell Test System. Details concerning the fuel cell conditioning, diagnostic measurements and AST operation and conditions have been reported elsewhere in White *et al.* [24]. The AST was performed by square wave voltage cycling of 1.4 V upper potential (60 s hold) and 0.6 V (30 s hold) lower potential. The MEA was fabricated using the catalyst coated membrane method, with 50:50 Pt/C ratio at 0.4/0.1 mg cm^{-2} Pt loadings and 23 weight percent (wt%) ionomer for cathode and anode electrodes, respectively. The catalyst layers were coated onto a Dupont Nafion® NR211 membrane with GDLs consisting of teflonated Avcarb® non-woven carbon paper coated with a micro-porous layer (MPL). The voltage cycling was performed outside the XCT system to allow for accurate temperature and humidity control by minimal gas line length and insulation as well as to free the XCT system for other imaging tasks; during *operando* imaging, the fuel cell was operated at room temperature conditions inside the XCT enclosure. This low temperature operation limited the amount of humidity that the input gases into the fuel cell carried and the liquid water observed directly results from the fuel cell electrochemical reaction, allowing for improved imaging of transient water distributions without contribution from inlet gas humidity or condensation along the gas lines.

The operational workflow can be itemized as follows: Conditioning and beginning-of-life (BOL) diagnostic measurements, such as polarization curves and EPSA measurement, were taken outside the XCT system with the small-scale fixture directly attached to the test station; small-scale fixture purged with ‘dry’ (100% RH at 25^{o}C) N_2 to remove all excess water and residual reactant gases; fixture moved into the XCT system and re-connected to gas lines and electrical connections leading to the test station; small-scale fixture and gas lines purged with N_2 for additional 30 min; H_2/air supplied to small-scale fixture and allowed to equilibrate while drawing a current density of 250 mA/cm^2 at room temperature conditions; after 30 min equilibration, imaging performed while fuel cell in operation with details of imaging parameters outlined in White *et al.* [24]; subsequent

imaging at current densities of 500 mA/cm^2 and 750 mA/cm^2 allowing for 30 min equilibration at each current density before imaging; following imaging, fixture purged with N_2 to remove all excess water for a minimum of 4 h; 'dry' image set collected with continuous N_2 flow; fixture taken out of the XCT system and subjected to an AST protocol; and diagnostic measurements subsequently performed after cycling with the previously outlined imaging steps repeated. This workflow extended the same location tracking of cathode catalyst degradation with GDL water distribution visualization at various current densities which has not been previously reported. The total imaging time was minimized to reduce the impact of X-ray irradiation on the fuel cell materials, with additional low energy X-ray filter used (proprietary and provided by Zeiss), and falls within the expected non-destructive impact time determined previously by White *et al.* [181].

GDL water segmentation

Following image acquisition, the set of radiographs was reconstructed using Zeiss proprietary software, which computes the 3D representation of the imaged area. To properly compare greyscale values of the resulting image stacks across multiple acquisition stages, the byte scaling was set consistently to the same value across all reconstructions. This results in the same pixel value for constant materials such as air and graphite plate material, which were unchanged throughout the experiment. To accurately segment liquid water from the pores of the GDL, it was necessary to subtract the 'wet' image set (obtained during current collection) from the 'dry' reference (no current, N_2 flow); however, prior to this step, it was crucial to properly align image sets in x, y and z directions. First, the image stacks were cropped to the region of interest to reduce unnecessary processing time and minimize data storage. Second, all image stacks were aligned to the beginning-of-life 'dry' image set using custom macros written in ImageJ macro language [209]. The macros allow the user to correct for in-plane tilt and align in x, y and z by comparing the standard deviation of the resultant subtracted image; the image pair with the smallest standard deviation is chosen to represent the translation and slice number of the aligned image stacks, which can then be applied manually after inspection. Following subtraction of the two image sets, 3D median filter as well as 3D anisotropic filter is used [166], [210], [211]. The result is then processed in Matlab using Otsu threshold to create binary images of the resultant water droplets. Noise and GDL fibers are also

removed using a custom processing script comparing eccentricity and size of the labelled objects [180]. These steps were repeated for all image stacks using the same parameters to keep consistency when comparing values across multiple image acquisition stages.

Cathode catalyst layer and membrane segmentation

A custom segmentation procedure, written in ImageJ macro language is used to obtain an accurate representation of the CCL and quantitatively determine morphological features such as thickness, crack area, and crack width. The script allows for automated separation of the cathode layer following thresholding by the user by Gaussian Mixed Model, [24] as well as 3D particle labelling using BoneJ plugin [212]. An overlay of the result from the segmentation and the accuracy is shown in 4.6. Membrane segmentation is obtained following separation of the anode and CCLs. Once both layers are segmented by the user using the aforementioned script, additional scripts written in Python (programming language, www.python.org) using NumPy (scientific computing package, www.numpy.org) as well as SciPy (scientific computing package, www.scipy.org) separate the membrane by using the boundary of the catalyst layers and nearest-neighbor interpolation to be robust against cracks or breaks in the segmented catalyst layers. This method of segmentation is required since the greyscale values of the membrane layer are similar to those of the carbon in the GDL, and noise levels make using texture filters such as entropy ineffective. Refer to section 4 for further details.

Composition calculation from cathode catalyst layer greyscale values

The X-ray attenuation of catalyst layer material changes following degradation, which can be observed directly by changes in pixel greyscale values [24], [213]. To quantify these changes, a greyscale calculation model was implemented. This model takes as input the greyscale values from a 2D image of the CCL and determines the corresponding material composition. To perform such a calculation, the following steps are required. First, imaging parameters and catalyst layer size are set such that minimal local tomography is performed, as this can affect greyscale values of the reconstruction output [214]. Second, the laboratory scale XCT system produces a non-monochromatic X-ray beam for imaging; thus, filters are used to narrow the energy distribution such that a single ‘effective’ energy is used in the calculation. This is an approximation, and the authors note that improved results could be obtained with the use of a monochromatic

beam. Lastly, a set of materials with known density and composition is used to calibrate and correlate greyscale value with X-ray linear attenuation values. The calibration curve obtained is shown in Figure 4.15 and follows an expected linear trend, indicating that a single energy assumption is valid in this case. With these experimental considerations, a model can be implemented. The calculation required is as follows:

$$GSV = m_{\text{cal}} \cdot \mu_{C_x H_x F_x O_x S_x Pt_x} + b_{\text{cal}} \tag{6.1}$$

Where m_{cal} and b_{cal} are slope and intercept from the calibration curve, respectively, and $\mu_{C_x H_x F_x O_x S_x Pt_x}$ is the linear attenuation coefficient from the constituents of the catalyst layer. NIST provides an online calculation to determine the mass attenuation of a composition of materials at a specified energy (https://physics.nist.gov/PhysRefData/FFast/html/form.html). However, for each new composition, a user must manually retrieve the corresponding mass attenuation value. Since the catalyst layer composition is unknown and varies widely, this is however not practical. Instead, a collection of one hundred values with uniform variation in fractional composition of carbon, platinum and ionomer (H, F, O, S) was collected. From this dataset, an implicit model was fitted using Support Vector Machine (SVM) regression with radial basis function from scikit-learn (http://scikit-learn.org), an open-source, python based library for artificial intelligence. To obtain linear attenuation values, the mass attenuation determined from the implicit model was multiplied by the density, which was calculated using the local thickness determined after segmentation of the CCL. Using this model, a constrained optimization routine was then implemented to minimize the difference between the experimental greyscale pixel value and the calculated value, as detailed in section 4.2. The optimization routine uses constrained optimization by linear approximation (COBYLA) from scipy library. The constraint function is the porosity calculation limited between 0 and 1:

$$\phi = 1 - \frac{\rho_{bulk}}{\rho_{particle}} \tag{6.2}$$

where void space is assumed to be filled with air; ρ_{bulk} is the calculated density from composition obtained from the optimization routine and local thickness; and $\rho_{particle}$ is calculated based on the known densities for carbon (graphite), platinum and ionomer, as listed in Table 4.2. The experimental greyscale values were obtained from the zero-current density ('dry') image set and projecting average through-plane greyscale values

to a single 2D image after segmentation of the CCL. For beginning-of-life (0 AST cycles), nominal values of the CCL composition were given as initial guess for the optimization routine. These are listed in Table 4.2 as $Nominal_x$. The ionomer content was assumed to not change following the presently used AST cycling, and was not altered during the subsequent optimization routine from 0 AST cycles, while carbon and platinum were free to change due to degradation. Initial values were taken from the 0 AST cycles model output such that the local variation in ionomer, Pt and C was considered. That is, the model was applied to the BOL catalyst layer to determine local variation in ionomer, C and Pt content, while calculations following AST cycles used these local values as inputs and adjusted the C and Pt content to match the greyscale values obtained from the experiment.

Results

Water distribution changes following catalyst layer degradation

Combined visualization of transient water distribution and CCL degradation by 4D *operando* imaging is presented for the first time. At the beginning of life stage, near the surface of the flow-field lands, under the conditions chosen, considerable volumes of liquid water are pooled by the reduced gas flow and decreased porosity by compressed GDL pores. Some droplets also reside on the surface of the GDL and are fed by connected flow networks from the CL surface. These droplets are stable enough to maintain their volume during the course of the imaging period. Following degradation, a significant change in the water content of the GDL is observed, as a result of significant carbon corrosion from voltage cycle AST. The location of most of the water pooling was situated under the lands of the flow field, which remained consistent throughout cycling and current density measurements, however the amount of water changed steadily. Shown in Table 6.1 is the saturation calculated under land and channel at 0 cycles (beginning of life) and at 750 cycles representing a heavily degraded state. This value was calculated by averaging the ratio of water volume to total pore volume for each 1.5 µm step of the 3D image stack. At 0 cycles, the obtained value of 0.37 is in good agreement with other saturation studies. [43] The porosity used for this calculation of the GDL under land and channel is shown in Appendix D. At 0 cycles, the water content in the GDL follows an expected trend, with steadily increasing water volume with increasing current density [16], as shown in Figure 6.3. The pattern for water pooling demonstrates high amounts of liquid droplets on the

surface of the GDL and near the surface of the land (approximately 120 µm on the x-axis), followed by a decrease moving through the GDL, and then another slight increase following the change in GDL structure as porosity decreases from invasion of the MPL. Upon initial cycling by AST and again measured at 250 cycles, the trend is consistent with beginning of life (BOL), however, with higher relative water volume at 500 mA cm^{-2} and 750 mA cm^{-2}. Following an additional 300 cycles, there is a turning point to a change in behavior of the water content in the MEA. At 250 mA cm^{-2} the water content is comparable to BOL, however for the higher current densities of 500 and 750 mA cm^{-2} there is a noticeable decrease in the water volume compared to the previous cycling stage. This trend continues with further cycling up to 750 cycles, making the change highly apparent, with almost all liquid water being removed for 750 mA cm^{-2} at a highly degraded state. This trend is consistent with previously reported results using neutron imaging by Fairweather *et al.* [179] which used the same voltage cycling procedure. Fairweather *et al.* imaged at constant voltage of 0.6 V, which corresponds approximately to 750 mA cm^{-2} operation for this study at high degradation stage. The addition of lower current density measurements presented here and the favorable resolution of the XCT technique provides further insight into the change in fuel cell behavior, as well as additional detailed imaging of the CCL changes.

Degradation stage	Saturation - Land	Saturation - Channel
0 cycles	0.37 ± 0.04	0.01 ± 0.01
750 cycles	0.009 ± 0.003	0.001 ± 0.003

Table 6.1: Saturation calculation in the cathode GDL region under the lands and channels of an operating PEFC at 750 mA cm^{-2} at the beginning-of-life (0 cycles) and end-of-life (750 cycles) degradation stages.

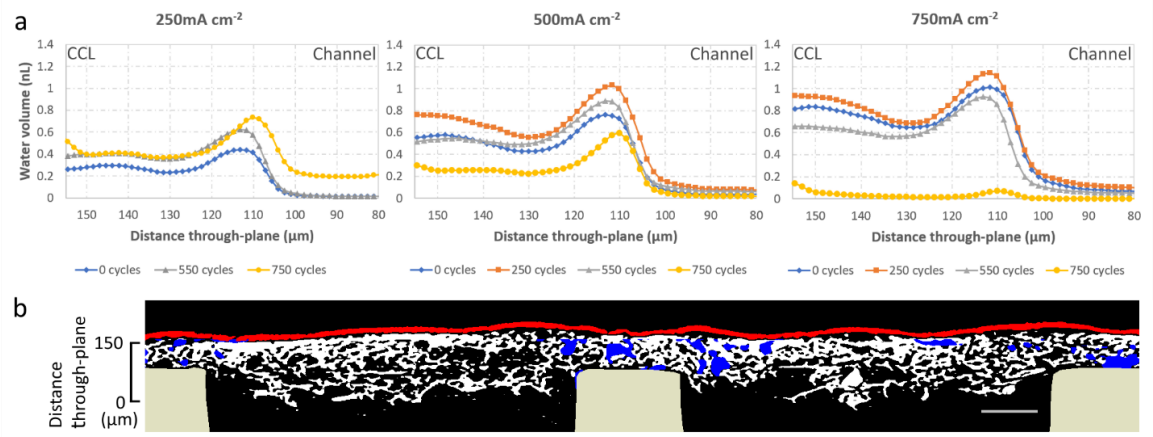

Figure 6.3: 4D operando liquid water visualization and assessment by XCT. (a) Quantified distribution of liquid water volume through the cathode GDL thickness at various current densities and at different degradation stages of the voltage cycling AST. (b) Segmented cross-sectional visualization of liquid water (blue) in the GDL (white), cathode catalyst layer (red), and lands (beige). The scale on the left identifies the location of water quantification in (a).

Catalyst coated membrane movement following cathode degradation

A unique observation afforded by the presently adopted visualization methodology, which involves XCT-based 4D *operando* imaging, is the identification of hydration-induced movements of CLs and membrane following stress cycles. As shown in Figure 6.4a (top row at no current), CCL crack formation and propagation are observed due to the corrosion of carbon support in the catalyst layer as well as from possible movement of the membrane. These images are acquired at room temperature with only nitrogen gas flow (100% RH at 25^{o}C) and without any hydration-inducing current withdrawal from the cell; accordingly this state of imaging is termed as a 'dry' state. Once the cell is operated with hydrogen and air under an applied load, water is produced leading to membrane water uptake and expansion [215]. As a result of this expansion, mechanical stresses are generated within the constrained membrane, forcing undulations due to buckling [180], [216]. As can be seen in Figure 6.4a (bottom row at 750 mA cm^{-2}), the CCL cracks can locally open or close depending on the bending direction within the adjacent membrane. The amount of bending in the through-plane direction is found to be substantial, particularly at highly degraded states, when observed using the cross-sectional views shown in Figure 6.4b. It is interesting to note that the amount of membrane movement/bending in the 'wet' state increases following the degradation cycles, however, the 'dry' state positions are largely unaltered from BOL to 750 cycles, with the CLs and

membrane returning to approximately the same position. These membrane undulations can produce local regions of separation between the CCL and MPL, thereby creating void spaces that may compromise the cell's water management functionality and promote local flooding. Moreover, the force applied from the through-plane movement of the membrane may produce locally over-compressed regions within the GDL, which may impact the porosity and consequently their liquid/gas transport properties.

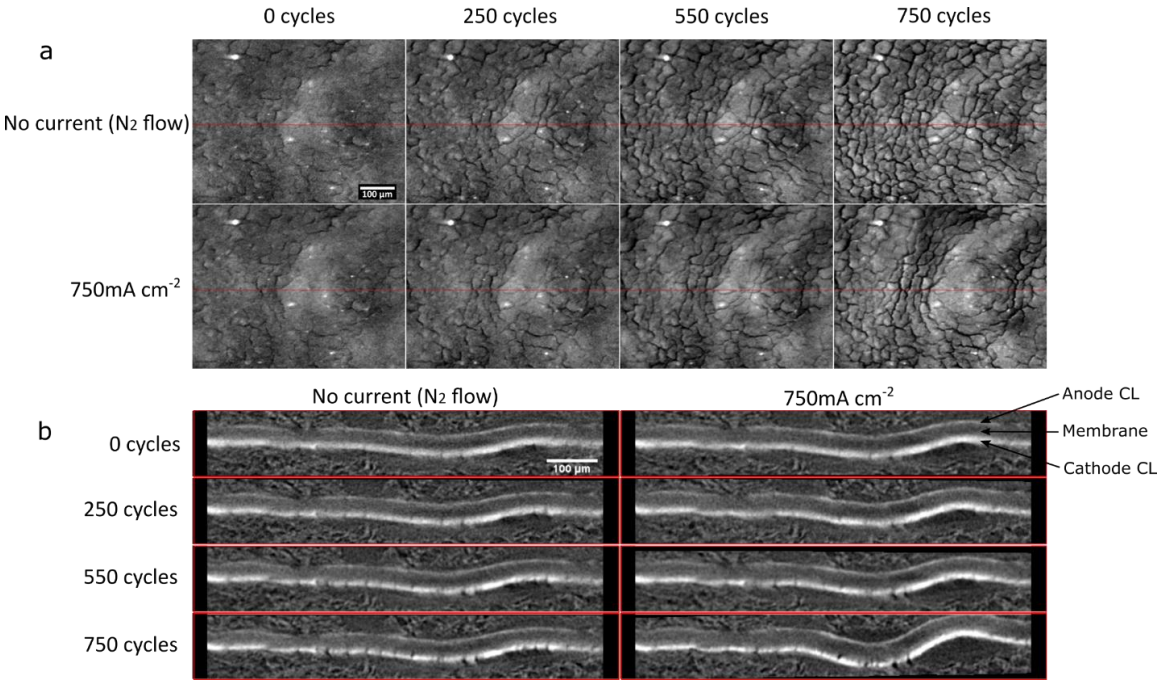

Figure 6.4: 4D operando images featuring (a) planar and (b) cross-sectional virtual slice views of the CCL and MEA, respectively, during 'dry' state (No current) and 'wet' state (750 mA cm^{-2}) at various degradation stages (as indicated by the cycle numbers), highlighting CCL crack formation and propagation and increased stress-induced membrane movement resulting from its expansion under hydrated conditions.

Carbon support degradation

Due to the applied cathode potentials above 1.0 V_{RHE}, carbon support material in the CCL undergoes oxidation and is lost in the form of CO_2/CO. This carbon corrosion weakens the catalyst structure and can eventually lead to crack formation and collapse in thickness [24], [116], [119], [217]. After segmentation of the CCL from the measured XCT data, quantification of morphology changes following degradation of carbon support can be obtained, such as CCL thickness, crack area and crack width. In addition, a local measure of the carbon loss can be calculated by using relative changes in the pixel

greyscale value. Previously, it has been shown that attenuation changes arise from degradation of the CCL, suggesting that a calculated CCL composition could be obtained along with its spatial and/or temporal distribution [24]. These results are highlighted in Figure 6.5a, where the calculated carbon loss (model) is validated against carbon loss measured from CO_2 output in the exhaust gas. The carbon loss calculation from the XCT data is found to be in good overall agreement with the CO_2 measurements. Some deviation from experimental values occur toward higher cycle numbers and may indicate inaccuracy resulting from the optimization search, as the calculated values have a larger deviation from nominal BOL values. It can also suggest however, that carbon loss from other sources besides the CL may be contributing toward the measured CO_2 [125]. Shown in Figure 6.5b is the comparison of morphological values with the obtained carbon loss. It is noted that a higher proportion of carbon is lost, altering the internal structure, than can be accounted for simply by reduction in thickness or crack formation. The relative local carbon loss is shown in Figure 6.5c, where the highest fraction is observed to correspond to crack formation where all solid is lost in this area, most notably occurring under the channel regions.

From the calculated local carbon loss, other properties such as local porosity can also be obtained, with the spatial porosity distribution and overall histogram shown in Figures 6.6a and 6.6b, respectively, as a function of degradation. As seen from the images and histogram, there is an incremental shift toward higher porosity until advanced stages of degradation, where the shift is reversed back toward low porosity, even below the original value at BOL. These results suggest a balance between CCL thickness and internal structure changes where internal corrosion can lead to increase in porosity (decrease in density) until the reduction in thickness is sufficient to cause collapse and reduce porosity (increase density) [200]. From local thickness measurement and composition distribution calculation, the perceived collapse is local at this stage of degradation with regions of variable ionomer content and thickness behaving differently than other regions. Following even further degradation, more uniform thickness will be present as a larger fraction of the catalyst area undergoes this collapse. This locally variable degradation stage will also play a role in heat generation, water production, and gas flow; all affecting the impact of local performance of the catalyst layer.

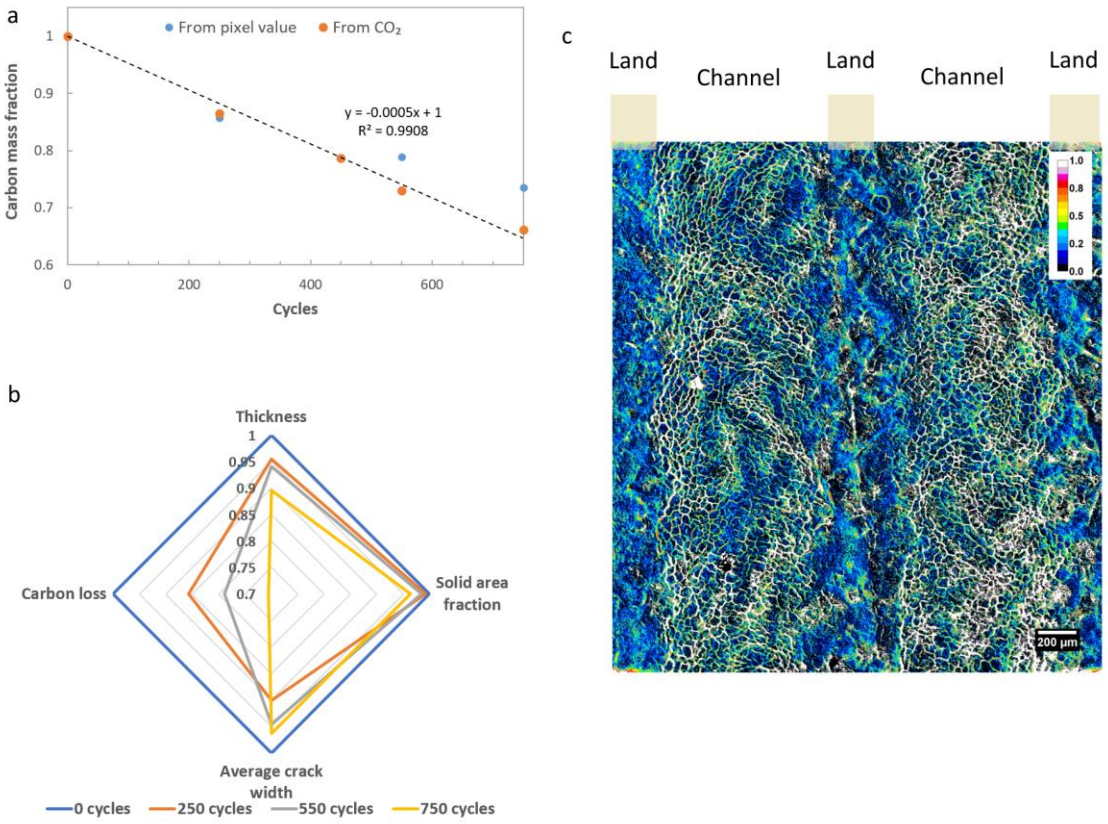

Figure 6.5: Quantification of morphological feature changes in the CCL through calculation of carbon loss from the changes in pixel greyscale value of the XCT datasets. (a) Comparison of calculated carbon loss with experimentally measured CO_2 output. (b) Comparison of morphological changes in the CCL during degradation with the changes in carbon loss. (c) Spatial distribution of fractional local carbon loss in the CCL from BOL to 750 cycles, shown through a pseudo-color overlay on a planar/top-down view of the CCL imaged by XCT.

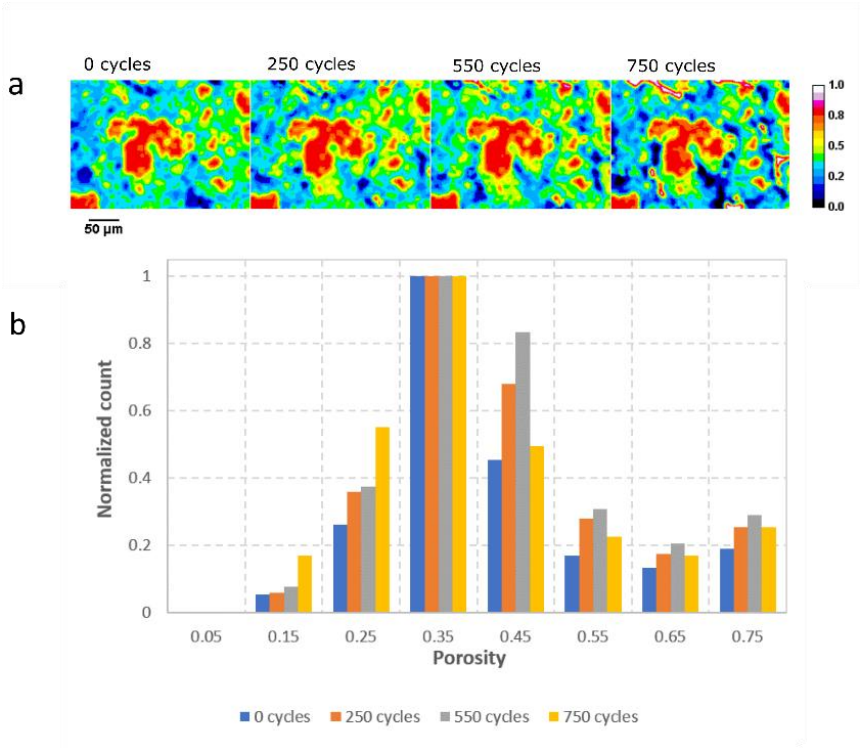

Figure 6.6: Quantification of porosity changes in the CCL during the voltage cycling AST, obtained through calculations based on pixel greyscale values. (a) Spatial distribution of porosity within the CCL plane shown with pseudo-color from a subset of the full-FOV. (b) Histogram plot showing the distribution of porosity values across the entire CCL FOV.

Fuel cell performance

In addition to the combined visualization of CCL degradation and liquid water distribution, fuel cell diagnostic information was also collected to monitor changes in electrochemical performance. Figure 6.7 shows the performance at various degradation stages as well as changes in the ECSA at the cathode from the small-scale fixture used for imaging. From the observed results, following stages of degradation by AST, a significant increase in mass transport loss occurs after 750 cycles. A more gradual and consistent decrease in ECSA occurs however, which follows good agreement with previous studies and relates well to the decrease in carbon support by corrosion and other damage features such as cracking [24], [119], [182].

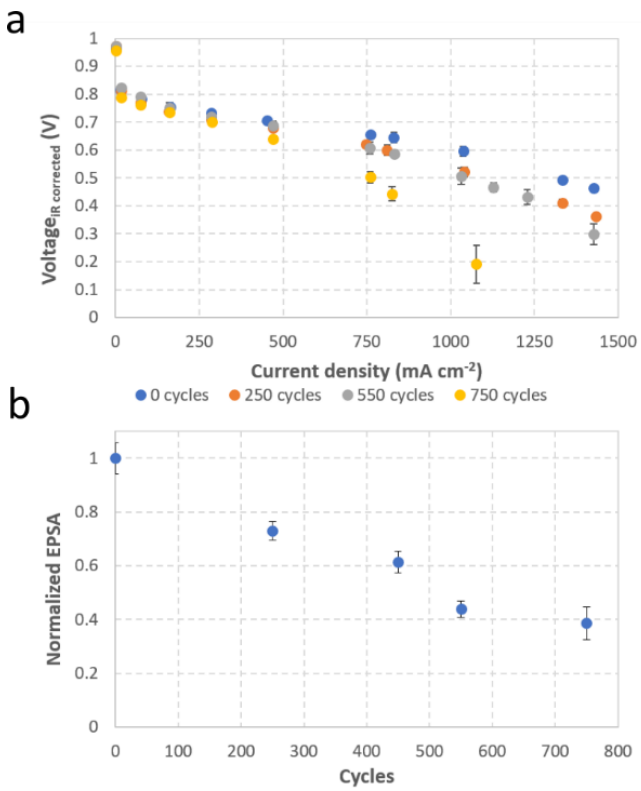

Figure 6.7: (a) Polarization curves and (b) cathode electrochemically active platinum surface area (EPSA) for the small-scale fuel cell at various degradation stages of the voltage cycling AST. The ECSA data shown are normalized against the BOL value.

Discussion

The combined visualization of water distribution and CCL degradation in a fuel cell, enabled by a customized XCT-based 4D *operando* imaging methodology and advanced post-processing techniques, is presented. This concurrent analysis offers novel insight into the interactions between various components that comprise a fuel cell system. Fairweather *et al.* had previously suggested that the observed decrease in liquid water content in the GDL following cathode corrosion likely results from temperature increase caused by elevated levels of heat generation that accompany performance losses associated with degradation of the CCL [179]. Observations made during the present work, such as CCL thinning and carbon loss, also suggest localized increase in heat production that could more readily facilitate vapor phase water transport from the CCL, where the water is produced, to the cathode gas channels where it is removed by the incoming gas flow. However, the increased membrane swelling and associated stress-induced movement observed at advanced degradation stages further suggests that the

rate of water removal from the catalyst layer may still be relatively slow, leading to an increase in local humidification within the MEA and flooding within the CCL. Degradation-induced damage features, such as increased crack formation and MPL-catalyst layer separation in some locations caused by significant membrane movement, can generate void spaces that may promote liquid water pooling and induce mass transport losses by blocking the diffusive pathways for incoming oxygen. The onset of significant performance losses in the mass transport region, particularly at 750 cycles, correlate well with the observed visualization results, as well as the aforementioned hypotheses of water evaporation within the GDL and local flooding within the catalyst layer. In addition, a decrease in contact area from membrane undulation can further increase associated losses. An approximate area of MPL separation is measured between 15-20% at high degradation state with large membrane movement. The gradual decrease in EPSA with degradation is likely a cumulative result of: (i) loss in solid catalyst layer area caused by crack formations; (ii) reduced interfacial contact caused by carbon support corrosion; and (iii) local flooding inhibiting the transport of gases to active sites in the catalyst layer [115], [182].

The present calculations of porosity (from greyscale pixel values) and carbon loss (Figure 6.6) correlate well with previous results from Star *et al.* [200], wherein carbon loss percentage was compared to porosity changes in PEFCs using a voltage cycling AST similar to that employed in the present work. The calculated results also indicate progressive changes in catalyst layer structure resulting from corrosion stages, where the porosity value increases initially due to pore formation from the removal of carbon support until the reverse effect from collapse of support structure becomes more dominant leading to a decrease in the local porosity value. This decrease in porosity will impact diffusive properties of the catalyst layer and inhibit gas diffusion leading to an increase in mass transport losses. The decreased porosity can also impact the CCL's water removal characteristics leading to additional flooding and increasing local humidity. Consequently, the ionomer membrane's local environment is altered by these elevated humidity levels, which allows for higher membrane water uptake leading to the increased expansion, mechanical stresses and buckling, as shown in Figure 6.4b. Table 6.2 shows the measured membrane thickness under both 'dry' N_2 conditions without current and 'wet' conditions during operation at 750 mA cm^{-2}. The thickness at 'dry' conditions shows no observable change from BOL up to 750 cycles, whereas the thickness under 'wet'

conditions appears to increase gradually with the progression of CCL degradation. In particular, the 'wet' membrane thickness is highest at 750 cycles which coincides with the increased amount of membrane undulation observed at this stage. Goulet *et al.* [189] had previously shown that the water uptake capacity and hydration-induced thickness change of the membrane does not vary much between the cases of: (i) presence and (ii) absence of bonded electrodes. Therefore, any degradation-induced variation in the restraining of membrane by the bonded CCL that may lead to the observed thickness increase is highly unlikely. Instead, the hypothesis of enhanced local hydration of the membrane environment caused by catalyst layer flooding seems more feasible and agrees with the various observations made in this work.

	Membrane thickness	
	at 0 current with N_2 flow (µm)	**at 750 mA cm^{-2} (µm)**
0 cycles	20.8 ± 1.7	21.1 ± 1.8
250 cycles	20.5 ± 1.7	23.4 ± 2.0
550 cycles	21.5 ± 1.6	23.2 ± 2.3
750 cycles	20.9 ± 1.5	26.1 ± 2.7

Table 6.2 Membrane thickness measured from the operando XCT images at various degradation stages under both 'dry' and 'wet' states. The increase in membrane thickness under 'wet' states correlate well with the observed increase in membrane and CL movement resulting from hydration-induced mechanical stresses. Plus-minus values indicate variation in the thickness across the full FOV.

Cathode catalyst layer cracks were almost non-existent at beginning of life post-conditioning (see Figure 6.4a). While the initial new crack formations reduced the average crack width from BOL to 250 cycles, as shown in Figure 6.5b, further crack propagation and carbon corrosion brought back the average crack width closer to the BOL value. As observed in Figure 6.4, significant movement results from expansion of the membrane at high current densities. In addition to the voltage cycling during the applied AST, it is plausible that the sequential 'dry' and 'wet' visualization scheme may also induce mechanical crack development due to the associated membrane movement. Given that the membrane movement from 'dry' to 'wet' states is negligible at the initial degradation stages and that the new crack formations seem to initiate during this period, the contribution of mechanical stresses/movement to the CCL crack development is likely to be marginal or negligible. This can be seen in the comparison of 'wet' state images of the cathode plane between BOL and 250 cycles (Figure 6.4a), wherein the new crack formations observed at 250 cycles are evidently a result of the intermediate voltage cycling. Nevertheless, increased water retention in the catalyst layer with progressive degradation may give rise to such mechanical crack formations at the later stages of

voltage cycling AST, when the membrane movement is more pronounced. It is further possible that hydrophilic species formation from the oxidation of carbon support could promote initial water retention, which could then trigger a chain-reaction like effect wherein higher water retention leads to both higher corrosion and greater membrane movement, collectively leading to increased rates of crack formation/growth and flooding.

Summary

For the first time, combined visualization of CL degradation stages and water distribution in PEFCs is presented. Upon applying an AST to simulate possible cathode potential swings during PEFC operation, degradation of the CL from corrosion of carbon support is observed. In addition, visualization and quantification of water distribution in the GDL is obtained and is shown to change significantly over the lifetime when measured *in operando* at constant current. Surprisingly, at the end-of-life stage, liquid water in the GDL is no longer present at moderate to high current densities, which indicates evaporation due to heat generation. In addition, catalyst layer movement from stresses applied by membrane swelling by water absorption is visualized and shown to increase significantly at advanced stages of cathode degradation. This occurs as a result of catalyst layer flooding as a result of porosity change and additional hydrophilic surface groups introduced from corrosion of carbon support, in addition to crack formation allowing for areas with which liquid water can accumulate. Additional degradation features such as separation of the CL from the MPL as well as CL crack opening and closing is observed. These degradation features will inhibit proper water removal from near the CL leading to additional performance losses. Quantification of CL composition change by calculation from pixel greyscale values obtained by XCT is also presented and shows excellent agreement with carbon loss from carbon corrosion as measured by CO_2 exhaust gas monitoring. In addition, this calculation allows for local carbon loss to be observed, as well as material property values such as porosity change to be calculated. During degradation, the CL porosity is first shown to increase before a sudden decrease at end-of-life. This signifies corrosion of the carbon support first leading to a hollowing effect eventually causing collapse of pores and increased density during the observed thinning of the CL at advanced degradation stages. This reduced porosity will also impact the removal of water and efficient operation of the CL with significant mass transport losses becoming apparent. From the combined visualization of water distribution in the GDL as well as *operando* visualization of the CL features and expansion behavior of the membrane, a strong

interplay between MEA components is presented in operating fuel cells. With technological improvements in visualization methods and processing, significant advances into the understanding of degradation induced changes that result during fuel cell lifetime has been achieved.

Chapter 7. Correlative X-ray tomographic imaging of catalyst layer degradation in fuel cells

The characterization of PEFC catalyst layer nano structure has been an area of significant research interest due to its complex structure and importance with modelling for improved catalyst layer architecture design. As discussed in Chapter 1.2, the cathode catalyst layer is a porous media comprised of platinum nanoparticles on carbon support intermixed with ionomer. This complex three phase system is necessary to allow for the electrochemical process to occur by means of transport for electrons, hydrogen/oxygen gas and protons to meet at a triple point, catalytically active location. To enhance performance of PEFCs, the abundant availability of oxygen at the cathode triple point locations is needed. This is often the most rate limiting step however as it requires diffusion of oxygen through the pore network. In addition, removal of excess water formed as a by-product of the electrochemical reaction also occurs through this pore network.

The combination of carbon support and ionomer forms the porous structure of the catalyst layer. Through carbon corrosion and cathode catalyst layer degradation this solid structure framework is altered, which directly impacts the porous structure and in turn results in voltage losses; see section 1.3 for further details. As a result of this, the understanding of complex changes that occur through the lifetime of the cathode catalyst layer is of significant interest. However, obtaining the structure of the cathode catalyst layer requires careful consideration. Various methods have been used to study the catalyst layer structure. The resolution requirements in order to study and observe the structure makes visualization difficult. Further discussion of various methods used previously is discussed below in this section and compared to nano-scale XCT imaging.

This present work focusses on the methodology required for accurate correlative *operando* and nano-scale XCT imaging; combining multi-scale imaging modalities to investigate a full scope of catalyst layer degradation from macro to nano-scale. Additionally, careful considerations for imaging mode (phase vs. absorption imaging) and post-processing are presented. Comparison of different analysis methods for diffusion coefficients are discussed which can be used in future modelling work. Microcracks and degradation features on the nano-scale are presented which shows unique insight previously not visualized. In addition, macroscale XCT imaging is also discussed by

utilizing the *operando* workflow presented in Chapter 6. New insights into macroscale degradation feature dynamics relating to GDL morphology are also presented which have never been identified before. Correlation to porosity values obtained by nano-scale XCT and macro-scale greyscale calculation are discussed as well as the impact on fuel cell performance through changes in polarization curves.

The following section is a formatted version of R. T. White, D.Ramani, S. H. Eberhardt, M. Najm, F. P. Orfino, M. Dutta, and E. Kjeang, **Correlative X-ray tomographic imaging of catalyst layer degradation in fuel cells**, *J. Electrochem. Soc.,* 166 (2019) F914-F925.

R.T.W. S.H.E. and M.N. performed fabrication, and operated and collected diagnostic measurements of the small-scale PEFC; R.T.W. and S.H.E. operated the small-scale PEFC during *operando* imaging; R.T.W. collected and analysed all XCT data; D.R. performed sample prep by FIB lift-out; R.T.W. drafted the manuscript.

Effective catalyst layer design is vital for high-performing polymer electrolyte fuel cells. However, the desired catalyst layer structure may be compromised by operational degradation, causing performance decay. The present work investigates the multi-scale catalyst layer structure and properties across different stages of degradation, including liquid water distribution in an operating fuel cell. A correlative, multi-scale imaging workflow with a combined analysis by *operando* lab-based micro-X-ray computed tomography (XCT) and nano-XCT is developed for this purpose. From *operando* XCT results, the catalyst layer solid area fraction was found to gradually decrease by 25% with crack formation and severe localized corrosion accompanied by up to 50% thinning and significantly altered liquid water distribution. Localized degradation features such as nano-scale cracks and internal pore-size distribution changes were resolved using nano-XCT and tracked by 3+1D imaging at different stages of degradation. Porosity changes quantified by nano-XCT on the order of 40% from beginning-of-life to end-of-life with reduction in connected pore fraction were observed as well as increase in average pore size by 50%. The effect of changes at the nano-scale on diffusion properties were calculated and an empirical model is proposed for degraded catalyst layer structures where Knudsen effects are dominant.

Introduction

Optimizing the performance of polymer electrolyte fuel cells (PEFCs) requires precise design of the catalyst layer porous structure. The porosity, tortuosity, and pore size distribution can each play significant roles in maximizing performance as well as improving lifetime where diffusion limitations become the dominant mode of performance losses. Balancing the inward flux of oxygen and outward removal of water requires that both fluid phases be easily transported through voids within the cathode catalyst layer structure; understanding of changes to this structure can therefore play a vital role in determining optimum architecture and robust material selection. Hence, there is a need to characterize this porous network to provide parameters for transport models as it is vital for optimal material design [218], [219].

Various methods have typically been used by convention to determine the structure of a porous material. Most simply, by using the thickness and the areal weight of a porous material one can calculate average porosity by using the bulk density of the material and the calculated density of the solid phase (from thickness and approximate composition) [220]. Alternatively, information regarding pore size distribution can be obtained by mercury intrusion porosimetry (MIP), which is a well-known method that utilizes the high surface tension of mercury to be non-wetting and infiltrate connected pores. The amount of mercury uptake as a function of applied pressure is used to calculate pore size distribution [221], [222]. However, this method poses the following limitations: (i) mercury, as a toxic substance, can be difficult to handle and also renders the piece of material unusable after measurement; (ii) only surface connected pores of the material will be infiltrated by the mercury to obtain the porosity and pore size distribution [223]; (iii) difficult to handle materials, such as those that become fragile after degradation, or materials which cannot be easily separated from other components, may convolute results and make analysis difficult which may lead to inaccurate results; and (iv) MIP is a bulk measurement with no local, targeted information available.

The use of various imaging methods overcomes several limitations associated with bulk measurement by providing local information, typically at the cost of smaller sampled volume. For instance, scanning electron microscopy (SEM) provides high contrast and high-resolution imaging which is often used for material characterization [11], [224]–[226]. However, SEM alone is limited to 2D visualization, requiring considerable sample handling

and preparation, and can suffer from edge effects and large depth of focus; making segmentation and interpretation of pores difficult. By combining SEM with focused ion beam milling (FIB), a three-dimensional visualization can be acquired by eroding a layer of material using an ion beam and imaging the newly exposed surface to obtain a stack of 2D images through the thickness of the material. The FIB method, however, requires special care when applied to soft materials such as catalyst layers in PEFCs. For example, the ion-beam has been shown to cause ionomer melting, carbon amorphization, and physical damage to the exposed catalyst layer. [227]. In order to obtain meaningful segmentation, filling the pore structure with an epoxy resin is necessary but problematic, since only connected pores can be properly filled. Moreover, the underlying physical structure may be altered by this method [228]. Though the resolution of SEM in the lateral dimension is high, the through-thickness resolution can vary depending on FIB milling conditions and material properties. Furthermore, since this methodology is invasive in nature, the section of sample imaged is destroyed.

Alternatively, transmission electron microscopy (TEM) has been used in conjunction with the ultramicrotome method for obtaining pore structure information [27]. The use of ultramicrotome has shown to be less damaging to the catalyst layer structure and composition as compared to the FIB technique [227]. Although TEM can achieve some of the highest spatial resolution, with the ability to resolve platinum nanoparticles on carbon support [227], as well as ionomer coating just ~10 nm thick around catalyst particles after staining with Cs^+ [229], ultramicrotome slicing can be upwards of 100 nm thick; thus, reducing the three-dimensional voxel resolution of the pore structure [27]. Typically, three-dimensional imaging is performed by placing powder samples on a TEM grid and imaging through a range of angles as is of a single carbon particle [201], [229], [230].

In contrast, the use of XCT seeks to resolve many of the aforementioned issues by allowing for three-dimensional imaging with symmetric resolution by volumetric imaging, and is non-intrusive where the sample is intact following imaging [27], [231]. Improvements in nano-XCT optics has allowed for high contrast and high-resolution imaging with 16 nm voxels from state-of-the-art laboratory systems [30], [57], [232]. This has allowed for visualization of the secondary pore and agglomerate structure of catalyst layers with additional studies attempting to resolve the thin ionomer volumes [27], [32], [231]. Previously, Epting *et al.* [27] showed that nano-XCT can be used to image pore and

solid structure of PEFC catalyst layers, where both Pt/C and ionomer regions were represented as solid phase. This was demonstrated using an 8 keV anode X-ray source and Zernike phase contrast imaging. Typically studies on catalyst layers have resolved pore sizes typically on the order of 100-200 nm in diameter, with pixel size of approximately 32 nm [27], [32], [56], [57]. In our group, Pokhrel *et al.* [185] visualized catalyst layer structures with pore sizes less than 100 nm using pixel size of 16 nm in absorption contrast imaging mode which provides higher flux and thus shorter scan times using a Zeiss Xradia Ultra 810 nano-XCT system with 5.4 keV anode X-ray source. This lower energy improves contrast by higher sensitivity to carbon rich solid phase and air, however, is still not believed to be sufficient to accurately detect low attenuating regions throughout the catalyst layer structure. The contrast between solid phase (Pt/C and ionomer) and air is only high for larger agglomerate regions with high attenuation value, rich in Pt and/or ionomer. As well, segmentation was performed globally by comparing the obtained porosity value to that expected from MIP measurement and manually selecting a greyscale value threshold. This is believed to substantially overestimate the pore sizes, and considerations for improvement are thus needed in future works. Pokhrel *et al.* [185] also applied a formulation to segment possible ionomer distribution, however this calculation was based on assumed nominal composition values of the full catalyst layer without regard of local variation. More recently, White *et al.* [233] showed that significant variation in composition can occur locally within the catalyst layer and knowledge of precise location of where the sample is selected for nano-XCT imaging is imperative.

Studies focusing on PEFC degradation using XCT have been primarily focused on macro-scale changes with recent work combining *operando* imaging to obtain water distribution changes within the gas diffusion layer (GDL) using micro-XCT [24], [47], [169], [170], [234], [235]. These studies have discussed changes in crack formation and propagation, and differences between land and channel degradation. In addition, the impact of catalyst layer crack formation on the propagation to membrane crack formation under continued mechanical cycling. Overall catalyst layer thickness change resulting from carbon corrosion and collapse of carbon support was also shown, which identified local variation in catalyst layer behavior related to variation in composition or differences in local corrosion rate. Combined analysis of water distribution changes and catalyst layer behavior under wet and dry conditions has also been shown to be very local in nature with increased buckling and movement observed under wet conditions when operated as well

as regions with possible higher local flooding [234]–[236]. The distribution of water also affects performance by flooding and gas blockage, it may also accelerate local corrosion due to its direct participation in the corrosion reaction. As such, observing degradation in relation to water distribution is of vital importance to improve understanding. In order to develop improved mitigation techniques as well as new materials for enhanced lifetime, a more thorough understanding of the adverse effects of carbon corrosion is needed which can only be obtained by direct visualization. In particular, local morphological features, which act as nucleation or concentration sites for degradation, warrant deeper investigation. This dynamic and locally variable nature of catalyst layer degradation demands the use of correlative imaging procedures for nano-XCT analysis.

Previous studies focusing on nano-scale analysis in PEFCs have targeted determination of catalyst layer and micro-porous layer (MPL) properties. A comprehensive study by Çeçen *et al.* [237] utilizing FIB-SEM to study MPL porous structure properties proposed several analysis tools to define the nano-porous structure such as tortuosity, chord-length and effective diffusivity. Epting *et al.* [27] utilized nano-XCT to perform similar image-based analysis of cathode catalyst layer properties, highlighting pore size distribution measurements. Alternatively, global analysis (non-spatially resolved) by electrochemical methods was performed by Soboleva *et al.* [110] where differences in pore sizes and carbon types were shown to impact water sorption and local flooding affecting fuel cell performance by blocking active sites. Many previous studies have focused on material properties from specifically fabricated catalyst layers suitable for imaging, such as deposition on polyimide films, or imaging catalyst layer powders which may differ considerably from the *in situ* fuel cell environment. To better understand fuel cell operation and degradation to improve lifetime, operated and cycled catalyst layers must be characterized. Star and Fuller [200] performed FIB-SEM imaging accelerated stress tested cathode catalyst layers mounted and embedded in epoxy, relating porosity to carbon loss by image processing of pores and mass balance calculation from thickness. Significantly reduced porosity was observed at end-of-life suggesting collapse, and proposed differences between inter-particle and intra-particle corrosion stages was presented, providing discussion for non-linear behavior of cathode catalyst layer degradation.

The main research objective of the present work is to determine the structural evolution of catalyst layer degradation in fuel cells by multi-scale XCT characterization at

different stages of degradation. For this purpose, a correlative workflow is developed for X-ray tomographic imaging of cathode catalyst layer degradation featuring four-dimensional (3D plus time) *operando* imaging and *ex situ* nano-scale imaging. Liquid water distribution and dynamic structural behavior of the membrane electrode assembly during operation and stages of degradation is shown. Following this, macroscale analysis of the cathode catalyst layer and the localized variation in morphology and composition is discussed. In addition, improved imaging of the fine porous structure within the cathode catalyst layer is presented, thus allowing for a comprehensive analysis of cathode catalyst layer structural degradation. Additionally, comparison to MIP pore size distribution and important differences in measurement are shown. Finally, quantification of morphological changes at different stages of degradation is investigated and compared to *operando* image features and water distribution changes in the cell.

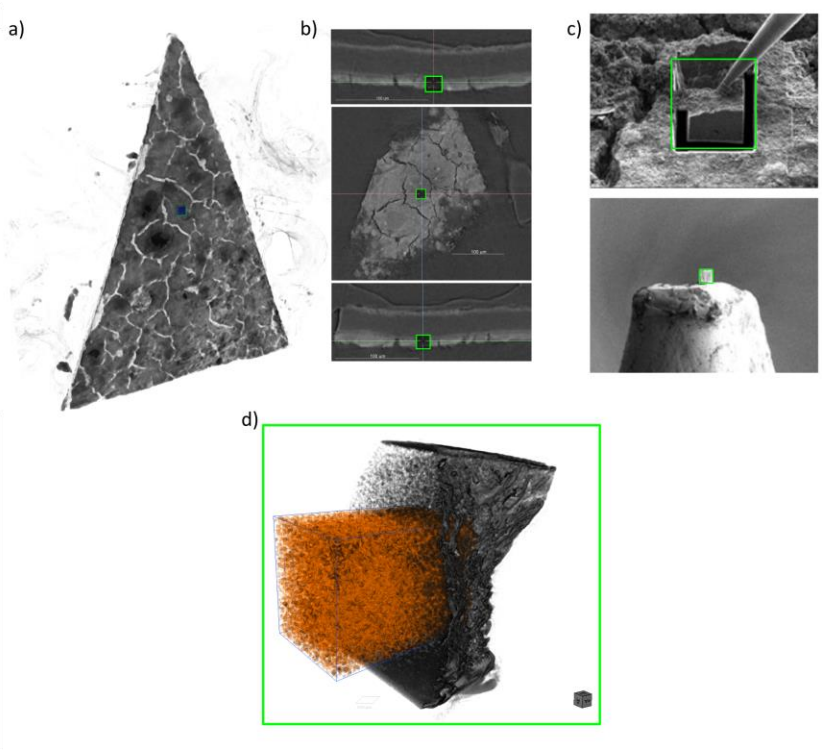

Figure 7.1: Combined visualization of the same location in the cathode catalyst layer from micro-scale (a,b) and nano-scale (d) XCT. a) Wedge shaped sample used for morphological quantification and screening to find a representative area to perform FIB liftout before imaging using nano-scale XCT. b) 2D cross-sectional planes virtually extracted from the 3D volume in (a). c) FIB lift-out needle is carefully attached to the sample using Pt deposition and the bridge is cut-off for sample lift-off; the lifted sample is then placed on a pin tip with 0.4 mm diameter. d) 3D rendering of the selected catalyst layer region imaged using nano-XCT with porosity volume segmentation shown in orange.

Experimental

Fuel cell materials — Fuel cell materials used in this study comprised of catalyst-coated membrane (CCM) with Dupont Nafion® NR211 membrane core and cathode and anode catalyst layers each with 23 wt.% ionomer and a 50:50 Pt/C ratio at 0.4/0.1 mg cm^{-2} Pt loadings, respectively. The GDL materials used consisted of teflonated Avcarb® non-woven carbon paper coated with micro-porous layer (MPL) for both anode and cathode. As part of this study, a high crack density catalyst layer was used to enrich the outcomes of visualization and for morphological change quantification such as crack propagation. However, it has been reported that the beginning-of-life crack density in the catalyst layer has minimal impact on the observed trends under sufficient degradation [234], [235].

Fuel cell operation and testing. — Fuel cell operation was performed on a Scribner 850C Fuel Cell Test System, with flow field plates and housing using a custom designed small-scale fixture, as detailed elsewhere [24]. The active area of the membrane electrode assembly (MEA) was 0.36 cm^2 after assembly by custom designed vacuum table framing. The anode and cathode flow fields comprised of two straight, parallel channels in co-flow mode, allowing for comparison between land and channel behavior of the PEFC. The assembled fuel cell was conditioned for 20 hours at 0.5 A/cm^2 under 100% relative humidity H_2 and air flows of 0.2/0.4 slpm at 65^{o}C for the anode and cathode respectively. Accelerated stress testing (AST) was employed to degrade the fuel cell materials in a controlled manner using established voltage cycling protocols applied under the same gas flow conditions [24], [119], [125]. Voltage cycling square wave steps of 0.6 V (30 s dwell) and 1.4 V (60 s dwell) were chosen to target carbon support degradation in the cathode catalyst layer, which can occur even at low operating voltages but was accelerated here by means of a high upper potential limit [108]. This helped de-convolute between other processes such as platinum dissolution, which has been shown to occur with lower upper potential limits and high number of cycles [117]. *Operando* imaging was performed at 750 mA/cm^2 while at room temperature (~25^{o}C) with 0.2/0.2slpm flow rates to limit the input of moisture as well as improve stability during long tomography scans with the lab-based system. Further details of the *operando* imaging procedure are discussed elsewhere [234].

Ex-situ sample preparation. — Following conditioning and application of a designated number of AST cycles, MEAs were removed from the fixture and cut with an

industrial blade into an isosceles triangular shape (Figure 7.1a). These MEAs were previously operated in the same housing as was used for *operando* imaging to ensure consistent conditions when comparing across datasets. The samples were visualized with micro-scale XCT to survey a triangular piece and obtain locations of regions of interest (see *X-ray imaging* below for details). The dataset was processed using established methods to obtain the thickness of the cathode catalyst layer over the full domain. The segmentation of the cathode catalyst layer was performed using automated thresholding followed by an automated script to isolate it from adjacent materials. [24]. Based on this, a desired location was chosen for nano-scale XCT characterization using the triangular tip as a point of reference to ensure exact location selection across imaging systems. This area was chosen from crack free catalyst layer regions which had a thickness equal to the average value across the full field of view to accurately obtain a representative portion of the active area. The same location was identified by SEM in preparation for FIB lift-out [238]. For optimal imaging using nano-scale XCT, a sample size of 16 µm or less is needed to fit in the field-of-view. This reduces noise and improves contrast as well as reduces the necessary tomography time. The use of FIB was thus performed to yield a suitable sample.

Using a FEI Helios Nano Lab 650 SEM/FIB system, the desired location was initially coated with a fine layer of Pt at voltage of 3 kV and 3.2 nA current over a region of 15 µm x 12 µm to prevent damage caused by the ion beam. The sample was tilted to 52° and trenches were milled on either side of the location with the ion beam (3kV, 2.5 nA). The sample was then tilted back to 0° and an L-shaped polygon was cut to a depth of *ca.* 8 µm with a small bridge still holding the sample. The lift-out manipulator was carefully attached to the sample using Pt deposition and the bridge was removed for sample lift-off. The lifted sample was placed on a pin tip with 0.4 mm diameter as illustrated in Figure 1c. Using the described procedure with the use of a triangular catalyst layer sample, an exact location can be correlated between the imaging stages; see Figure 7.1.

X-ray imaging. — To properly characterize the representative area used for nano-scale imaging and to quantify macroscale features such as thickness and cracks in the cathode catalyst layer, an initial lower resolution survey scan was performed of the whole triangular MEA sample. This initial scan also enabled exact location identification for FIB liftout, as described above, and subsequent nano-scale imaging. For this survey scan, micro-scale imaging was performed using a commercial laboratory scale XCT system (ZEISS Xradia 520 Versa, Carl Zeiss X-ray Microscopy, Pleasanton, CA). This instrument employs the

use of objective lenses which provide an achievable pixel size down to 0.1 µm. In the present work, all images and tomographic datasets using this system were acquired at an anode accelerating voltage of 80 kV with additional low energy filter, which corresponds to an emitted X-ray spectrum with a mean energy of 32.5 keV, determined through experimental calibration [234]. These system settings provided the most appropriate energy spectrum to enhance the contrast of the cathode catalyst layer as well as minimize radiation damage by exposure. The pixel resolution employed was 0.69 µm corresponding to voxels of 0.33 μm^3 with a field of view of 680 µm. *Operando* imaging during steady state fuel cell operation inside the XCT chamber was performed under the same imaging conditions with a larger pixel size of 1.5 µm and a larger field of view of 3 mm, which allowed for the full active area width to be visualized. The relatively long scan times required for lab-based XCT limited the water distribution visualization to transient liquid water in the GDL, where consistent water channels were formed and remained constant through the imaging time of ~2.5 hours. *Operando* imaging was performed at each stage of degradation enabling a four-dimensional approach with temporal information on catalyst layer degradation and the impact on liquid water distribution.

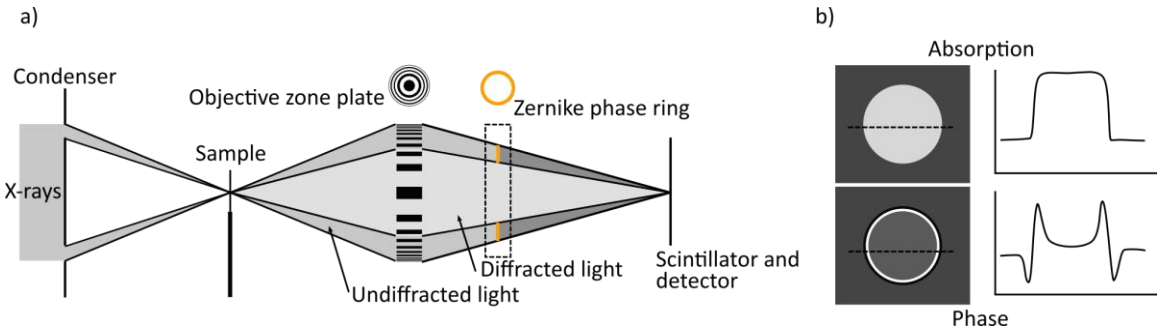

Figure 7.2: a) Nano X-ray computed tomography optical set-up showing the Zernike phase ring that is used to improve contrast of low attenuating features. b) Resulting reconstruction slice from a tomography of a spherical object with line profile showing relative greyscale value differences observed when imaging in phase and absorption mode. The edge effect and shade-off obtained in phase contrast mode can be seen in comparison to absorption only mode.

For nano-scale imaging a ZEISS Xradia 810 Ultra laboratory scale XCT system was employed. This system uses a sequence of X-ray optics to achieve spatial resolution of 50 nm or below, with a pixel size of 16 nm within a 16 µm field of view. The system uses a semi-monochromated X-ray beam of 5.4 keV by emission from a chromium anode. For contrast enhancement of pore and solid phases, a specialized gold phase ring is placed

between the objective (Fresnel) zone plate and scintillator (see Figure 7.2) which shifts the phase of undiffracted X-rays by 3π/2 allowing for constructive and destructive interference to occur at the scintillator, yielding pronounced edge contrast [147]. This ring acts to enhance high spatial frequency features and enables the visualization of low density and low atomic number materials where attenuation of X-rays is low and thus results in lower contrast. A secondary effect of Zernike phase contrast is termed “shade off”, where the contrast within material domains away from the interface is low, thereby making segmentation difficult [239]. It has been shown however that features with length scales less than a few hundred nanometers do not suffer from “shade off” since the interference drop-off is sufficient to provide enhanced contrast over the whole solid or pore region [27]. Due to the need for large scan times often required for phase contrast imaging, detector binning is often employed to increase signal at a cost of pixel resolution. This enables a reduction in noise and faster scan time but reduces the pixel size by a factor (i.e. pixel size 16 nm at binning 1 will become a pixel size of 32 nm at binning 2). Additional visualization was also performed using absorption mode to ascertain the changes in material properties by qualitative analysis of the greyscale pixel values which are directly related to density and composition of the sample material. Although adopted in other studies of fuel cell catalyst layers, absorption mode imaging did not produce sufficient contrast to accurately obtain pore volume segmentation for the catalyst layer structures and imaging conditions used in the present work.

Image processing. — Zeiss XMReconstructor software was used for the 3D reconstruction of all tomography datasets based on filtered back projection algorithm. The reconstructed 3D datasets were exported as TIFF images to be further processed in Fiji/ImageJ [209] and Dragonfly by Object Research Systems (www.theobjects.com). Segmentation of the cathode catalyst layer from macroscale image sets of the MEA utilized a custom and semi-automated process by macros written in ImageJ. Following this, additional scripts to obtain thickness and crack data were employed. Additionally, processing for liquid water visualization was performed using custom scripts for alignment and anisotropic diffusion filtering following subtraction of dry and wet datasets to remove noise and improve segmentation [77], [234], [239]. For nano-scale analysis, a 3D sub-domain dataset was selected 1 µm from the edges of the volume to avoid artifacts from the FIB milling process. Dataset volumes varied depending on the thickness of the catalyst

layer, with beginning-of-life (BOL) having the largest volume of 250 μm^3 and end-of-life (EOL) having the smallest volume of 128 μm^3 due to the reduction in thickness.

Fourier power spectrum analysis was employed to quantitatively determine feature resolution from nano-scale datasets. This algorithm was custom coded in Python (python.org) and takes the Fourier power spectrum of a line profile from features of interest and background noise, typically chosen as air, as shown in Figure 7.3a. The power spectra were plotted using wave-number and converted to a distance using the half-wavelength to define a feature size [27]. That is:

$$k = \frac{2\pi}{\lambda};\ \Delta x = \rho\frac{\lambda}{2} \tag{7.1}$$

where *k* is the wave-number output from the power spectra, Δx is the distance across the feature, λ is the wavelength, and ρ is the scaling from pixels to nm, i.e., 16 nm/pixel. Figure 7.3b shows the power spectra for catalyst layer material and air from a 1 µm vertical line, in addition to an insert as a measure of a single pore feature identified by eye from a 200 nm line which agrees well with the manual measurement of 40 nm, indicating that pore features of this size are resolvable.

Segmentation of the pore volume was obtained using an adaptive local thresholding algorithm [240] adapted in ImageJ with a neighborhood window of 15 pixels, which is well suited for the variation in greyscale from phase imaging and composition of material. Other local and global thresholding methods were also investigated however many were found to over-estimate the pore volume and did not account well for regions with varying greyscale values; for reference, the results using the proposed algorithm are compared to those of the local Otsu method in Figure 7.3c.

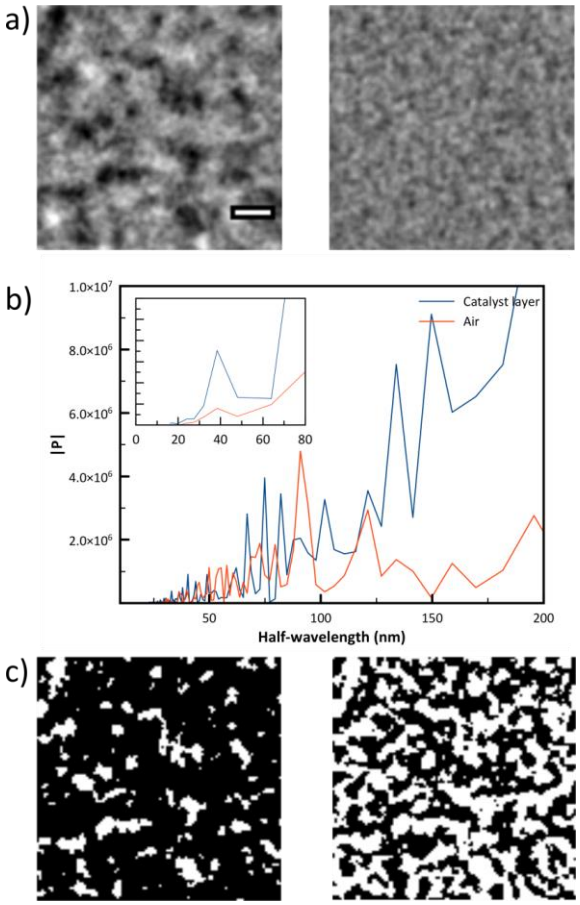

Figure 7.3: a) Subsection of raw greyscale image of catalyst layer (left) and air (right) regions for nano-XCT phase imaging, where the scale bar represents 250 nm. b) Fourier analysis of features observed in catalyst layer compared to air noise signal demonstrating the spatial resolution of 50 nm, with in-set of 40 nm pore measured by Fourier method. c) Comparison of segmentation methods of local threshold using Phansalkar adaptive thresholding (left) and Otsu method (right) where white corresponds to pores segmented.

Mercury intrusion porosimetry. — Cathode catalyst layers coated on Nafion® NR211 membrane, also known as half catalyst coated membrane, were sampled with a knife (0.3 g) and inserted into the penetrometer of a Micromeritics AutoPoreIII Porosimeter. The capillary tube was then filled with mercury at 0.59 psia, pressurized in the low-pressure port to 20 psia, and subsequently switched over to the high-pressure chamber and run to 60000 psia to obtain ~4 nm mean diameter pores. The instrument measures the incremental pore volume and cumulative pore volume normalized by the sample weight. The data was then normalized to the catalyst layer weight using the approximate material composition, loading, and nominal membrane area and then subsequently normalized to compare to nano-XCT data, as shown in Figure 7.7a. In order

to compare with XCT results and eliminate porosity due to cracks or larger pores, only intrusion volume for <300 nm pores was included in the porosity calculation.

Results and Discussion

In the following sections, observations and results obtained with the correlative imaging workflow from *operando* XCT as well as from *ex situ* micro- and nano-XCT are analyzed and discussed at different stages of cathode catalyst layer degradation. Various quantitative morphological characteristics such as cathode catalyst layer thickness, crack formation, porosity, and diffusion characteristics are also extracted and discussed.

***4D Operando imaging*. —** Liquid water distribution within the MEA of a fuel cell is a result of a complex combination of fluid dynamics, temperature, humidity, structure, and material surface properties. The result of these interactions can heavily affect the performance of a fuel cell in current limiting ranges as well as lifetime where water content plays a significant role in several key degradation processes, including carbon corrosion [16], [119], [182], [215]. Previously, White *et al.* [234] showed the combined visualization of water distribution changes within an operating MEA and the related cathode catalyst layer degradation macro-scale (using micro-XCT). To compare with nano-scale imaging, 4D *operando* imaging of MEAs with the same catalyst layer material was performed here at 750 mA/cm^2 across four key stages of degradation. Figure 7.4a illustrates the water volume calculated from *operando* XCT imaging in the cathode GDL as a function of distance from the catalyst layer interface to the flow field plate interface; which is in general agreement with previous findings by White *et al.* [234] and Fairweather *et al.* [179] where a high water content is observed under the lands and near the surface of the GDL, with slight decrease moving toward the MPL followed by additional increase once in the MPL region of the GDL. Furthermore, a significant reduction in water saturation is observed at advanced degradation stages after 350 and 450 AST cycles. This agrees with previous studies where it was attributed to water evaporation as a consequence of increased heat generation at reduced voltage efficiency. [179], [234]. In addition, the *operando* results show an interesting phenomenon relating to crack dynamic behavior in pertinence to GDL/MPL structure. A GDL/MPL void was observed close to the cathode catalyst layer interface as well as catalyst layer crack formation at dry, zero current state after 250 AST cycles. When operating at a steady state current density of 750 mA cm^{-2}, significant catalyst layer movement occurred as a result of membrane hygral expansion directly

underneath the GDL/MPL feature as shown in Figure 7.4b. A similar undulation was previously reported by White *et al.* [234] at higher degradation stages where catalyst layer crack opening/closing occurred, however there was no observable GDL/MPL structure related to this movement. Recently, Normile *et al.* [241] observed similar membrane undulation with GDL voids present however no catalyst layer crack observation was described. This shows that the GDL structure can greatly impact membrane movement and catalyst layer crack formation/propagation which can induce further degradation features and losses not only in the catalyst layer but also additional stresses on the membrane and can lead to mechanical fatigue [235]. Under varying RH conditions, the CCM tends to move into sections where the contact pressure is zero i.e. void or clearance between the CCM and the MPL/GDL. Specifically, the clearances under channel portions of the gas flow fields due to the low compressive force are influenced by the GDL/MPL surface shapes. Cycling of this nature generates cracks in the CCL by strain accumulation.

The cathode catalyst layer local porosity distribution was approximately calculated using thickness and greyscale calculation as described by White *et al.* [234] and is shown in Figure 7.5a and b under the dry state after applying dry N_2 for four hours. This method considers the linear attenuation of the catalyst layer from a proposed composition and iteratively updates the composition until the calculated greyscale matches the observed greyscale value at that location. This results in an approximate local composition, with calculated porosity from the measured thickness. A broadening porosity distribution is observed through degradation stages where new high porosity regions are typically observed adjacent to cracks and in regions with minimal thickness change, along with lower porosity regions observed at island centers and areas of severe degradation from thickness collapse. Due to the relatively low sensitivity of X-rays to the ionomer, the absolute porosity value is rather difficult to validate, however these values agree well with previous reports by SEM thickness measurement and mass balance from nominal composition values calculated at 68% porosity at BOL and 53% porosity at EOL [185]. Local changes in porosity were observed between different islands of the catalyst layer solid. This is related to variation in local ionomer content and thickness and could be speculated that local current density may also impact the degradation rate. Observations from these calculated porosity measurements suggest a combined contribution from increase in porosity by corrosion, mainly by expanding cracks and discontinuities, and regions of increased density from reduced thickness by structural collapse, reducing the

rate of further local corrosion. Further discussion and implication of the porosity structure is discussed below from nano-XCT measurements.

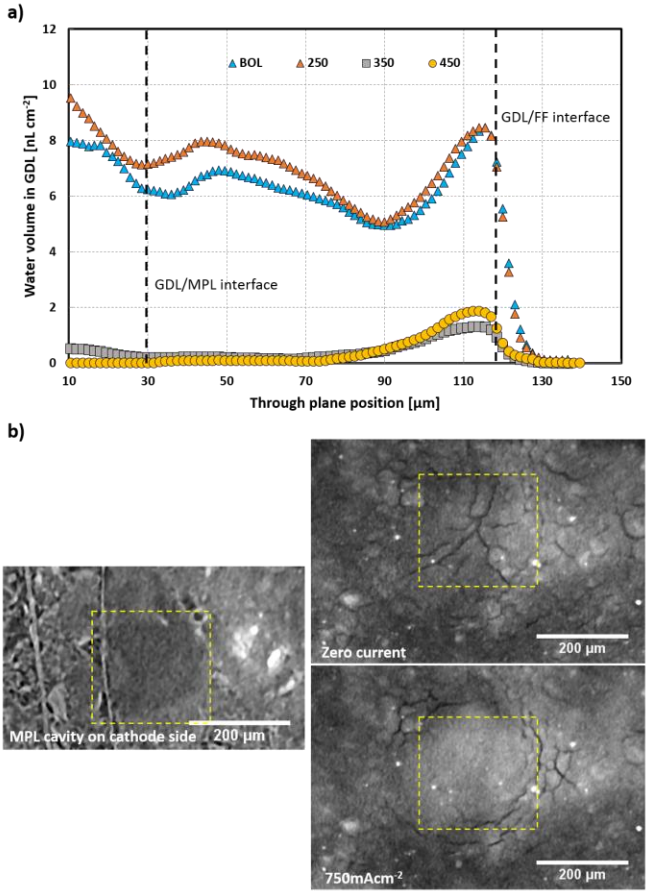

Figure 7.4: Key interactions between cathode catalyst layer degradation and liquid water observed by 4D macro-scale operando imaging: a) liquid water distribution across the cathode GDL (at 750 mA cm^{-2}) from the catalyst layer interface to the flow field plate interface at different stages of degradation; and b) cathode catalyst layer crack opening and closing under dry and wet operating conditions, respectively.

Macro-scale analysis. — Macro-scale *ex situ* XCT imaging was performed to identify regions of interest as well as to determine macro-scale degradation features such as cracks and thickness; thus, was used for surveying as well as quantifying catalyst layer properties at different stages of degradation. The MEA was operated in the small-scale fixture, using the same procedures as for the *operando* analysis described above. After operation, the MEA was removed from the hardware and cut into a triangular shape for micro-XCT imaging, with the tip used as a reference landmark to identify the exact location for the FIB-liftout technique applied to extract a smaller sample for nano-XCT imaging. A

summary of the macro-scale morphological changes as well as the electrochemical surface area (ECSA) and cell voltage is shown in Figure 7.5c as a function of the number of AST cycles. All values were normalized against the corresponding value at BOL since each measurement was taken from a different MEA. The most notable change was in the average crack width, which shows a steep and steady increase during degradation before levelling out at advanced degradation stages. An initial decrease in average crack width was also observed, which is consistent with previous studies, where initiation sites for cracks are formed before propagating and widening following further degradation [24]. The solid area fraction, which considers the number and size of cracks deducted from the total catalyst layer planar area, decreased by 25% from BOL to EOL in accordance with the growth in crack width. This not only impacts the ECSA but also the contact area with the GDL, introducing higher contact resistance. In addition, the observed catalyst layer thinning of up to 50% will also reduce ECSA and increase transport resistance and further voltage loss. The ECSA steadily decreased due to loss of carbon support and Pt agglomeration, in agreement with previous reports [12], [24], [117], [119]. The impact on performance is summarized by observing the change in cell voltage at 750 mA cm^{-2} (full polarization curves are discussed below). The performance was not impacted greatly until late degradation stages where significant voltage losses occurred due to a combination of the aforementioned factors. This demonstrates the balance that can occur within the fuel cell system, where compensation in local areas must occur causing high local current densities to account for other areas which begin to fail. This can lead to high local temperature in areas where the local current density is high and possibly account for water evaporation, reducing the GDL water content, as discussed above. However, the major drop in GDL water content at advanced degradation stages could also be attributed to the crack growth which occurred at the same stages, possibly shifting the local sites of water production in the catalyst layer as well as the liquid water transport pathways within the MEA.

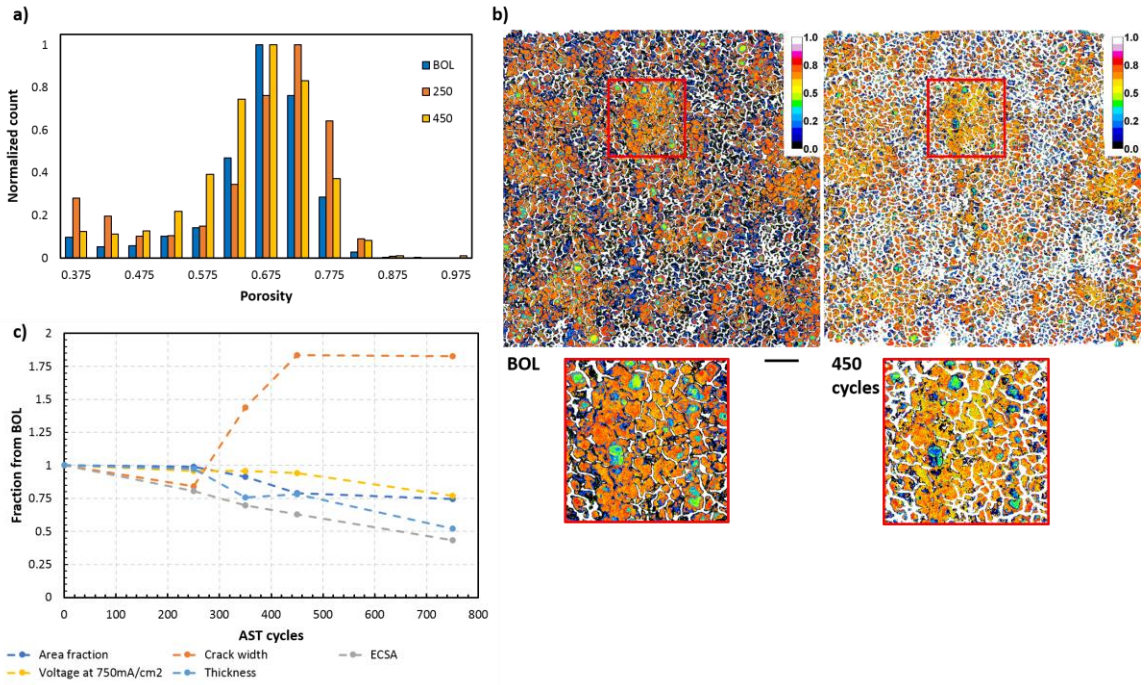

Figure 7.5: Morphological quantification of cathode catalyst layer structure from the 4D macro-scale operando images: a) local porosity distribution calculated by pixel greyscale from XCT and thickness measurement; b) planar map of local porosity values calculated; and c) summary of degradation induced changes in thickness, crack width, solid area fraction, ECSA, and cell voltage at 750 mA cm^{-2}. Scale bar represents 250 µm.

Nano-scale imaging. — Nano-scale *ex situ* imaging was performed on a region of the cathode catalyst layer which showed an average change in thickness as a representative volume of the typical catalyst layer properties. This was selected at a central location away from cracks, as observed by the macro-scale imaging discussed above. To properly ascertain the pore volume of the cathode catalyst layer, an accurate understanding of the resolution limitations is first needed, which has generally not been addressed in previous publications. To be able to perform accurate segmentation, sufficient contrast between two phases is necessary. Hence, having a pixel size of 16 nm or specified spatial resolution of 50 nm does not warrant that images obtained will provide this optimum resolution for the specific sample. The comparison between absorption mode and Zernike phase contrast imaging for the same sample is illustrated in Figure 7.6 a, b and c. A significant difference between the two modes of imaging can be seen, with bright large regions in the absorption image corresponding to high material density (platinum rich/ionomer dense areas), while more crisp structure characterized by dark pores is seen in the phase image. Qualitatively, it is evident from these two images that phase contrast

is needed to obtain accurate pore volume information by the observed additional structure. Small micro-cracks are also observed which extend into the volume. The sub-micrometer cracks are only observable at this high-resolution imaging and could be a precursor for the larger cracks discussed previously.

Composition change. — Adopting absorption imaging mode enables a qualitative understanding of material composition changes. Previously, Venkatesan *et al. of* our research group [242] performed 2D TEM imaging of BOL and EOL cathode catalyst layers that suffered significant carbon corrosion during voltage cycling AST using a lower upper potential of 1.3 V, compared to the 1.4 V used in the present study. Fluorine concentration mapping displayed uniform distribution at BOL, however EOL revealed non-uniformly distributed and large ionomer-rich regions. This non-uniform structure results from the degradation and collapse of the carbon backbone structure within the catalyst layer causing irregular agglomerates to form. Figure 7.6a and b show single slices of the 3D volume obtained in absorption mode which highlights the impact of carbon corrosion within the cathode catalyst layer at each stage of degradation. Similar qualitative behavior to previous TEM results is observed in the present absorption contrast images, over a larger length scale due to the larger field of view of XCT. The solid structure at BOL is much more homogeneous with no abnormalities in structure, except for a micro-crack initiating from the GDL interface. As degradation stages progress, solid structure changes occur. Initiating at 250 cycles, larger regions of solid structure begin to show signs of platinum loss, in particular close to the membrane interface where greyscale pixels are darker, suggesting density decrease from carbon corrosion and platinum loss by dissolution. Other features such as cracks also become present, however in contrast to BOL, show signs for initiation at the membrane interface. Regions of heterogeneity form as localized collapse occurs in conjunction with overall thinning. The most obvious change occurs at 750 cycles, where considerable collapse occurs by the significant change in thickness, accompanied by brighter overall greyscale pixel values than at all preceding stages, again indicating density increase from structural collapse. More prominent solid changes are also observed which agree with the inhomogeneity observed in TEM studies. This also suggests that although different upper potentials are used between the two studies, with a more rapid degradation rate at 1.4 V used here, the features that arise (at EOL) are similar in nature and can be compared to the severity of degradation from carbon corrosion. The bright feature seen in all images shown in Figure 7.6b at the left most edge

is the surface protective Pt coating applied during FIB lift-out. The diffusion depth of the Pt protective coating can be seen to be approximately 1 µm, indicating that the sub-volume region chosen for pore analysis is sufficient to avoid any structural artifacts from the deposited layer.

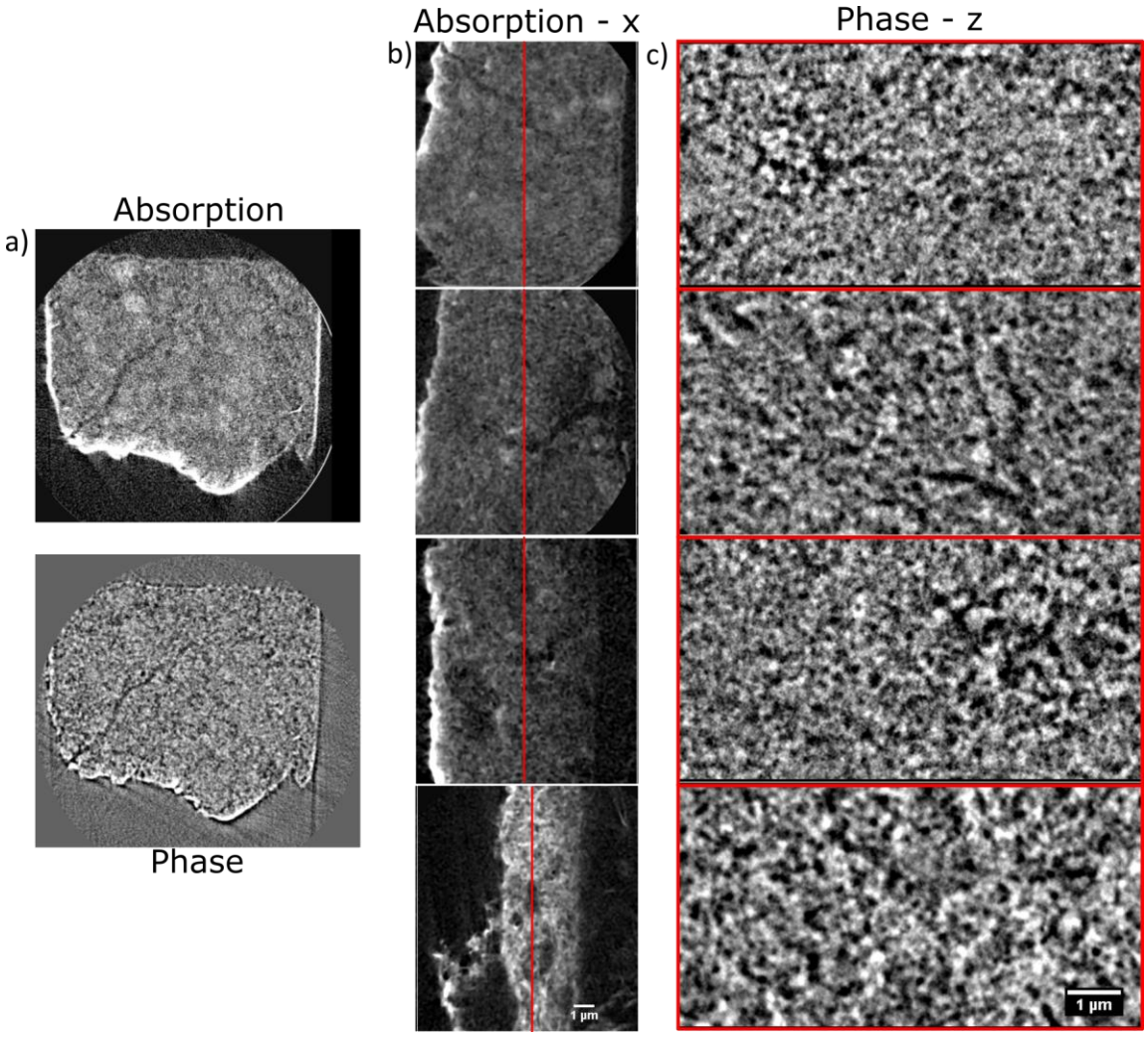

Figure 7.6: Nano-XCT imaging of cathode catalyst layer degradation: a) absorption and phase contrast images of an identical location; b) absorption images from the x-plane showing the through-plane material composition (GDL interface on left; membrane interface on right) at different stages of degradation for BOL, 250, 450, and 750 AST cycles; and c) phase contrast images from the z-plane showing the in-plane porous structure in black. The red line indicates the location of each slice taken.

Porosity and pore-size distribution. — Adoption of nano-scale XCT in phase contrast mode enables the resolution of pores down to 50 nm, allowing for an accurate three-dimensional quantification of cathode catalyst layer structure. The obtained pore

structure was correlated with BOL pore volume determined by MIP. In contrast to MIP, however, the pore structure from nano-XCT represents the exact local information as well as the true three-dimensional structure. As a comparison, the pore size distribution obtained from MIP was analyzed against the segmented pore structure obtained by nano-scale XCT and applied local thickness algorithm in ImageJ, [188] which uses sphere packing to accurately determine the three-dimensional pore and throat size. Additionally, since MIP has limitations in only determining pore structure of those pores connected to the outer surface where the mercury can flow into the structure, a simulated MIP measurement was calculated using Porespy [243] to accurately evaluate the comparison. As shown in Figure 7.7a, the obtained structure from nano-scale XCT simulated for MIP shows excellent agreement with that of the actual MIP pore-size distribution curve. Additionally, when comparing to the actual pore-size distribution from nano-XCT, a different distribution curve is seen which highlights the limitations of MIP measurement in determining the actual, local pore sizes of internal pores that are accessed via smaller throats. This discrepancy is mainly evident in the 80 – 200 nm range of pore sizes. Furthermore, pore structures smaller than the resolution limit of XCT resolved by MIP indicate that the porosity data obtained between these two measurements are not expected to be the same, considering that most of these small pores will be resolved as solid structure in XCT, thus reducing the actual porosity measurement. This is also what is observed where the porosity obtained from MIP is 54% whereas the porosity from nano-scale XCT is 33%. In addition, MIP results likely include pore volume contributions from macroscopic cracks and voids given the considerably larger sample size than for nano-XCT. Similarly, the porosity results previously discussed from *operando* macro-scale XCT imaging and quantification of material composition by grayscale value (GSV) analysis using thickness and mass-balance measurement are generally higher than the nano-XCT data, provided that all pores and cracks/voids are broadly considered. A similar trend was observed by Star *et al.* [200], where a FIB-SEM approach was adopted to obtain the pore structure and porosity calculated by mass-balance. The calculated porosity was significantly higher than the porosity observed by the three-dimensional visualization. This observed difference between macro-scale calculation and nano-scale observation is most likely due to the density values used in the calculation from mass balance and thickness. This suggests that the nano-structure of composite materials may differ from that of their individual parts and highlights the importance of imaging to correlate and validate findings.

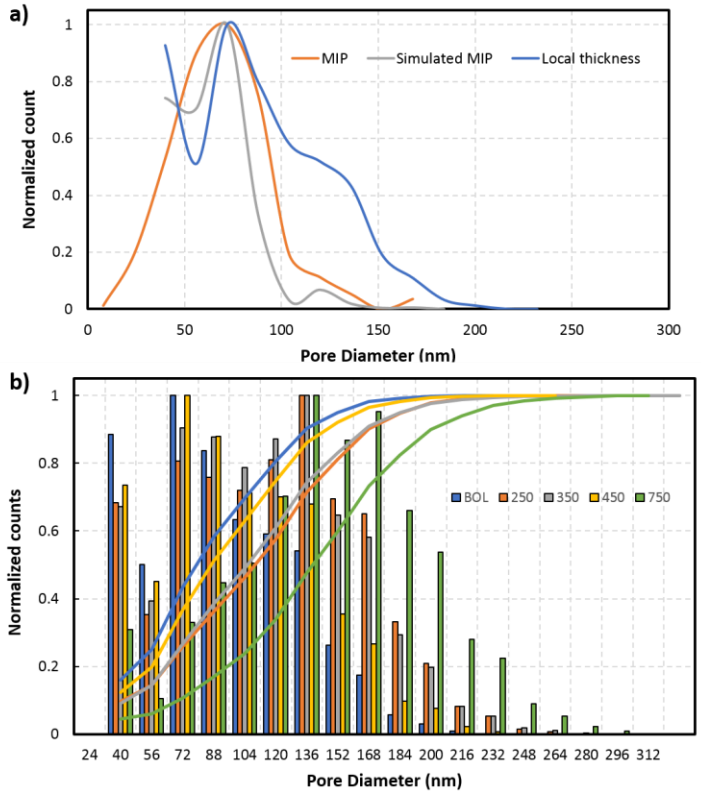

Figure 7.7: Quantification of the catalyst layer porous structure by nano-XCT. a) Comparing nano-XCT collected structure to MIP collected data following segmentation and quantification of pore-size by local thickness [188] as well as with simulation of MIP from Porespy python library [245]. (b) Pore size distribution (bars) and cumulative pore volume (line) for different degradation stages of the cathode catalyst layer obtained using the nano-XCT based local thickness method.

Following validation of the obtained structure by nano-XCT, a comparison of material property changes can be quantified through various degradation stages from BOL to EOL. A combined plot of the pore size distribution and cumulative pore volume is shown for the cathode catalyst layer samples at each degradation stage in Figure 7.7b. The observed changes are generally subtle; however, a general trend can be made. Initially with corrosion there is an increase in pore size (BOL to 250 cycles), followed by a negligible change until 350 cycles. Upon further corrosion (350 to 450 cycles), a major collapse in pore size occurs, leading to significant decrease in the pore size distribution. Another major increase in pore size then occurs from internal corrosion with limited

thickness change until EOL (450 to 750 cycles). This dynamic change can be regarded as a local trend and depends heavily on the local microstructure composition, surrounding compression, water management, crack presence, as well as membrane movement. The samples imaged here were all from the same location within the active area of the fuel cell, under the center land; thus, would subsequently have higher local water content, lower gas and water fluxes, and less membrane movement. A further investigation could be to observe the variations in corrosion stages that occur under different local environments such as land and channel, to account for any possible compositional differences and other local environment conditions that could influence the relative degradation rate. As shown in Table 7.1, the porosity values obtained by nano-XCT visualization agrees well with the trend observed by quantification from GSV and thickness obtained by micro-XCT described above (*Operando imaging*) where the same intermediate state with increase in porosity from partial corrosion was calculated, followed by overall compaction until EOL, further validating this technique when comparing changes with respect to BOL.

Lifetime stage	Porosity by GSV calculation	Porosity by Nano-scale observation
BOL	0.68	0.33
250 cycles	0.70	0.36
EOL	0.67	0.26

Table 7.1: Average porosity values calculated for the cathode catalyst layer at different degradation stages by macro-scale pixel greyscale values (GSV) and nano-scale morphology

Tortuosity, diffusion and performance. — In addition to the pore size and porosity, an important structural property that directly affects performance is the tortuosity. Tortuosity is the ratio of the relative path length required to travel from one side of a structure to the other with respect to a direct path. The more tortuous a structure is, the slower the diffusion rate will be. This can lead to losses by increased mass transport resistance as well as possible flooding. Figure 7.8a displays the tortuosity plotted against the porosity in each principal direction *x*, *y*, and *z*; where *z* is the through-plane direction from membrane to GDL. The tortuosity was calculated using TauFactor, an open-source application available for MATLAB developed by Cooper *et al.* [244]. Significant increase in the tortuosity is observed for the EOL (750 cycles) structure with the lowest porosity. This structure also had the largest pore sizes from the calculated distribution. This corresponds to large disconnected pores. Incidentally, the ratio between non-connected and connected pore volume was measured to be 0.0058 for BOL; however, it almost

doubled to 0.012 at EOL, supporting this hypothesis. Some variation in porosity and tortuosity for other stages of degradation is observed and generally follows the same trend as pore size distribution discussed previously. The Bruggeman relation of $\tau = \varepsilon^{-0.5}$ for particle packing is also shown for reference by the dotted lines in Figure 7.8a. This relation is found to underestimate the tortuosity of the catalyst layer material across all degradation stages, thus warranting more detailed investigation such as the present nano-XCT analysis. It is noted that the through-plane direction (z) consistently has the lowest tortuosity value whereas the in-plane directions (x and y) vary inconsistently.

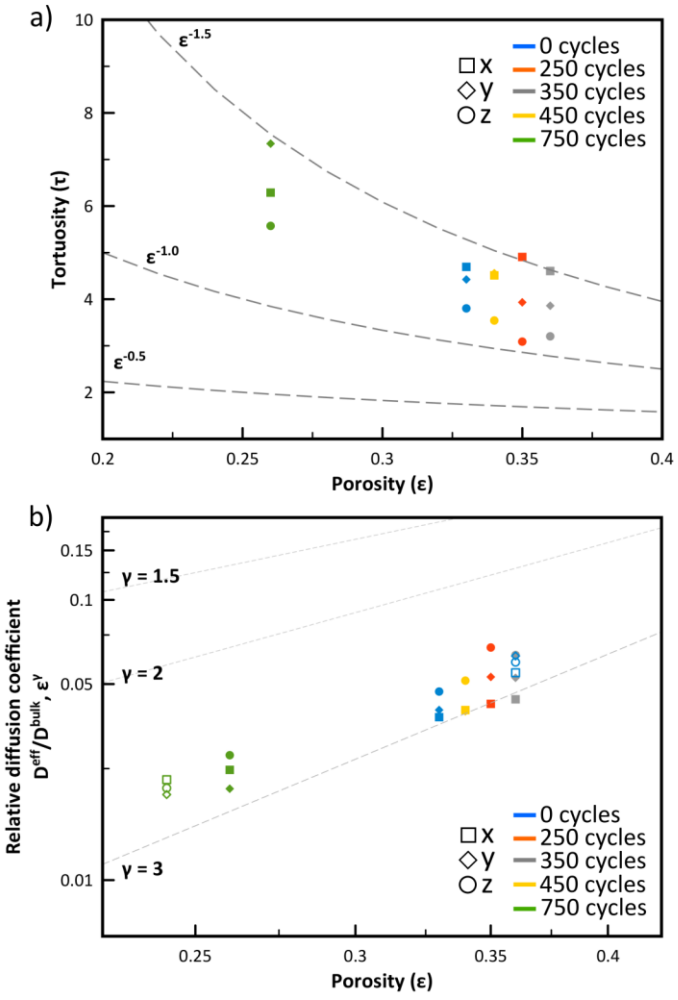

Figure 7.8: Catalyst layer tortuosity (a) and diffusivity ratio (b) calculated from the nano-XCT reconstructed structures at each degradation stage. Tortuosity data were calculated using Taufactor [246] for x, y, and z directions while relative diffusion solid data points were calculated from Equation 7.2 and unfilled data points were calculated from simulation [248], [249]. Dotted lines indicate fitting from Equation 7.2.

The diffusivity ratio is plotted in Figure 7.8b, which considers Knudsen effects for effective diffusion, and can be compared to known structures such as particle packing as described by Inoue *et al.* [245] where:

$$D^R = \frac{D^{\text{eff}}}{D^{\text{bulk}}} = \frac{\varepsilon}{\tau_i}\left(\frac{1}{1+\left(\frac{D^{\text{bulk}}}{D^{\text{k}}}\right)}\right) \tag{7.2}$$

Here, ε is the porosity, τ_i is the tortuosity in direction i, and D^{k} is the Knudsen diffusion coefficient determined using the pore size distribution from nano-XCT. The calculations here are determined using a temperature of 80°C and 2 atm pressure. For the simplified case of neglected Knudsen diffusion, stated here for reference only, this relation becomes $D^R = \frac{\varepsilon}{\tau} = \varepsilon^{\gamma}$ with $\gamma = 1.5$ (based on Bruggeman approximation) and for a purely vertical structure $\gamma = 1$ since $\tau = 1$ [245]. The effective diffusivity was also calculated using a numerical algorithm formulated by El Hannach *et al.* [246], [247] which includes Knudsen diffusion. The obtained results for BOL and EOL (Figure 8b) show good agreement between the calculations from El Hannach *et al.* and Equation 2. These results are considerably lower than those of the Bruggeman approximation, indicating the importance of including the detailed microstructure and Knudsen effects in the calculations. Based on the calculated results, the simplified relationship $\boldsymbol{D^R = \varepsilon^{\gamma}}$ with $\boldsymbol{\gamma = 2.8}$ has the best fit for these catalyst layer structures, and could be used as a less expensive calculation method that combines the impact of Knudsen effects and tortuosity and only requires the porosity to be obtained from XCT images. In addition, the values reside consistently on this linear fit suggesting there is not a significant change in the relative type of structure with degradation, but the decrease in porosity impacts diffusion rather than abrupt changes in structure. Correspondingly, the impact on fuel cell performance is evident in the mass transport loss that occurs at various levels of degradation as shown in Figure 7.9. At early stages of degradation, the main performance losses observed were kinetic in nature and attributed to ECSA loss (see Figure 7.5c) due to partial carbon support corrosion and Pt dissolution and agglomeration. No major ohmic related losses were induced due to the degradation. The mass transport losses, in contrast, were evident at the later stages of degradation after 250 cycles and increased dramatically toward EOL, in general agreement with the trends observed in the diffusivity calculations. The significant impact of loss in carbon support structure affects the diffusion of oxygen to active sites within the catalyst layer and increases the vulnerability for flooding. In addition, crack formation and

propagation on the macro-scale also reduces the active area and can further lead to flooding locations and loss in connectivity. Hence, to reduce the impact on performance, the porous structure should be preserved to assist the gas diffusion in catalyst layers

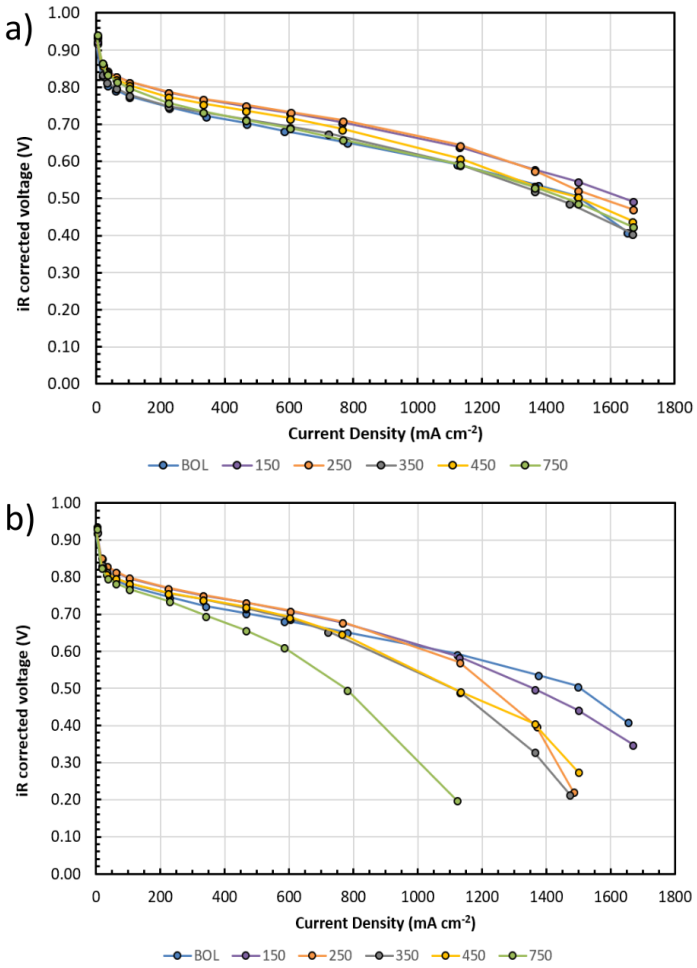

Figure 7.9: Fuel cell polarization (iR – corrected) curves measured for each MEA inside the small-scale fixture: a) BOL data measured for each individual MEA prior to degradation; and b) polarization curves measured after accelerated stress test cycling, but prior to XCT. The legend indicates the number of AST cycles prior to measurement.

Summary

The multi-scale evolution of catalyst layer degradation in fuel cells was characterized using a correlative imaging workflow that combines macro- and nano-scale X-ray computed tomography. This approach allowed for a full-scale visualization of water distribution in operating fuel cells, macro-scale degradation features such as

cracks, and nano-scale structural changes that occur during degradation of fuel cell catalyst layers. From this combined workflow, correlation between the observed performance trends as well as degradation features such as thickness loss and crack formation with nano-scale pore size measurement was presented. Differences between MIP data and the nano-scale XCT obtained structures were identified, and correlation between the two measurements highlighted the need for combined analysis when presenting models using experimental inputs. Localized degradation features such as nano-scale cracks and internal pore-size distribution changes were resolved in three dimensions using nano-XCT and tracked through degradation stages using the 3+1D approach. The dynamic morphology changes of the porous structure showed non-linear trends and were likely influenced by the local environment; however, these changes could still be generalized in terms of internal particle corrosion or collapse of solid structure. Further pore phase model calculations revealed a significant rise in tortuosity accompanied by a drop in Knudsen-dominated diffusivity primarily attributed to reduced catalyst layer porosity resulting from corrosion induced collapse and compaction of the material at an advanced stage of degradation. Increased catalyst layer crack area and reduced active area were also determined during this process. Catalyst layer crack formation was also observed at intermediate degradation stages, originating from hydration induced buckling of the catalyst coated membrane, while crack growth was attributed to local corrosion and liquid water dynamics. This was correlated to a sizable drop in fuel cell performance at the same degradation stage and associated with increasing mass transport losses due to highly constrained oxygen diffusion in the degraded structure. An empirical relationship between porosity, tortuosity, and diffusivity ratio was established based on the observed structural changes with degradation in order to aid future work. Overall, the morphological changes observed in relation to macro-scale cracks and thinning as well as the nano-scale changes in the porous structure were linked to overall performance loss by advancing changes to gas diffusion properties, potential liquid water flooding, increased local temperature, reduced connectivity of both solid and pore phases, and delamination and buckling. By combining an overview macroscale analysis with nanoscale analysis, this clarifies these local differences and we can understand more clearly the various complex facets of catalyst layer degradation. Future work on more precise local environmental impacts such as land vs. channel or crack edge vs. internal structure as well as regions of high vs. low current density will help obtain a comprehensive understanding on local catalyst layer

degradation and its specific origins. Although its primary intended purpose is for durability investigations, the correlative multiscale characterization method developed in this work and its associated results could also be employed for catalyst layer design and computational modeling of fuel cells.

Chapter 8. Conclusions and Recommendations

The work presented in this thesis introduces the application of lab-based X-ray Computed Tomography in the investigation of cathode catalyst layer degradation in Polymer Electrolyte Fuel Cells. By means of developing a novel small-scale fuel cell fixture that mimics the performance and degradation features of a full-scale PEFC assembly, unique insight into the dynamics and interactions between PEFC components was obtained.

Lab-based XCT provides a unique opportunity to investigate time-resolvable changes in an evolving system by allowing for unhindered access to XCT imaging; compared to synchrotron XCT where investigations requiring extended beamline time over weeks or months is unachievable due to the very limited availability and high cost. First, prototyping of various fixture designs was investigated which incorporated the application of computer aided design and 3D printing to achieve rapid prototyping and development. Through consideration of previous work and customization pertaining to unique design requirements, the result allowed for *in-situ* visualization of a full MEA assembly by lab-based XCT. In addition, the use of 3D printing to obtain a working fuel cell device showed additional promise for future revision and customization to unique flow field designs, only achievable by additive manufacturing process. By presenting an *in-situ* visualization workflow, investigation into the water distribution through the GDL with average porosity and saturation values on the order of 80% and 20% respectively were obtained. In addition, liquid water condensation at the catalyst layer surface was observed for the first-time using lab-based XCT with an approximate droplet diameter of 20 µm and liquid water area coverage of 17%. Furthermore, dynamic changes following membrane swelling by 25% through the absorption of water were resolved which identified considerations for future investigation when considering catalyst layer damage features, such as cracking. This work was published in the *Journal of Electrochemical Society* as well as presented at the *Electrochemical Society* international conference.

Limitations to this 3D printed material fixture however were associated with the plastic material used as it limited performance and application of cyclic voltage ASTs to study catalyst layer degradation. To this end, the same fixture design was instead fabricated out of standard flow field material of compressed carbon/graphite with cured

resin using CNC. This final iteration of the small-scale fixture was used for all future experiments, as well as made into several copies to allow for other PhD students involved with the project to use for their own research. Due to the extended imaging time required for *in-situ* experiments which allow for temporal investigations of PEFC degradation, additional testing into the impact of X-rays of the material properties was employed. This work was investigated first for the cathode catalyst layer and separately for the membrane, in collaboration with *Y. Singh* and *D. Ramani.* Upon investigation it was shown that negligible impact is expected from X-ray exposure upwards to 100 hours for catalyst layer studies and up to 50 hours or more for the membrane. These results were an important validation for future work, and emphasis is also placed upon other works which do not consider the possible impact of ionizing X-ray radiation where necessary. These works were published in *Journal of Electrochemical Society* and *Journal of Power Sources*.

The application of using the developed small-scale fixture toward four-dimensional *in-situ* investigation into cathode catalyst layer degradation by carbon corrosion was investigated for the first time and published in *Journal of Power Sources*. The results were correlated to standard MEA testing with validation of the proposed small-scale fixture and four-dimensional *in-situ* workflow by electrochemical measurements. In addition, a novel image processing workflow allowing for the accurate segmentation of the cathode catalyst layer was used to obtain quantitative information of the morphological changes following degradation. A gradual progression in cathode catalyst layer thinning up to 40% was measured. The thinning was correlated to a gradual increase in density by collapse of the carbon support structure; as observed by changes in relative attenuation of incident X-ray beam by the cathode catalyst layer from beginning-of-life to end-of-life. Analysis comparing specific regions under land and channel were also discussed for the first time using the *in-situ* approach. A higher rate of degradation under the channel was observed and was attributed to the higher local reaction rates and higher rates of water production and erosion under the channels. Finally, identical-location tracking of individual cathode catalyst layer cracks was demonstrated for the first time. Both formation of new cracks and propagation/growth of existing cracks were observed over time. Local variation in the relative attenuation of the X-ray beam suggested that regions with high vulnerability to corrosion exist by variation in cathode catalyst layer properties following fabrication as shown by crack initiation and propagation. These morphological changes observed were also shown to be in good agreement with the gradually increasing losses in fuel cell

performance, as well as the distinct decay trend in electrochemical double layer capacitance. This demonstrated a clear correlation between conventional *in-situ* diagnostics by standard MEA testing and newly presented XCT results: severe carbon corrosion, responsible for losses in electrode capacitance and mass transport performance, manifests itself in the form of catalyst layer thinning, crack growth and overall compaction of the remaining porous solid phase, and triggers eventual electrode failure. The additional local information and observation of crack initiation and growth as well as discrepancy between land and channel behaviour were all unique insights provided by XCT.

The insight provided by these *in-situ* studies, and the need to better understand the role of liquid water in the catalyst layer corrosion process, provided the motivation to further develop the small-scale fixture workflow to allow for *operando* imaging. The main hardware challenge in this configuration is cable and tubing management, as well as the hygrothermal equilibration of inlet gases and small-scale fixture. Due to the long gas lines needed, heated tubing was employed for the inlet gas lines, however these still proved insufficient with condensation still heavily occurring. The mitigation for this was to use room temperature gas and also operate the small-scale fixture at room temperature. This allowed for minimal water vapour input into the system as well as a less convoluted investigation into the liquid water channels produced by the operating fuel cell, as these were the only transient liquid water pathways visualized. Results obtained in this manner were still consistent to observations at typical elevated temperature. In future investigations, a strategy could be to have a humidification system for the input gas lines inside the XCT enclosure, close to the inlet into the small-scale fixture. This would minimize condensation and improve temperature equilibrium at a higher operating range. Safety was another major consideration as hydrogen gas was flowing into an enclosed chamber with the possibility for a combustion event. Investigation into the rate of gas turnover inside the enclosed XCT chamber was performed as well as the set-up of a hydrogen sensor and shutdown procedure to ensure that combustive conditions are never reached. In addition, it was found that high levels of UV are produced by either the X-ray source or scattering events upon interaction of the X-rays with material in the beam path. For this reason, a smoke detector was installed instead of a UV detector which is typically used. These preventative hazard assessment investigations not only allowed for the safe operation of the small-scale fuel cell fixture inside the XCT system, but also paved the way

for future environmental chamber standards that may be used in future projects of this type.

For the first time, combined visualization of CL degradation stages and water distribution in PEFCs was presented. Upon applying an AST to simulate possible cathode potential swings during PEFC operation, degradation of the CL from corrosion of carbon support was observed. In addition, visualization and quantification of water distribution in the fuel cell was obtained at varying current density. Surprisingly, at the end-of-life stage, liquid water in the GDL was no longer present at moderate to high current densities, which indicates evaporation due to heat generation. In addition, catalyst layer movement from stresses applied by membrane swelling by water absorption was visualized and shown to increase significantly at advanced stages of cathode degradation. This is hypothesized to occur as a result of catalyst layer flooding, in addition to crack formation allowing for areas with which liquid water can accumulate and cause the membrane to swell, resulting in undulations by local stresses. Additional degradation features such as separation of the CL from the MPL as well as CL crack opening and closing was observed. These degradation features will inhibit proper water removal from near the CL leading to additional performance losses. Quantification of CL composition change by calculation from pixel greyscale values obtained by XCT was also presented by a unique image processing model developed in this work and showed excellent agreement with carbon loss from carbon corrosion as measured by CO_2 exhaust gas monitoring. From the combined visualization of water distribution in the GDL as well as *operando* visualization of the CL features and expansion behavior of the membrane, a strong interplay between MEA components was presented in operating fuel cells. This work was published in *Scientific Reports* as well as presented at *Microscopy and Microanalysis* international conference; earning a student research award presented by *Microscopy Society of America*, as well as an award for best presentation by the *Microscopical Society of Canada*.

Following the development of *operando* imaging, multi-scale correlative imaging by integrating the use of both macro- and nano-scale X-ray computed tomography allowed for a full-scale visualization of water distribution in operating fuel cells, macro-scale degradation features such as cracks, and nano-scale structural changes that occur during carbon corrosion in fuel cell catalyst layers. From this combined workflow, correlation between the observed performance trends as well as degradation features such as

thickness loss and crack formation with nano-scale pore size measurement and diffusivity was presented. Differences between MIP data and the structure visualized by nano-scale XCT were identified, and correlation between the two measurements highlighted the need for combined analysis when presenting models using experimental inputs. The dynamic morphology changes of the porous structure showed non-linear trends and were likely influenced by the local environment; however, these changes could still be generalized in terms of internal particle corrosion or collapse of solid structure. Further pore phase model calculations revealed a significant rise in tortuosity accompanied by a drop in Knudsen-dominated diffusivity primarily attributed to reduced catalyst layer porosity resulting from corrosion induced collapse and compaction of the material at advanced stages of degradation. An empirical relationship between porosity, tortuosity, and diffusivity ratio was established based on the observed structural changes with degradation in order to aid further work. Overall, the morphological changes observed in relation to macro-scale cracks and thinning as well as the nano-scale changes in the porous structure were linked to overall performance loss by advancing changes to gas diffusion properties, potential liquid water flooding, increased local temperature, reduced connectivity of both solid and pore phases, and delamination and buckling. Future work on more precise local environment impact such as land vs. channel or crack edge vs. internal structure as well as regions of high vs. low current density will help obtain a comprehensive understanding on local catalyst layer degradation and its specific origins. The workflow presented can be used to target such specific locations and correlate between *operando* imaging and *ex-situ* nano-scale visualization.

Additional future work should be focused on understanding the nano-scale morphological changes, as these are primary inputs into computation models and can be used to predict lifetime, as well as investigate new catalyst layer designs, since a high correlation to the overall catalyst layer structure and performance has been shown in the presented work. Investigations into different catalyst layer materials and degradation studies similar to those performed in this thesis could be applied, such as toward low-Pt/PGM free electrodes. In addition, with the development of more advanced 3D printing technologies, studies into alternative catalyst layer and MEA architectures, such as patterned GDLs with specific hydrophobic and hydrophilic locations, or stratified cathode catalyst layers can be studied using this workflow potentially unlocking new higher performance and cheaper fuel cell materials. Additionally, many other electrochemical

devices such as electrolysis cells could also be investigated using similar workflow with extracted morphological details for accurate modeling.

As presented by this thesis, catalyst layer crack initiation and growth is an interesting phenomenon which plays a significant role in many aspects of the dynamic behavior. Questions remain on the over-all interactive nature between GDL and membrane surrounding these cracks and possible ways of mitigation since these are related to further degradation features and performance losses. Investigating different fabrication methods and materials will help elucidate possible mitigation strategies.

References

[1] A. Chrisafis and A. Vaughan, “France to ban sales of petrol and diesel cars by 2040 | Business | The Guardian,” *The Guardian*, 2017. [Online]. Available: https://www.theguardian.com/business/2017/jul/06/france-ban-petrol-diesel-cars-2040-emmanuel-macron-volvo. [Accessed: 15-Oct-2017].

[2] S. Swinford, “Diesel and petrol car ban: Plan for 2040 unravels as 10 new power stations needed to cope with electric revolution,” *The Telegraph*, 2017. [Online]. Available: http://www.telegraph.co.uk/news/2017/07/25/new-diesel-petrol-cars-banned-uk-roads-2040-government-unveils/. [Accessed: 15-Oct-2017].

[3] Ballard, “Markets - Fuel Cell Technology Solutions.” [Online]. Available: http://ballard.com/markets. [Accessed: 07-Jan-2018].

[4] “Transportation — Fuel Cell & Hydrogen Energy Association,” *Fuel Cell and Hydrogen Energy Association*. [Online]. Available: http://www.fchea.org/transportation. [Accessed: 15-Oct-2017].

[5] “Conferences | International Hydrail Conference | Appalachian State University.” [Online]. Available: https://hydrail.appstate.edu/conferences. [Accessed: 15-Oct-2017].

[6] Y. Wang, K. S. Chen, J. Mishler, S. C. Cho, and X. C. Adroher, “A review of polymer electrolyte membrane fuel cells: Technology, applications, and needs on fundamental research,” *Appl. Energy*, vol. 88, no. 4, pp. 981–1007, 2011.

[7] C. Santoro, C. Arbizzani, B. Erable, and I. Ieropoulos, “Microbial fuel cells: From fundamentals to applications. A review,” *J. Power Sources*, vol. 356, pp. 225–244, 2017.

[8] A. Choudhury, H. Chandra, and A. Arora, “Application of solid oxide fuel cell technology for power generation - A review,” *Renewable and Sustainable Energy Reviews*, vol. 20. pp. 430–442, 2013.

[9] P. R. Shearing *et al.*, “Using synchrotron X-Ray nano-CT to characterize SOFC electrode microstructures in three-dimensions at operating temperature,” *Electrochem. solid-State Lett.*, vol. 14, no. 10, pp. B117–B120, 2011.

[10] S. Tsushima and S. Hirai, “In situ diagnostics for water transport in proton exchange membrane fuel cells,” *Prog. Energy Combust. Sci.*, vol. 37, no. 2, pp. 204–220, 2011.

[11] A. Tavassoli *et al.*, “Effect of catalyst layer defects on local membrane degradation in polymer electrolyte fuel cells,” *J. Power Sources*, vol. 322, pp. 17–25, 2016.

[12] S. Zhang *et al.*, “A review of platinum-based catalyst layer degradation in proton exchange membrane fuel cells,” *J. Power Sources*, vol. 195, no. 4, pp. 1142–1148, 2010.

[13] Q. Meyer *et al.*, “Investigation of Hot Pressed Polymer Electrolyte Fuel Cell Assemblies via X-ray Computed Tomography,” *Electrochim. Acta*, vol. 242, pp. 125–136, 2017.

[14] P. Satjaritanun, “Micro-Scale Analysis of Liquid Water Breakthrough inside Gas Diffusion Layer for PEMFC Using X-ray Computed Tomography and Lattice Boltzmann Method,” *J. Electrochem. Soc.*, vol. 164, no. 11, pp. E3359–E3371, 2017.

[15] M. A. Safi, N. I. Prasianakis, J. Mantzaras, A. Lamibrac, and F. N. Büchi, “Experimental and pore-level numerical investigation of water evaporation in gas diffusion layers of polymer electrolyte fuel cells,” *Int. J. Heat Mass Transf.*, vol. 115, pp. 238–249, 2017.

[16] J. Eller, J. Roth, F. Marone, M. Stampanoni, and F. N. Büchi, “Operando Properties of Gas Diffusion Layers: Saturation and Liquid Permeability,” *J. Electrochem. Soc.*, vol. 164, no. 2, pp. F115–F126, 2017.

[17] M. G. George *et al.*, “Accelerated Degradation of Polymer Electrolyte Membrane Fuel Cell Gas Diffusion Layers I,” *J. Electrochem. Soc.*, vol. 164, no. 7, pp. F714–F721, 2017.

[18] Y. Singh, R. M. H. Khorasany, A. Sadeghi Alavijeh, E. Kjeang, G. G. Wang, and R. K. N. D. Rajapakse, “Ex situ measurement and modelling of crack propagation in fuel cell membranes under mechanical fatigue loading,” *Int. J. Hydrogen Energy*, vol. 42, pp. 19257–19271, 2017.

[19] Y. Singh, F. P. Orfino, M. Dutta, and E. Kjeang, “3D visualization of membrane failures in fuel cells,” *J. Power Sources*, vol. 345, pp. 1–11, 2017.

[20] F. C. Cetinbas *et al.*, “Hybrid approach combining multiple characterization techniques and simulations for microstructural analysis of proton exchange membrane fuel cell electrodes,” *J. Power Sources*, vol. 344, pp. 62–73, 2017.

[21] I. V. Zenyuk *et al.*, “Investigating Evaporation in Gas Diffusion Layers for Fuel Cells with X-ray Computed Tomography,” *J. Phys. Chem. C*, vol. 120, no. 50, pp. 28701–28711, 2016.

[22] S. Malik, L. Smith, J. Sharman, E. M. Holt, and S. P. Rigby, “Pore Structural Characterization of Fuel Cell Layers Using Integrated Mercury Porosimetry and Computerized X-ray Tomography,” *Ind. Eng. Chem. Res.*, vol. 55, pp. 10850–10859, 2016.

[23] T. Agaesse, A. Lamibrac, F. N. Büchi, J. Pauchet, and M. Prat, “Validation of pore network simulations of ex-situ water distributions in a gas diffusion layer of proton exchange membrane fuel cells with X-ray tomographic images,” *J. Power Sources*, vol. 331, pp. 462–474, 2016.

[24] R. T. White, A. Wu, M. Najm, F. P. Orfino, M. Dutta, and E. Kjeang, “4D in situ visualization of electrode morphology changes during accelerated degradation in fuel cells by X-ray computed tomography,” *J. Power Sources*, vol. 350, pp. 94–102, 2017.

[25] Q. Meyer *et al.*, “Effect of gas diffusion layer properties on water distribution across air-cooled, open-cathode polymer electrolyte fuel cells: A combined ex-situ X-ray tomography and in-operando neutron imaging study,” *Electrochim. Acta*, vol. 211, pp. 478–487, 2016.

[26] S. Prass, S. Hasanpour, P. K. Sow, A. B. Phillion, and W. Mérida, “Microscale X-ray tomographic investigation of the interfacial morphology between the catalyst and micro porous layers in proton exchange membrane fuel cells,” *J. Power Sources*, vol. 319, pp. 82–89, 2016.

[27] W. K. Epting, J. Gelb, and S. Litster, “Resolving the three-dimensional microstructure of polymer electrolyte fuel cell electrodes using nanometer-scale X-ray computed tomography,” *Adv. Funct. Mater.*, vol. 22, no. 3, pp. 555–560, 2012.

[28] S. Chevalier *et al.*, “In operando measurements of liquid water saturation distributions and effective diffusivities of polymer electrolyte membrane fuel cell gas diffusion layers,” *Electrochim. Acta*, vol. 210, pp. 792–803, 2016.

[29] A. Pokhrel *et al.*, “Failure analysis of fuel cell electrodes using three-dimensional multi-length scale X-ray computed tomography,” *J. Power Sources*, vol. 329, pp. 330–338, 2016.

[30] M. Andisheh-Tadbir, F. P. Orfino, and E. Kjeang, “Three-dimensional phase segregation of micro-porous layers for fuel cells by nano-scale X-ray computed tomography,” *J. Power Sources*, vol. 310, pp. 61–69, 2016.

[31] D. Kennouche, Y. K. Chen-Wiegart, C. Riscoe, J. Wang, and S. A. Barnett, “Combined electrochemical and X-ray tomography study of the high temperature evolution of Nickel – Yttria Stabilized Zirconia solid oxide fuel cell anodes,” *J. Power Sources*, vol. 307, pp. 604–612, 2016.

[32] S. Komini Babu, H. T. Chung, P. Zelenay, and S. Litster, “Resolving Electrode Morphology’s Impact on Platinum Group Metal-Free Cathode Performance Using Nano-CT of 3D Hierarchical Pore and Ionomer Distribution,” *ACS Appl. Mater. Interfaces*, vol. 8, no. 48, p. 32764−32777, 2016.

[33] P. A. García-Salaberri, G. Hwang, M. Vera, A. Z. Weber, and J. T. Gostick, “Effective diffusivity in partially-saturated carbon-fiber gas diffusion layers: Effect of through-plane saturation distribution,” *Int. J. Heat Mass Transf.*, vol. 86, pp. 319–333, 2015.

[34] S. Odaya, R. K. Phillips, Y. Sharma, J. Bellerive, A. B. Phillion, and M. Hoorfar, “X-ray tomographic analysis of porosity distributions in gas diffusion layers of proton exchange membrane fuel cells,” *Electrochim. Acta*, vol. 152, pp. 464–472, 2015.

[35] J. Lee *et al.*, “Investigating the effects of gas diffusion layer substrate thickness on polymer electrolyte membrane fuel cell performance via synchrotron X-ray radiography,” 2017.

[36] F. C. Cetinbas *et al.*, “Microstructural Analysis and Transport Resistances of Low-Platinum-Loaded PEFC Electrodes,” *J. Electrochem. Soc.*, vol. 164, no. 14, pp. F1596–F1607, 2017.

[37] N. Ge *et al.*, “Calibrating the X-ray attenuation of liquid water and correcting sample movement artefacts during in operando synchrotron X-ray radiographic imaging of polymer electrolyte membrane fuel cells,” *J. Synchrotron Radiat.*, vol. 23, no. 2, pp. 590–599, 2016.

[38] P. Antonacci, S. Chevalier, J. Lee, R. Yip, N. Ge, and A. Bazylak, “Feasibility of combining electrochemical impedance spectroscopy and synchrotron X-ray radiography for determining the influence of liquid water on polymer electrolyte membrane fuel cell performance,” 2015.

[39] O. F. Selamet, P. Deevanhxay, S. Tsushima, and S. Hirai, “Investigation of gas generation in regenerative fuel cells by low-energy X-rays,” *J. Power Sources*, vol. 296, pp. 133–141, 2015.

[40] I. Mayrhuber, F. Marone, M. Stampanoni, T. J. Schmidt, and F. N. Büchi, “Fast X-ray Tomographic Microscopy: Investigating Mechanisms of Performance Drop during Freeze Starts of Polymer Electrolyte Fuel Cells,” *ChemElectroChem*, vol. 2, no. 10, pp. 1551–1559, 2015.

[41] S. Hasanpour, M. Hoorfar, and A. B. Phillion, “Different Methods for Determining Porosity of Gas Diffusion Layer using X-ray Microtomography,” *Electrochim. Acta*, vol. 185, pp. 34–39, 2015.

[42] M. Santini *et al.*, “Three-dimensional X-ray microcomputed tomography of carbonates and biofilm on operated cathode in single chamber microbial fuel cell,” *Biointerphases*, vol. 10, no. 3, p. 031009, 2015.

[43] I. V. Zenyuk, D. Y. Parkinson, G. Hwang, and A. Z. Weber, “Probing water distribution in compressed fuel-cell gas-diffusion layers using X-ray computed tomography,” *Electrochem. commun.*, vol. 53, pp. 24–28, 2015.

[44] P. Mandal, B. K. Hong, J.-G. Oh, and S. Litster, “3D Imaging of Fuel Cell Electrode Structure Degraded under Cell Voltage Reversal Conditions Using Nanoscale X-Ray Computed Tomography,” *ECS Trans.*, vol. 69, no. 17, pp. 443–453, 2015.

[45] M. Bosomoiu, G. Tsotridis, and T. Bednarek, “Study of effective transport properties of fresh and aged gas diffusion layers,” *J. Power Sources*, vol. 285, 2015.

[46] T. M. M. Heenan, D. J. L. Brett, and P. R. Shearing, “Uncovered Mapping electrochemical activity in solid oxide fuel cells X-ray nano computed tomography of heterogeneous microstructures,” *Mater. Today*, vol. 20, no. 3, 2017.

[47] P. Deevanhxay, T. Sasabe, K. Minami, S. Tsushima, and S. Hirai, “Oblique soft X-ray tomography as a non-destructive method for morphology diagnostics in degradation of proton-exchange membrane fuel cell,” *Electrochim. Acta*, vol. 135, pp. 67–76, 2014.

[48] S. H. Eberhardt, F. Marone, M. Stampanoni, F. N. B??chi, and T. J. Schmidt, “Quantifying phosphoric acid in high-temperature polymer electrolyte fuel cell components by X-ray tomographic microscopy,” *J. Synchrotron Radiat.*, vol. 21, no. 6, pp. 1319–1326, 2014.

[49] T. Sakamoto, P. Deevanhxay, K. Asazawa, S. Tsushima, S. Hirai, and H. Tanaka, “In-situ visualization of N2 evolution in operating direct hydrazine hydrate fuel cell by soft X-ray radiography,” *J. Power Sources*, vol. 252, pp. 35–42, 2014.

[50] T. Arlt *et al.*, “Synchrotron X-ray radioscopic in situ study of high-temperature polymer electrolyte fuel cells - Effect of operation conditions on structure of membrane,” *J. Power Sources*, vol. 246, pp. 290–298, 2014.

[51] N. Khajeh-Hosseini-Dalasm, T. Sasabe, T. Tokumasu, and U. Pasaogullari, “Effects of polytetrafluoroethylene treatment and compression on gas diffusion layer microstructure using high-resolution X-ray computed tomography,” *J. Power Sources*, vol. 266, pp. 213–221, 2014.

[52] J. Eller and F. N. Büchi, “Polymer electrolyte fuel cell performance degradation at different synchrotron beam intensities,” *J. Synchrotron Radiat.*, vol. 21, no. 1, pp. 82–88, 2014.

[53] T. Arlt *et al.*, “Influence of Artificial Aging of Gas Diffusion Layers on the Water Management of PEM Fuel Cells,” *ECS Electrochem. Lett.*, vol. 3, no. 2, pp. F7–F9, 2014.

[54] D. Froning, W. Maier, J. Groß, T. Arlt, I. Manke, and W. Lehnert, “Evaluation of structural changes of HT-PEFC electrodes from in-situ synchrotron X-ray radiographs,” *Int. J. Hydrogen Energy*, vol. 39, no. 17, pp. 9447–9456, 2014.

[55] A. Pfrang, S. Didas, and G. Tsotridis, “X-ray computed tomography of gas diffusion layers of PEM fuel cells: Segmentation of the microporous layer,” *J. Power Sources*, vol. 235, pp. 81–86, 2013.

[56] S. Litster, W. K. Epting, E. A. Wargo, S. R. Kalidindi, and E. C. Kumbur, “Morphological analyses of polymer electrolyte fuel cell electrodes with nano-scale computed tomography imaging,” *Fuel Cells*, vol. 13, no. 5, pp. 935–945, 2013.

[57] T. M. M. Heenan *et al.*, “Three-Phase Segmentation of Solid Oxide Fuel Cell Anode Materials Using Lab Based X-ray Nano-Computed Tomography,” *Fuel Cells*, vol. 17, no. 1, pp. 75–82, 2017.

[58] J. Roth, J. Eller, F. Marone, and F. N. Büchi, “Investigation of the Representative Area of the Water Saturation in Gas Diffusion Layers of Polymer Electrolyte Fuel Cells,” *J. Phys. Chem. C*, vol. 117, no. 49, pp. 25991–25999, 2013.

[59] H. Markötter *et al.*, “Influence of cracks in the microporous layer on the water distribution in a PEM fuel cell investigated by synchrotron radiography,” *Electrochem. commun.*, vol. 34, pp. 22–24, 2013.

[60] E. A. Wargo, T. Kotaka, Y. Tabuchi, and E. C. Kumbur, “Comparison of focused ion beam versus nano-scale X-ray computed tomography for resolving 3-D microstructures of porous fuel cell materials,” *J. Power Sources*, vol. 241, pp. 608–618, 2013.

[61] A. Schröder *et al.*, “Water evolution in direct methanol fuel cell cathodes studied by synchrotron X-ray radiography,” *Fuel Cells*, vol. 13, no. 3, pp. 371–379, Jun. 2013.

[62] P. Deevanhxay, T. Sasabe, S. Tsushima, and S. Hirai, “Observation of dynamic liquid water transport in the microporous layer and gas diffusion layer of an operating PEM fuel cell by high-resolution soft X-ray radiography,” *J. Power Sources*, vol. 230, pp. 38–43, 2013.

[63] S.-G. Kim and S.-J. Lee, “A review on experimental evaluation of water management in a polymer electrolyte fuel cell using X-ray imaging technique,” *J. Power Sources*, vol. 230, pp. 101–108, 2013.

[64] G. S. Hwang, D. Y. Parkinson, A. Kusoglu, A. A. MacDowell, and A. Z. Weber, “Understanding water uptake and transport in Nafion using X-ray microtomography,” *ACS Macro Lett.*, vol. 2, no. 4, pp. 288–291, 2013.

[65] T. Takeda *et al.*, “Phase-Contrast X-ray Images of Ice and Water on Carbon Paper for Fuel Cells Measured by Diffraction-Enhanced Imaging Technique,” *Jpn. J. Appl. Phys*, vol. 52, 2013.

[66] R. Quey, H. Suhonen, J. Laurencin, P. Cloetens, and P. Bleuet, “Direct comparison between X-ray nanotomography and scanning electron microscopy for the microstructure characterization of a solid oxide fuel cell anode,” *Mater. Charact.*, vol. 78, pp. 87–95, 2013.

[67] E. A. Wargo, V. P. Schulz, A. Çeçen, S. R. Kalidindi, and E. C. Kumbur, “Resolving macro- and micro-porous layer interaction in polymer electrolyte fuel cells using focused ion beam and X-ray computed tomography,” *Electrochim. Acta*, vol. 87, pp. 201–212, 2013.

[68] R. Banerjee *et al.*, “Transient Liquid Water Distributions in Polymer Electrolyte Membrane Fuel Cell Gas Diffusion Layers Observed through In-Operando Synchrotron X-ray Radiography,” *J. Electrochem. Soc.*, vol. 164, no. 2, pp. F154–F162, 2017.

[69] O. F. Selamet, P. Deevanhxay, S. Tsushima, and S. Hirai, “Visualization of gas bubble behavior of a regenerative fuel cell in electrolysis mode by soft X-ray radiography.,” *ECS Trans.*, vol. 58, no. 1, Polymer Electrolyte Fuel Cells 13, p. 353–360, 8 pp., 2013.

[70] J. P. James, H.-W. Choi, and J. G. Pharoah, “X-ray computed tomography reconstruction and analysis of polymer electrolyte membrane fuel cell porous transport layers,” *Int. J. Hydrogen Energy*, vol. 37, no. 23, pp. 18216–18230, 2012.

[71] G. J. Nelson *et al.*, “Three-dimensional microstructural changes in the Ni-YSZ solid oxide fuel cell anode during operation,” *Acta Mater.*, vol. 60, no. 8, pp. 3491–3500, 2012.

[72] K. Yakal-Kremski, J. S. Cronin, Y.-C. K. Chen-Wiegart, J. Wang, and S. A. Barnett, “Studies of Solid Oxide Fuel Cell Electrode Evolution Using 3D Tomography,” *Fuel Cells*, vol. 13, no. 4, pp. 449–454, Aug. 2013.

[73] Q. Li, D. Spernjak, P. Zelenay, and Y. S. Kim, “Electrode Degradation of Direct Methanol Fuel Cells Evidenced by X-ray Tomography,” *ECS Trans.*, vol. 50, no. 2, pp. 2199–2205, 2013.

[74] Y. C. Karen Chen-Wiegart, J. S. Cronin, Q. Yuan, K. J. Yakal-Kremski, S. A. Barnett, and J. Wang, “3D Non-destructive morphological analysis of a solid oxide fuel cell anode using full-field X-ray nano-tomography,” *J. Power Sources*, vol. 218, pp. 348–351, 2012.

[75] J. Laurencin, R. Quey, G. Delette, H. Suhonen, P. Cloetens, and P. Bleuet, “Characterisation of Solid Oxide Fuel Cell Ni–8YSZ substrate by synchrotron X-ray nano-tomography: from 3D reconstruction to microstructure quantification,” *J. Power Sources*, vol. 198, pp. 182–189, Jan. 2012.

[76] J. Hinebaugh, J. Lee, and a. Bazylak, “Visualizing Liquid Water Evolution in a PEM Fuel Cell Using Synchrotron X-ray Radiography,” *J. Electrochem. Soc.*, vol. 159, no. 12, pp. F826–F830, 2012.

[77] J. Eller, T. Rosén, F. Marone, M. Stampanoni, A. Wokaun, and F. N. Büchi, “Progress in In Situ X-Ray Tomographic Microscopy of Liquid Water in Gas Diffusion Layers of PEFC,” *J. Electrochem. Soc.*, vol. 158, no. 8, p. B963, 2011.

[78] T. Sasabe, P. Deevanhxay, S. Tsushima, and S. Hirai, “Investigation on the effect of microstructure of proton exchange membrane fuel cell porous layers on liquid water behavior by soft X-ray radiography,” *J. Power Sources*, vol. 196, no. 20, pp. 8197–8206, 2011.

[79] S. Chevalier *et al.*, “Synchrotron X-ray Radiography as a Highly Precise and Accurate Method for Measuring the Spatial Distribution of Liquid Water in Operating Polymer Electrolyte Membrane Fuel Cells,” *J. Electrochem. Soc.*, vol. 164, no. 2, pp. 107–114, 2017.

[80] J. Kim, J. Je, M. Kaviany, S. Y. Son, and M. Kim, “Fuel crossover and internal current in polymer electrolyte membrane fuel cell from water visualization using X-ray radiography,” *J. Power Sources*, vol. 196, no. 20, pp. 8398–8401, 2011.

[81] P. Krüger *et al.*, “Synchrotron X-ray tomography for investigations of water distribution in polymer electrolyte membrane fuel cells,” *J. Power Sources*, vol. 196, no. 12, pp. 5250–5255, 2011.

[82] A. Pfrang, D. Veyret, G. J. M. Janssen, and G. Tsotridis, “Imaging of membrane electrode assemblies of proton exchange membrane fuel cells by X-ray computed tomography,” *J. Power Sources*, vol. 196, no. 12, pp. 5272–5276, 2011.

[83] Y. Guan *et al.*, “Analysis of the three-dimensional microstructure of a solid-oxide fuel cell anode using nano X-ray tomography,” *J. Power Sources*, vol. 196, no. 4, pp. 1915–1919, 2011.

[84] R. Flückiger, F. Marone, M. Stampanoni, A. Wokaun, and F. N. Büchi, “Investigation of liquid water in gas diffusion layers of polymer electrolyte fuel cells using X-ray tomographic microscopy,” *Electrochim. Acta*, vol. 56, no. 5, pp. 2254–2262, 2011.

[85] A. Pfrang, D. Veyret, F. Sieker, and G. Tsotridis, “X-ray computed tomography of gas diffusion layers of PEM fuel cells: Calculation of thermal conductivity,” *Int. J. Hydrogen Energy*, vol. 35, pp. 3751–3757, 2010.

[86] W. Maier *et al.*, “In-situ synchrotron X-ray radiography on high temperature polymer electrolyte fuel cells,” *Electrochem. commun.*, vol. 12, no. 10, pp. 1436–1438, 2010.

[87] R. Kuhn *et al.*, “Measuring device for synchrotron X-ray imaging and first results of high temperature polymer electrolyte membrane fuel cells,” *J. Power Sources*, vol. 196, pp. 5231–5239, 2010.

[88] Y. Guan *et al.*, “The study of the reconstructed three-dimensional structure of a solid-oxide fuel-cell cathode by X-ray nanotomography,” *J. Synchrotron Radiat.*, vol. 17, no. 6, pp. 782–785, 2010.

[89] P. Rama *et al.*, “An X-Ray Tomography Based Lattice Boltzmann Simulation Study on Gas Diffusion Layers of Polymer Electrolyte Fuel Cells,” *J. Fuel Cell Sci. Technol.*, vol. 7, no. 3, p. , 2010.

[90] L. Holzer *et al.*, “Microstructure-property relationships in a gas diffusion layer (GDL) for Polymer Electrolyte Fuel Cells, Part I: effect of compression and anisotropy of dry GDL,” *Electrochim. Acta*, vol. 227, pp. 419–434, 2017.

[91] H. Ostadi, P. Rama, Y. Liu, R. Chen, X. X. Zhang, and K. Jiang, “Influence of threshold variation on determining the properties of a polymer electrolyte fuel cell gas diffusion layer in X-ray nano-tomography,” *Chem. Eng. Sci.*, vol. 65, no. 6, pp. 2213–2217, 2010.

[92] C. Hartnig *et al.*, “High resolution synchrotron X-ray investigation of carbon dioxide evolution in operating direct methanol fuel cells,” *Electrochem. commun.*, vol. 11, no. 8, pp. 1559–1562, 2009.

[93] I. Manke *et al.*, “In situ synchrotron X-ray radiography investigations of water transport in PEM fuel cells,” *Fuel Cells*, no. 1, pp. 26–34, 2009.

[94] J. R. Izzo *et al.*, “Nondestructive Reconstruction and Analysis of SOFC Anodes Using X-ray Computed Tomography at Sub-50 nm Resolution,” *J. Electrochem. Soc.*, vol. 155, no. 5, p. B504, 2008.

[95] S. J. Lee, N.-Y. Lim, S. Kim, G.-G. Park, and C.-S. Kim, “X-ray imaging of water distribution in a polymer electrolyte fuel cell,” *J. Power Sources*, vol. 185, pp. 867–870, 2008.

[96] W. Zhu, Z. W. Dunbar, and R. I. Masel, “MicroCT X-ray imaging of water movement in a PEM fuel cell,” *ECS Trans.*, vol. 16, no. 2, pp. 995–1000, 2008.

[97] F. H. Garzon, “Micro And Nano X-Ray Tomography Of PEM Fuel Cell Membranes After Transient Operation,” *Fuel Cell*, vol. 11, no. 1, pp. 1139–1149, 2007.

[98] S. Griesser, G. Buchinger, T. Raab, D. P. Claassen, and D. Meissner, “Characterization of Fuel Cells and Fuel Cell Systems Using Three-Dimensional X-Ray Tomography,” *J. Fuel Cell Sci. Technol.*, vol. 4, no. 1, p. 84, 2007.

[99] I. Manke *et al.*, “Investigation of water evolution and transport in fuel cells with high resolution synchrotron x-ray radiography,” *Appl. Phys. Lett.*, vol. 90, no. 17, p. 174105+3, 2007.

[100] Sinha, Halleck, and C.-Y. Wang, “Quantification of liquid water saturation in a PEM fuel cell diffusion medium using X-ray microtomography,” *Electrochem. Solid-State Lett.*, vol. 9, no. 7, pp. A344-8, 2006.

[101] L. Holzer *et al.*, “Microstructure-property relationships in a gas diffusion layer (GDL) for Polymer Electrolyte Fuel Cells, Part II: pressure-induced water injection and liquid permeability,” *Electrochim. Acta*, vol. 241, pp. 414–432, 2017.

[102] V. Julie *et al.*, “3D phase mapping of solid oxide fuel cell YSZ/Ni cermet at the nanoscale by holographic X-ray nanotomography,” *J. Power Sources*, vol. 243, pp. 841–849, 2013.

[103] S. Kreitmeier, P. Lerch, A. Wokaun, and F. N. Büchi, “Local Degradation at Membrane Defects in Polymer Electrolyte Fuel Cells,” *J. Electrochem. Soc.*, vol. 160, no. 4, pp. F456–F463, 2013.

[104] J. Lee, J. Hinebaugh, and A. Bazylak, “Synchrotron X-ray radiographic investigations of liquid water transport behavior in a PEMFC with MPL-coated GDLs,” *J. Power Sources*, vol. 227, pp. 123–130, 2013.

[105] J. Eller, “X-Ray Tomographic Microscopy of Polymer Electrolyte Fuel Cells,” ETH Zurich, 2013.

[106] F. A. de Bruijn, R. C. Makkus, R. K. A. M. Mallant, and G. J. M. Janssen, *Materials for State-of-the-Art PEM Fuel Cells*, vol. 1. 2007.

[107] R. W. Atkinson, Y. Garsany, B. D. Gould, K. E. Swider-Lyons, and I. V Zenyuk, “The Role of Compressive Stress on Gas Diffusion Media Morphology and Fuel Cell Performance,” *ACS Appl. Energy Mater.*, p. acsaem.7b00077, 2017.

[108] O. Gröger, H. a. Gasteiger, and J.-P. Suchsland, “Review—Electromobility: Batteries or Fuel Cells?,” *J. Electrochem. Soc.*, vol. 162, no. 14, pp. A2605–A2622, 2015.

[109] K. Karan, “PEFC catalyst layer: Recent advances in materials, microstructural characterization, and modeling,” *Curr. Opin. Electrochem.*, vol. 5, no. 1, pp. 27–35, 2017.

[110] T. Soboleva, K. Malek, Z. Xie, T. Navessin, and S. Holdcroft, “PEMFC catalyst layers: The role of micropores and mesopores on water sorption and fuel cell activity,” *ACS Appl. Mater. Interfaces*, vol. 3, no. 6, pp. 1827–1837, 2011.

[111] L. Carrette and K. A. Friedrich, “Fuel Cells : Principles , Types , Fuels , and Applications,” *ChemPhysChem*, pp. 162–193, 2000.

[112] M. M. Mench, *Fuel cell engines. Hoboken*. 2008.

[113] M. S. Wilson, F. H. Garzon, K. E. Sickafus, and S. Gottesfeld, “Surface Area Loss of Supported Platinum in Polymer Electrolyte Fuel Cells,” *J. Electrochem. Soc.* , vol. 140, no. 10, pp. 2872–2877, 1993.

[114] N. Macauley *et al.*, “JES FOCUS ISSUE ON PROTON EXCHANGE MEMBRANE FUEL CELL (PEMFC) DURABILITY Carbon Corrosion in PEM Fuel Cells

and the Development of Accelerated Stress Tests," *J. Electrochem. Soc.*, vol. 165, no. 6, pp. 3148–3160, 2018.

[115] K. H. Lim, H.-S. Oh, S.-E. Jang, Y.-J. Ko, H.-J. Kim, and H. Kim, "Effect of operating conditions on carbon corrosion in polymer electrolyte membrane fuel cells," *J. Power Sources*, vol. 193, no. 2, pp. 575–579, 2009.

[116] S. Maass, F. Finsterwalder, G. Frank, R. Hartmann, and C. Merten, "Carbon support oxidation in PEM fuel cell cathodes," *J. Power Sources*, vol. 176, no. 2, pp. 444–451, 2008.

[117] A. P. Hitchcock *et al.*, "Carbon corrosion of proton exchange membrane fuel cell catalyst layers studied by scanning transmission X-ray microscopy," *J. Power Sources*, vol. 266, pp. 66–78, 2014.

[118] N. Yousfi-Steiner, P. Moçotéguy, D. Candusso, and D. Hissel, "A review on polymer electrolyte membrane fuel cell catalyst degradation and starvation issues: Causes, consequences and diagnostic for mitigation," *J. Power Sources*, vol. 194, no. 1, pp. 130–145, 2009.

[119] A. P. Young, V. Colbow, D. Harvey, E. Rogers, and S. Wessel, "A Semi-Empirical Two Step Carbon Corrosion Reaction Model in PEM Fuel Cells," *J. Electrochem. Soc.*, vol. 160, no. 4, pp. F381–F388, 2013.

[120] S. Zhang *et al.*, "A review of accelerated stress tests of MEA durability in PEM fuel cells," *Int. J. Hydrogen Energy*, vol. 34, no. 1, pp. 388–404, 2009.

[121] C. A. Reiser *et al.*, "A Reverse-Current Decay Mechanism for Fuel Cells," *Electrochem. solid-State Lett.*, vol. 8, no. 6, pp. 273–276, 2005.

[122] J. Durst *et al.*, "Degradation heterogeneities induced by repetitive start/stop events in proton exchange membrane fuel cell: Inlet vs. outlet and channel vs. land," *Appl. Catal. B Environ.*, vol. 138–139, pp. 416–426, 2013.

[123] A. Lamibrac, G. Maranzana, J. Dillet, O. Lottin, and S. Didierjean, "Local degradations resulting from repeated start-ups and shut- downs in Proton Exchange Membrane Fuel Cell (PEMFC)," *Energy Procedia*, vol. 29, pp. 318–324, 2012.

[124] H. Schulenburg, B. Schwanitz, N. Linse, G. Scherer, A. Wokaun, and F. Polytechnique, “3D Imaging of Catalyst Support Corrosion in Polymer Electrolyte Fuel Cells,” *J. Phys. Chem. C*, vol. 115, no. November 2015, pp. 14236–14243, 2011.

[125] A. P. Young, J. Stumper, and E. Gyenge, “Characterizing the Structural Degradation in a PEMFC Cathode Catalyst Layer: Carbon Corrosion,” *J. Electrochem. Soc.*, vol. 156, no. 8, pp. B913–B922, 2009.

[126] R. M. Darling and J. P. Meyers, “Kinetic Model of Platinum Dissolution in PEMFCs,” *J. Electrochem. Soc.*, vol. 150, no. 11, p. A1523, 2003.

[127] T. Yoda, H. Uchida, and M. Watanabe, “Effects of operating potential and temperature on degradation of electrocatalyst layer for PEFCs,” *Electrochim. Acta*, vol. 52, no. 19, pp. 5997–6005, 2007.

[128] F. A. de Bruijn, V. A. T. Dam, and G. J. M. Janssen, “Review: Durability and Degradation Issues of PEM Fuel Cell Components,” *Fuel Cells*, vol. 8, no. 1, pp. 3–22, Feb. 2008.

[129] A. A. Topalov, S. Cherevko, A. R. Zeradjanin, J. C. Meier, I. Katsounaros, and K. J. J. Mayrhofer, “Towards a comprehensive understanding of platinum dissolution in acidic media,” *Chem. Sci.*, vol. 5, no. 2, pp. 631–638, 2014.

[130] N. Macauley *et al.*, “Accelerated Membrane Durability Testing of Heavy Duty Fuel Cells,” *J. Electrochem. Soc.*, vol. 162, no. 1, pp. F98–F107, 2014.

[131] C. A. Rice, P. Urchaga, A. O. Pistono, B. W. McFerrin, B. T. McComb, and J. Hu, “Platinum Dissolution in Fuel Cell Electrodes: Enhanced Degradation from Surface Area Assessment in Automotive Accelerated Stress Tests,” *J. Electrochem. Soc.*, vol. 162, no. 10, pp. F1175–F1180, 2015.

[132] P. J. Ferreira *et al.*, “Instability of Pt/C Electrocatalysts in Proton Exchange Membrane Fuel Cells,” *J. Electrochem. Soc.*, vol. 152, no. 11, p. A2256, 2005.

[133] P. W. Voorhees, “The Theory of Ostwald Ripening,” *J. Stat. Phys.*, vol. 38, p. V003T08A024, 1985.

[134] R. C. Gonzalez and R. E. Woods, *Digital Image Processing*, 3rd ed. New Jersey: Pearson International, 2008.

[135] G. N. Hounsfield, “Computerized transverse axial scanning (tomography): Part I. Description of system,” *Br. J. Radiol.*, vol. 46, pp. 1016–1022, 1973.

[136] A. M. Cormack, “Representation of a function by its line integrals, with some radiological applications. II,” *J. Appl. Phys.*, vol. 35, no. 10, pp. 2908–2913, 1964.

[137] W. A. Kalender, “X-ray computed tomography,” *Phys. Med. Biol.*, vol. 51, pp. R29–R43, 2006.

[138] L. A. Shepp and B. F. Logan, “The Fourier reconstruction of a head section,” *IEEE Trans. Nucl. Sci.*, vol. 21, no. 3, pp. 21–43, 1974.

[139] M. Sak, N. Duric, P. Littrup, M. Sherman, and G. Gierach, “Ultrasound tomography imaging with waveform sound speed: Parenchymal changes in women undergoing tamoxifen therapy.,” *Proc. SPIE--the Int. Soc. Opt. Eng.*, vol. 10139, no. 10, pp. 1651–1666, 2017.

[140] V. Cnudde and M. N. Boone, “High-resolution X-ray computed tomography in geosciences: A review of the current technology and applications,” *Earth Sci. Rev.*, vol. 123, pp. 1–17, 2013.

[141] C. A. Carlsson and G. A. Carlsson, “Basic physics of X-ray imaging,” *Linkoping Univ.*, pp. 3–29, 1996.

[142] “Inside the synchrotron,” *Canadian Light Source*. [Online]. Available: https://www.lightsource.ca/inside_the_synchrotron. [Accessed: 24-Nov-2018].

[143] Zeiss TM, “ZEISS Xradia 520 Versa submicron X-ray imaging : extending the limits of exploration,” 2013. [Online]. Available: https://www.zeiss.com/content/dam/Microscopy/us/download/pdf/Products/xradia520versa/xradia-520-versa-product-information.pdf.

[144] M. J. Berger *et al.*, “XCOM: Photon Cross Sections Database | NIST,” 2010. [Online]. Available: https://www.nist.gov/pml/xcom-photon-cross-sections-database. [Accessed: 24-Nov-2018].

[145] D. Wildenschild and A. P. Sheppard, “X-ray imaging and analysis techniques for quantifying pore-scale structure and processes in subsurface porous medium systems,” *Adv. Water Resour.*, vol. 51, pp. 217–246, 2013.

[146] J. Beutel, H. L. Kundel, R. L. Van Metter, and Society of Photo-optical Instrumentation Engineers., *Handbook of Medical Imaging, Volume 1. Physics and Psychophysics*. SPIE, 2000.

[147] C. Holzner, M. Feser, S. Vogt, B. Hornberger, S. B. Baines, and C. Jacobsen, “Zernike phase contrast in scanning microscopy with X-rays,” *Nat. Phys.*, vol. 6, no. 11, pp. 883–887, 2010.

[148] A. S. Kumar, P. Mandal, Y. Zhang, and S. Litster, “Image segmentation of nanoscale Zernike phase contrast X-ray computed tomography images,” *J. Appl. Phys.*, vol. 117, no. 18, 2015.

[149] J. Gelb *et al.*, “Sub-micron X-ray Computed Tomography for Non-Destructive 3D Visualization and Analysis,” *Microsc. Microanal.*, vol. 15, no. S2, pp. 618–619, 2009.

[150] S. C. Mayo, A. W. Stevenson, and S. W. Wilkins, “In-Line Phase-Contrast X-ray Imaging and Tomography for Materials Science,” *Materials (Basel).*, vol. 5, no. 12, pp. 937–965, 2012.

[151] D. S. Eastwood *et al.*, “The application of phase contrast X-ray techniques for imaging Li-ion battery electrodes,” *Nucl. Instruments Methods Phys. Res. Sect. B Beam Interact. with Mater. Atoms*, vol. 324, pp. 118–123, 2014.

[152] F. Tariq *et al.*, “In-Operando X-ray Tomography Study of Lithiation Induced Delamination of Si Based Anodes for Lithium-Ion Batteries,” *Ecs Electrochem. Lett.*, vol. 3, no. 7, pp. A76–A78, 2014.

[153] M. Mostafavi, S. A. McDonald, P. M. Mummery, and T. J. Marrow, “Observation and quantification of three-dimensional crack propagation in poly-granular graphite,” *Eng. Fract. Mech.*, vol. 110, pp. 410–420, 2013.

[154] A. Schneider, C. Wieser, J. Roth, and L. Helfen, “Impact of synchrotron radiation on fuel cell operation in imaging experiments,” *J. Power Sources*, vol. 195, no. 19, pp. 6349–6355, 2010.

[155] J. Roth, J. Eller, and F. N. Buchi, “Effects of Synchrotron Radiation on Fuel Cell Materials,” *J. Electrochem. Soc.*, vol. 159, no. 8, pp. F449–F455, 2012.

[156] J. Coenen, E. Tchouparova, X. Jing, S. I. Exploration, and B. V Production, “Measurement Parameters and Resolution Aspects of Micro X-Ray Tomography for Advanced Core Analysis,” in *Proceedings of the international symposium of the society of core analysts*, 2004, p. SCA 2004-36.

[157] R. T. White, M. El Hannach, O. Luo, F. P. Orfino, M. Dutta, and E. Kjeang, “3D printed flow channel fixture for visualization of water condensation in PEFC by X-ray Computed Tomography R. White,” in *228th ECS meeting*, 2015, p. 58394.

[158] K. Kinoshita and P. Stonehart, *Modern Aspects of Electrochemistry*, vol. 12, no. 3_4. New York: Plenum Press, 1977.

[159] Y. Singh *et al.*, “Tracking the evolution of mechanical degradation in fuel cell membranes using 4D in situ visualization,” *J. Power Sources*, vol. 412, no. November 2018, pp. 224–237, Feb. 2019.

[160] A. Sadeghi Alavijeh *et al.*, “Decay in Mechanical Properties of Catalyst Coated Membranes Subjected to Combined Chemical and Mechanical Membrane Degradation,” *Fuel Cells*, vol. 15, no. 1, pp. 204–213, 2015.

[161] M. N. Silberstein and M. C. Boyce, “Constitutive modeling of the rate, temperature, and hydration dependent deformation response of Nafion to monotonic and cyclic loading,” *J. Power Sources*, vol. 195, no. 17, pp. 5692–5706, 2010.

[162] M. A. Goulet *et al.*, “Mechanical properties of catalyst coated membranes for fuel cells,” *J. Power Sources*, vol. 234, pp. 38–47, 2013.

[163] A. Kusoglu, Y. Tang, M. H. Santare, A. M. Karlsson, S. Cleghorn, and W. B. Johnson, “Stress-strain behavior of perfluorosulfonic acid membranes at various

temperatures and humidities: Experiments and phenomenological modeling," *J. Fuel Cell Sci. Technol.*, vol. 6, no. 1, pp. 0110121–0110128, 2009.

[164] A. S. Alavijeh *et al.*, "Microstructural and Mechanical Characterization of Catalyst Coated Membranes Subjected to In Situ Hygrothermal Fatigue," *J. Electrochem. Soc.*, vol. 162, no. 14, pp. 1461–1469, 2015.

[165] The University of Texas High- Resolution X-ray CT Facility, "DigiMorph.org," 2007. [Online]. Available: http://www.digimorph.org/specimens/Chamaeleo_calyptratus/whole/.

[166] P. Perona and J. Malik, "Scale-space and edge detection using anisotropic diffusion," *IEEE Trans. Pattern Anal. Mach. Intell.*, vol. 12, no. 7, pp. 629–639, 1990.

[167] J. Weickert, *Anisotropic Diffusion in Image Processing*. B.G. Teubner Stuttgart, 2008.

[168] Q. Lin, S. Shi, L. Wang, X. Chen, and G. Chen, "Biaxial fatigue crack propagation behavior of perfluorosulfonic-acid membranes," *J. Power Sources*, vol. 384, no. April, pp. 58–65, 2018.

[169] Y. Singh, F. P. Orfino, M. Dutta, and E. Kjeang, "3D Failure Analysis of Pure Mechanical and Pure Chemical Degradation in Fuel Cell Membranes," *J. Electrochem. Soc.*, vol. 164, no. 13, pp. 1331–1341, 2017.

[170] D. Ramani, Y. Singh, F. P. Orfino, M. Dutta, and E. Kjeang, "Characterization of Membrane Degradation Evolution in Fuel Cells using X-ray Computed Tomography," *J. Electrochem. Soc.*, vol. 165, no. 6, pp. F3200–F3208, 2018.

[171] S. M. Seltzer, "Calculation of photon mass energy-transfer and mass energy-absorption coefficients.," *Radiat. Res.*, vol. 136, no. 2, pp. 147–170, 1993.

[172] M. Ebner, F. Marone, M. Stampanoni, and V. Wood, "Visualization and quantification of electrochemical and mechanical degradation in Li ion batteries," *Sceince*, vol. 342, no. November, pp. 716–721, 2013.

[173] S. Shukla, “Experimental analysis of inkjet printed polymer electrolyte fuel cell electrodes,” University of Alberta, 2016.

[174] “Environment and Climate Change Canada - Sustainable Development - Addressing Climate Change and Air Quality, Goal 1: Reducing Greenhouse Gas Emissions, Reducing Canada’s greenhouse gas emissions.” [Online]. Available: https://www.ec.gc.ca/dd-sd/default.asp?lang=En&n=AD1B22FD-1. [Accessed: 23-Jan-2019].

[175] M. K. Debe, “Electrocatalyst approaches and challenges for automotive fuel cells,” *Nature*, vol. 486, no. 7401, pp. 43–51, 2012.

[176] Z. Tayarani-Yoosefabadi, D. Harvey, J. Bellerive, and E. Kjeang, “Stochastic microstructural modeling of fuel cell gas diffusion layers and numerical determination of transport properties in different liquid water saturation levels,” *J. Power Sources*, vol. 303, pp. 208–221, 2016.

[177] R. Lin, F. Xiong, W. C. Tang, L. Técher, J. M. Zhang, and J. X. Ma, “Investigation of dynamic driving cycle effect on the degradation of proton exchange membrane fuel cell by segmented cell technology,” *J. Power Sources*, vol. 260, pp. 150–158, 2014.

[178] C. Lim *et al.*, “Membrane degradation during combined chemical and mechanical accelerated stress testing of polymer electrolyte fuel cells,” *J. Power Sources*, vol. 27, pp. 102–110, 2014.

[179] J. D. Fairweather *et al.*, “Effects of Cathode Corrosion on Through-Plane Water Transport in Proton Exchange Membrane Fuel Cells,” *J. Electrochem. Soc.*, vol. 160, no. 9, pp. F980–F993, 2013.

[180] R. T. White *et al.*, “3D Printed Flow Field and Fixture for Visualization of Water Distribution in Fuel Cells by X-ray Computed Tomography,” *J. Electrochem. Soc.*, vol. 163, no. 13, pp. F1337–F1343, 2016.

[181] R. T. White, M. Najm, M. Dutta, F. P. Orfino, and E. Kjeang, “Communication—Effect of Micro-XCT X-ray Exposure on the Performance of Polymer Electrolyte Fuel Cells,” *J. Electrochem. Soc.*, vol. 163, no. 10, pp. 1206–1208, 2016.

[182] D. Spernjak, J. Fairweather, R. Mukundan, T. Rockward, and R. L. Borup, “Influence of the microporous layer on carbon corrosion in the catalyst layer of a polymer electrolyte membrane fuel cell,” *J. Power Sources*, vol. 214, pp. 386–398, 2012.

[183] G. S. Hwang *et al.*, “Phase-change-related degradation of catalyst layers in proton-exchange- membrane fuel cells,” *Electrochim. Acta*, vol. 95, pp. 29–37, 2013.

[184] Z.-K. Huang and K.-W. Chau, “A new image thresholding method based on Gaussian mixture model,” *Appl. Math. Comput.*, vol. 205, no. 2, pp. 899–907, 2008.

[185] A. Pokhrel, M. El Hannach, F. P. Orfino, M. Dutta, and E. Kjeang, “Failure analysis of fuel cell electrodes using three-dimensional multi-length scale X-ray computed tomography,” *J. Power Sources*, vol. 329, pp. 330–338, 2016.

[186] H.-K. Song *et al.*, “Electrochemical Porosimetry,” *J. Electrochem. Soc.*, vol. 151, no. 3, p. E102, 2004.

[187] H. Keiser, K. D. Beccu, and M. A. Gutjahr, “Estimation of the pore structure of porous electrodes from impedance measurements,” *Electrochim. Acta*, vol. 21, no. 8, pp. 539–543, Aug. 1976.

[188] R. Dougherty and K.-H. Kunzelmann, “Computing Local Thickness of 3D Structures with ImageJ,” *Microsc. Microanal.*, vol. 13, no. S02, 2007.

[189] M. A. Goulet, S. Arbour, M. Lauritzen, and E. Kjeang, “Water sorption and expansion of an ionomer membrane constrained by fuel cell electrodes,” *J. Power Sources*, vol. 274, pp. 94–100, 2015.

[190] U. N. Shrivastava and K. Tajiri, “Sources of Current Density Distribution in the Land-Channel Direction of a PEMFC,” *J. Electrochem. Soc.*, vol. 163, no. 9, pp. F1072–F1083, 2016.

[191] C. Tötzke *et al.*, “Three-dimensional study of compressed gas diffusion layers using synchrotron X-ray imaging,” *J. Power Sources*, vol. 253, pp. 123–131, 2014.

[192] S. Kundu, M. W. Fowler, L. C. Simon, and S. Grot, “Morphological features (defects) in fuel cell membrane electrode assemblies,” *J. Power Sources*, vol. 157, no. 2, pp. 650–656, 2006.

[193] S. Kreitmeier, A. Wokaun, and F. N. Büchi, “Local Catalyst Support Degradation during Polymer Electrolyte Fuel Cell Start-Up and Shutdown,” *J. Electrochem. Soc.*, vol. 159, no. 11, pp. F787–F793, 2012.

[194] Fuel Cell & Hydrogen Energy Association, “Transportation.” [Online]. Available: http://www.fchea.org/transportation. [Accessed: 07-Jan-2018].

[195] A. Hoffrichter, “Hydrogen-Powered Railway Vehicles (Hydrail): A Vision,” in *International Hydrail Conference*, 2017.

[196] “Demonstration Experiments Begin for the Hydrogen Fuel Cell of the Future - Device Development Is Also Accelerated,” *Panasonic Newsroom Global*, 2017. [Online]. Available: http://news.panasonic.com/global/stories/2017/45928.html. [Accessed: 20-Feb-2018].

[197] Ballard, “Fuel Cell System Development for Freight Transport Applications,” 2016.

[198] P. Stahl, J. Biesdorf, P. Boillat, J. Kraft, and K. A. Friedrich, “Water Distribution Analysis in the Outer Perimeter Region of Technical PEFC Based on Neutron Radiography,” *J. Electrochem. Soc.*, vol. 162, no. 7, pp. F677–F685, 2015.

[199] T. Gaumont, G. Maranzana, O. Lottin, J. Dillet, L. Guétaz, and J. Pauchet, “In Operando and Local Estimation of the Effective Humidity of PEMFC Electrodes and Membranes,” *J. Electrochem. Soc.*, vol. 164, no. 14, pp. 1535–1542, 2017.

[200] A. G. Star and T. F. Fuller, “FIB-SEM Tomography Connects Microstructure to Corrosion-Induced Performance Loss in PEMFC Cathodes,” *J. Electrochem. Soc.*, vol. 164, no. 9, pp. F901–F907, 2017.

[201] B. T. Sneed *et al.*, “3D Analysis of Fuel Cell Electrocatalyst Degradation on Alternate Carbon Supports,” *ACS Appl. Mater. Interfaces*, vol. 9, no. 35, pp. 29839–29848, 2017.

[202] F. A. De Bruijn, V. A. T. Dam, and G. J. M. Janssen, “Review: Durability and Degradation Issues of PEM Fuel Cell Components,” *Fuel Cells*, vol. 8, no. 1, pp. 3–22, Feb. 2008.

[203] I. V Zenyuk, P. K. Das, and A. Z. Weber, “Understanding Impacts of Catalyst-Layer Thickness on Fuel-Cell Performance via Mathematical Modeling,” *J. Electrochem. Soc.*, vol. 163, no. 7, pp. F691–F703, 2016.

[204] D. Ramani, Y. Singh, F. P. Orfino, M. Dutta, and E. Kjeang, “Characterization of Membrane Degradation Growth in Fuel Cells Using X-ray Computed Tomography,” *J. Electrochem. Soc.*, vol. 165, no. 6, pp. F3200–F3208, 2018.

[205] S. S. Alrwashdeh *et al.*, “In Operando Quantification of Three-Dimensional Water Distribution in Nanoporous Carbon-Based Layers in Polymer Electrolyte Membrane Fuel Cells,” *ACS Nano*, vol. 11, no. 6, pp. 5944–5949, 2017.

[206] R. A. Ketcham and W. D. Carlson, “Acquisition, optimization and interpretation of x-ray computed tomographic imagery: Applications to the geosciences,” *Comput. Geosci.*, vol. 27, no. 4, pp. 381–400, 2001.

[207] A. P. Hitchcock *et al.*, “Characterizing automotive fuel cell materials by soft X-ray scanning transmission X-ray microscopy,” in *AIP Conference Proceedings*, 2016, vol. 1696, no. 10, pp. 20012–20002.

[208] D. B. V. H. A. P. S. J. Susac, “STXM Characterization of PEM Fuel Cell Catalyst Layers,” *ECS Trans.*, vol. 50, no. 2, pp. 405–413, 2012.

[209] J. Schindelin *et al.*, “Fiji: an open-source platform for biological-image analysis,” *Nat. Methods*, vol. 9, no. 7, pp. 676–682, 2012.

[210] P. Kovesi, “MATLAB and Octave Functions for Computer Vision and Image Processing.” [Online]. Available: http://www.peterkovesi.com/matlabfns/. [Accessed: 10-Jan-2018].

[211] G. Gerig, O. Kubler, R. Kikinis, and F. a Jolesz, “Nonlinear anisotrophic filtering of MRI data,” *IEEE Trans. Med. Imaging*, vol. 11, no. 2, pp. 221–232, 1992.

[212] M. Doube *et al.*, “BoneJ: Free and extensible bone image analysis in ImageJ,” *Bone*, vol. 47, no. 6, pp. 1076–1079, 2010.

[213] E. Maire and P. J. Withers, “Quantitative X-ray tomography,” *Int. Mater. Rev.*, vol. 59, no. 1, pp. 1–43, 2014.

[214] P. Pietsch and V. Wood, “X-Ray Tomography for Lithium Ion Battery Research: A Practical Guide,” *Annu. Rev. Mater. Res*, vol. 471229, no. 1, pp. 1–12, 2017.

[215] Y.-H. Lai, C. K. Mittelsteadt, C. S. Gittleman, and D. A. Dillard, “Viscoelastic Stress Analysis of Constrained Proton Exchange Membranes Under Humidity Cycling,” *J. Fuel Cell Sci. Technol.*, vol. 6, no. 2, p. 021002, 2009.

[216] P. Pietsch *et al.*, “Quantifying microstructural dynamics and electrochemical activity of graphite and silicon-graphite lithium ion battery anodes,” *Nat. Commun.*, vol. 7, p. 12909, 2016.

[217] S. V. Venkatesan, M. Dutta, and E. Kjeang, “Mesoscopic degradation effects of voltage cycled cathode catalyst layers in polymer electrolyte fuel cells,” *Electrochem. commun.*, vol. 72, pp. 15–18, 2016.

[218] M. Sabharwal, L. M. Pant, A. Putz, D. Susac, J. Jankovic, and M. Secanell, “Analysis of Catalyst Layer Microstructures: From Imaging to Performance,” *Fuel Cells*, vol. 16, no. 6, pp. 734–753, 2016.

[219] J. H. Nam and M. Kaviany, “Effective diffusivity and water-saturation distribution in single- and two-layer PEMFC diffusion medium,” *Int. J. Heat Mass Transf.*, vol. 46, no. 24, pp. 4595–4611, 2003.

[220] P. Gode, F. Jaouen, G. Lindbergh, A. Lundblad, and G. Sundholm, “Influence of the composition on the structure and electrochemical characteristics of the PEFC cathode,” *Electrochim. Acta*, vol. 48, no. 28, pp. 4175–4187, 2003.

[221] M. F. Mathias, J. Roth, J. Fleming, and W. Lehnert, “Diffusion media materials and characterisation,” *Handb. Fuel Cells*, vol. 3, pp. 517–537, 2010.

[222] L. M. Anovitz and D. R. Cole, “Characterization and Analysis of Porosity and Pore Structures,” *Rev. Mineral. Geochemistry*, vol. 80, pp. 61–164, 2015.

[223] S. Diamond, “Mercury porosimetry An inappropriate method for the measurement of pore size distributions in cement-based materials,” *Cem. Concr. Res.*, vol. 30, pp. 1517–1525, 2000.

[224] M. Espinoza, B. Sunden, M. Andersson, and J. Yuan, “Analysis of Porosity and Tortuosity in a 2D Selected Region of Solid Oxide Fuel Cell Cathode Using the Lattice Boltzmann Method,” *ECS Trans.*, vol. 65, no. 1, pp. 59–73, 2015.

[225] M. G. George *et al.*, “Accelerated Degradation of Polymer Electrolyte Membrane Fuel Cell Gas Diffusion Layers II,” *J. Electrochem. Soc.*, vol. 164, no. 7, pp. F714–F721, 2017.

[226] S. hee Kim and C. C. Chu, “Pore structure analysis of swollen dextran-methacrylate hydrogels by SEM and mercury intrusion porosimetry,” *J. Biomed. Mater. Res.*, vol. 53, no. 3, pp. 258–266, 2000.

[227] L. G. de A. Melo *et al.*, “Evaluating focused ion beam and ultramicrotome sample preparation for analytical microscopies of the cathode layer of a polymer electrolyte membrane fuel cell,” *J. Power Sources*, vol. 312, pp. 23–35, 2016.

[228] M. Salzer, T. Prill, A. Spettl, D. Jeulin, K. Schladitz, and V. Schmidt, “Quantitative comparison of segmentation algorithms for FIB-SEM images of porous media,” *J. Microsc.*, vol. 257, no. 1, pp. 23–30, 2015.

[229] M. Lopez-Haro *et al.*, “Three-dimensional analysis of Nafion layers in fuel cell electrodes,” *Nat. Commun.*, vol. 5, pp. 1–6, 2014.

[230] S. Yakovlev and K. H. Downing, “Visualization of clusters in polymer electrolyte membranes by electron microscopy,” *Phys. Chem. Chem. Phys.*, vol. 15, no. 4, pp. 1052–1064, 2013.

[231] A. Pokhrel, E. Kjeang, M. Dutta, F. Orfino, and M. El Hannach, “3D Failure Analysis of PEM Fuel Cell Catalyst Layers Using Multi-Length Scale X-Ray Computed Tomography,” *Meet. Abstr.*, vol. MA2015-02, no. 37, pp. 1357–1357, 2015.

[232] U. Klement, J. Ekberg, and S. T. Kelly, “3D Analysis of Porosity in a Ceramic Coating Using X-ray Microscopy,” *J. Therm. Spray Technol.*, vol. 26, no. 3, pp. 456–463, 2017.

[233] R. T. White *et al.*, “Four-dimensional joint visualization of electrode degradation and liquid water distribution inside operating polymer electrolyte fuel cells,” *Sci. Rep.*, 9, pp. 1843, 2018.

[234] Y. Singh *et al.*, “Tracking the Evolution of Mechanical Degradation in Fuel Cell Membranes using 4D in situ Visualization,” *J. Power Sources*, 412, 224-237, 2018.

[235] R. T. White, S. Eberhardt, M. Najm, F. P. Orfino, M. Dutta, and E. Kjeang, “Quantification of Material Property Changes During Electrode Degradation in Polymer Electrolyte Fuel Cells Using X-ray Computed Tomography,” *Microsc. Microanal.*, vol. 23, no. S1, pp. 2044–2045, 2017.

[236] A. Çeçen, E. A. Wargo, A. C. Hanna, D. M. Turner, S. R. Kalidindi, and E. C. Kumbur, “3-D Microstructure Analysis of Fuel Cell Materials: Spatial Distributions of Tortuosity, Void Size and Diffusivity,” *J. Electrochem. Soc.*, vol. 159, no. 3, pp. B299–B307, 2012.

[237] R. Singh, A. R. Akhgar, P. C. Sui, K. J. Lange, and N. Djilali, “Dual-Beam FIB/SEM Characterization, Statistical Reconstruction, and Pore Scale Modeling of a PEMFC Catalyst Layer,” *J. Electrochem. Soc.*, vol. 161, no. 4, pp. F415–F424, 2014.

[238] O. O. Taiwo, D. P. Finegan, J. Gelb, C. Holzner, D. J. L. Brett, and P. R. Shearing, “The use of contrast enhancement techniques in X-ray imaging of lithium-ion battery electrodes,” *Chem. Eng. Sci.*, vol. 154, pp. 27–33, 2016.

[239] S. H. Eberhardt *et al.*, “Imaging Phosphoric Acid Migration in High Temperature Polymer Electrolyte Fuel Cells by X-Ray Tomographic Microscopy,” *J. Electrochem. Soc.*, vol. 162, no. 3, pp. F310–F316, 2015.

[240] N. Phansalkar, S. More, A. Sabale, and M. Joshi, “Adaptive local thresholding for detection of nuclei in diversity stained cytology images,” *ICCSP 2011 - 2011 Int. Conf. Commun. Signal Process.*, pp. 218–220, 2011.

[241] S. J. Normile *et al.*, “Direct observations of liquid water formation at nano- and micro-scale in platinum group metal-free electrodes by operando X-ray computed tomography,” *Mater. Today Energy*, vol. 9, pp. 187–197, 2018.

[242] S. V. Venkatesan, M. Dutta, and E. Kjeang, “Mesoscopic degradation effects of voltage cycled cathode catalyst layers in polymer electrolyte fuel cells,” *Electrochem. commun.*, vol. 72, pp. 15–18, 2016.

[243] M. D. R. Kok, T. Tranter, M. Lam, and J. T. Gostick, “PoreSpy: An image analysis toolkit for voxel images of porous materials,” *J. Open Source Softw.*, 2018.

[244] S. J. Cooper, A. Bertei, P. R. Shearing, J. A. Kilner, and N. P. Brandon, “TauFactor: An open-source application for calculating tortuosity factors from tomographic data,” *SoftwareX*, vol. 5, pp. 203–210, 2016.

[245] G. Inoue *et al.*, “Theoretical examination of effective oxygen diffusion coefficient and electrical conductivity of polymer electrolyte fuel cell porous components,” *J. Power Sources*, vol. 327, pp. 610–621, 2016.

[246] M. El Hannach and E. Kjeang, “Stochastic Microstructural Modeling of PEFC Gas Diffusion Media,” *J. Electrochem. Soc.*, vol. 161, no. 9, pp. F951–F960, 2014.

[247] M. El Hannach, R. Singh, N. Djilali, and E. Kjeang, “Micro-porous layer stochastic reconstruction and transport parameter determination,” *J. Power Sources*, vol. 282, pp. 58–64, 2015.

Appendix A.

Stack Alignment and Greyscale Scaling

Purpose

Given two image sets, say ‘wet’ and ‘dry’, degraded and beginning of life, sample1 and sample2 – how can you align them such that the same x,y,z coordinate represents the same location in both images sets (or even across multiple, indefinite number of sets)?

This is the purpose of the procedure below. It is ideal to be able to exactly align image sets in a way that the user can be confident the same location is represented by the same x,y,z coordinates. This makes analysis easier and quicker, and conclusions more accurate. In this same regard, it is also very useful to have the image sets not only have the same coordinate system, but also the same greyscale values (pixel values) for materials which are consistent between them, such as air, or solid which is unchanging. Only in this way can ‘wet’ be subtracted from ‘dry’ or observations on material composition be made accurately.

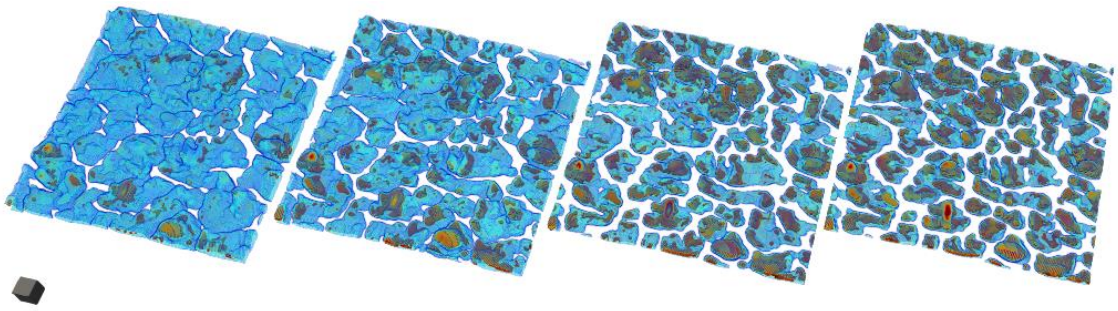

FigureA1: Same location tracking of catalyst layer following degradation (from left to right). Colour changes are associated with increase in X-ray attenuation from material composition change following carbon corrosion – brighter regions are in brown/red.

Greyscale Scaling

Typically, for image sets of the same sample or for comparison of one sample to another, the same byte scaling is required, that is the same conversion from CT units to 16-bit greyscale values following reconstruction from a computed tomography scan. This

requires that the exact same imaging settings be used to collect the tomography (exposure, projections, pixel size, source-detector positions etc.).

For best accuracy the byte scaling, or greyscale normalization must be done at time of reconstruction. It is possible to perform a greyscale scaling in ImageJ/Fiji but this may cause errors due to linear extrapolation. This method won't be discussed here as it is not recommended.

At the time of reconstruction, choose one image set as base. Consider the image set with the brightest (most attenuating) material to copy byte scale settings from. This is the dataset all others will be normalized against, called the base image set from here on. If the dataset with the brightest (most attenuating) material is unknown, incorrect scaling can occur from limiting high attenuating materials of different types to the same value of 65535 (capped).

Reconstruct this base image-set in the usual manner utilizing Zeiss Reconstructor software applying center shift, rotation, beam hardening etc. however applying byte scaling such that same material greyscale values are consistent between separate scans.

When opening an image, greyscale values for air or other similar materials should be the same, within about ~100-200 gsv, although this will depend on the greyscale values. For example, air with gsv of ~22000 has a mean within ~10 gsv between two image sets as shown here.

This means any greyscale changes in catalyst layer or other material components should be due to composition or density changes. It is important to note however that the closer the two image sets are taken in time, the better – ideally the same day following each other such as during an operando run between wet and dry. This is due to slight changes in X-ray beam as the (X-ray) anode is rotated, aged or replaced.

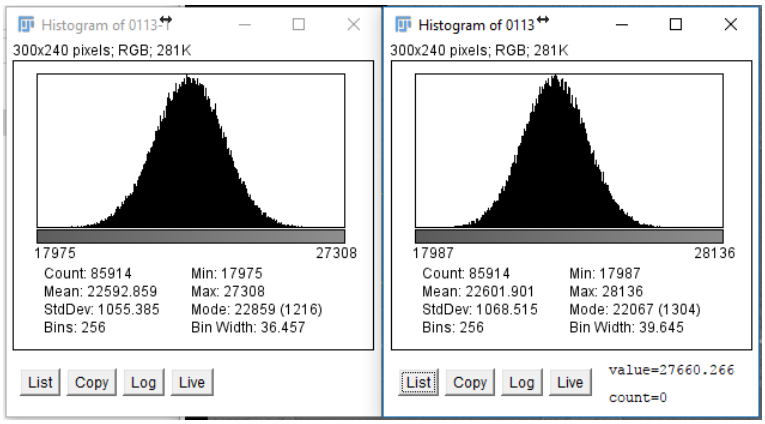

Figure A2: Air phase greyscale histograms between two different image sets after applying byte scaling showing the normalization of greyscale values

Align image stacks

Performed for same location tracking when imaging in 4D. In this example we use dry (N_2 gas flow at room temperature) and wet (750mA/cm^2, H_2/Air) conditions to then be used to subtract non-water material from wet stack for water distribution calculations in the gas diffusion layer. Here 'dry' will be used as the base, or reference sample and it will be aligned to the 'wet' stack. This can be extended to other 4D imaging sets such as BOL and EOL, compressed GDLs etc.

The algorithm steps are to first crop the data such that excess volume is not considered during the alignment step which can bias the accuracy. Following, tilt correction is applied. This is the amount by which the region of interest (ROI) moves in the y-direction between the start slice and the end slice, as shown below. To correct this, an algorithm was developed (for ImageJ) to shift each image in the image stack based on a predefined tilt. In addition, rotation correction is applied. This should now level the MEA in the 3D volume. An example of the result of these steps is shown below in Figure A.3.

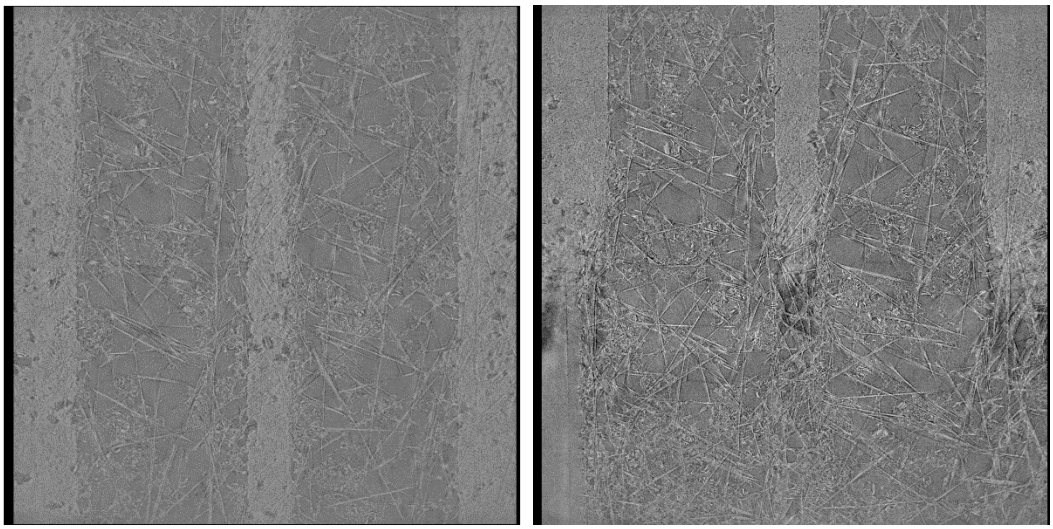

Figure A3: Left: Final result of tilt and rotation correction showing that the flow field lands appear evenly at the exact same slice across the full area of the gas diffusion layer. Right: Initial tilt.

Following the above steps for each image set, the two can now be aligned. First this is done in the z-direction using a macro developed to align a reference image to a range of images in the z-direction. Each image is subtracted to find the best alignment and a z-shift is applied to the target dataset. The macro uses StackReg to align in the planer direction across multiple images. Following the application of the above, the result is an aligned image stack in 3D with a base image set.

An example is shown below where 750cycles_dry is aligned to BOL dry and 750cycles_750wet was aligned to 750cycles_dry such that it is also aligned to BOL. In this way we can have multiple image sets aligned across degradation stages and at different current density for water quantification.

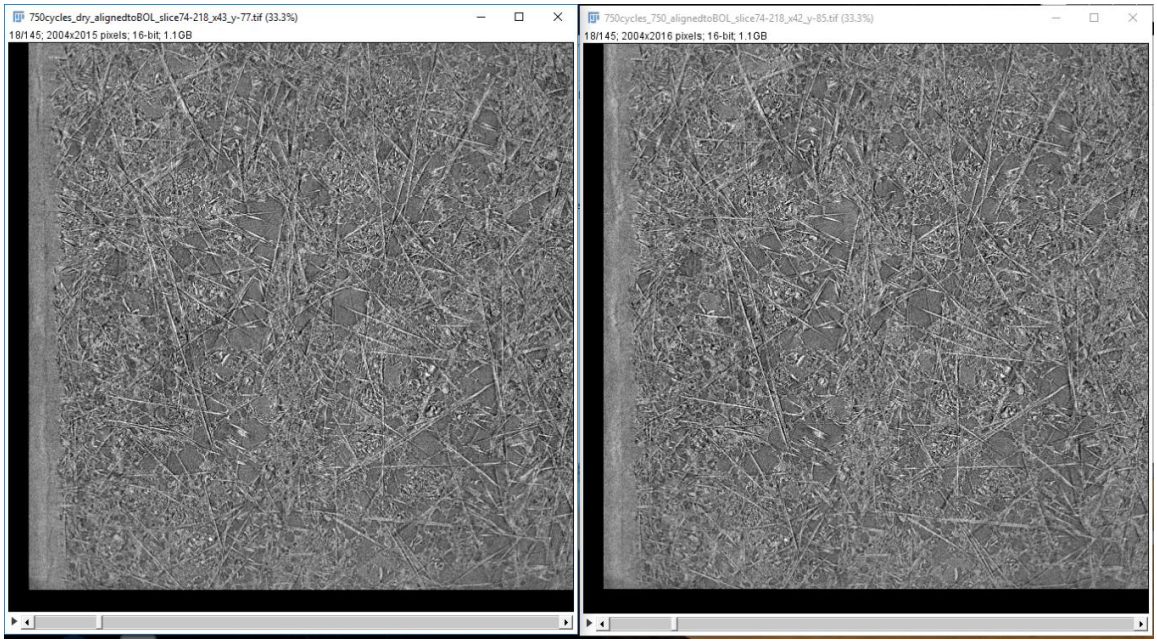

Figure A4: Final image stacks aligned to ref image stack (not shown) for two separate image stacks after 750 AST cycles (left) and after AST cycles with current drawn (right). Highlights repeatability of the above procedure across multiple image stacks.

Appendix B.

Cathode Catalyst Layer Segmentation

Preprocessing image stacks

Although it is not required, running noise removal such as 3D median filter can be used to improve results, this will need to be determined by the user and should be consistently applied to any subsequent image sets which are used for comparison. Rotation correction in the X and Y planes (Tilt) is also not completely necessary but will help with segmentation and analysis later.

Crop

First cropping is performed to reduce image size. See Appendix A for further details. In this example we will use a sample which is not housed in the small-scale fixture for comparison. A region of interest (ROI) is cropped and shown below; where a reference side used in tilt/rotation is also included.

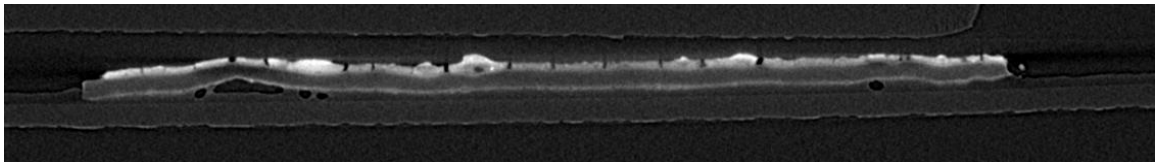

Figure B1: Dataset cropped to region of interest with holder included to be used as reference since catalyst layer is not flat.

Following details outlined in Appendix A, the result is to be able to have the full catalyst layer in a single slice. This however is often not fully achieved since parts of the catalyst layer may be differently rotated than others. It is up to the user to decide on how to get as much of the catalyst layer in a single slice as possible. As was mentioned, these steps are not absolutely necessary, and the separator macro will run well without them. Below shows a comparison with and without rotation and tilt correction of a single through-plane slice through the cathode catalyst layer.

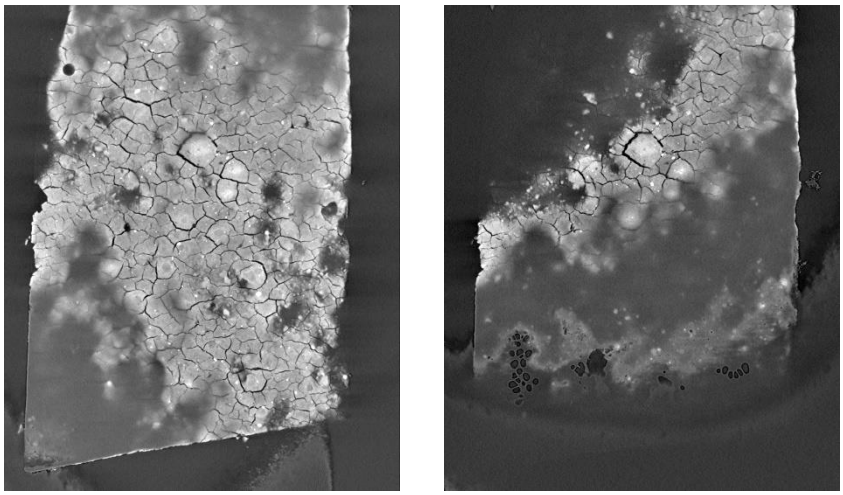

Figure B2: [Left] With tilt/rotation correction as outlined above [Right] Without correction. As can be seen a better view of the catalyst layer is achieved after correction.

Thresholding

Although thresholding can be performed a number of different ways, a simple and repeatable method is to utilize some user input and automated assignment of threshold value. One method is to use the ROI tool in ImageJ to select a region such that two gaussian peaks are distinguishable, i.e. as shown below. This can then easily allow for a thresholding algorithm to separate the two gaussians and give a good threshold value, shown below.

Here IsoData algorithm is used (Ridler, TW & Calvard, S (1978), "Picture thresholding using an iterative selection method", *IEEE Transactions on Systems, Man and Cybernetics* **8**: 630-632) however the separation algorithm is not sensitive to the thresholding method used and can be determined from user preference, as long as it is consistently applied and stated.

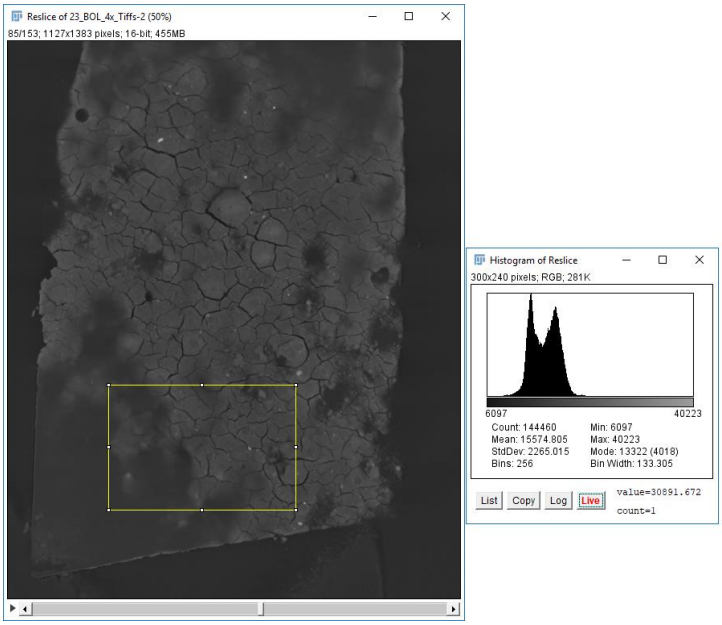

Figure B3: Sample location used for auto-thresholding with clear gaussian peaks shown for separation of catalyst layer and air/membrane

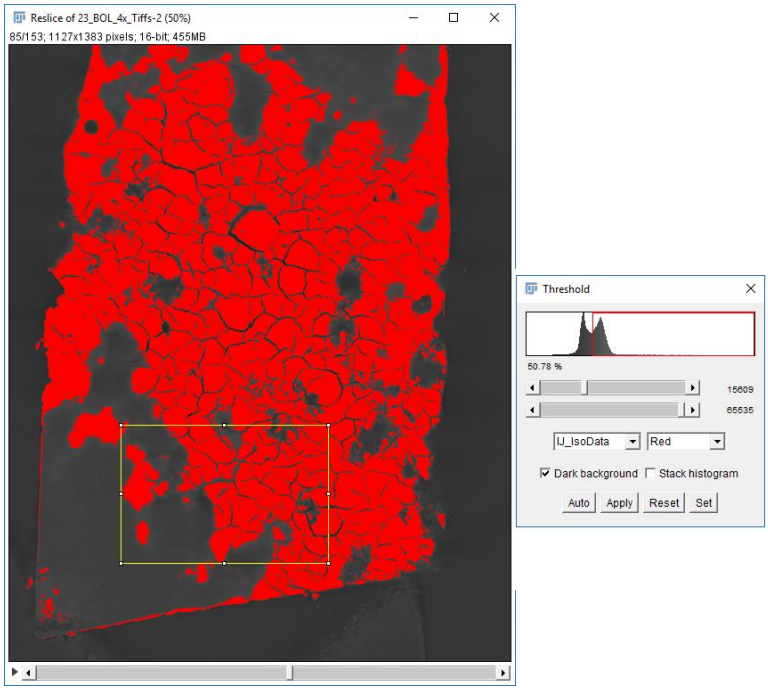

Figure B4: IsoData algorithm used for separation of gaussian peaks for automated segmentation of catalyst layer.

The following shows the initial result following thresholding. As can be seen from the orthogonal views, poor isolation (segmentation) of the cathode catalyst layer is performed with much of the anode remaining in view. This will be even more prominent if GDL fibres are also present. Next, we will run the Cathode Separator macro to clean up the segmentation.

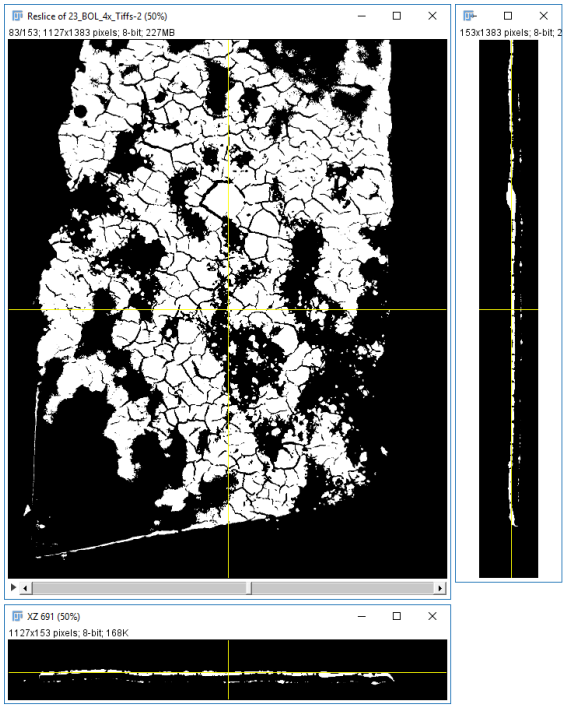

Figure B5: Resulting segmentation shown for all 3-planes. Note some of the additonal noise from anode catalyst layer.

Cathode Separator

The script will first run through a generic noise removal by despeckle and median filters. Once this completes, the macro applies a gaussian blur which acts to connect the cathode into one object. The user is prompted to select a threshold which is used to define the connected catalyst layer. The threshold should be chosen such that the cathode is fully connected and not touching other components, an example is shown below:

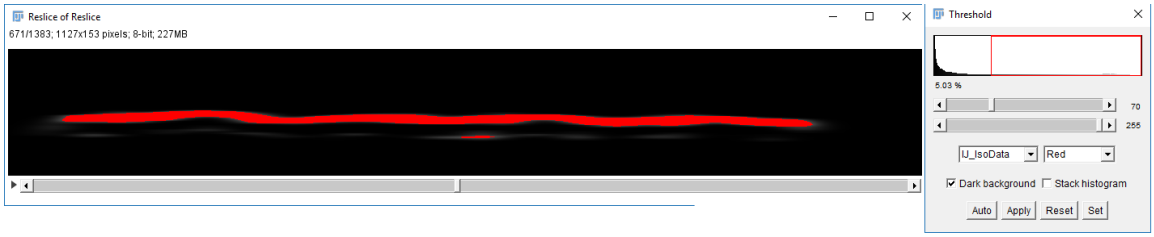

Figure B6: Following gaussian blurring to connect cathode catalyst layer in x-z plane, user is prompted to select a threshold.

Following this the script will use particle labeler from BoneJ to select the largest volume object only. It will subsequently output the cathode isolated as well as a thickness image, which is the sum of pixels in the through-plane direction. This can later be multiplied by the pixel size in microns to yield a real thickness.

The following are example outputs:

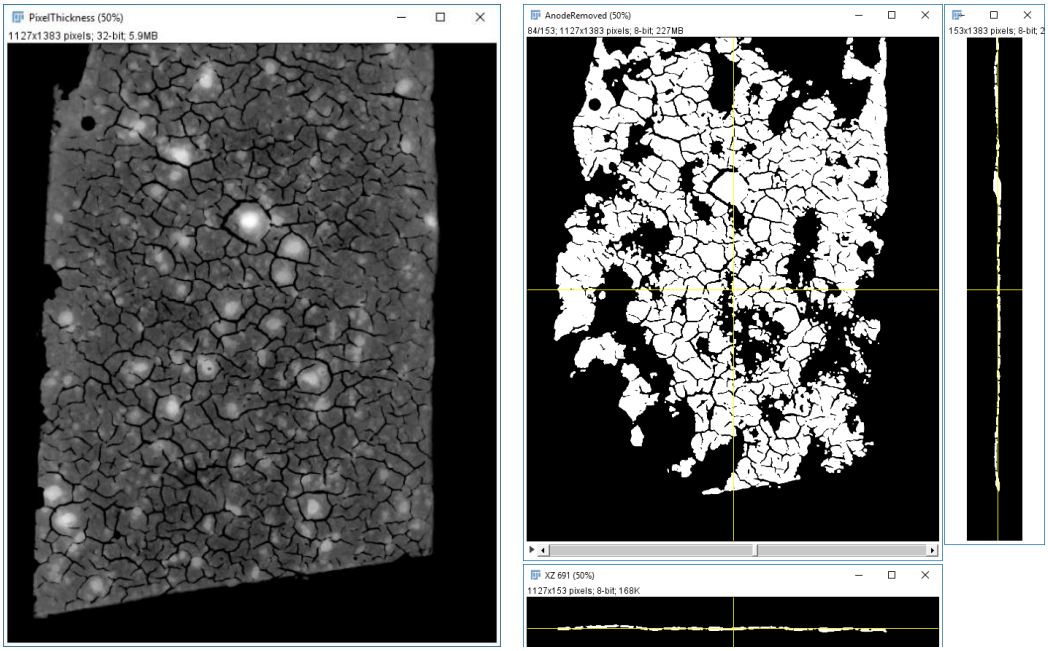

As can be seen the anode noise has been cleanly removed and we have accurate segmentation of the cathode catalyst layer for further analysis.

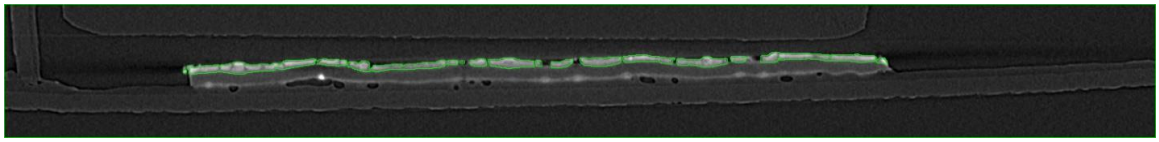

Figure B8: Comparison of result on original greyscale image with segmentation outlined in green to assist user with hecking accuracy.

Figure B7: [Left] 2D image showing local thickness following completion of separation algorithm. [Right] 3D dataset segmentation, note the removal of the anode noise without removing fine details of cathode catalyst layer.

Appendix C.

Gaussian Mixed Model for cathode catalyst layer analysis

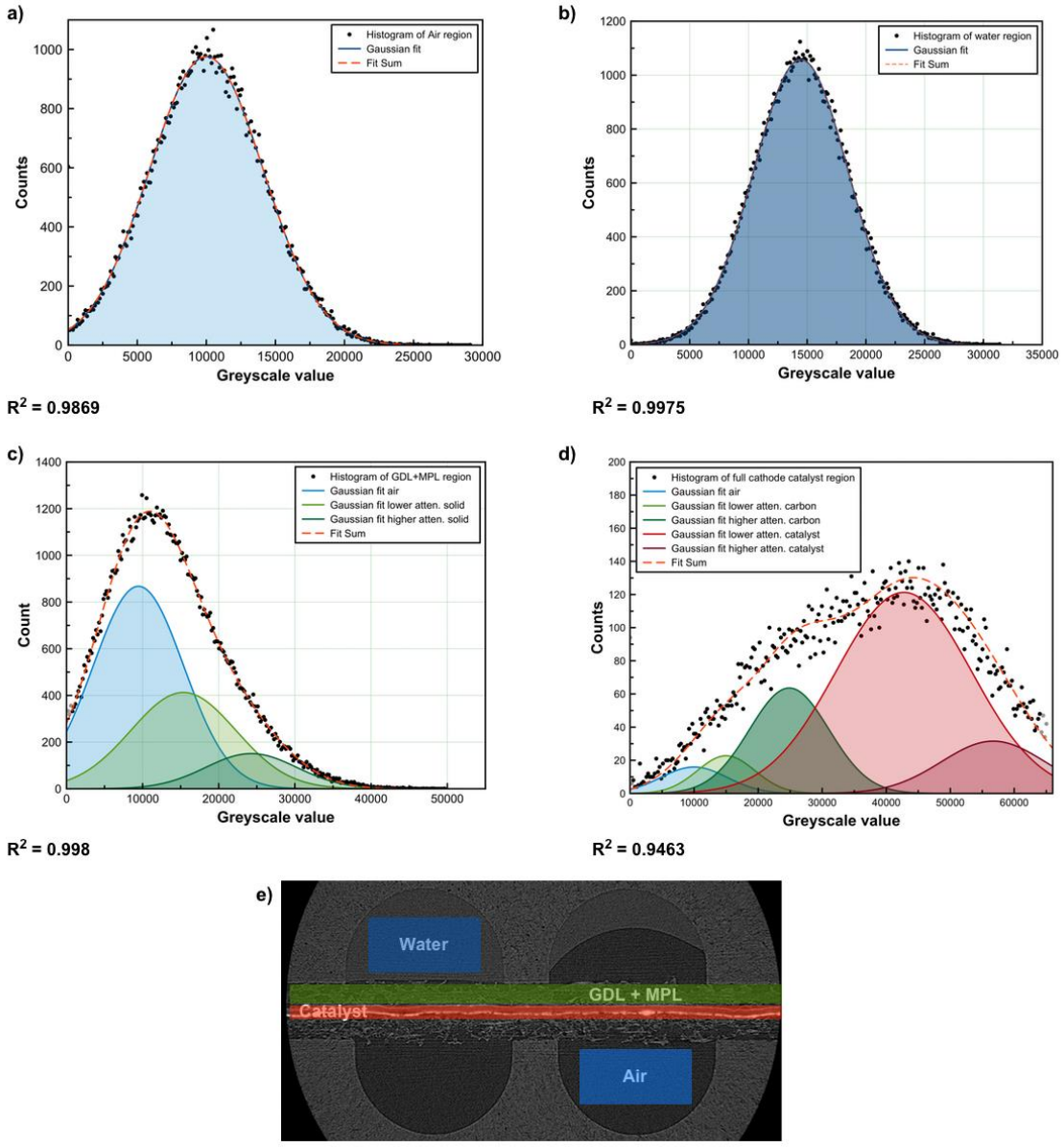

Figure C1: Histogram curve fitting of different parts of the fuel cell assembly from the X-ray attenuation spectrum measured by micro-XCT: a) air; b) liquid water; c) GDL/MPL; d) CCM; and e) supporting illustration showing the relevant sections used for the histograms in each case.

Appendix D.

Porosity Distribution Through GDL Under Land and Channel

An automated script that sections areas under land and channel regions was developed. A result of this is shown in Figure D1 used for analysis in Chapter 7. Porosity is determined by segmentation of the cathode GDL structure from 'dry' beginning-of-life and is shown for the specific areas under land and channel in Figure D1. The land boundary is indicated by the dotted line and the distance is relative to the surface of the GDL in the channel.. A noticeable decrease in porosity is observed for the region of approximately 15 µm below the edge of the land, indicating compression reduced pore size. Higher variation under the land also indicates variation in pore sizes dependent on the reaction of GDL regions under compression; that is, how much the compression pressure affects that particular region of the GDL. Additionally, the impact of compression is partially extended to the channel region, as seen by the small dip in porosity after the start of the land (dotted line in Figure D1). The GDL region close to the catalyst layer including certain portions of the microporous layer (MPL) cannot be accurately segmented due to the limit on resolution and is hence treated as solid.

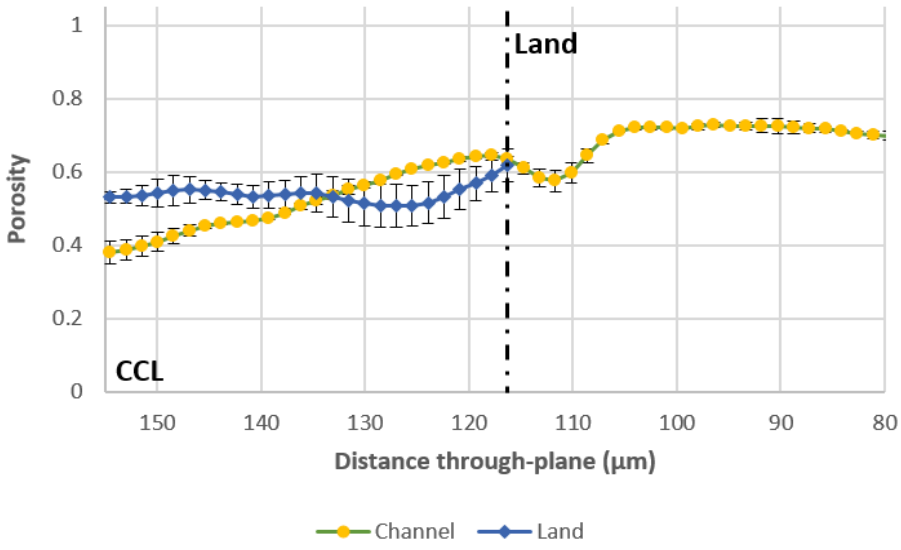

Figure D1: Porosity measurement of the cathode gas diffusion layer under land and channel regions from segmentation of the XCT image dataset obtained in the 'dry' beginning-of-life state.